UNIVERSITÀ DEGLI STUDI DI PADOVA

CENTRO INTERDIPARTIMENTALE *"CENTRO RICERCHE FUSIONE"*

INSTITUTO SUPERIOR TÉCNICO

JOINT RESEARCH DOCTORATE IN FUSION SCIENCE AND ENGINEERING

CYCLE XXVII

Beam emission spectroscopy studies in a H⁻/D⁻ beam injector

Coordinator:	Prof. Paolo Bettini
Academic supervisor:	Prof. Piergiorgio Sonato
Co-supervisors:	Dr. Lorella Carraro
	Dr. Barbara Zaniol
	Dr. Roberto Pasqualotto

PhD student: Marco Barbisan

The science of today is the technology of tomorrow.
Edward Teller

Contents

Abstract

The limited availability of the present energetic resources and the climate changes induced by the increase of the level of CO_2 in the atmosphere are pushing humanity to completely rethink the ways to produce and consume energy. In the long term, a significant contribution to the solution of the world energy issue may come from nuclear fusion: the raw materials, deuterium and lithium, are worldwide accessible and in sufficient quantity to feed the future fusion reactors for several centuries.

The largest fusion experiment is ITER, in phase of construction in France. The ITER machine is designed to produce a fusion power of $500\,MW$, 10 times the input power. Moreover ITER will be the first experiment to continuously operate with deuterium-tritium plasmas, and will have to stand the neutron irradiation produced by nuclear fusion. To reach the desired performances various additional heating systems are foreseen to heat the plasma core up to $10 \div 15\,keV$. One of the most important heating systems will be composed by 2 neutral beam injectors (NBIs), which produce 2x16.7 MW beams, composed by H/D atoms. To obtain the beams H⁻/D⁻ ions produced by an ion source will be accelerated at high energy (870 keV for hydrogen, 1 MeV for deuterium) and then neutralized thanks to the charge exchange interaction with the molecules of a H_2/D_2 gas. The construction of such a system is very challenging and 2 prototypes will be built and tested in Padua at Consorzio RFX. The first one, SPIDER (*Source for the Production of Ions o Deuterium Extracted from an Rf plasma*), operative in 2016, aims at studying the source part of the NBI, accelerating ions at lower energies, up to $100\,keV$. The prototype of the full ITER negative NBI system is MITICA (*Megavolt ITer Injector Concept and Advancement*), it will start operating in 2019. Both SPIDER and MITICA will be equipped with a large number of diagnostics: in particular, the Beam Emission Spectroscopy (BES) will measure the spectrum of the radiation produced by the beam when interacting with the background gas in order to measure the divergence and the uniformity of the beam produced by the ion source. The divergence is a key parameter for the safety of the test facilities, since it is related to the power deposition of the beam on the beam line component. The beam uniformity is crucial for the heating effectiveness of the beam itself.

The PhD activity was mostly devoted to develop the BES diagnostics of SPIDER and MITICA, with the target to measure divergence in the range $3 \div 7\,mrad$ (e-folding) with a relative error below 10%, and values of uniformity in the range $90 \div 100\%$. In particular, the work consisted in:

- developing a set of codes (dBES) for the simulation of the behavior of the BES diagnostics;

- studying and improving the methods of analysis for the data that will be collected by BES.

- completing the design of the BES diagnostics, also selecting and testing its hardware components;

Experimental data of the test facilities BATMAN (*BAvarian Test MAchine for Negative ions*), MANITU (*Multi Ampere Negative Ion Test Unit*) and ELISE (*Extraction from a Large Ion Source Experiment*) at the Max Planck Institut für Plasmaphysik (IPP) in Garching, have been used to validate the numerical model at the base of dBES and to improve the method of analysis of the BES spectra. During my stays at the ITED group of IPP Garching the results of dBES were also benchmarked against those of the BBC-NI code, developed at IPP for similar purposes.

Besides SPIDER and MITICA the studies were also addressed to NIO1 (*Negative Ion Optimization 1*), hosting an RF ion source which produces a 130 mA beam composed by H⁻ ions. The test facility was jointly built by Consorzio RFX and INFN-LNL, with the aim of studying and improving the production of negative ions, as well as testing concepts and instrumentation for SPIDER and MITICA. For NIO1 the BES diagnostic was entirely designed; the tests on NIO1 of this diagnostic will allow a first experimental validation of the design of those for SPIDER and MITICA.

The PhD research is described in this thesis as follows:

- Chapter 1 gives a briefly describes the ITER reactor. The principle of operation of the neutral beam injectors is then explained, together with the characteristics of the considered experiments: SPIDER and MITICA, BATMAN, MANITU, ELISE and NIO1. The main diagnostics installed in the negative ion sources and more generally in the NBIs are presented, too.

- Chapter 2 describes the work done on the simulation codes dedicated to Beam Emission Spectroscopy. The physical phenomena at the base of the BES diagnostic operation are explained. The code dBES, developed for the simulation of the BES diagnostic and for the analysis of its measurements, is described. dBES is then benchmarked against the BBC-NI code and with the experimental data of the BES diagnostics in the BATMAN, MANITU and ELISE test facilities.

- Chapter 3 presents the design of the BES diagnostics in the experiments NIO1, SPIDER and MITICA, carried out by means of the dBES code.

- Chapter 4 presents the experimental activities carried out to test the available instrumentation for the BES and the optical emission spectroscopy diagnostics in NIO1, SPIDER and MITICA; the design activity of some components is also illustrated.

- The summary is reported in chapter 5. There follows the list of the articles published and of the technical notes written during the PhD.

Prefazione

La disponibilità limitata delle attuali risorse energetiche e i cambiamenti climatici indotti dall'aumento della concentrazione di CO_2 nell'atmosfera impongono all'umanità di ripensare completamente i modi di produrre e consumare energia. Nel lungo termine, un contributo importante alla soluzione del problema energetico mondiale potrebbe arrivare dalla fusione nucleare: le materie prime, deuterio e litio, sono accessibili in tutto il globo e in quantità sufficiente per alimentare i futuri reattori a fusione per diversi secoli.

Il più grande esperimento a livello mondiale sulla fusione è ITER, in fase di costruzione in Francia. ITER è progettato per produrre dalla fusione fino a $500\,MW$, 10 volte la potenza in ingresso. Inoltre, ITER sarà il primo esperimento a operare permanentemente con plasmi di deuterio e trizio, quindi conterrà materiale radioattivo (il trizio) e dovrà sopportare l'irraggiamento neutronico prodotto dalla fusione nucleare. Per raggiungere le prestazioni volute serviranno varie forme di riscaldamento addizionale, in modo da portare la temperatura centrale del plasma a $10 \div 15\,keV$. Uno dei sistemi di riscaldamento più importanti sarà costituito da 2 iniettori di neutri (NBI), che producono fasci da $16.7\,MW$ composti da particelle neutre (H/D). Per ottenere i fasci ioni H$^-$/D$^-$, prodotti da un'apposita sorgente, verranno accelerati ad energie elevate ($870\,keV$ per l'idrogeno, $1\,MeV$ per il deuterio) e successivamente neutralizzati grazie alle reazioni di scambio carica con le molecole di un gas di idrogeno/deuterio. Costruire un sistema simile è un'operazione complessa, per questo 2 prototipi saranno costruiti e testati a Padova presso il Consorzio RFX. Il primo, SPIDER (*Source for the Production of Ions o Deuterium Extracted from an Rf plasma*), che sarà operativo dal 2016, verrà utilizzato per studiare la produzione e accelerazione (fino a $100\,keV$) degli ioni negativi. Il secondo sarà il prototipo di un intero iniettore di neutri per ITER, MITICA(*Megavolt ITer Injector Concept and Advancement*), che entrerà in funzione nel 2019. Sia SPIDER che MITICA saranno dotati di un gran numero di diagnostiche: in particolare, la Beam Emission Spectroscopy (BES) misurerà lo spettro della radiazione prodotta dall'interazione tra fascio e gas di fondo, con lo scopo di misurare la divergenza e l'uniformità del fascio prodotto dalla sorgente di ioni. La divergenza è un parametro chiave per la sicurezza degli impianti, poichè è legata alla potenza depositata dal fascio sulle strutture degli esperimenti. L'uniformità del fascio è cruciale per l'efficacia del fascio stesso nel riscaldamento del plasma.

L'attività di dottorato è stata dedicata in gran parte a sviluppare le diagnostiche BES di SPIDER e MITICA, con l'obiettivo di misurare la divergenza nell'intervallo $3 \div 7\,mrad$ (e-folding) con un errore relativo sotto il 10%, e valori di uniformità nell'intervallo $90 \div 100\%$.

In particolare, il lavoro è consistito nel:

- sviluppare un set di codici (dBES) per la simulazione del comportamento della diagnostica BES;

- studiare e migliorare i metodi di analisi dei dati che saranno raccolti dalla BES;

- completare il design della diagnostica, anche individuando e testando la sua componentistica hardware;

Le misure raccolte negli impianti sperimentali BATMAN (*BAvarian Test MAchine for Negative ions*), MAN-ITU (*Multi Ampere Negative Ion Test Unit*) ed ELISE (*Extraction from a Large Ion Source Experiment*) al Max Planck Institut für Plasmaphysik (IPP) a Garching, sono state utilizzate per validare il modello numerico alla base di dBES a per migliorare il metodo di analisi degli spettri BES. Durante le visite al gruppo ITED di IPP Garching i risultati di dBES sono stati confrontati con quelli del codice BBC-NI, sviluppato a IPP per scopi analoghi.

Oltre che su SPIDER e MITICA gli studi si sono concentrati anche su NIO1 (*Negative Ion Optimization 1*), dotato di una sorgente RF che produce un fascio di $130\,mA$ composto da ioni H^-. L'esperimento è frutto di una collaborazione tra Consorzio RFX e INFN-LNL, con lo scopo di studiare e migliorare la produzione di ioni negativi, nonchè di testare la strumentazione per SPIDER e MITICA. Per NIO1 è stata interamente progettata la diagnostica BES; i test su NIO1 di questa diagnostica permetteranno una prima verifica sperimentale del design delle diagnostiche analoghe per SPIDER e MITICA.

Il lavoro di dottorato è descritto nella tesi come segue:

- Il capitolo 1 fornisce una breve descrizione del reattore ITER. Viene poi illustrato il principio di funzionamento degli iniettori di neutri, nonchè le caratteristiche dei esperimenti presi in considerazione: SPIDER e MITICA, BATMAN, MANITU, ELISE e NIO1. Vengono inoltre presentate le principali diagnostiche installate nelle sorgenti di ioni negativi e più in generale negli iniettori di neutri.

- Il capitolo 2 descrive il lavoro svolto sui codici di simulazione per la Beam Emission Spectroscopy. Vengono illustrati i fenomeni fisici alla base del funzionamento della diagnostica. Viene successivamente presentato il codice dBES, sviluppato per la simulazione della diagnostica BES e per l'analisi dei dati raccolti dalla diagnostica stessa. Segue la verifica delle simulazioni di dBES con i risultati del codice BBC-NI e con i dati delle diagnostiche BES negli esperimenti BATMAN, MANITU ed ELISE.

- Il capitolo 3 presenta il design delle diagnostiche BES per gli esperimenti NIO, SPIDER e MITICA, realizzato con il supporto del codice dBES.

- Il capitolo 4 presenta le attività sperimentali svolte per caratterizzare la strumentazione disponibile per le diagnostiche BES e optical emission spectroscopy in NIO1, SPIDER e MITICA; viene illustrata anche la progettazione di alcune componenti delle diagnostiche.

- Nel capitolo 5 vengono sintetizzati e discussi i risultati presentati nella tesi. Seguono infine la lista degli articoli pubblicati e delle note tecniche scritte durante il dottorato.

Chapter 1

Introduction

1.1 Why do we need fusion?

The research on nuclear fusion draws its motivations from the growing need of energy of the mankind. The current sources of energy, mainly fossil fuels, are not infinite: according to the present estimates[1] the reserves of coal, crude oil and natural gas, with the present rate of consumption, should last for respectively more than one century, 56 and 60 years. There are several reasons to stop using these fuels much earlier than their depletion. The first one is that these sources are too precious to be simply burnt: oil, for example, is the most important raw material for the production of plastic and many organic chemical substances. The second reason is that the world population is growing: as shown in figure 1.1, according to the statistical models adopted by the United Nations[2] the number of people on Earth should increase from 6.1 billions in 2000 to 8.9 billions (with an interval of confidence from 7.4 to 10.6 billions) in 2050. Substantially, each year the world population grows of an amount of people comparable to the population of Italy.
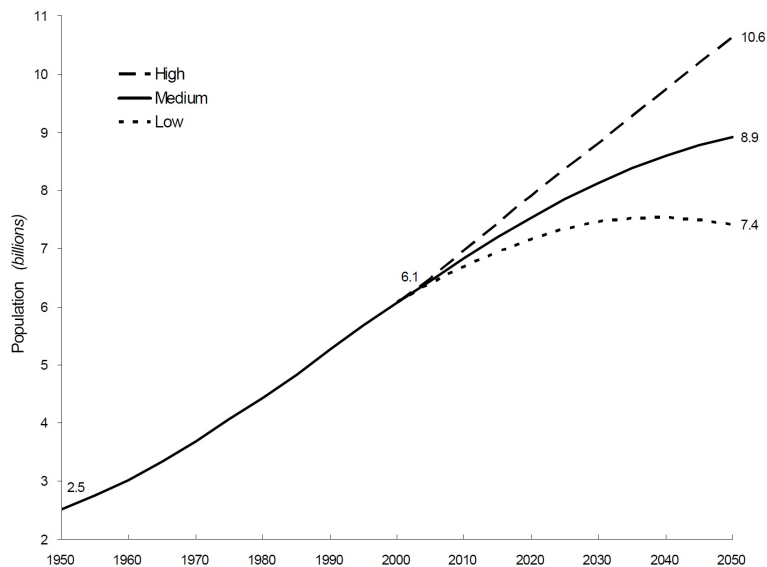
Figure 1.1: Estimated world population, 1950-2000, and projections: 2000-2050 [2]

The world energy consumption is then destined to increase, but much more than proportionally to the population growth. 99% of the demographic growth will come from the less developed countries. As shown by statistics[3], improving the quality of life of the people up to a decorous level implies

an increase of the energy consumption *per capita*, therefore a future (and desirable) amelioration of the conditions of the less developed countries will require a further increase of the availability of energy sources.

The research on fusion is not simply due to the limitedness of the fossil fuels: even if they were available in unlimited amounts, it must be taken into account that burning these fuels contributes to the increase of the concentration of greenhouse-gases (GHG) in the atmosphere. Figure 1.2 shows the origin of the main green-house gases produced by human activities; as it can be seen, the main contribution to the global warming is related to the energy production. Similarly to the reasoning done before, a higher quality of life implies a higher (but not always more justified) production of green-house gases, therefore a (rightful) improvement of the welfare of the less developed countries will imply extra emissions in the atmosphere.
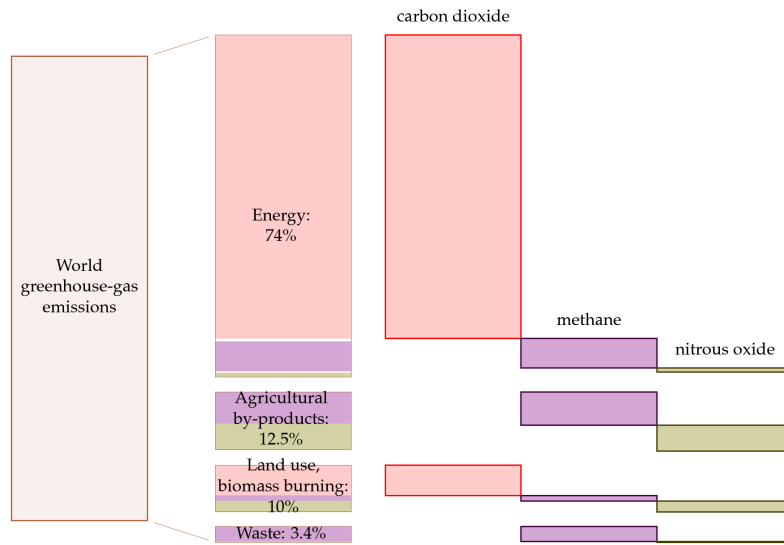
Figure 1.2: Breakdown of world greenhouse-gas emissions (2000) by cause and gas [4].

In conclusion, the energetic needs of mankind are constantly growing and must be satisfied avoiding further emissions of greenhouse gases. The renewable sources of energy are the most immediate solution to the problem, however they are inconstant in time and to collect enough energy the plants should be spread over too large areas. Nuclear fusion technology, according to the present forecast, will be available from the middle of the XXI century; the production of energy is based on the following possible reactions:

$$
\begin{aligned}
{}^{2}D + {}^{2}D &\overset{50\%}{\Rightarrow} {}^{3}He\,(0.82\,MeV) + n\,(2.45\,MeV) \\
{}^{2}D + {}^{2}D &\overset{50\%}{\Rightarrow} {}^{3}T\,(1.01\,MeV) + {}^{1}H\,(3.02\,MeV) \\
{}^{2}D + {}^{3}T &\Rightarrow {}^{4}He\,(3.5\,MeV) + n\,(14.1\,MeV) \\
{}^{2}D + {}^{4}He &\Rightarrow {}^{4}He\,(3.6\,MeV) + {}^{1}H\,(14.7\,MeV)
\end{aligned}
\tag{1.1}
$$
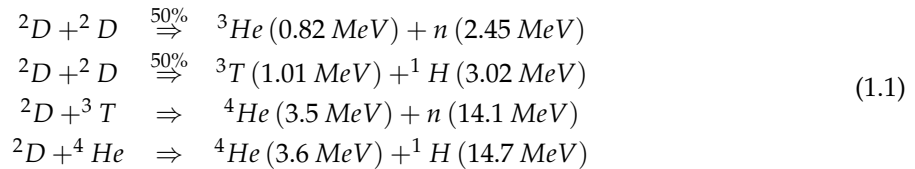
Figure 1.3 shows the dependence of the considered reactions as function of the energy of the deuterium atom, assuming that the other atom is at rest. As it can be seen, the reaction with the highest cross section at low temperature ("low" in relation to the other ones) is the one involving deuterium and tritium.

Deuterium is present in the water of the oceans in a concentration of 33 *g* per ton: the total available quantity of deuterium is practically limitless respect to the needs for the future fusion reactors. Tritium instead is rather rare on Earth, but can be obtained by using lithium and the neutrons produced by the fusion reactions themselves:

$$
n + {}^{6}Li \Rightarrow {}^{4}He\,(2.1\,MeV) + {}^{3}T\,(2.7\,MeV)
\tag{1.2}
$$
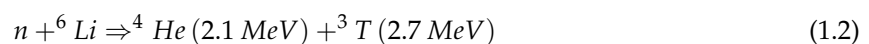
The availability of lithium sets a limit to the "era" of DT reactors: considering only the ore deposits the lithium should be enough (if entirely used only for fusion) for less than 1000 years [5]. This time limit could be extended to more than 20 million years if it were possible to extract lithium from seawater. In any case, the time of DT reactors will be enough to prepare the coming of the subsequent generation of reactors, which will exploit the reactions with only deuterium (extremely more abundant). The research on fusion, even if long and difficult, will give mankind access to a practically limitless source of energy.

Figure 1.3: Cross sections of the possible fusion reactions[6]. The curve "D-D" represents the sum of the cross section for the first two reactions listed in formula 1.1.

1.2   Magnetic confinement experiments: ITER

Currently the most important step on the road of fusion research is represented by the experiment ITER, in course of construction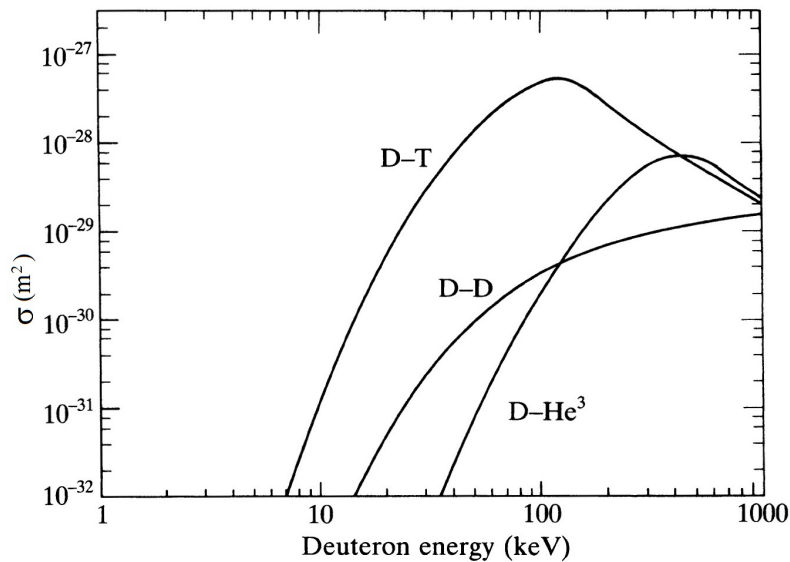 in Cadarache (FR). Its project was signed in 2006 by the European Union, the USA, Russia, China, India, South Corea, Japan; the beginning of the experimental activity is scheduled for 2020. In ITER the reactants of the fusion reaction (deuterium and tritium) reach temperatures at which their atoms are ionized in form of plasma; this is confined in the toroidal chamber of the reactor by means of magnetic fields. ITER will be the first reactor to operate for most of its lifetime with deuterium-tritium mixtures; the reactor will then contain a non negligible quantity of radioactive material, therefore it will have to respect all the safety rules foreseen for nuclear plants. Anyway, the decay time of the involved radioactive materials is much shorter than to that of the substances present in a fission reactor: the half-life of tritium is only 12 years, while the plasma facing components, with a proper choice of the materials, should remain radioactive for about one century. The levels of radioactivity and the risk of contamination impose that the internal maintenance will have to be performed remotely.

Besides the presence of tritium, the plasma facing components (PFC) will undergo high fluxes of heat and neutron irradiation (produced by fusion). The first wall will be covered with boron, carbon and tungsten (according to the position in the vacuum chamber) to avoid contaminating the plasma. The structure will have to resist to intense mechanical and thermal stresses caused by the plasma instabilities: in ITER the plasma volume ($\sim 10^3\ m^3$, major radius 6.2 m, minor radius 2.0 m) is much higher than in the previous fusion experiments, therefore the thermal and magnetic energy which could be released during plasma instabilities is much higher and could produce severe damages. The systems of real time survey and control of the plasma instabilities will have a fundamental role in the reliability and

availability of the reactor.

The magnetic confinement will follow the tokamak scheme: a strong toroidal magnetic field (5.3 T in center of the torus) plus a poloidal field one order of magnitude weaker; this will be generated by the plasma current itself (max. 15 MA) and by the six poloidal field coils, made with the superconducting material NbTi. The toroidal field will be instead produced by 18 coils, made in Nb_3Sn (always super-conductive); this material will be adopted also for the central solenoid, needed to induce the plasma current. All the coils will be kept at 4°K to reach superconductivity.
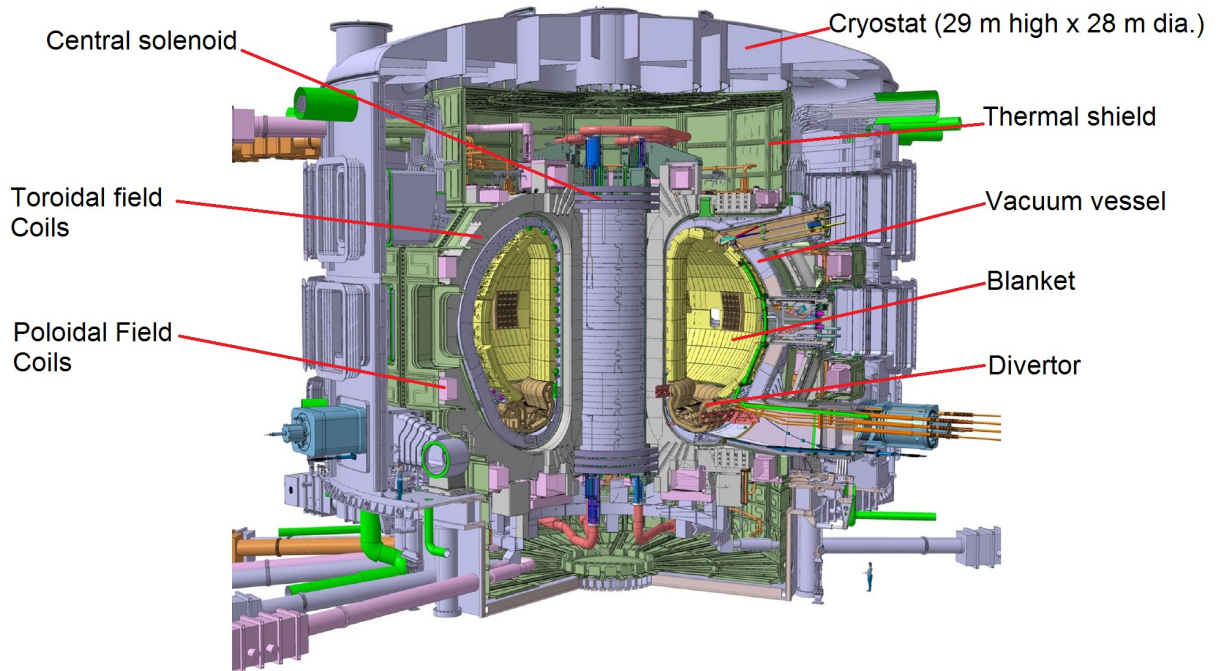
Figure 1.4: 3D representation of the ITER reactor.

Between the coils and the first wall there will be the blanket, to shield the coils from heat and radiation fluxes coming from the plasma. ITER will be provided with a divertor for the removal of impurities and helium (produced by the fusion) from the plasma; the divertor will be the plasma facing component (PLC) subject to the most instense heat fluxes, in the order of several MW/m^2.

On the whole, ITER will have to produce up to 500 MW, 10 times more than the power requested in input by the reactor. In addition to all the physical and technological challenges described previously, in ITER possible solutions will be studied to obtain a continuous mode operation; moreover, possible systems to produce and extract tritium inside the reactor itself will be studied. A 3D representation of the main components of the ITER reactor is shown in figure 1.4. The results of ITER will be used to prepare the first fusion power plant: DEMO.

1.3   Neutral beam injectors

The ITER experiment will have to produce up to 10 times more power than the one given in input. The energetic performance of a reactor is function of the triple product $nT\tau_E$, where the 3 quantities are respectively the average density, the average temperature and the energy confinement time of the plasma. Figure 1.5 shows the triple product and the plasma temperature which will be reached in ITER with respect to the existing tokamas.

Figure 1.5: Typical values of temperature and triple product (plasma average density times the average temperature and the energy confinement time) reached in ITER and many present and past experiments [7]. The year at which these values were obtained is indicated in the right vertical axis. Q is the ratio between the output and the input power in the reactors.
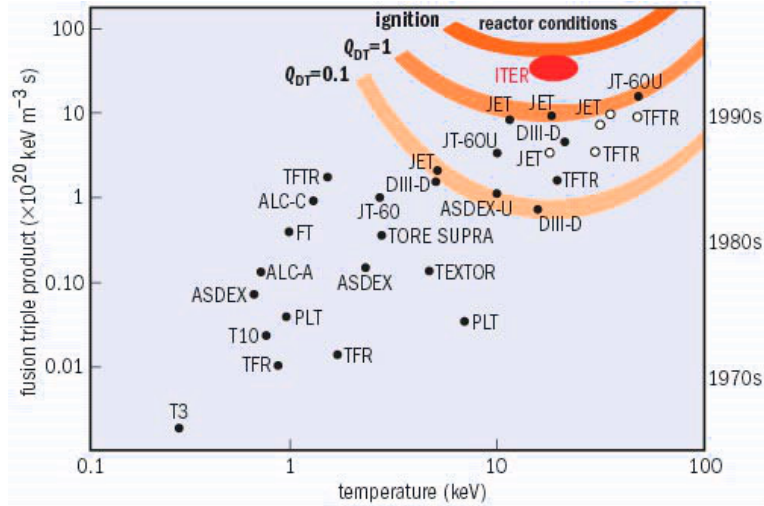
To reach such performances in terms of plasma temperature and confinement, ITER will heat the plasma with the ohmic heating (i.e. resistive dissipation of the plasma current) plus a number of additional systems: radiofrequency heating and neutral beam injection. The first method consist in injecting radiowaves in order to excite specific resonances of electrons, of ions or of the whole plasma. According to the type of resonance, the systems are called ECRH (Electron Cyclotron Resonance Heating), ICRH (Ion Cyclotron Resonance Heating) and LH (Lower Hybrid heating); each one should deliver up to 20 *MW* to the plasma. Neutral beam Injectors instead inject a beam of high energy deuterium or hydrogen atoms into the plasma; simple hydrogen is not useful for deuterium-tritium reactions, however it will be used in the first phase of the operations in ITER to not immediately activate the materials. In ITER two NBIs are foreseen[1], each one delivering 16.7 *MW*. Both NBIs and RF systems are used not only to increase the plasma temperature but also to drive more current in the plasma (from 1.8 *MA* to 2.8 *MA* [8]). This will be useful to modify the $q(r)$ profile, counteract the growth of instabilities and to increase the duration of the discharges towards a steady state operation.

To be effective, a neutral beam must interact with the plasma to release its energy. The penetration depth of the beam must be not too short, otherwise only the plasma edge would be heated, but neither too long, otherwise the beam would cross the plasma and damage the opposite side of the first wall. The beam particle could undergo a charge exchange process with the plasma ions, or be ionized by collision with the electrons and the ions in the plasma. The energy of the beam particles influence the cross sections of these processes, and therefore the mean free path (or penetration distance) λ_{path} of the particles themselves into the plasma:

$$\lambda_{path} = \frac{1}{n\sigma_{tot}} \tag{1.3}$$

where n is the plasma density and σ_{tot} is the comprehensive cross section of the 3 above mentioned reactions. In ITER the plasma has a density of the order of 10^{20} m^{-3} and a radius of about 2 *m*: this length must be compared with λ_{path}, shown in figure 1.6 as function of the energy of the beam particles (in the case of deuterium). The best match between the plasma dimensions and the penetration of the beam is found assuming that the beam particles have an energy around 1 *MeV*.

---

[1]If it were necessary, in ITER there is also the possibility to install a third NBI.
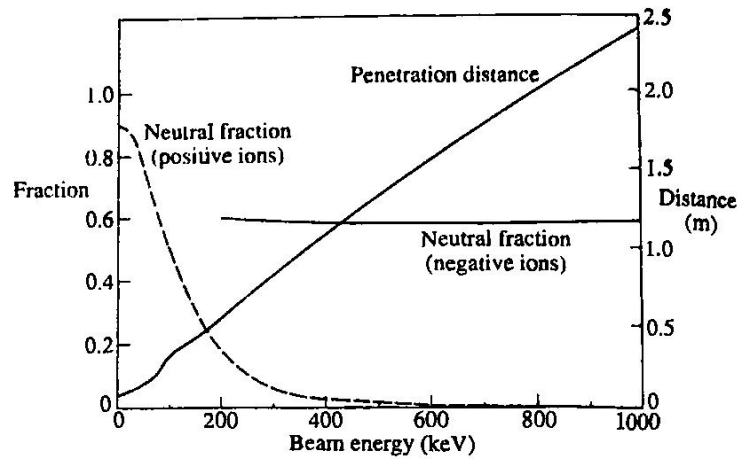
Figure 1.6: Best neutralization fraction obtainable for positive and negative deuterium ions as function of their energy[6]. The plot shows also the penetration distance of the negative deuterium atoms into an hypothetical plasma of density 10^{20} m^{-3}.

Most of NBIs are based on a positive ion source, and the resulting H^+/D^+ ions are neutralized by charge exchange with the molecules of a gas of hydrogen/deuterium. The same collisions however can cause the reionization of the just neutralized particles: in the end, the fraction of neutralized to positive particles in the beam is given by the ratio of the cross sections of neutralization and reionization. The dependence of this ratio on the energy of the fast particles is shown in figure 1.6. As it can be seen, at high energy the reionization prevails and it is not possible to obtain a neutral beam. For this reason the new generation of high energy NBIs are based on negative ion sources; in this case the collisions with the molecules of the gas mix the composition of the beam between the ionic species D^-, D^0 and D^+. The resulting neutralization fraction, as shown in figure 1.6, remains high also at energies of several hundreds of *keV* or even at 1 *MeV*, but without ever exceeding 60 %.

The NBI for ITER is composed by 4 stages: production and acceleration of (negative) ions, neutralization of the beam, removal of the residual ions and transfer of the beam to the tokamak, retaining also the possibility to stop the beam for maintenance or diagnostic purposes. Each stage corresponds to a specific device inside the NBI, respectively the negative ion source with the accelerator stage, the neutralizer, the RID (Residual Ion Dump) and the calorimeter (figure 1.7). Here follows a brief description of these devices.
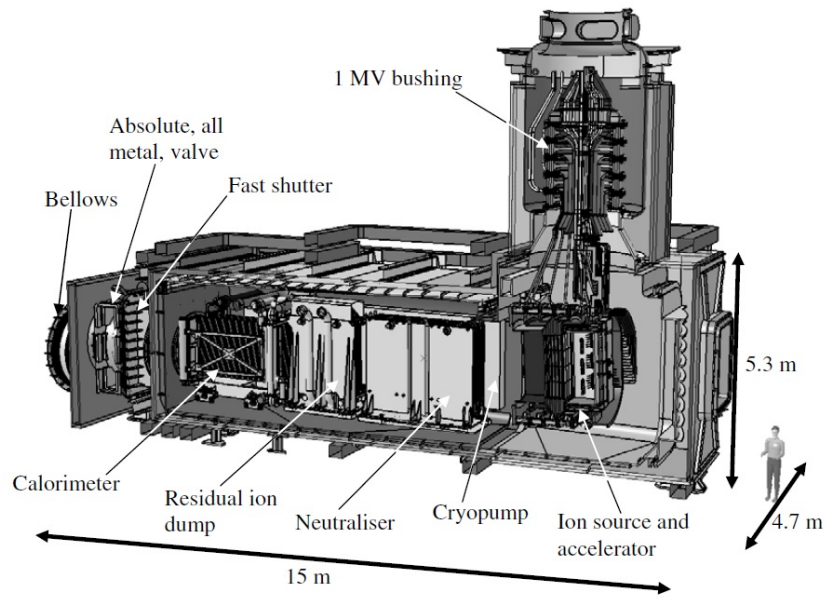
Figure 1.7: Structure of a NBI for the ITER reactor [9].

1.3.1 The negative ion source and the accelerator

The negative ions are produced by a source whose typical structure is schematized in figure 1.8.
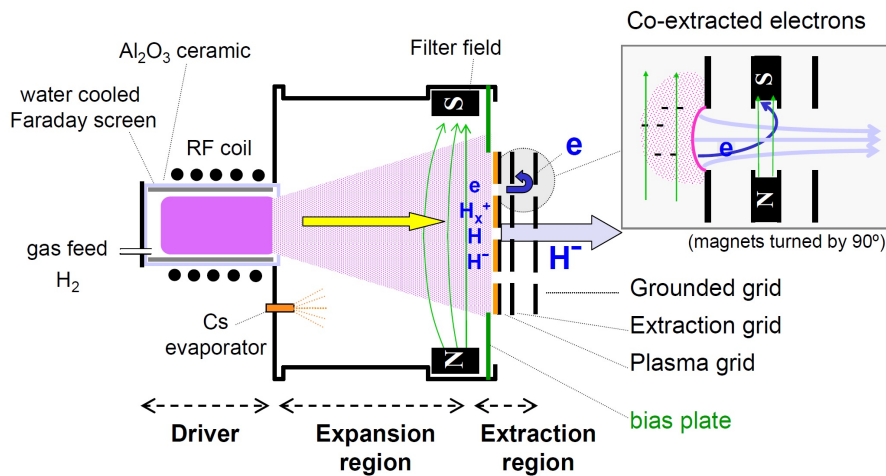
Figure 1.8: Main components of a RF negative ion source[10].

The driver is an alumina cylinder inside which a partially ionized plasma[2] is created. The plasma receives energy from the RF[3] emitted by a coil surrounding the cylinder. The coupling between the coil and the plasma is purely inductive because of a Faraday shield inside the cylinder which protects the alumina from the interaction with the plasma. Sustaining the plasma with an external RF coil is a robust solution because of its ease of maintenance, however the RF generator must be properly matched to the coil following the evolution of the plasma conditions. The driver is connected to an expansion region, in which the plasma diffuses. In the expansion the temperature of the electrons decreases from about $10\,eV$ in the driver to about $4\,eV$, condition which favors the production of negative ions by the dissociation

---

[2]The initial H_2/D_2 density is usually around $7 \cdot 10^{19}\,m^{-3}$, while the electron density is about $5 \cdot 10^{18}\,m^{-3}$ [9].
[3]The frequency of the radiowaves is typically of the order of $1\,MHz$.

of H_2/D_2 molecules which were vibrationally excited by a collision with an electron[11]:

$$
\begin{aligned}
H_2 + e &\Rightarrow H_2(\nu) + e && (\nu \geq 5 \text{ for H}, \nu \geq 8 \text{ for D}) \\
H_2(\nu) + e &\Rightarrow H + H^-
\end{aligned}
\tag{1.4}
$$
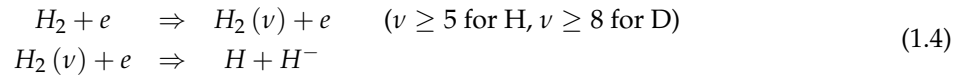
This is commonly defined as the "volume process" as it happens in the plasma region. The just produced negative ions must however survive to the reactions of mutual neutralization and electron detachment by impact with electrons, atoms or molecules. The volume process alone would not be sufficient to produce the flux of ions for the ITER NBI; luckily, much more negative ions (one order of magnitude more than in volume process) are instead produced with a surface process, in which the atoms in the plasma impact on the Plasma Grid (PG) and pick up the extra electron. The PG separates the expansion region from the acceleration stage; to facilitate the production of negative ions the surface of this grid is covered with a layer with cesium, a material with a low work function ($2\,eV$). The deposition of Cs is performed with an oven which releases Cs vapors inside the source. Since Cs liquifies at 28°C, the source body is kept at about 40°C to avoid the uncontrolled deposition of this substance; the optimal deposition of Cs on the PG has been obtained by heating the grid at 120°C ÷ 150°C [12, 13]. The negative ions created by the surface process are backscattered towards the expansion region, however near the PG holes they are attracted by the electric field on the other side of the PG. To avoid losing negative ions the apertures in the plasma grid are chamfered to steer the scattered ions inside the holes. Moreover, next to the PG a magnetic filter field ($\sim 10^{-2}\,T$) parallel to the PG itself lowers the electron temperature below $2\,eV$; the field reduces the speed of the electrons perpendicular to the PG and then it counteracts the electron detachment processes which could significantly reduce the amount of negative ions produced. In fact, H$^-$/D$^-$ ions are rather "delicate": the binding energy of the excess electron is just $0.75\,eV$. The filter field has also the positive effect of reducing the amount of electrons extracted together with the relative ions. Indeed, a crucial target in the operation of a negative ion source is keeping the ratio of extracted electrons and ions as low as possible. A too high amount of produced electrons would compromise the energetic efficiency and the safety of the NBI, because the power carried by the electrons doesn't contribute to the one of the beam but deposits on the acceleration grids and the beam line components; the resulting thermal load on these components could lead to sever damages. In addition to the filter field, the other countermeasure to reduce the amount of coextracted electrons adopted in the source consists in biasing the PG positively against the source body; to the source walls it is connected the bias plate (BP), placed next to the PG and covering the borders of the grid external to the extraction area. Aim of the BP is to lead the source potential close to the PG, improving the effectiveness of the bias. The filter filed intensity and the voltage bias of the PG with respect to BP and source must be properly set: the simultaneous presence of magnetic field and voltage gradients (given by the BP and the plasma sheath on the PG) produces a drift of the plasma; besides, the bias voltage can reduce not only the amount of coextracted electrons but also slightly the amount of negative ions[10].

After the ions have passed through the apertures of the PG, they are accelerated up to the desired energy by the electric field produced by a number of grids. These are set at increasing negative voltages, up to the Grounded Grid (GG) which is at $0\,V$. Many are the issues connected to the acceleration stage:

- To reduce the fraction of coextracted electrons accelerated with the negative ions, the charged particles exiting the PG apertures are first accelerated by the so called Extraction Grid (EG), which has permanent magnets embedded around its apertures. The magnetic field intensity is such that the trajectory of the ions is slightly deviated whereas the electrons are dumped on the EG surface. The voltage of the EG is normally kept below $10\,kV$ to limit the acceleration of the electrons and therefore the power carried by them.

- To mantain the thermal load of the beam line components within safety levels it is necessary that

divergence of the beamlets[4] produced by the grids' apertures is as low as possible. The trajectory of the ions is determined by the lens effect of the electric field produced by the grids. More specifically, the electric field is determined by the voltage of the grids, the distance between them and the shaping of their apertures, but also by the current of the beamlets. The geometry of the electric field in the region between PG and EG is the most determinant for the divergence of the beamlets. At the PG, the intensity of the electric field and the plasma density define the shape of the meniscus, i.e. the surface at which the negative ions are at $0\,V$ with respect to the plasma. Figure 1.9 shows the simulation of the trajectories of the ions in a system composed by 2 grids. In case a) the plasma density and the current of extracted ions are so low that there is a depletion of negative ions at the aperture of the PG. The meniscus is then strongly concave, with the consequence that the focal point of the beamlet is too close to the PG. The result is a too divergent beamlet. In case c) the plasma density and then the extracted current are instead so high that the curvature of the meniscus is minimal; the beamlet diverges too much also in this case. The lowest divergence is obtained in case b), whose conditions are intermediate between those of cases a) and c). The 3 situations shown in figure 1.9 could have been obtained by keeping the beamlet current constant and decreasing the voltage difference between the grids from case a) to case b). The optic determined by PG and EG can be parametrized by the perveance

$$P = \frac{I_{ext}}{U_{ext}^{3/2}} \tag{1.5}$$

where I_{ext} is the extracted current and U_{ext} is the extraction voltage, i.e. the voltage difference between EG and PG. To compare the values of P between different machines the perveance is often normalized with respect to its value P_0 given by the Child-Languir law, i.e. when the flow of the beam particles is limited only by their space charge:

$$P_0 = \frac{4}{9}\pi\epsilon_0\sqrt{\frac{2e}{m}}\left(\frac{R}{d_{grids}}\right)^2 \tag{1.6}$$

where ϵ_0 is the dielectric constant, e and m are the charge and the mass of the electron, R is the radius of the grid holes and d_{grids} is the spacing between the grids. The lowest value of divergence is obtained for a certain value of P/P_0; in the cases a) and c) of figure 1.9 the perveance is respectively lower (under perveant condition) and higher (over perveant condition) with respect to the best value. The extraction voltage must then be adjusted according to the extracted current, but also according to the isotope used: as shown in eq. 1.6, $P_0 \propto m^{-1/2}$. It must be remembered, however, that the final divergence of the beamlets depends from the whole acceleration chain, and therefore by the voltages of all the grids.
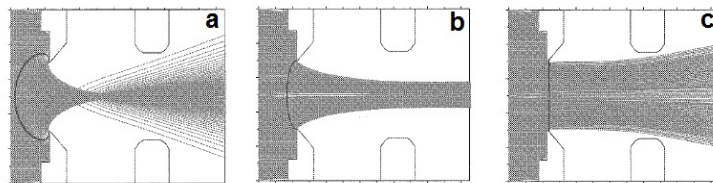

Figure 1.9: AXCEL-INP simulation of a system of 2 grids, assuming increasing values of plasma density from case a) to case c), but keeping the same voltage drop[14].

---

[4]A beamlet is defined as the beam produced by a single aperture, while the term beam is generally used to indicate the sum of all the beamlets exiting from the grids of the accelerator.

- The shaping of apertures and the geometry of the electric field must minimize the production of the so called halo, a component of the beamlet at higher divergence respect to the normal. The halo is generated by the aberrations of the optics of the grids, but also by the deposition of cesium on the downstream face of the apertures of the PG [15, 16]; the ions produced in those points have a higher transversal speed, giving the halo a higher divergence.

- The pressure of the gas between the grids must be kept as low as possible: the molecules of the gas could hit the H⁻/D⁻ ions and strip their excess electron, and the resulting neutral particles would be no longer affected by the electric field of the grids. The result of this process are the so called "stripping losses", a component of the beamlets at lower energy and higher divergence (because of the incomplete focusing). The stripping reactions produce electrons, too, increasing the fraction of coextracted electrons and therefore the thermal load on grids and beam line components. The most critical point is the region between PG and EG, because of the gas flux coming out from the source through the PG. For this reason the pressure inside the ion source must be limited.

- The shape of the apertures and their relative position between the various grids must be adjusted in order to compensate the mutual repulsion of the beamlets and the spurious effects of the magnetic filter fields. The deflection of the beamlets caused by the magnetic fields depends also on the hydrogen isotope used, because for a given acceleration energy the mass of the particles determines their speed, and in turn the speed influences the Larmor radius of the particles.

- At the exit of the grids the beamlets could cause the ionization of atoms in the background gas. This is positive because the positive ions compensate the space charge of the beamlets and therefore avoid an increase of the beamlets' divergence along their trajectories. Some of the positive ions however can enter the GG and be accelerated in the opposite direction towards the ion source. The heat load of the backstreaming ions could reach several tens of MW/m^2 in small spots at the bottom of the plasma drivers, causing damages to the bottom surface of the driver. Another negative consequence is that the copper on the surface can be sputtered and deposit on the PG, burying the Cs layer. The solutions to the problem consist in a careful design of the active cooling of the driver and in coating the endangered surfaces with materials which have a low sputtering yield, like molibdenum [17, 18].

1.3.2   The neutralizer

After exiting the GG the beamlets enter the neutralizer, in which the negative ions get neutralized by charge exchange with the background gas. Inside the neutralizer the gas density is obviously higher than in the surrounding component of the NBI. To obtain this the gas is injected in the center of the neutralizer and pumped away once it comes out from the neutralizer. In the case of ITER NBIs the volume inside the neutralizer is vertically divided in 4 sections to reduce the conductance and then the required gas flow. The neutralizer is kept at proper distance from the accelerator stage to avoid increasing the gas pressure between the grids. The pumping around the neutralizer but also the other beamline components is performed mainly by cryopumps at the sides of the vacuum vessel.

1.3.3   The residual ion dump

The beam exiting the neutralizer cannot be injected directly into the plasma because of the still high fraction of ions present. These ions would be deflected by the magnetic field of the tokamak and damage the first wall. The ions are therefore removed in the RID (*Residual Ion Dump*) by means of an electric

or a magnetic field. In the case of the ITER NBI the beam enters a volume vertically divided into 4 regions, whose vertical surfaces have voltages alternated between $0\,V$ and $-20\,kV$ to create the deflecting electric field. The collection of the ions creates an important flow of gas, which must be removed by the surrounding pumping system. After the RID, indeed, the gas density must be kept as low as possible to prevent the reionization of the neutral beam.

1.3.4 The calorimeter and the duct

The produced neutral beam now is ready to be injected through a duct towards the plasma of the reactor. For maintenance or diagnostic purposes the beam can be absorbed by a calorimeter just after the RID. In the NBI of ITER the calorimeter is composed by two panels forming a V shape; the cooling circuits are arranged in such a way that is possible to get a rough power deposition profile of the beam. To let the beam pass the panels are simply moved at the sides of the vacuum vessel, opening the V. Between the calorimeter and the duct a fast shutter and an absolute valve are mounted. The fast shutter is a light gate which can rapidly ($\sim 1\,s$) isolate the NBI from the tokamak, to prevent the flow of tritium towards the NBI or the flow of gas towards the tokamak during the regeneration of the cryopumps in the NBI. The absolute valve instead is more robust and can be used in rare cases of extraordinary maintenance, in which either the NBI or the reactor must be vented at atmospheric pressure.

1.4 SPIDER
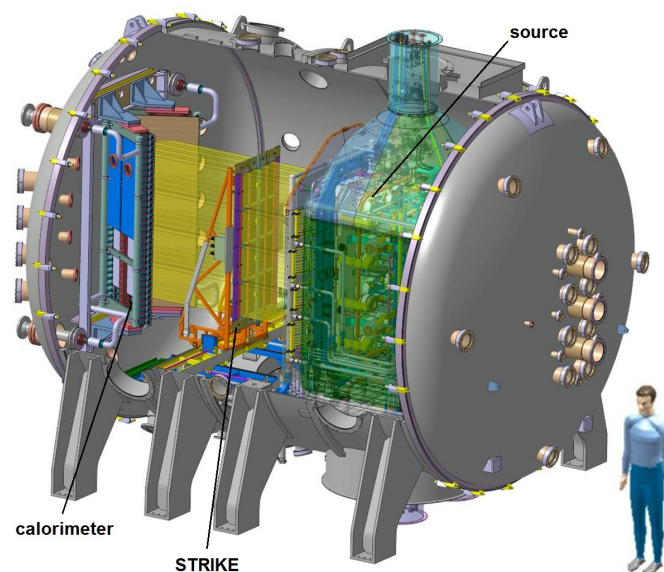
Figure 1.10: 3D model of the SPIDER experiment [19].

The prototype of the NBI for ITER will be built and operated in the PRIMA (*Padova Research on Megavolt Accelerator*) test facility. The building of this prototype will be preceded by the construction and operation of the experiment SPIDER (*Source for Production of Ions of Deuterium Extracted from an Rf plasma*). SPIDER (figure 1.10) reproduces the negative ion source for the ITER NBI, except for using a reduced number of grids and accelerating the H⁻/D⁻ ions to the lower energy of $100\,keV$. The produced beam is then absorbed by a calorimeter similar to what described in sec. 1.3.4, or optionally by the diagnostic calorimeter STRIKE (*Short-Time Retractable Instrumented Kalorimeter Experiment*)[20].

The source is composed by 2(h)x4(v) plasma drivers[5], open on a unique expansion region. The ions are extracted and accelerated by a system of 3 grids: PG ($-100\,kV$), EG ($\sim -90\,kV$) and GG ($0\,V$). The grids have 1280 holes of $7\,mm$ diameter, spaced $20\,mm$ horizontally and $22\,mm$ vertically. The holes and therefore the beamlets are divided in groups of 5(h)x16(v). The complete scheme of the apertures is shown in figure 1.11. The whole acceleration stage is open at the sides to allow the pumping system to more efficiently remove the gas exiting the PG. In the end, the beamlets follow straight horizontal trajectories towards one of the calorimeters.

Figure 1.11: Layout of the apertures of the GG. All the distances are in mm [21].

---

[5]The plasma driver is the alumina cylinder with the Faraday shield and the RF coil, as shown in figure 1.8.

The performances requested for the SPIDER beam source are listed in table 1.1.

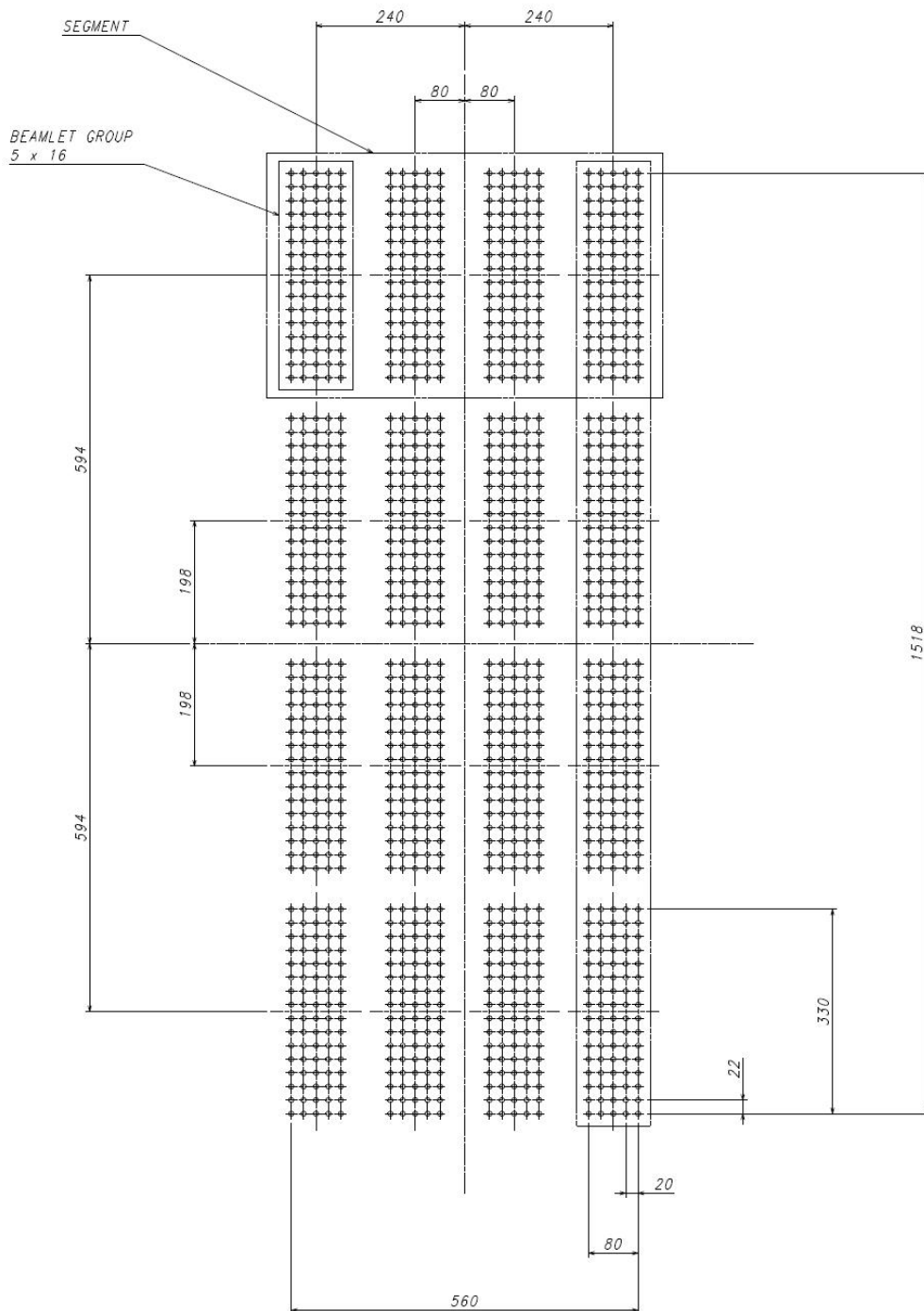| Source H_2/D_2 pressure	$< 0.3\,Pa$
Energy of the ions	$100\,keV$
Extracted current density	$285\,A/m^2$ (D), $350\,A/m^2$ (H)
Accelerated current	$40\,A$ (D), $46\,A$ (H)
Pulse duration	$> 3600\,s$ (D) $> 400\,s$ (H)
Beam homogeneity	$> 90\,\%$
beamlet divergence ϵ (e-folding)	$\leq 7\,mrad$
halo divergence (e-folding)	$\leq 30\,mrad$
current density ratio of electrons to ions accelerated	$j_e/j_{D^-} < 1$ $j_e/j_{H^-} < 0.5$

Table 1.1: Target performances of the SPIDER negative ion source[21, 22].

The operation of SPIDER will be monitored by several diagnostics[23], checking all the components of the facility. The plasma in the source is monitored by 84 Langmuir probes placed on the bias plate and the PG; the probes will measure the electron density (n_e) and temperature (T_e), besides the plasma homogeneity next to the PG. A more complete characterization of the plasma parameters is performed by the Optical Emission Spectroscopy (OES) system[24, 25], based on the study of the light emitted by the plasma [26, 27]. The instrumentation collects the light along Lines of Sight (LOSs) which are parallel and close to the PG; some of them are instead perpendicular to the PG and cross the plasma drivers to monitor the ignition of the plasma. For the calculation of many quantitites the OES technique uses collisional-radiative (CR) models[26, 27, 28] to link the spectra of the observed emissions to the plasma parameters. The quantities observed by OES are listed in table 1.2, together with the measurements taken as input of the calculations; all the results are line-integrated along the LOSs.

Plasma parameters	Experimental data
Driver ignition	Plasma light
Cs density and density of impurities (O, Cu,...)	Absolute line intensities
$\langle T_e \rangle, \langle n_e \rangle$	ratio of Balmer lines
vibrational and rotational temperature of molecules	Fulcher band spectrum
dissociation degree of H_2/D_2	$H_\gamma/H_{Fulcher}, D_\gamma/D_{Fulcher}$
negative ion density	$H_\alpha/H_\beta, D_\alpha/D_\beta$

Table 1.2: Quantities measured by OES, together with the data used as input [24, 25].

Parallel to the LOSs of OES there are also the lines of sight of Cavity Ring Down Spectroscopy (CRDS) [29], a diagnostic able to measure the line integrated density of negative ions. The technique is based on the repeated absorption of part of a laser pulse traveling between 2 mirrors; more details on this diagnostic can be found in chap. **??**. PG, EG and GG are monitored by thermocouples to control the thermal dilatation and avoid damages caused by excessive thermal loads. Downstream the grids, the uniformity and the divergence of the beamlets are measured by Beam Emission Spectroscopy (BES), which exploits the doppler effect undergone by the light emitted by the beam as it interacts with the background gas. This diagnostic is one of the topics of the thesis, all the details are reported in chap. 2. The power density profile of the beam will be measured by tomographic techniques, collecting the H_α radiation emitted by the beam along 3000 LOSs [30]. The power density profile can also be measured

with a high spatial resolution (2 *mm*) by the intrumented calorimeter STRIKE; it is composed by 16 CFC tiles, whose back side is observed by IR cameras to measure the thermal footprint; STRIKE however cannot stand the power load of the beam for more than 10 *s* [20]. The shape of the beam will be measured also by the main calorimeter, by detecting the neutrons emitted in the DD fusion reactions between the beam particles and the deuterium atoms implanted in the materials[31].

1.5   MITICA

The experience on negative ions sources gained with the SPIDER and ELISE test facilities will be exploited in MITICA (*Megavolt ITer Injector Concept and Advancement*)[17]. MITICA is the prototype of the full NBI for ITER; its features follow what explained in sec. 1.3. The negative ion source and the accelerator have the same prescription indicated for SPIDER in table 1.1, except for the energy of the ions which is 870 *keV* for hydrogen and 1 *MeV* for deuterium. Moreover, the system of grids follows the MaMuG (*Multi-aperture Multi-Grid*) configuration, developed by JAEA in Japan [32]: the extraction of the ions happens between the PG and the EG, while the acceleration of the ions is completed by 4 grids, the last of which is the GG[6] (figure 1.12). The difference of voltage between adjacent grids downstream the EG is 200 *kV*. The EG and the intermediate grids have magnets to deflect the electrons; the effect of the magnetic field on the beamlets is better compensated with the shaping of the apertures and by using special configurations for the positioning of the permanent magnets [33]. The aperture of the grids will be shifted in order to steer the beamlets according to a specific scheme.
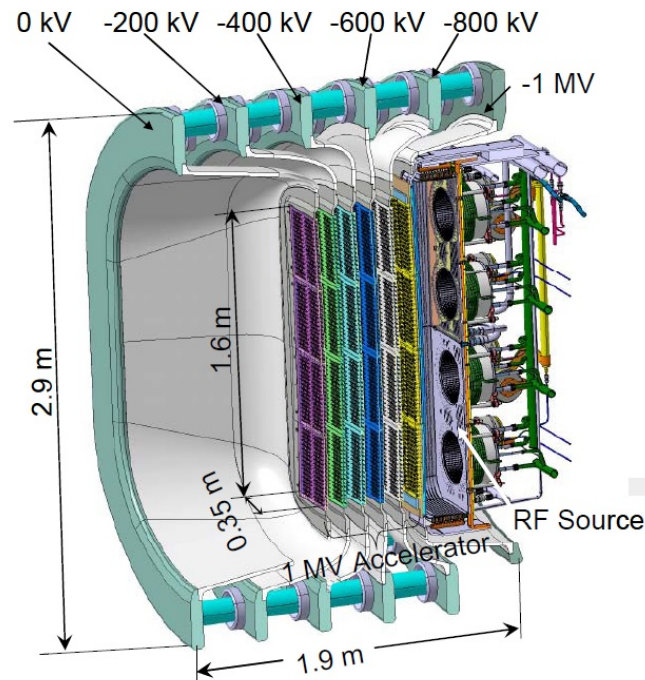

Figure 1.12: 3D representation of the ion source and acceleration stage in MITICA[34].

---

[6]The intermediate grids are conventionally named AG1, AG2, AG3.
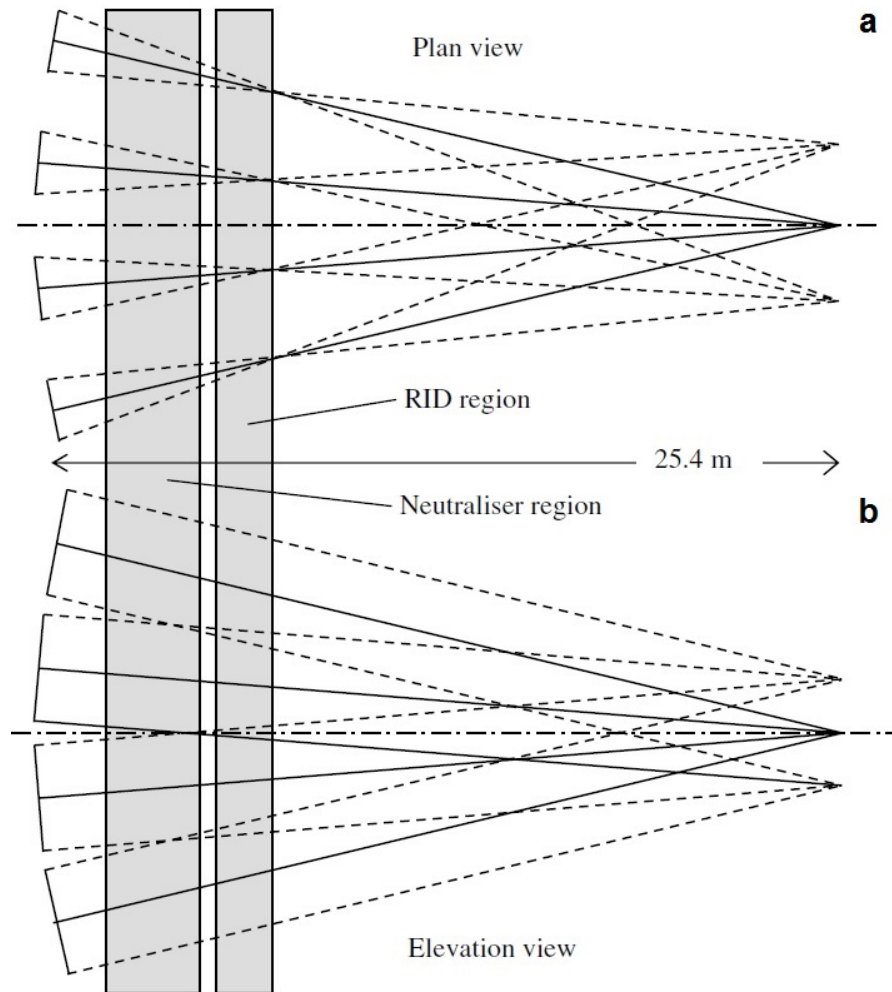
Figure 1.13: Scheme of the directions of the beamlets, projected on the horizontal (a) and vertical (b) plane[9].

As shown in figure 1.11, the beamlets are divided in 4x4 groups of 5(h)x16(v) beamlets each. Projecting the directions of the beamlets in the horizontal plane (figure 1.13a), it can be seen that the each beamlet group is pointing towards a position at a distance of 25.4 *m* from the GG, corresponding to the duct exit of the NBI in ITER. In each beamlet group the columns of beamlets intersecate at the exit of the RID, i.e. at 7.2 *m*. The result is that each one of the 20 columns of beamlets composing the beam has a specific direction in the horizontal plane.

In the projection on the vertical plane (figure 1.13b) it can be seen that the beamlet groups point at the exit plane of the beam at 25.4 *m* from the GG; in this case, however, within each beamlet group the rows of beamlets proceed parallel. On the whole, the beamlets can have only 4 directions in vertical plane: 23.3 *mrad*, 7.77 *mrad* and their opposite. The vertical and horizontal directions of the beamlets allows the beam to pass safely through the beam line components and at the same time it increases the uniformity of the beam itself.

At last, the source and the grids are connected to the vacuum vessel by a couple of hinges, in such a way that the beam can be tilted 49 *mrad* downwards. This was foreseen for the ITER NBI to off-axis deposit the power of the beam in the plasma.

The diagnostics in MITICA will be the same as in SPIDER, with few differences. The ion source won't have the system of electrostatic probes and there won't be an instrumented calorimeter like STRIKE. On the other side, lines of sight of BES and tomography[35] will be present between the GG and the neutralizer, between the neutralizer and the RID and between the RID and the calorimeter. Obviously

the temperature of all the beam line components will be kept under observation to prevent damages caused by excessive thermal loads.

1.6   The ion sources at IPP

The RF negative ion source chosen as reference for the ITER NBI have been developed at IPP Garching as an alternative solution to the filamented arc sources. These, indeed, need to be opened regularly to replace the tungsten filaments; this would obviously be a problem since the whole NBI will be activated by tritium. Moreover, tests showed that the tungsten vapors produced by the filaments deposit on the PG, reducing the effectiveness of Cs in helping the formation of negative ions and then increasing the consumption of this substance[36].

The IPP facilities based on on negative in sources and considered in this thesis are BATMAN (*BAvarian Test MAchine for NegAtive ions*), MANITU (*Multi Ampere Negative Ion Test Unit*) and ELISE (*Extraction from a Large Ion Source Experiment*).

1.6.1   BATMAN

BATMAN has the IPP prototype ion source with one driver. The source [37, 11, 10] has one plasma driver, and the ions are accelerated by means of 3 grids (PG, EG, GG) up to $18 \div 25\,keV$ (figure 1.14). The shape and the positioning of the apertures of the grids follow the LAG (Large Area Grid) scheme[10]. The GG apertures have a diameter of $8\,mm$, for a total area of about $70\,cm^2$; the beamlets exiting the GG have a divergence of some degrees.
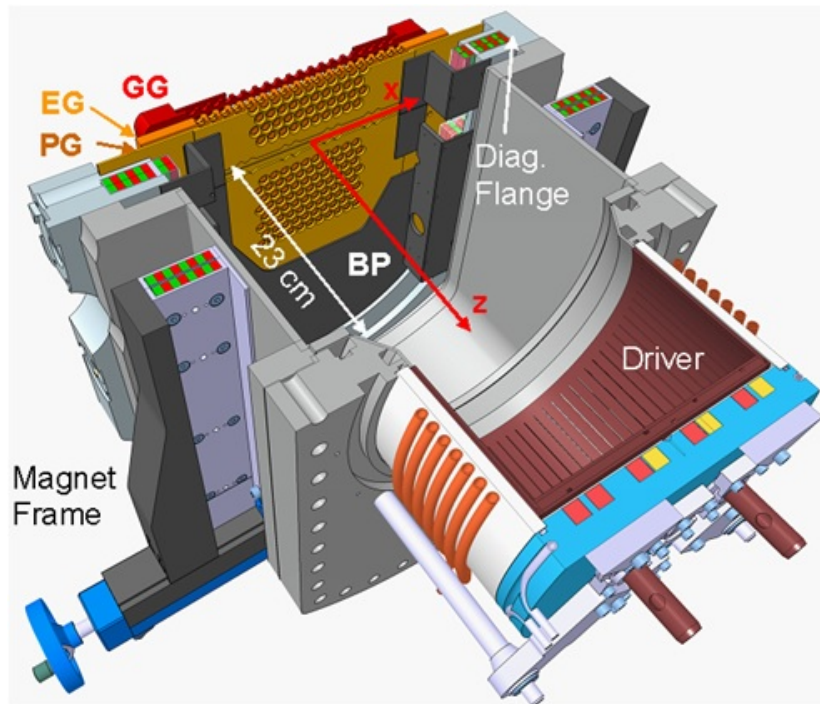

Figure 1.14: 3D representation of the BATMAN source[38].

Aim of of the experiment was to demonstrate that a RF driven source was able to produce negative ions, both H⁻ and D⁻, with a ratio of coextracted electrons below 1 and with an accelerated current density as high as expected for the NBI in ITER, i.e. $200\,A/m^2$ or D⁻ and $300\,A/m^2$ for H⁻[9, 39]. Both

the goals were reached and the produced current density was even higher than requested [11]. The duration of the extraction phase is of about $4\,s$. The main characteristics and achievements of this source are listed in table 1.3.

Parameter	BATMAN	MANITU	ELISE
Accelerated Current density	$230\,A/m^2$ (D⁻) $330\,A/m^2$ (H⁻)	$120\,A/m^2$ (D⁻) $250\,A/m^2$ (H⁻)	$200\,A/m^2$ (D⁻,expected) $300\,A/m^2$ (H⁻, expected)
Source pressure	$0.3\,Pa$	$0.3 \div 0.4\,Pa$	$0.3\,Pa$
j_e/j_{H-}	< 1	< 1	< 1
j_e/j_{D-}	< 0.5	~ 1	(expected)
Extraction area	$0.007\,m^2$	$0.019\,m^2$	$0.1\,m^2$
Energy of ions	$\sim 20\,keV$	$\sim 20\,keV$	$< 60\,keV$
Pulse length	$< 4\,s$	$< 3600\,s$ (D) $< 800\,s$ (H)	10s extraction at interv. of 3 min

Table 1.3: Results of the test beds BATMAN, MANITU and ELISE [11, 18, 13, 40, 39].

The ion source is monitored by langmuir probes [41], OES [26] and CRDS[42]. To control the Cs density instead the laser absorption tecnique was used [43]: it consists in measuring the intensity and shape of a specific line of the Cs absorption spectrum. The beam is characterized by the BES diagnostic, which in the past had two lines of sight; recently the optical system has been upgraded, with 5 LOSs in total[44] (more details can be found in sec. 2.5). The negative ion beam is then absorbed and studied at the calorimeter, composed by a copper plate equipped with 29 thermocouples placed as a cross. Further measurements of the beam power density profile have been provided by the mini-STRIKE calorimeter, composed by 2 CFC tiles monitored on the rear side by an IR camera [20, 45]. Mini-STRIKE has been used also to validate the design of the STRIKE calorimeter. The optic heads of BES and the two calorimeters are shown in fig. 1.15
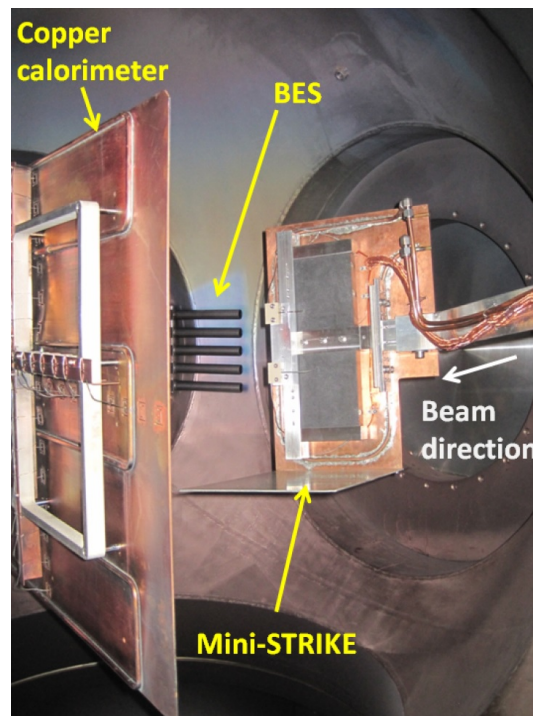

Figure 1.15: View of the BES optic heads and of the two calorimeters (seen on the rear side) used in BATMAN[45].

1.6.2   MANITU

Respect to BATMAN, MANITU was projected and built to have a larger extraction area and to produce the ion beam for much longer pulses (table 1.3); the source instead is the same as in BATMAN. The beam extraction time was extended to 1 hour, in agreement with the requirements of the ITER NBI (tab 1.1); the final current density and the electron to ion ratio were respectively lower and higher than desired. The diagnostics of MANITU are substantially the same used in BATMAN, except for the absence of mini-STRIKE. The BES diagnostic had a much higher number of LOSs, 7 in the vertical plane and 13 in the horizontal plane (further details in sec. 2.5). This allowed to study the beam uniformity under various operating conditions [46]. Now MANITU is no longer in operation.

1.6.3   ELISE

ELISE (figure 1.16) is the ion source test facility which should satisfy both the ITER requirements regarding the current density and the duration of the beam (table 1.3)[13, 40, 39]. . The source has half the dimensions of that in the ITER NBI; it is composed by 4 plasma drivers, open to a common expansion region. Because of the dimensions of the system the filter field is produced by a current flowing vertically in the PG, solution which allows also to optimize the magnetic field intensity to the operating conditions. The extraction area is half the one foreseen for the ITER NBI; having the same current density, the total current produced should be 20 A for deuterium. The grids have 640 apertures, which have a diameter of 14 mm and are 20 mm far from each other both in vertical and horizontal direction. The apertures are grouped as one vertical half of the scheme shown in figure 1.11. Because of limitations of the high voltage power supply the extraction of the ions can be performed in intervals of 10 s separated by 3 min, while the plasma in the source can be sustained up to 1 h.
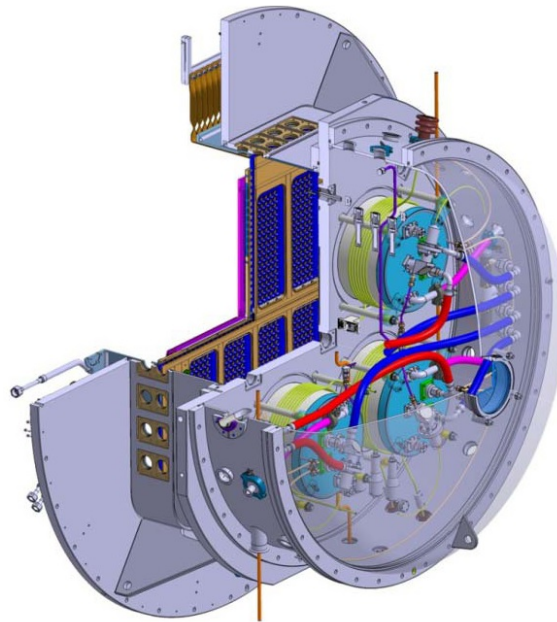
Figure 1.16: 3D representation of the source and the acceleration system in ELISE[18].

The source is monitored by OES[47] and langmuir probes, while the beam is examined by 3 diagnostics[39] (figure 1.17) with the main aim of studying its uniformity. The first one is the W-wire calorimeter, placed at 1.8 m from the GG and composed by 50 vertical and 50 horizontal tungsten wires, 0.2 mm thick and 20 mm spaced one from each other. The wires become more or less incandescent according to the power density profile of the beam. Collecting the light produced by the wires with a simple CCD camera, it

is possible to measure the beam shape. The second one is beam emission spectroscopy, which has 16 horizontal and 4 vertical LOSs, 2 m far from the GG. The third diagnostic is the calorimeter, placed at 3.5 m from the GG; it is composed by 4 copper plates whose surface is slotted in order to create square elements 4 cm wide. The thermal conductivity between these elements is low, in order to preserve the spatial resolution of the thermal footprint taken by the IR camera.
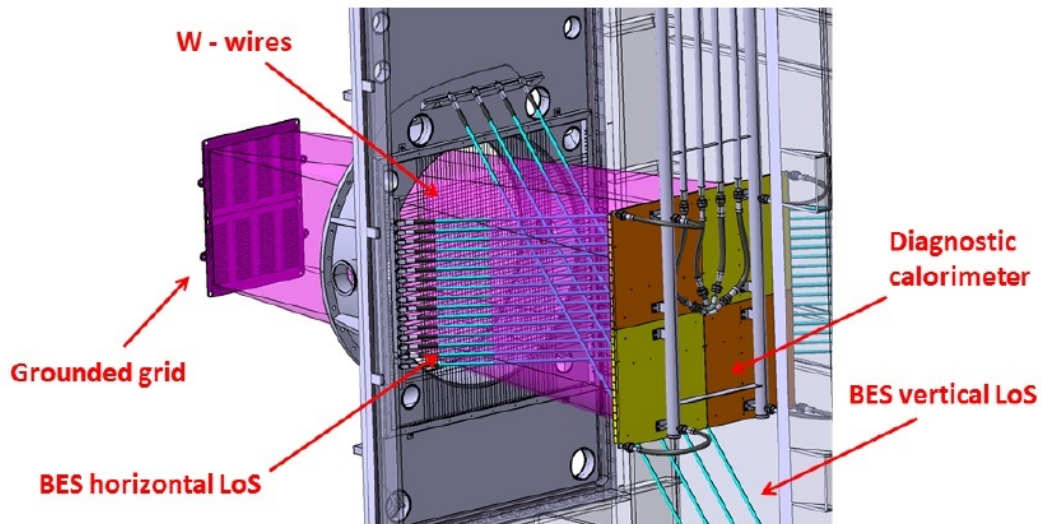
Figure 1.17: The diagnostics dedicated to analyze the beam in ELISE: beam emission spectroscopy and the two calorimeters [48].

1.7 NIO1
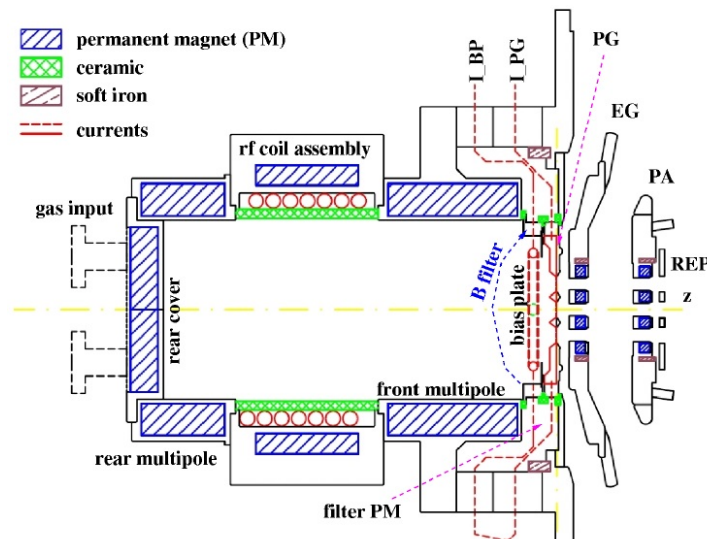
Figure 1.18: Scheme of the NIO1 source [49].

The NIO1 (*Negative Ion Optimization 1*) facility has been projected and built jointly by Consorzio RFX and INFN-LNL [49, 50, 51]. It has a small RF negative ion source, designed to have a high degree of flexibility in the hardware configuration; indeed, aim of the experimentation on NIO1 is to optimize the functioning of negative ion sources; the facility will be used also to test part of the materials and the instrumentation foreseen for SPIDER and MITICA. The scheme of the source is shown in figure 1.18:

the main differences with respect to the IPP ion sources are the absence of the Faraday screen and of the expansion region. The inner surface of the source is made of copper except in the middle where an alumina cylinder isolates the region in vacuum from the RF coil. To protect the inner surfaces and reduce the plasma losses a set of permanent magnets is mounted in the source body[51] (also around the RF coil) in order to create a magnetic bottle. Similarly to ELISE, the magnetic filter field is generated by a current flowing in the bias plate and the plasma grid. The grids of the acceleration stage are 3 (PG, EG, PA-post acceleration grid) plus a repeller (REP) grid, to stop backstreaming positive ions and to influence the space charge compensation of the beam. The 9 apertures have a diameter of $7\,mm$ and are 9, spaced $14\,mm$ one from each other both vertically and horizontally, according to a square lattice of 3x3. The source will operate only in hydrogen and the ions will be accelerated up to $60\,keV$, to form a beam of maximum $130\,mA$. The current density should then reach the target value for the ITER NBI. The power supply and the cooling of the system were dimensioned in order to allow the continuous ($> 1000\,s$) operation of the source.

There are many diagnostic in the NIO1 facility [52, 53]: the properties of the plasma in the source and the density of negative ions and Cs next to the PG will be monitored by OES, CRDS and laser absorption; these diagnostics will share the small viewports parallel to the PG, as well as the 4 viewports looking longitudinally from the rear of the source (figure 1.19a)[7]. The beam will be characterized by

- a fast emittance scanner (FES) of Alison type, to measure the ion distribution in the position and velocity spaces;

- beam emission spectroscopy, with LOSs intercepting the rows and the columns of beamlets (more details in sec. 3.1);

- a tomography system observing the H_α light emitted by the beam;

- The copper calorimeter, with 13 independent vertical cooling circuits to measure the vertically integrated profile of the beam. For a better measurement of the power density profile the calorimeter has a lattice of holes, through which the beam passes to reach a scintillator coupled to a CCD camera.

All the beam diagnostics are mounted in or on the diagnostic chamber (figure 1.19b), which hosts also the pumping system.

---
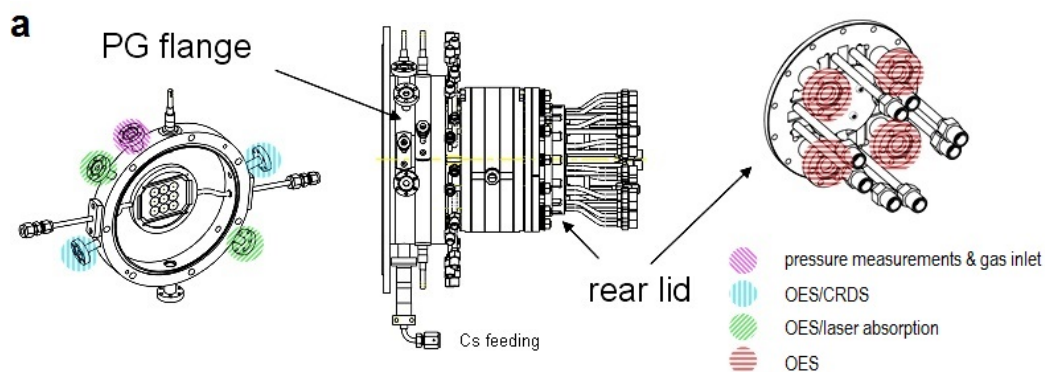
[7]The inner diameter of the ports looking parallel and perpendicularly to the PG is respectively of $8\,mm$ and $12\,mm$.
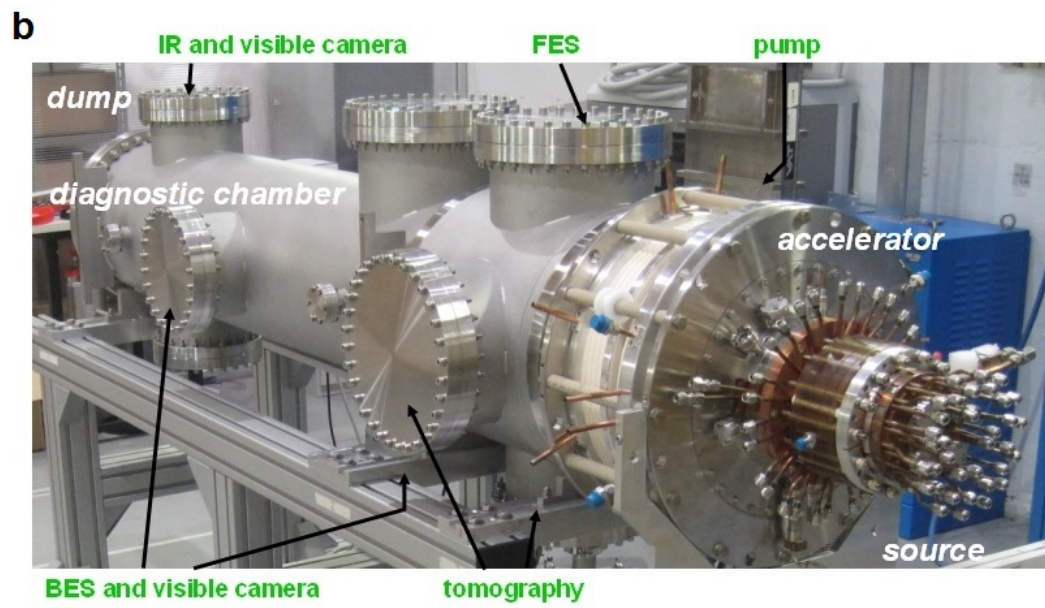
Figure 1.19: a) Assignment of the viewports of the source to the diagnostics dedicated to it. b) Positioning of the beam diagnostics in the NIO1 diagnostic chamber. [52].

Chapter 2

Beam Emission Spectroscopy and the dBES code

As mentioned in the previous chapter, Beam Emission Spectroscopy is a key diagnostic to measure the beamlets' divergence, crucial for the safety of the beamline components, and the beam uniformity, which defines the quality of the produced beam itself. Most of the work of thesis was dedicated to complete and improve the design of the BES diagnostics in SPIDER and MITICA, which have to be capable to measure the divergence of beamlets, expected to be in the range $3 \div 7$ *mrad*, with an error below 10%, and the beam uniformity, expected to be above 90%, with an error within 10%. A code (dBES) was developed whose principal aim is to simulate the signal (i.e. the beam emission spectra) as acquired by a real BES diagnostic. Thanks to this approach it was possible to study the impact of each diagnostic technical specification in the overall diagnostic performances. To check the validity of its results dBES was benchmarked against the BBC-NI code (both in its simple and advanced versions) [12], developed at IPP with an analogous purpose. The benchmark helped pointing out strengths and weaknesses of dBES, nevertheless confirming its usefulness to address the ultimate design of SPIDER and MITICA BES diagnostics. This work was accompanied by the analysis of the spectra collected by the BES diagnostics in the BATMAN, MANITU and ELISE test facilities, in order to check the correspondence of the simulations with the experimental data. This analysis was carried out using part of dBES routines since the code can be used both in predictive mode (data simulation) than in deductive mode (data analysis).

2.1 Principles of operation of BES

Beam Emission Spectroscopy is based on the interaction of the energetic beam particles with the molecules of the gas present in the vacuum vessel of the facilities. The collision with the molecules can excite the beam particles with a subsequent emission of radiation. In the frame of reference of the laboratory, the wavelength of this radiation is Doppler shifted according to the following formula:

$$\lambda' = \lambda_0 \frac{1 - \beta \cos \alpha}{\sqrt{1 - \beta^2}} \tag{2.1}$$

where λ' and λ_0 are the observed and the nominal transition wavelength, β is the ratio between the speed of the ions and the speed of light, α is the angle between the beam particles velocity and the direction of the emitted photons. λ' is blue or red shifted according to the value of α. The relativistic Doppler formula has been used due to the high energy of the particles, since β can reach 1.5% in SPIDER and 4.3% in MITICA.

27

For hydrogen or deuterium beams, the most convenient line emission to observe is H_α/D_α radiation ($\lambda_0 = 656.2793\ nm$ for H , $\lambda_0 = 656.1032\ nm$ for D), being the most intense line in the visible spectrum. The H_α/D_α photons are produced by the de-excitation to the $n = 2$ level of H/D atoms previously excited to the $n = 3$ level by the following reactions:

$$H^-_{beam} + H_2 \implies H^*_{beam} + H_2 + e \tag{2.2}$$

$$H_{beam} + H_2 \implies H^*_{beam} + H_2 \tag{2.3}$$

$$H^+_{beam} + H_2 \implies H^*_{beam} + H_2^+ \tag{2.4}$$

$$H^-_{beam} + H_2 \implies H_{beam} + H + H^* + e \tag{2.5}$$

$$H_{beam} + H_2 \implies H_{beam} + H + H^* \tag{2.6}$$

$$H^+_{beam} + H_2 \implies H^+_{beam} + H + H^* \tag{2.7}$$
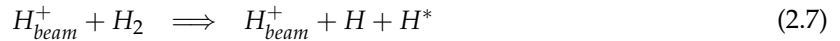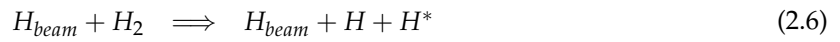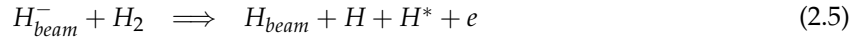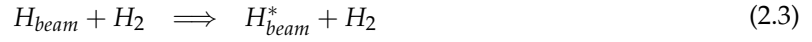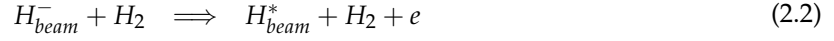
where the neutrals and the positive ions of the beam where produced in the interaction of the beam itself with the background gas. The first 3 reactions lead to the excitation of the fast beam particles: the wavelength of the resulting photons is Doppler shifted according to eq. 2.1. A typical spectrum of D_α radiation emitted by a beam and acquired in counter beam direction ($\alpha < 90°$) using a high resolution spectrometer is shown in figure 2.1. The peak at lowest wavelength corresponds to the blue shifted D_α radiation produced by the beam particles at full energy. The small peak at 654.8 nm corresponds to the Doppler shifted emissions of the stripping losses, i.e. ions neutralized before exiting the GG and therefore not fully accelerated by the electric field of the grids. The contribution of the stripping losses to the spectrum is usually peaked at the wavelength corresponding to the extraction energy, since the neutralization of the ions depends on the gas pressure, which is higher in the region between the PG and the EG. The peak at λ_0 is the result of the reactions 2.5, 2.6 and 2.7, in which one of the atoms of the D_2 molecules is excited; in this case the speed of the emitting particles is so low that $\lambda' \approx \lambda_0$.
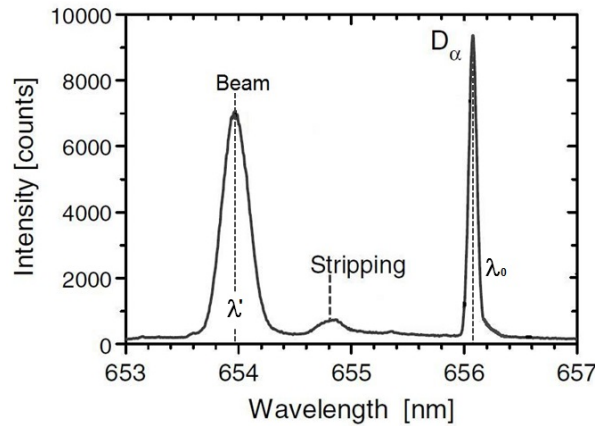
Figure 2.1: A typical spectrum of D_α radiation emitted by a deuterium beam and collected by a BES diagnostic.

From the analysis of a BES spectrum several information on the beam can be deduced, in particular:

- The beam direction, in terms of the angle α between the beam itself and the direction along which the H_α/D_α photons are collected. α is calculated by means of eq. 2.1, knowing β from the full acceleration voltage and measuring the wavelength separation between the main Doppler peak and the unshifted H_α/D_α peak.

- The beam divergence, i.e. the width of the angular distribution of the beam particles' trajectories

around their main direction given by α. Through formula 2.1 fluctuations of α are translated in fluctuations of λ', which are globally observed as a broadening of the main Doppler shifted peak.

- The fraction of stripping losses with respect to the full energy beam particles, by comparing the integral of the part of the spectrum occupied by the stripping losses with the integral of the main Doppler peak. The comparison must take into account the energy dependence of the excitation cross sections.

All the BES diagnostics described in this thesis have a similar design. The beam H_α/D_α emission is collected by several optic heads looking at the beam through viewports the vacuum vessel. The optic heads are distributed along the horizontal and vertical dimensions of the beam to characterize the beam itself with a certain spatial resolution. Optical fibers carry the light from the optical heads to one or more spectrometers, usually of Czerny-Turner type, to obtain the BES spectra. The ends of many fibers are vertically piled in front of the entrance slit of the same spectrometer; as many spectra are produced at the spectrometer exit port, which can be simultaneously acquired by a 2D CCD camera.

2.2   Other phenomena involved in BES

To reproduce the spectra collected by a BES diagnostic it is necessary to take into account two fundamental aspects. The first is that the shape of a BES spectrum mainly depends on the statistical distribution of the angle between the trajectory of the beam particles and the direction of the photons collected by an optic head. This angular distribution is determined by the divergence of the beamlets, in addition to their position and orientation with respect to the optic head. The second aspect is the calculation of the rate of photons collected by a BES diagnostic, which is given by the integral

$$\int_{V_{LOS}} n_{beam} n_{gas} \left(\sigma_{1,3} \frac{A_{3,2}}{A_{3,1} + A_{3,2}} \right) v \frac{\Omega}{4\pi} dx^3 \tag{2.8}$$

where V_{LOS}, is the volume of the line of sight of a given optic head, n_{beam} is the density of the beam particles, n_{gas} is the density of the gas in the vacuum vessel of the test facility, $\sigma_{1,3}$ is the cross section of the reactions which excite H/D atoms to the $n = 3$ level, v is the speed of the beam particles respect to the gas molecules and Ω is the solid angle under which the emitting particles see the clear aperture of the optic head. $A_{3,2} = 4.41 \cdot 10^7 \, s^{-1}$ and $A_{3,1} = 5.58 \cdot 10^7 \, s^{-1}$ [54] are the transition probabilities from the $n = 3$ excited state to the states $n = 2$ and $n = 1$; the two de-excitation channels are related to the Balmer-α and Lyman-β line emissions. The quantities involved in the integral must be treated carefully; more specifically:

- V_{LOS} is determined by the configuration of the optic heads.

- n_{beam} depends on the divergence of the beamlets, but also on the position and orientation of the beamlets with respect to the volume of a LOS.

- The density of the gas could not be uniform in the volume of the vacuum vessel; the gas density profile however cannot be measured, therefore it must be calculated by means of dedicated numerical codes [12, 55].

- As indicated in sec. 2.1 there are many reactions which excite the atoms to the $n = 3$ level, and each one has its specific cross section. The negative ions, the neutrals and the positive ions of the beam are involved in different reaction, therefore it's necessary to know the ion composition of the beam to weight the contributions of the various reactions. The ionic composition is not constant in space, but depends on the distance from the GG along the beam axis.

- $\sigma_{1,3}$ and v depend on the energy of the beam particles, which is not unique; the integral 2.8 must then take into account the energy distribution of the beam particles.

A secondary aspect related to the production of H_α/D_α photons is the non zero lifetime of the $n = 3$ excited state. Taking into account the fine structure of the quantum levels is unfeasible, because also the population rate of the specific sublevels should be considered. From the transition probabilities of the de-excitation channels $n = 3 \to 2$ (Balmer-α) and $n = 3 \to 1$ (Lyman-β), it results that the decay time of the $n = 3$ state is $\tau = 10\,ns$. The typical distance between the points of excitation and the de-excitation is $2.4\,cm$ for hydrogen atoms at $30\,keV$, or $13\,cm$ for hydrogen at $870\,keV$. The consequence of this is that the terms inside the integral 2.8 must be convoluted with the exponential decay of the excited states along the beam path.

The only way to keep into account all the mentioned issues, in particular those connected to the elevated number of beamlets and their geometry, is the use of numerical codes, like dBES.

2.3   Simulation Codes: dBES

The dBES code was developed to simulate the spectrum that would be acquired by a BES diagnostic, keeping the phenomena described in the previous section into account. To calculate the amount and the angular distribution of the photons collected by an optic head an analytical approach was adopted. The simulation codes are also accompanied by routines dedicated to the analysis of the spectra (simulated or real). The physical and numerical models adopted in dBES are now described.

2.3.1   The beamlets

The angular distribution of the beamlets' particles follows the model adopted in the ITER DDD 5.3 [21], which foresees that the power density distribution of a beamlet is Gaussian:

$$I\left(\vartheta\right)/I_{max} = \frac{1-f}{\pi\left(X\epsilon\right)^2}\cdot e^{-\left(\frac{\theta}{\epsilon}\right)^2} + \frac{f}{\pi\left(X\epsilon'\right)^2}\cdot e^{-\left(\frac{\theta}{\epsilon'}\right)^2} \tag{2.9}$$

where I_{max} is the power density (W/m^2) at the beamlet axis, θ is the angle of the considered position respect to the beamlet axis, f is the fraction of halo composing the beam, X is the distance along the beamlet axis from the GG, ϵ and ϵ' are the e-folding divergences[1] respectively of the main part of the beam and of the halo. It was implicitly assumed that the divergence doesn't increase with X because of insufficient space charge compensation or because of the collisions with the background gas molecules. It can be easily calculated that $I\left(\vartheta\right) = E\cdot n_{beam}\left(\vartheta\right)v$ (E is the energy carried by a single particle), therefore also the transverse profile of the beamlets' density is Gaussian. To be precise, the mean density n_{GG} of the beamlets at the GG apertures is given by

$$n_{GG} = \frac{I_{GG}}{N\cdot\pi r_{holes}^2\cdot e\beta c} \tag{2.10}$$

where I_{GG} is the beam current downstream the GG, N is the number of apertures in the GG[2] and r_{holes} is the radius of the apertures of the GG. In a frame of reference with x as axial coordinate of a beamlet (starting at the GG) and y,z as transverse coordinates, the beamlet density as function of space is given

---

[1]With gaussian distributions, the e-folding widths correspond to the "sigma" widths multiplied by $\sqrt{2}$.
[2]The GG has 126 apertures in BATMAN, 262 in MANITU, 640 in ELISE, 9 in NIO1, 1280 in SPIDER and MITICA.

by

$$n(x,y,z) = \frac{n_{GG}r_{holes}^2 f}{(\sigma_{GG}+X\cdot\tan\epsilon)^2} \cdot e^{-\frac{y^2+z^2}{(\sigma_{GG}+X\cdot\tan\epsilon)^2}} +$$

$$+ \frac{n_{GG}r_{holes}^2(1-f)}{(\sigma_{GG}'+X\cdot\tan\epsilon')^2} \cdot e^{-\frac{y^2+z^2}{(\sigma_{GG}'+X\cdot\tan\epsilon')^2}}$$

(2.11)

where σ_{GG} and σ_{GG}' are the radii corresponding to ϵ and ϵ' at the GG. In addition to the distinction between core and halo of the beamlets, it must be remembered that the beamlets are made of fully accelerated particles and stripping losses. In dBES each beamlet is modelled as the sum of many components, all having a Gaussian power density distribution but different particles' energy, divergence and intensity. What distinguishes each component from the others are the fraction of the beam which is represented, the energy of the particles, the divergence and σ_{GG}; moreover, each component can have a different direction with respect to the nominal beamlet axis. Subsequently, each beamlet produced by the GG is virtually positioned in the space, in a frame of reference (x, y, z) with the origin in the center of the GG[3]. The x axis corresponds to the axis of the whole source/NBI, while the y and z axes are oriented horizontally and vertically in the plane of the GG. If it is foreseen by the operation of the machine, all the beamlets are oriented according to the desired scheme (the case of MITICA is shown in figure 1.11) and according to the tilting of the grid's system. Anyway, the beamlets can be set singularly to undergo additional rotations, useful to study the effects of real deviations of the beamlets caused by the magnetic field of the EG.

2.3.2 The LOSs

The photons emitted by the beamlets' particles are spread isotropically in all directions, but only part of them is effectively collected by the optic heads This fraction can be quantified in terms of a solid angle Ω, which is a function of the position with respect to the considered telescope. To calculate Ω it is considered a model in which the lens of the telescope creates an image of the fiber head at a distance Q (figure 2.2).

Figure 2.2: Scheme of the optical simulation of the LOSs.

According to the laws of optics, Q is related to the focal length f of the lens and the distance P between the fiber and the lens:

$$Q = \frac{Pf}{P-f}$$

(2.12)

---

[3]In MITICA, the origin is taken assuming that the GG is not tilted downwards.

By adjusting the value of P it's possible to set Q so that the beamlets are present at an intermediate distance between the lens and the image. The radius W of the image depends on the diameter d_{fib} of the core of the fiber (400 μm in all the considered diagnostics):

$$W = \frac{Q}{P} \cdot \frac{d_{fib}}{2} \tag{2.13}$$

The LOS can be represented as a truncated cone, whose bases are the aperture of the lens, of radius L, and the image of the fiber head in Q. To calculate the solid angle Ω at every LOS point, it is used the property that a light ray departing from the image is conveyed into the fiber at the condition that the ray passes also through the lens aperture. Ω comprises all the directions that intercept both the image and the lens. A generic section of the cone at a distance p from the lens ($0 < p < Q$) is divided in small areas according to polar coordinates χ, φ; the same operation is done for the area of the image, using the polar coordinates r, θ. Now let's consider a small element A of the section in p and another one B in the image: by placing the origin of the (cartesian) coordinates in the center of the disk in p, the coordinates of the two elements are

$$\vec{A} = (0; \chi \cos \varphi; \chi \sin \varphi) \qquad \vec{B} = (Q - p; r \cos \theta; r \sin \theta) \tag{2.14}$$

where the first coordinate is along the beamlet axis. The trajectory of a light ray passing through the two point can be parametrized as follows:

$$\vec{F}(t) = \vec{v}t + \vec{A}, \qquad \vec{v} = \vec{B} - \vec{A} \tag{2.15}$$

In particular, the trajectory hits the plane of the lens in $\vec{F}(t_1)$, where

$$t_1 = -\frac{p}{Q - p} \tag{2.16}$$

This "direction" belongs to Ω if

$$F_2^2(t_1) + F_3^2(t_1) < L^2 \tag{2.17}$$

Using eq. 2.14, 2.15 and 2.16 the formula 2.17 becomes

$$\left[-(r \cos \theta - \chi \cos \varphi) \frac{p}{Q-p} + \chi \cos \varphi \right]^2 \quad + $$
$$+ \quad \left[-(r \sin \theta - \chi \sin \varphi) \frac{p}{Q-p} + \chi \sin \varphi \right]^2 \quad < L^2 \tag{2.18}$$

If the condition is satisfied, the solid angle $d\Omega$ with which A observes B is calculated:

$$d\Omega = \frac{r + dr/2}{\|\vec{v}\|^2} dr d\theta \cdot \frac{Q - p}{\|\vec{v}\|} \tag{2.19}$$

Keeping the element of A fixed and scanning all the elements of the image, it is possible to obtain the total solid angle of collection from that specific element of A. This operation is repeated for all the elements of the disk in p, subsequently all the calculation is repeated for disks at other distances p. The result is a map of Ω with respect to the axial and radial (χ) coordinates.

2.3.3   Gas density and ionic composition of the beamlets

Knowing n_{gas} in the space occupied by the beam is fundamental for the simulation to calculate the intensity of the spectra, but also for the analysis phase, when the spectra of LOSs placed in different positions are compared. In the simulations of dBES regarding BATMAN, MANITU and ELISE the background gas density is assumed to be uniform, it's calculated by the pressure measurements of each specific pulse and in the hypothesis that the gas is at room temperature (300°K). In NIO1 and SPIDER, n_{gas} can be assumed constant at $1.21 \cdot 10^{19} \, m^{-3}$ (corresponding to $0.05 \, Pa$ at 300°K), instead in the case of MITICA the gas denity is not uniform; the AVOCADO program[56] showed that the main variations of n_{gas} are function of the distance from the source. The variations of n_{gas} in the plane perpendicular to the beam amount to $\sim 5\%$ and to $\sim 22\%$, respectively for the LOSs upstream and downstream the neutralizer. These variations are not considered in the code, the profile of n_{gas} varies only along the main axis of MITICA (figure 2.3).
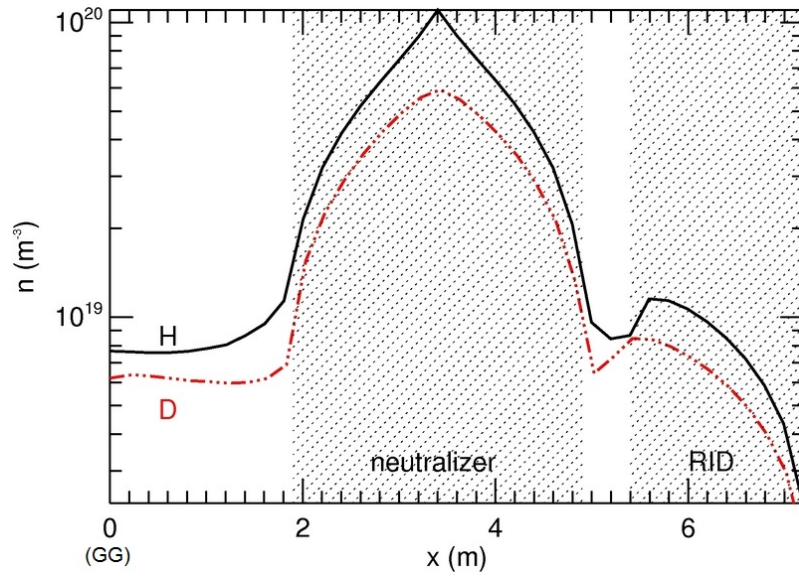

Figure 2.3: Profile [56] of n_{gas} along the main axis of MITICA, assuming that the gas is at a uniform room temperature (300°K) and that the gas is introduced at half the length of the neutralizer, with a throughput of $25 \, Pa \cdot m^{-3}/s$ for H, $19 \, Pa \cdot m^{-3}/s$ for D.

The profile of n_{gas} is important also to calculate the evolution of the ionic composition of a beamlet along its path. This can be calculated by solving the following set of differential equations

$$\left(\begin{array}{c} \frac{dn^-}{dX} \\ \frac{dn^0}{dX} \\ \frac{dn^+}{dX} \end{array} \right)\Bigg|_X = n_{gas}\left(X\right) \left(\begin{array}{ccc} -\sigma_{-10} - \sigma_{-11} & 0 & 0 \\ \sigma_{-10} & -\sigma_{01} & \sigma_{10} \\ \sigma_{-11} & \sigma_{01} & -\sigma_{10} \end{array} \right)\Bigg|_E \left(\begin{array}{c} n^- \\ n^0 \\ n^+ \end{array} \right)\Bigg|_X \tag{2.20}$$

where n^-, n^0 and n^+ are the densities of H⁻, H^0 and H⁺ respectively, X is the coordinate along the axis of the beamlet and E is the energy of the beamlet particles. The cross sections are related to the reactions of ionization and neutralization of the ionic species; the subscript index indicates the initial and final charge of the beam particles. The dependency of these cross sections on E is shown in figure 2.4.
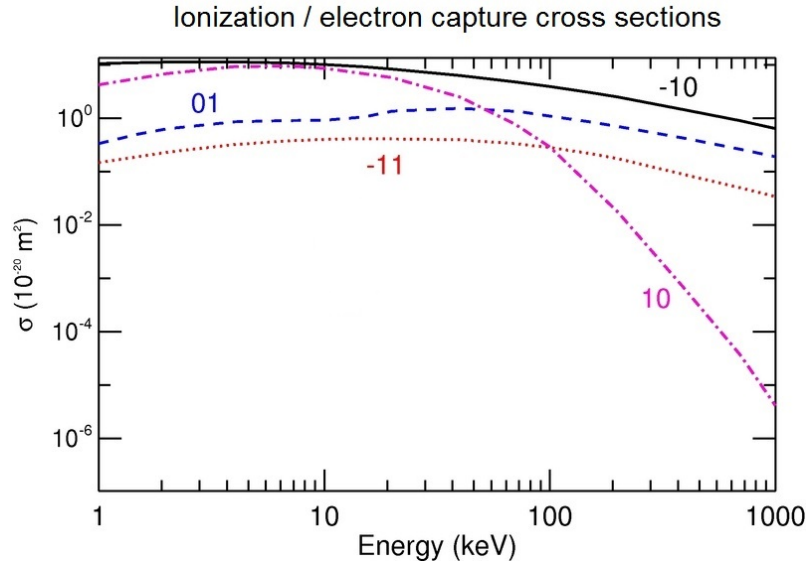
Ionization / electron capture cross sections

Figure 2.4: Cross sections of the reactions through which the beam particles ($H^-/H^0/H^+$) interact with the background gas and change their charge. The couples of numbers next to the curves indicate the initial and the final charges of the fast particle. The data are taken from the pages A-28, E-6, F-8 and F-10 of ref. [57].

The solving of the differential equations is performed with a Runge-Kutta 4th order method. The resulting composition of the beamlets, assuming that they are all parallel to the machine axis, is shown in figure 2.5, figure 2.6 and figure 2.7 for NIO1, SPIDER and MITICA respectively[4]. The results depend on the used isotope of hydrogen, because for the same value of energy the speed of the projectile particle is different. The shaded areas/vertical lines indicate the intervals of distance from the grids at which the LOSs intersect the beamlets. A first prediction that can be made, for example, is that in MITICA there will be a difference of 12% (H) / 23% (D) between the intensities of the Doppler shifted lines of the LOSs of the first section (GG-neutralizer) and the second (neutralizer-RID) section.
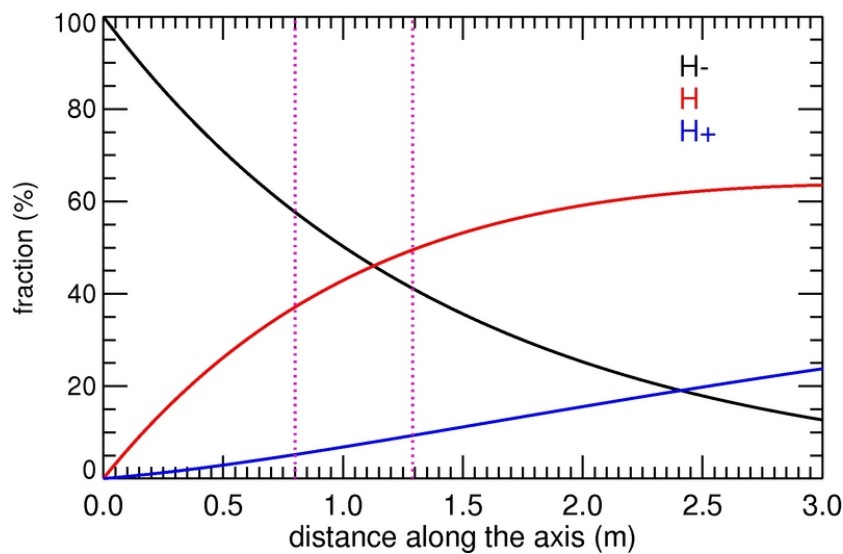
NIO1 - H - main beam composition

Figure 2.5: Fractions of H^-, H^0 and H^+ composing the beamlets of SPIDER. The shaded areas indicate (from left to right) the distances at which the horizontal LOSs and the bottom vertical LOSs intersect the beamlets. It is assumed that $n_{gas} = 1.21 \cdot 10^{19}$ m^{-3} (gas at 0.05 Pa and 300°K) uniformly.

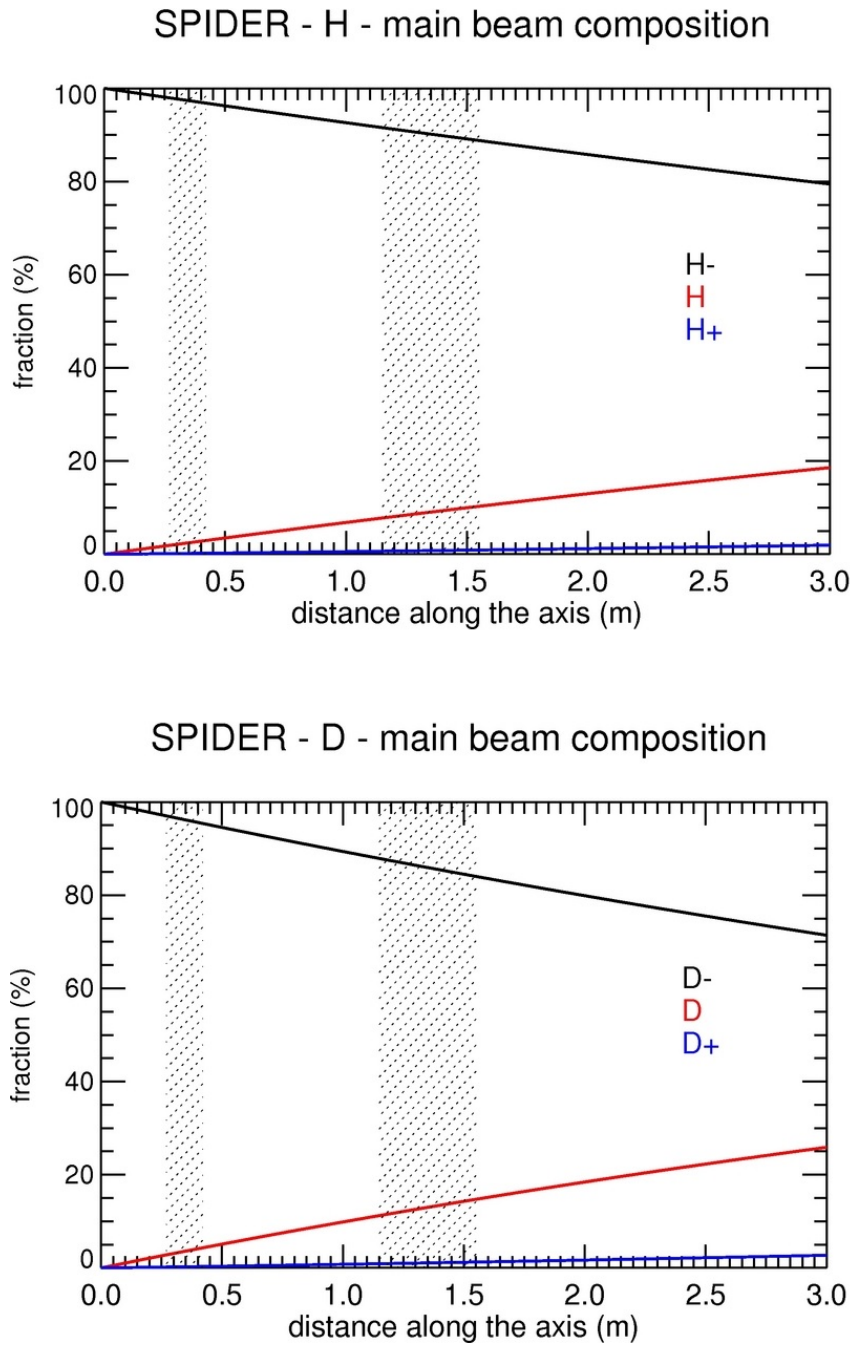[4]The situation in the IPP test facilities is not shown because n_{gas} varies from pulse to pulse.

Figure 2.6: Fractions of H^-/D^-, H^0/D^0 and H^+/D^+ composing the beamlets of SPIDER. The shaded areas indicate (from left to right) the distances at which the horizontal LOSs and the bottom vertical LOSs intersect the beamlets. It is assumed that $n_{gas} = 1.21 \cdot 10^{19} \; m^{-3}$ (gas at 0.05 Pa and 300°K) uniformly.

MITICA - H - main beam composition

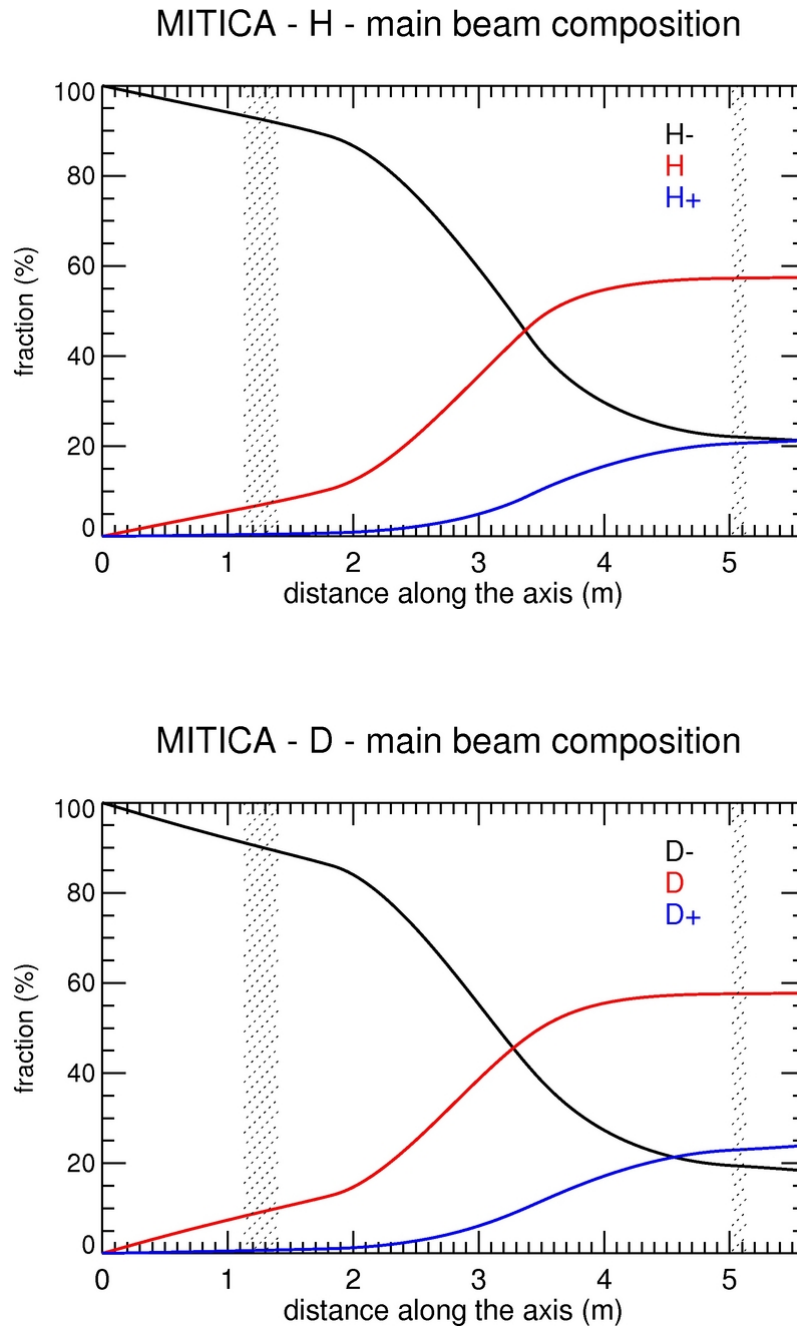## MITICA - D - main beam composition

Figure 2.7: Fractions of H^-/D^-, H^0/D^0 and H^+/D^+ composing the beamlets of MITICA. The shaded areas indicate (from left to right) the distances at which the LOSs between grids and neutralizer and the LOSs between neutralizer and RID intersect the beamlets.

In the case of MITICA the profiles displayed in the figure must be projected to the actual direction of the beamlet, therefore the solution of the differential equations must be performed for each beamlet. This approach should be extended in general to all the test facilities, because even if the beamlets were parallel to the machine axis their intersection with the LOS is not at the same distance from the grids. Anyway, it has been checked that only in the case of SPIDER the variation of the ion composition from beamlet to beamlet is not negligible and must then be taken into account. For the stripping losses the evolution of the ionic composition must be calculated for each energetic component. The calculation is not performed for each beamlet because this choice would slow down too much the program in comparison to the benefits. The ionic composition of the stripping losses is therefore calculated for only one direction, assuming the axis of the beam as trajectory.

2.3.4 The emission cross sections

The ionic composition of the beamlets, calculated as described in the previous paragraph, allows to treat separately the reactions 2.2-2.7 which lead to the excitation of the beam particles to the $n = 3$ level. Figure 2.8 shows the cross sections of these reactions as function of the energy of the beam particles; the values shown in the figure are already multiplied by the branching ratio r of the H_α radiation:

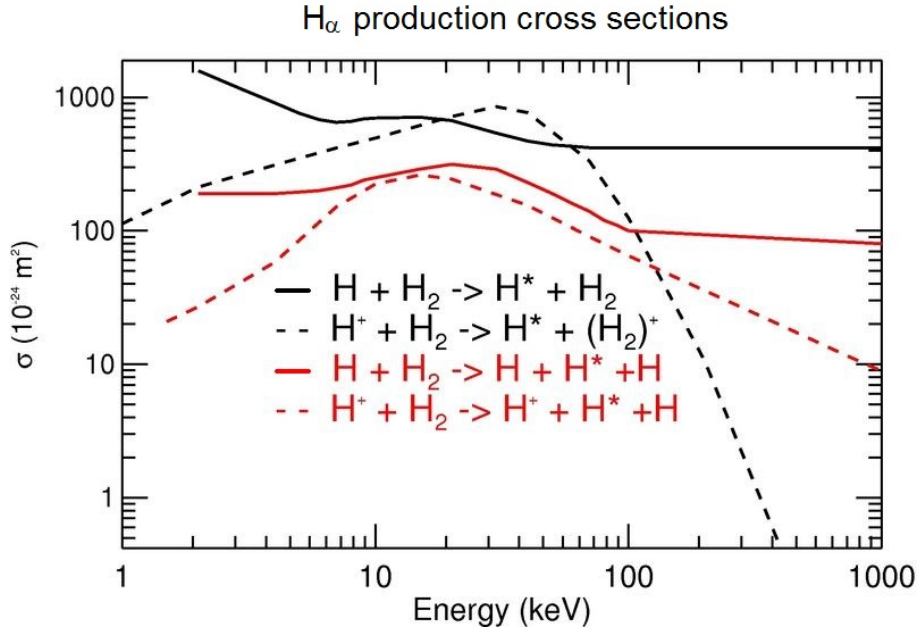$$r = \frac{A_{3,2}}{A_{3,1} + A_{3,2}} \tag{2.21}$$

Figure 2.8: Cross sections of the reactions related to the production of H_α photons, as function of the energy of the beam particles. The legend indicates the reactions which produce the excited atoms responsible for the H_α radiation. The data are taken from the pages B-12, C-12 and C-56 of ref. [57].

H^-/D^- and H/D are treated together because there are no specific data for the cross sections related to the negative ions over a sufficient interval of energy; moreover, the binding energy of the excess electron is much lower than the level of the involved energies. The maximum energy for which there are available data is $100\,keV$ for reactions 2.2, 2.3, 2.5 and 2.6, $1\,MeV$ for the reaction 2.4 and $400\,keV$ for the reaction 2.7. To cover the whole range of energies up to $1\,MeV$ the missing part of the curves was extrapolated from the last two available points. The values of the cross sections for the reactions in deuterium can be obtained by the same data, but considering only half the particles' energy.

2.3.5 The spectral broadening of the H_α radiation

To correctly simulate the BES spectra it is necessary to take into account the spectral broadening undergone by the H_α/D_α radiation. The model adopted to calculate these broadening effects is based on ref. [58]; the same model is at the base of the algorithms used to measure the beamlets' divergence ϵ from the width of the main Doppler peak in simulated or experimentally acquired spectra. It is assumed that each contribution to the spectrum is a gaussian, whose centroid is determined by the Doppler-shift formula 2.1. The photons emitted in the particles' de-excitation are collected by a lens of finite dimensions. As a consequence the observation angle α has a statistical fluctuation ω, that causes a broadening of the

components of the BES spectra. ω can be calculated in first approximation as

$$\omega = \arctan\left(\frac{L}{l_{los}}\right) \tag{2.22}$$

(L is the radius of the lens and l_{los} is the distance between the point of emission and the lens). This formula is useful during the phase in which the design of the telescopes is not decided. Once the optical configuration of the telescopes is established, it's possible to perform the optical simulation described in par. 2.3.5 and obtain the solid angle of collection Ω as function of space. From Ω it is then possible to calculate ω more accurately:

$$\omega = \arccos\left(1 - \frac{\Omega}{2\pi}\right) \tag{2.23}$$

The value of ω to be associated to a beamlet must be averaged over the volume of intersection between the beamlet itself and the LOS. In practice, dBES calculates the values of ω for each of the volume elements of the integration in eq. 2.37; the averaging is then computed weighting the values of ω with the contribution of each volume element to the integral. [5]

In a perfectly similar way to ω, the angle of obsevation α may also vary because of the angular distribution of the beamlet particles (figure 2.9). The quantity which statistically quantifies the angular spread of the particles' trajectories is the divergence ϵ. Because in the propagation of the errors all the fluctuations are considered in terms of standard deviation, the quantity $\sigma_\epsilon = \epsilon/\sqrt{2}$ will be used.
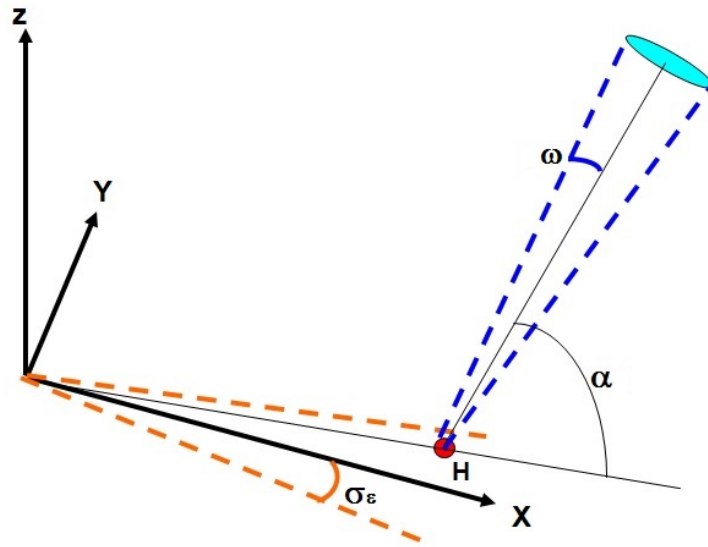

Figure 2.9: Representation of the angles used in the formulas.

Another cause of broadening of the emitted line are the voltage fluctuations σ_V on the grids, that alter the energy of the negative ions and so β; the worst case is in MITICA, in which the voltage ripple could reach 5 % of the working tension [59]. At last, the width of the line would be different from zero also in absence of the previous factors, since the H_α/D_α radiation has an intrinsic spectral width $\sigma_{\lambda I} \approx 0.0132\,nm$ and is broadened by the spectrometer ($\sigma_{\lambda S}$). This last term can be calculated from the FWHM of the diagnostic system instrumental function, that in a good spectrometer can be roughly calculated as the ratio between the spectrometer entrance slit width F and the detector pixel size (p_{size})[6].

---

[5]Substancially, ω is weighted with the intensity of the H_α radiation produced in the volume element and collected by the optics.

[6]This assumption is valid for a spectrometer with magnification 1.

This parameter can be converted in a spectral width by using the plate factor (or dispersion) d of the optics:

$$\sigma_{\lambda S} = \frac{Fd}{2\sqrt{2\ln 2} \cdot p_{size}} \tag{2.24}$$

The total (sigma) broadening $\sigma_{\lambda TOT}$ is obtained summing all the contribution according to the propagation of errors:

$$
\begin{aligned}
\sigma_{\lambda TOT} &= \sqrt{\sigma_{\lambda I}^2 + \sigma_{\lambda S}^2 + \left(\frac{\partial \lambda}{\partial \alpha}\right)^2 (\omega^2 + \sigma_{\epsilon}^2) + \left(\frac{\partial \lambda}{\partial \beta}\frac{\partial \beta}{\partial V}\right)^2 \sigma_V^2} \\
&= \sqrt{\sigma_{\lambda I}^2 + \sigma_{\lambda S}^2 + \left(\frac{\lambda \beta \sin \alpha}{\sqrt{1-\beta^2}}\right)^2 (\omega^2 + \sigma_{\epsilon}^2) + \left(\frac{e\lambda}{m\beta}(\beta - \cos \alpha)\right)^2 \sigma_V^2}
\end{aligned}
\tag{2.25}
$$

where e and m are respectively the charge and the mass of the electron.

2.3.6 The intersection between beamlets and LOSs

Given a certain LOS, to calculate the amount of collected photons it is necessary to integrate the particles' density of the beamlets within the volume of the LOS itself. Firstly, dBES searches for the beamlets whose axes are close enough to the LOS; to save computational time dBES searches the beamlets effectively crossed by the selected LOS, calculating the distances between their axes. The axes of the LOS and a beamlet (figure 2.10) can be thought as two vectors $\vec{v}$ and $\vec{w}$ laying on the lines L (for the Line of sight) and B (for the Beamlet) and starting respectively from the points L_0 (the centre of the lens) and B_0 (the centre of the aperture in the GG).
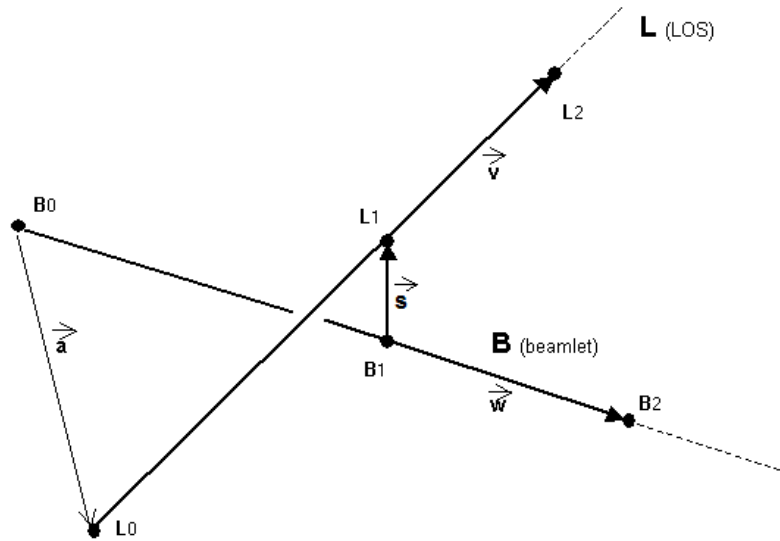

Figure 2.10: Calculation of the distance between a beamlet and a LOS.

The two vectors are calculated from L_2 and B_2, two points given together with L_0 and B_0 by the routines which define the position and the aiming of beamlets and LOSs:

$$\vec{v} = L_2 - L_0 \qquad \vec{w} = B_2 - B_0 \tag{2.26}$$

Once having defined the vector $\vec{a} = L_0 - B_0$, the distance s between the axes is obtained by exploiting

the properties of the triple product:

$$\left|\vec{d}\right| = \frac{\left|\vec{a} \cdot (\vec{v} \wedge \vec{w})\right|}{\left|\vec{v}\right|\left|\vec{w}\right|} \tag{2.27}$$

After having normalized $\vec{v}$ and $\vec{w}$, L_1 and B_1 are calculated with the following formula:

$$\begin{aligned} L_1 &= L_0 + \beta\vec{v} \\[2mm] B_1 &= B_0 + \gamma\vec{w} \end{aligned} \tag{2.28}$$

where:

$$\begin{aligned} \beta &= \frac{(\vec{a}\cdot\vec{v})-(\vec{a}\cdot\vec{w})(\vec{v}\cdot\vec{w})}{1-(\vec{v}\cdot\vec{w})^2} \\[3mm] \gamma &= \frac{(\vec{a}\cdot\vec{w})-(\vec{a}\cdot\vec{v})(\vec{v}\cdot\vec{w})}{1-(\vec{v}\cdot\vec{w})^2} \end{aligned} \tag{2.29}$$

For MITICA L_1 and B_1 can be used to evaluate how much the density of the background gas varies within the intersection region: the routines showed that the difference between the densities in those points is less than 5% , so the density can be assumed constant in all the space of the intersection. β and γ are very important, too, because they are the distance of the intersection from respectively the lens and the hole of the beamlet; in fact, the transversal dimensions of the LOS and the beamlet at the intersection points can be obtained by the aperture of the former, the divergence of the latter and these two distances. The intersection is calculated only if the distance between the axes of LOS and beamlet is less than the sum of their transversal dimensions (t_{LOS} and t_{beam} , respectively):

$$\begin{aligned} s \quad &< \quad t_{LOS}\left(L_1\right) + t_{beam}\left(B_1\right) \\[3mm] t_{LOS}\left(L_1\right) &= \quad L + \frac{W-L}{q}\beta \\[3mm] t_{beam;i}\left(B_1\right) &= \quad \sigma_{GG} + \gamma \cdot \tan\frac{3\epsilon_i}{\sqrt{2}} \end{aligned} \tag{2.30}$$

where the quantities L, W, q, σ_{GG} are defined as in the par.s 2.3.1 and 2.3.2. This condition is checked separately for each i-th component of the beamlets (par. 2.3.1), since each one can have a different value ϵ_i of divergence; as consequence, all the calculations that follow are carried out separately for each component.

Once having recognized a valid intersection, the code calculates the angle α [7]:

$$\alpha = \pi - \arccos\left(\frac{\vec{v}\cdot\vec{w}}{\left|\vec{v}\right|\left|\vec{w}\right|}\right) \tag{2.31}$$

At this point the origin of the axes is moved to the center of the lens and the axes are rotated in order to make the z axis coincide with the axis of the line of sight (figure 2.11, case on the left): in this reference frame, the x' and y' limits of the intersection volume correspond to those of the LOS

$$x'^2 + y'^2 = \left[t_{LOS}\left(L_1\right)\right]^2 \tag{2.32}$$

In the formula it has been (reasonably) assumed that the aperture angle of the LOS is too low to significantly vary t_{LOS} within the intersection volume.

---

[7]It must be remembered that the direction of the photons is not $\vec{v}$ but $-\vec{v}$.
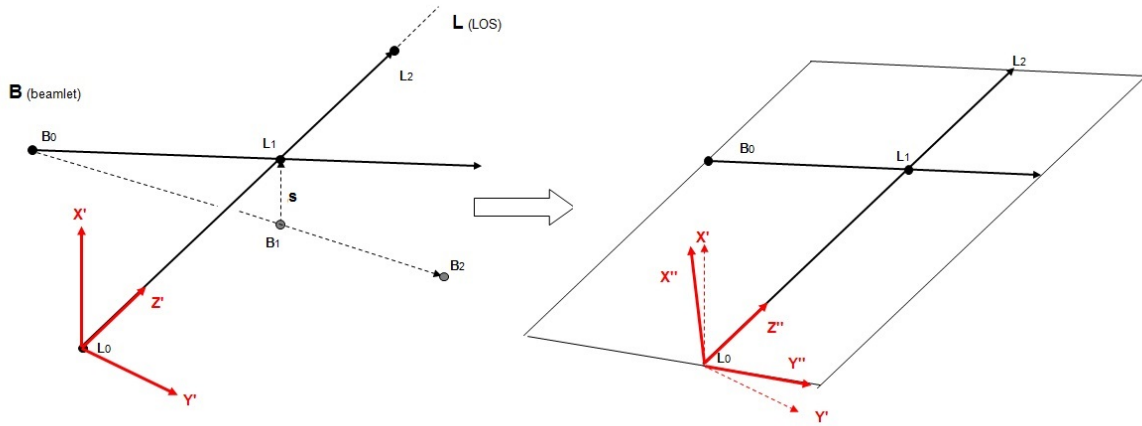
Figure 2.11: Transformations used to find the outermost values for z.

To calculate the outermost values of z' it is considered the case of the maximum intersection volume, in which $d = 0$; in practice, it is supposed that the axis of the beamlet passes in L_1 and not in B_1, so L_0, B_0 and L_1 lay in a same plane. The reference frame undergoes a new temporary rotation around the z' axis, so that the y' and z' axes lay in the new plane; the transformation is sketched in figure 2.11, case on the right.
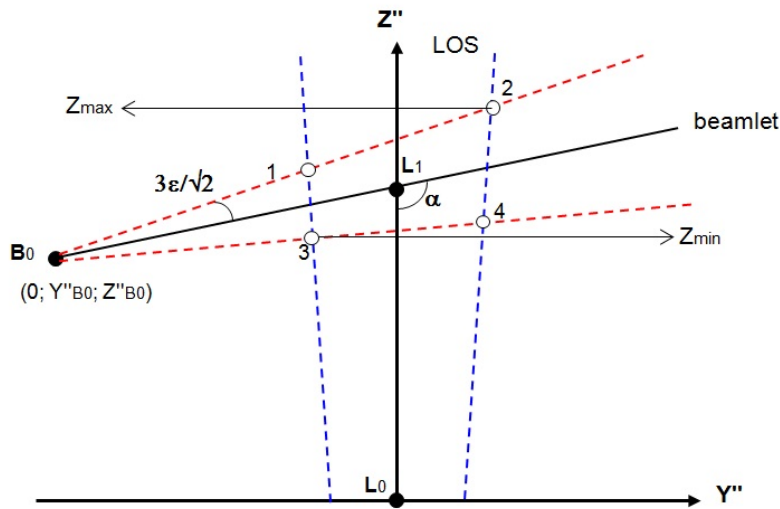

Figure 2.12: Intersection of LOS and beamlet in the plane X"Y"Z".

Thanks to this rotation the problem of finding the minimum and maximum values of z' is reduced from 3 to 2 dimensions: on the plane, the edges of beamlet and line of sight can be represented by straight lines (figure 2.12); in particular, the dimensions of the beamlet are given by the triple of its divergence[8] (as sigma, i.e. $\epsilon / \sqrt{2}$) to avoid missing a not negligible fraction of the beamlet. z'_{min} and z'_{max} are the minimum and maximum z' coordinates chosen between those of the points of intersection of the

---

[8]A subsequent check showed that a wider limit doesn't give perceptible changes in the results.

edges (white points in the figure). These values for z are

$$
\begin{aligned}
z'_1 &= z''_{B_0} + \left[-t_{LOS}(L_1) - y''_{B_0} \right] \tan \xi_{sup} \\[8pt]
z'_2 &= z''_{B_0} + \left[t_{LOS}(L_1) - y''_{B_0} \right] \tan \xi_{sup} \\[8pt]
z'_3 &= z''_{B_0} + \left[-t_{LOS}(L_1) - y''_{B_0} \right] \tan \xi_{inf} \\[8pt]
z'_4 &= z''_{B_0} + \left[t_{LOS}(L_1) - y''_{B_0} \right] \tan \xi_{inf}
\end{aligned}
\tag{2.33}
$$

where

$$
\xi_{sup} = \begin{cases} \alpha - \frac{\pi}{2} + \frac{3\epsilon}{\sqrt{2}} & \text{if } y''_{B_0} < 0 \\[8pt] \frac{\pi}{2} - \alpha - \frac{3\epsilon}{\sqrt{2}} & \text{if } y''_{B_0} > 0 \end{cases}
\qquad
\xi_{inf} = \begin{cases} \alpha - \frac{\pi}{2} - \frac{3\epsilon}{\sqrt{2}} & \text{if } y''_{B_0} < 0 \\[8pt] \frac{\pi}{2} - \alpha + \frac{3\epsilon}{\sqrt{2}} & \text{if } y''_{B_0} > 0 \end{cases}
\tag{2.34}
$$

The reference frame is then brought back to $X'\,Y'\,Z'$; considering the i-th observed component of a certain beamlet and the j-th reaction for the excitation $n = 1 \to 3$, the corresponding photon emission rate P_{ij} is calculated as follows:

$$
P_{ij} = \int\limits_{V_{LOS}} n_{gas}(L_1)\, g_i n_i \left(x';y';z' \right) b_j \sigma_j r v_i \frac{\Omega \left(x';y';z' \right)}{4\pi} dx'dy'dz'
\tag{2.35}
$$

where g_i is the fraction of the beamlet represented by its i-th component, n_i is the density of the beamlet particles according to the model of formula 2.11 and adopting the divergence ϵ_i of the i-th component, b_j is the fraction of the particles (H^-/D^-, H/D, H^+/D^+) involved in the j-th reaction, σ_j is the cross section of the j-th reaction that produces $n = 3$ excited atoms, r is the branching ratio of the H_α/D_α de-excitation, v_i is the speed of the particles of the i-th component of the beamlets and Ω is the solid angle under which the photons are collected (par. 2.3.2). In practice, the calculation is split into two levels, the first of which estimates the integrals

$$
I_i = \int\limits_{V_{LOS}} \frac{\Omega \left(x';y';z' \right)}{4\pi} \frac{n_{gas} r^2_{holes}}{\left(\sigma_{GG} + z' \cdot \tan \epsilon_i \right)^2} \cdot e^{-\left(x^2 + y^2 \right) / \left(\sigma_{GG} + z' \cdot \tan \epsilon_i \right)^2} dx'dy'dz'
\tag{2.36}
$$

The integration is carried out in cylindrical coordinates:

$$
I_i = \int\limits_{z'_{min}}^{z'_{max}} dz \int\limits_0^{t_{LOS}} \rho \frac{\Omega \left(z;\rho \right)}{4\pi} d\rho \int\limits_0^{2\pi} d\varphi \frac{n_{gas} r^2_{holes}}{\left(\sigma_{GG} + z \cdot \tan \epsilon_i \right)^2} \cdot e^{-\rho^2 / \left(\sigma_{GG} + z \cdot \tan \epsilon_i \right)^2}
\tag{2.37}
$$

To speed up the calculation, the Simpson 1/3 integration method was adopted to lower the number of steps required. By default the effect of the non zero de-excitation time of the $n = 3$ level is not taken into account, being the de-excitation length short respect to the possible gradients in the gas density profile. Optionally, if this effect is considered the estimation of I_i becomes

$$
I_i = \int\limits_{z_{min}}^{z_{max}} dz \int\limits_0^{t_{LOS}} \rho \frac{\Omega \left(z;\rho \right)}{4\pi} d\rho \int\limits_0^{2\pi} d\varphi\, r^2_{holes} e^{-\rho^2 / \left(\sigma_{GG} + s \cdot \tan \epsilon_i \right)^2} \int\limits_0^z ds \frac{n_{gas}(s)}{\left(\sigma_{GG} + s \cdot \tan \epsilon_i \right)^2} \frac{1}{\beta c \tau} e^{-\frac{z-s}{\beta c \tau}}
\tag{2.38}
$$

in the approximation that $\epsilon_i \ll 1$ and therefore $\sqrt{z^2 + \rho^2} \sim z$; in this way the decay length $\beta c \tau$ can

be compared not the single particle trajectories (linked to the transversal distribution of the beamlets[9]) but directly to the coordinate z.

The second level of the calculation completes the evaluation of the terms P_{ij} for the considered beamlet:

$$P_{ij} = I_i \cdot g_i n_{GG} v_i r b_j \sigma_j (v_i) \tag{2.39}$$

The calculations are performed for all the beamlets which have some of their components crossed by the LOS.

Finally, to find the signal effectively acquired by a BES diagnostic each term P_{ij} must be multiplied by an attenuation factor l that represents the optical losses introduced by the lens, the fibre, the spectrometer and the couplings between each optical component, by the exposure time t_{exp} of the CCD and by a factor Q that combines the quantum efficiency and the amplification of the CCD. The resulting contributions expressed in ADC counts are then distributed on the spectrum as Gaussian profiles, whose centroids are calculated by means of formula 2.1 from α, v_i and the type of reaction[10]. The width $\sigma_{\lambda TOT}$ of the Gaussians is calculated as in eq. 2.25 . The final signal is given by the sum of all these Gaussians; the Poisson noise is added to the signal, too.

2.3.7 Analysis of the spectra

Besides simulating the spectra of the BES diagnostics, dBES has routines also to analyze the spectra and derive the desired quantities. For the measurement of the average divergence on observed beamlets, the width $\sigma_{\lambda TOT}$ of the main Doppler peak is obtained by a numerical fit of the spectral line profile; subsequently, the divergence is calculated by inverting formula 2.25:

$$\sigma_\epsilon = \left(\frac{\lambda \beta \sin \alpha}{\sqrt{1-\beta^2}} \right)^{-1} \left[\sigma_{\lambda TOT}^2 - \sigma_{\lambda I}^2 - \sigma_{\lambda S}^2 - \left(\frac{\lambda \beta \sin \alpha}{\sqrt{1-\beta^2}} \right)^2 \sigma_\omega^2 + \right.$$
$$\left. - \left(\frac{e\lambda}{m\beta} (\beta - \cos \alpha) \right)^2 \sigma_V^2 \right]^{\frac{1}{2}} \tag{2.40}$$

To carry out the calculation various data are requested in input: $\sigma_{\lambda I}$ is known, $\sigma_{\lambda S}$ can be measured preliminarily during the setup of the diagnostic, β is known from the voltage measurements on the grids, while α can be obtained from the spectral separation between the main Doppler peak and the unshifted H_α/D_α line:

$$\alpha = \arccos \left[\frac{1}{\beta} \left(1 - \frac{\lambda'}{\lambda_0} \sqrt{1 - \beta^2} \right) \right] \tag{2.41}$$

This esteem has obviously an error; σ_α is derived with the standard propagation rules considering the measurement error σ_{V_0} on the total acceleration voltage V_0 (which determines β) and the error in the determination of λ'. The wavelength of the main Doppler peak is measured from the reading of the CCD, which gives an array of counts as function of the pixels:

$$\lambda' = \lambda_0 + \left(p_{dop} - p_0 \right) d \tag{2.42}$$

where p_{dop} and p_0 are the centroids (in pixels) of the fits of the main Doppler peak and the unshifted H_α/D_α line. Both the centroids are determined with an error, σ_G, which was roughly estimated as 0.05 *pix* in typical acquisition conditions. The plate factor d is usually measured as the ratio between

---

[9]The term $(\sigma_{GG} + s \cdot \tan \epsilon)^2$ is kept inside the convolution operation because it affects the density along the beamlet axis.

[10]As explained in sec. 2.1, in some reactions the excited particle is a fast particle of the beam, in others the H_α/D_α radiation is produced by slow particles deriving from the dissociation of the gas molecules.

the difference of two known wavelengths and the difference of the respective positions in pixels on the CCD:

$$d = \frac{\lambda_1 - \lambda_2}{p_1 - p_2} \tag{2.43}$$

Assuming that $\sigma_1 = \sigma_2 = \sigma_G$, it is

$$\sigma_d = \sqrt{2}\frac{\lambda_1 - \lambda_2}{(p_1 - p_2)^2}\sigma_G = \frac{\sqrt{2}d\sigma_G}{p_1 - p_2} \approx 0.002d \qquad \text{if} \quad p_1 - p_2 = 100 \tag{2.44}$$

The propagation of errors showed that in all the considered BES diagnostics σ_α is in the order of $10^{-3}\ rad$. The error in the measurement of α propagates in formula 2.40, therefore also the measure of divergence has an error, Σ_ϵ [11]. However, σ_α is not the only source of error; the instrumental broadening has an error $\Sigma_{\lambda S}$ because of the uncertainty on d and because in real diagnostic F is determined by the width (in pixels) of test lines in the spectrum:

$$\Sigma_{\lambda S}^2 = \left(\frac{d}{2\sqrt{2\ln 2}}\right)^2 \sigma_G^2 + \left(\frac{F}{2\sqrt{2\ln 2} \cdot p_{size}}\right)^2 \sigma_d^2 \tag{2.45}$$

Analogously, $\sigma_{\lambda TOT}$ has an error $\Sigma_{\lambda TOT}$ because of the uncertainty of d and the error in the fit of the Doppler peak:

$$\sigma_{\lambda TOT} = \sigma_{\lambda TOT[pixel]}d \implies$$

$$\Sigma_{\lambda TOT} = \sqrt{d^2\Sigma_{\lambda TOT[pixel]}^2 + \sigma_{\lambda TOT}^2\sigma_d^2} = \sqrt{d^2\sigma_G^2 + \sigma_{\lambda TOT}^2\sigma_d^2} \tag{2.46}$$

ω is another delicate input parameter for formula 2.40: it varies within the intersection volume of each beamlet with the LOS, but also from one intersection volume of a beamlet to another one. The value of ω is obtained by simulating the spectrum to be analyzed with dBES. The code keeps track of the value of ω in each volume element of the integration in formula 2.37; the average and the standard deviation of ω were calculated for each beamlet weighting the single values of ω with the contribution of each volume element to the integration. The mean value of ω over the observed beamlets is then computed. To calculate the error Σ_ω in the estimation of ω the following procedure is adopted: the extreme values of ω within each beamlet are considered, i.e. $\omega - \Sigma_{\omega;beamlet}$ and $\omega + \Sigma_{\omega;beamlet}$, where $\Sigma_{\omega;beamlet}$ is the standard deviation of ω for a specific beamlet. The minimum and the maximum of these values were used to calculate Σ_ω:

$$\Sigma_\omega = \frac{\max\left(\omega + \Sigma_{\omega;beamlet}\right) - \min\left(\omega - \Sigma_{\omega;beamlet}\right)}{2\sqrt{3}} \tag{2.47}$$

where $\sqrt{3}$ was inserted roughly assuming that the values of ω are uniformly distributed in the interval set by the numerator of formula 2.47. It resulted that in the considered test facilities Σ_ω is within the range $15 \div 25\%$.

At last, the error Σ_ϵ on the measurement of the divergence is influenced by the errors σ_{V_0} and Σ_V, with which the total acceleration voltage and the voltage ripple are respectively measured. The complete propagation of errors for Σ_ϵ is shown in the following formula:

$$\Sigma_\epsilon^2 = \left(\frac{\partial\sigma_\epsilon}{\partial\sigma_{\lambda TOT}}\right)^2 \Sigma_{\lambda TOT}^2 + \left(\frac{\partial\sigma_\epsilon}{\partial\sigma_{\lambda S}}\right)^2 \Sigma_{\lambda S}^2 + \left(\frac{\partial\sigma_\epsilon}{\partial\alpha_0}\right)^2 \sigma_\alpha^2 +$$

$$\left(\frac{\partial\sigma_\epsilon}{\partial V}\right)^2 \sigma_{V_0}^2 + \left(\frac{\partial\sigma_\epsilon}{\partial\omega}\right)^2 \Sigma_\omega^2 + \left(\frac{\partial\sigma_\epsilon}{\partial\sigma_V}\right)^2 \Sigma_V^2 \tag{2.48}$$

---

[11]The symbol Σ_ϵ was adopted to not confuse this quantity with σ_ϵ.

where the appearing partial derivatives are:

$$\frac{\partial \sigma_\epsilon}{\partial \sigma_{\lambda TOT}} = \sigma_{\lambda TOT} \left(\frac{\partial \lambda'}{\partial \alpha}\right)^{-1} [\cdots]^{-1/2},$$

$$\text{with } [\cdots] \equiv \sigma_{\lambda TOT}^2 - \sigma_{\lambda I}^2 - \sigma_{\lambda S}^2 - \left(\frac{\partial \lambda'}{\partial \alpha_0}\right)^2 \sigma_\omega^2 - \left(\frac{\partial \lambda'}{\partial V_0}\right)^2 \sigma_{V_0}^2$$

$$\frac{\partial \sigma_\epsilon}{\partial \sigma_{\lambda S}} = -\sigma_{\lambda I} \left(\frac{\partial \lambda'}{\partial \alpha}\right)^{-1} [\cdots]^{-1/2}$$

$$\frac{\partial \sigma_\epsilon}{\partial \omega} = -\omega \left(\frac{\partial \lambda'}{\partial \alpha}\right)^{-1} [\cdots]^{-1/2} \tag{2.49}$$

$$\frac{\partial \sigma_\epsilon}{\partial \sigma_V} = -\sigma_V \left(\frac{\partial \lambda'}{\partial \alpha}\right)^{-1} \left(\frac{\partial \lambda'}{\partial V}\right)^2 [\cdots]^{-1/2}$$

$$\frac{\partial \sigma_\epsilon}{\partial \alpha} = -\left(\frac{\partial \lambda'}{\partial \alpha}\right)^{-2} \frac{\partial^2 \lambda'}{\partial \alpha^2} [\cdots]^{1/2} - \left(\frac{\partial \lambda'}{\partial \alpha}\right)^{-1} [\cdots]^{-1/2} \left[\omega^2 \frac{\partial \lambda'}{\partial \alpha} \frac{\partial^2 \lambda'}{\partial \alpha^2} + \sigma_V^2 \frac{\partial \lambda'}{\partial V} \frac{\partial^2 \lambda'}{\partial \alpha \partial V}\right]$$

$$\frac{\partial \sigma_\epsilon}{\partial V} = -\left(\frac{\partial \lambda'}{\partial \alpha}\right)^{-2} \frac{\partial^2 \lambda'}{\partial V \partial \alpha} [\cdots]^{1/2} - \left(\frac{\partial \lambda'}{\partial \alpha}\right)^{-1} [\cdots]^{-1/2} \left[\omega^2 \frac{\partial \lambda'}{\partial \alpha} \frac{\partial^2 \lambda'}{\partial V \partial \alpha} + \sigma_V^2 \frac{\partial \lambda'}{\partial V} \frac{\partial^2 \lambda'}{\partial V^2}\right]$$

The first and second derivatives of λ' with respect to α and V are

$$\frac{\partial \lambda'}{\partial \alpha} = \frac{\lambda_0 \beta \sin \alpha}{\sqrt{1-\beta^2}} \qquad \frac{\partial^2 \lambda'}{\partial \alpha^2} = \frac{\lambda_0 \beta \cos \alpha}{\sqrt{1-\beta^2}} \qquad \frac{\partial^2 \lambda'}{\partial \alpha \partial V} = \frac{e \lambda_0 \sin \alpha}{m \beta}$$

$$\frac{\partial \lambda'}{\partial V} = \frac{e \lambda_0}{m} \left(1 - \frac{\cos \alpha}{\beta}\right) \qquad \frac{\partial^2 \lambda'}{\partial V \partial \alpha} = \frac{e \lambda_0 \sin \alpha}{m \beta} \qquad \frac{\partial^2 \lambda'}{\partial V^2} = \frac{e^2 \lambda_0 \cos \alpha}{\beta^3 m^2} \left(1 - \beta^2\right)^{3/2} \tag{2.50}$$

The main input parameter of this calculations is $\sigma_{\lambda TOT}$, which can be obtained with a Gaussian fit of the main Doppler peak. If the angle α between the beamlets and the considered LOS vary strongly from beamlet to beamlet, the main Doppler peak will be distorted. If these fluctuations were not symmetrically distributed around the average value α it could be possible to notice an asymmetrization of the main Doppler peak. If instead the variations of α are much higher than ϵ multiple Doppler peaks would be observed , more or less overlapped between them. In this case a fit with multiple Gaussians can be performed. Another issue are the stripping losses, whose emissions are partially superimposed to the Doppler peak, changing its shape. This problem affects more the low energy side of the Doppler peak, while the other side can be exploited for the fit.

Besides measuring the direction and the divergence of the beamlets, a BES diagnostic should be able to characterize the uniformity of the beam. This could be done by comparing the integral of the main Doppler peak in the spectra collected by different LOSs; an absolute calibration should be obviously done on the optical systems. The integrals of the Doppler peaks, however, depend on the number of observed beamlets and their proximity to the LOS, conditions which are practically different for each LOS. The integrals should therefore be weighted using the values of P_{ij} obtained by dBES using input parameters which reflect the real condition. To calculate the terms P_{ij}, the position of the LOSs with respect to the beamlets has to be known; this information can be retrieved by tomographic systems or by the calorimeter, but with a precision which could not be sufficient. An alternative method to measure the beam uniformity [12] simply consists in measuring the horizontal and vertical trends of the divergence in the beam: as described in par. 1.3.1, the divergence of the beamlets is determined by the optics of the grids, which in turn are influenced by the extracted current density. Beamlets carrying different values of current have therefore different values of divergence, and vice versa. It was estimated [12] that to obtain measures of uniformity with a relative error below 10% the divergence should be measured with

an error below 5%. Necessary conditions for a comparison of this type is that different LOSs mustn't observe beamlets in common, and that a LOS mustn't receive light from beamlets with different values of divergence. In practice, the dimensions of the beamlets (determined by the divergence) at the point of observation and the characteristic length of the gradients of divergence ($\epsilon/\nabla\epsilon$) must be shorter than the spacing of the LOSs. Moreover, it must be proved that in the considered operative conditions ϵ depends linearly on the current density, or anyway an exact relation between the two quantities must be determined in order to correctly weight the variations of ϵ.

2.4   IPP BES diagnostics and codes for the benchmark of dBES

To be able to give realistic indications for the future diagnostics, a model or a code must be validated by experimental results. A benchmark was made possible at IPP Garching, where BES diagnostics have been installed and are (or have been) operative on the BATMAN, MANITU and ELISE test facilities. To simulate the BES spectra dBES was coupled to the codes BBC-NI-advanced (*Bavarian Beam Code for Negative Ions*) [12] and EAMCC (*Electrostatic Accelerator Monte Carlo simulation Code*) [60, 61]. The spectra generated by dBES were compared to the experimental ones and to those simulated by the code BBC-NI in both its "simple" and "advanced" configuration. Moreover, dBES was modified in 2 optional versions, dBES-2 and dBES-3, to take into account alternative algorithms of effects neglected in the standard version. The information on the BES diagnostics of the IPP test facilities is now presented, together with the details of the codes which supported the benchmark of dBES.

2.4.1   The BES diagnostic in BATMAN

The BES diagnostic in the BATMAN has not been the same during all the lifetime of the test facility, but has been upgraded in 2013 [62]. Before the upgrade the diagnostic was equipped with two horizontal LOSs, observing the beam from a viewport of the vaccum vessel. The main characteristics of the diagnostic (in the old configuration) are listed in table 2.1. Differently from the setup described in par. 2.3.2, inside the 2 optic heads the end of the fiber is placed at the focal distance (30 *mm*) of the lens. It was verified a posteriori that the LOSs created by these optic heads is not cylindrical but slightly diverges with angle of about 0.6° [12]. The image of the fiber head is therefor virtual, on the same side of the fiber respect to the lens; the distance between fiber and lens is about 29.7 *mm*. The optic simulation described in par. 2.3.2 gave the solid angle Ω of collection of the photons, as function of the axial and radial coordinates of the LOS (figure 2.13).

Quantity	value
typical range of measured values of ϵ (e-folding)	$20 \div 150 \, mrad$
α (LOS 1/ LOS 2)	$63.58°/61.06°$
Distance of LOSs from the GG along the beam axis (x)	$1.5 \, m$
Horizontal distance of LOSs from the beam axis (y)	$0.6 \, m$
Vertical distance of LOSs from the beam axis (z)	$-5 \, cm$ (LOS 1) $1.5 \, cm$ (LOS 2)
Clear aperture of the lenses ($2L$)	$20 \, mm$
Focal length of the lenses	$30 \, mm$
Diameter of fiber core	$400 \, \mu m$
Plate factor of the spectrometer (d)	$7 \, pm/pix$
Entrance slit width of the spect. (F)	$70 \, \mu m$
$\sigma_{\lambda S}$ (sigma width of instrumental function)	$0.018 \, nm$
Pixel size of CCD (p_{size})	$13 \, \mu m$
Number of pixels in the CCD	1024x1024

Table 2.1: Characteristics of the BES diagnostic in BATMAN. The double values refer to the 2 LOSs singularly [12, 63].
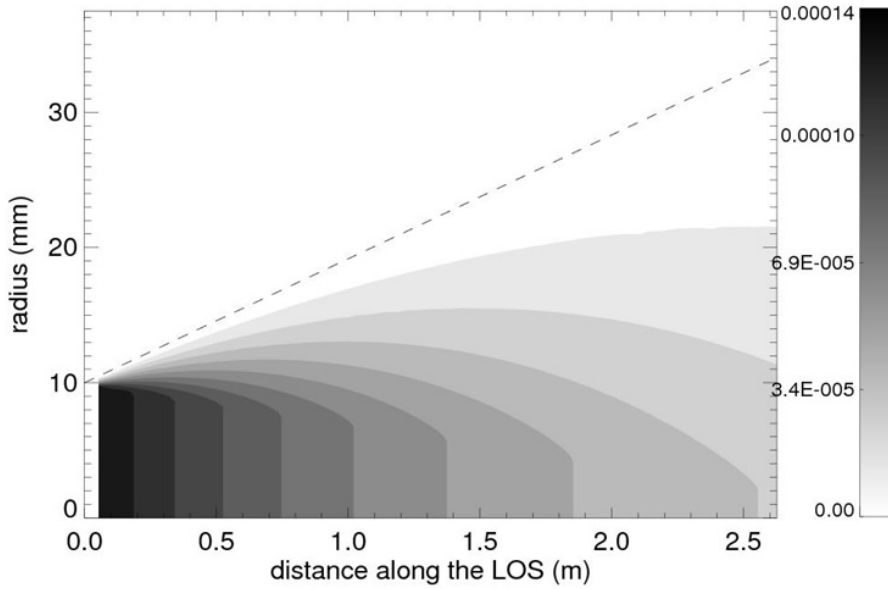
Figure 2.13: Solid angle (in srad) of collection of the optic heads in BATMAN and ELISE, as function of the longitudinal and radial distances respect to the axis of the LOS (beware the different units used in the axes of the plot).

Following the procedure indicated in par. 2.3.7, the information of table 2.1 and figure 2.13 was used in preliminary runs of dBES to get the plane angle of observation of the lens ω and its variation Σ_ω. It resulted that $\omega = 5.7 \, mrad$ and $\Sigma_\omega = 0.79 \, mrad$ (14%). In principle ω could vary according to the divergence and the positioning of the beamlets; the simulations of dBES however indicated that these variations are well within Σ_ω for both the LOSs and in the range of the measured values of ϵ.

With the upgrade of the BES diagnostic [62, 12, 44] the configuration of the optic heads was not changed, therefore the results of the optic simulation are the same of figure 2.13; however, the optic heads were installed inside the vacuum chamber and their number was increased to 5. All the optic heads are oriented in horizontal direction; figure 2.14a shows the optic heads installed inside the vacuum chamber, whereas figure 2.14b shows the vertical position of the axes of the LOSs with respect to the

apertures of the GG. The radius of the LOSs at the center of the GG is of about 16 *mm*.
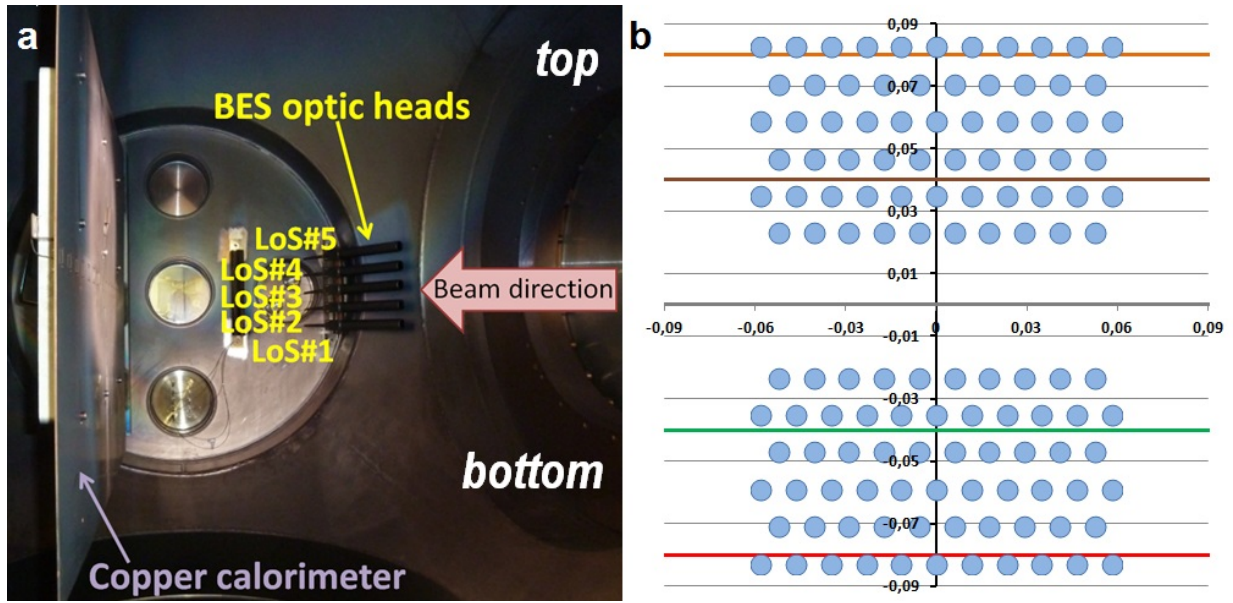

Figure 2.14: a) Position and numbering of the LOSs for the new BES diagnostic in BATMAN[64]. b) Height of the axes of the LOSs with respect to the apertures of the GG. At the center of the GG the radius of the LOSs is of about 16 mm. The values indicated in the Cartesian axes are in meters.

With the upgrade of the system the spectrometer and the CCD camera were changed, too. Their properties and those of the new BES diagnostic are listed in table 2.2. As it is shown, the plate factor of the spectrometer is not constant along the acquired portion of the spectrum.

Quantity	value
typical range of measured values of ϵ (e-folding)	$20 \div 150\ mrad$
α	$57°$
Distance of LOSs from the GG along the beam axis (x)	$1.2\ m$
Horizontal distance of LOSs from the beam axis (y)	$0.5\ m$
Clear aperture of the lenses ($2L$)	$20\ mm$
Focal length of the lenses	$30\ mm$
Diameter of fiber core	$400\ \mu m$
Plate factor of the spectrometer (d) ($\lambda_{min} = 647.7\ nm$, $\lambda_{max} = 661.6\ nm$)	$15\ pm/pix$ @λ_{min} $12\ pm/pix$ @λ_{max}
Entrance slit width of the spect. (F)	$70\ \mu m$
$\sigma_{\lambda S}$ (sigma width of instrumental function)	$0.045\ nm$
Pixel size of CCD (p_{size})	$26\ \mu m$
Number of pixels in the CCD	1024×255

Table 2.2: Characteristics of the BES diagnostic (latest setup) in BATMAN. λ_{min} and λ_{max} are the outermost values of wavelength observed by the CCD camera[12].

The information of figure 2.14 and table 2.2 were used in preliminary simulations of dBES to estimate the values of ω and Σ_ω; it resulted that $\omega = 4.9\ mrad$ and $\Sigma_\omega = 0.7\ mrad$ (14%). It was verified that the position of the LOSs and the beamlets' divergence cause variations of ω well within the interval given by Σ_ω.

The measures of divergence are obtained by the BES spectra by means of the so called IPP standard evaluation method: this consists in fitting the main Doppler peak with a Gaussian curve to get its (sigma) width $\sigma_{\lambda TOT}$; the fit is applied on the upper part of the peak, from the 30% of its height. The divergence

(in e-folding) is obtained by the formula

$$\epsilon = \sqrt{2} \cdot \frac{\sqrt{\sigma_{\lambda TOT}^2 - \sigma_{\lambda S}^2}}{|(\lambda' - \lambda_0) \tan \alpha|} \tag{2.51}$$

The fraction of stripping losses f_{strip} instead is measured by comparing the integral of the contribution of the stripping losses I_{strip} with the integral I_{main} of the main Doppler peak:

$$f_{strip} = \frac{I_{strip}/\sigma\left(U_{ext}\right)}{I_{strip}/\sigma\left(U_{ext}\right) + I_{main}/\sigma\left(U_{tot}\right)} \tag{2.52}$$

where σ is the comprehensive cross section for the production of H_α/D_α photons, calculated at the extraction energy (U_{ext}) and at the full acceleration energy (U_{tot}). I_{strip} is measured by integrating the signal of the spectrum in an interval of $\pm 0.25\,nm$ around the wavelength corresponding to the extraction voltage [12].

2.4.2 The BES diagnostic in MANITU

In MANITU the beam was observed along 13 horizontal LOSs and 7 vertical LOSs, arranged as shown in figure 2.15; the optic heads used in the diagnostic had the same characteristics of those used in BAT-MAN. The key parameters of the whole BES diagnostic are listed in table 2.3.

As in BATMAN, using the data of the optical simulations and the information on the diagnostic it was possible to calculate that $\omega = 5.5\,mrad$ and $\Sigma_\omega = 1.0\,mrad$ (18%).

The methods of analysis to measure the divergence and the fraction of stripping losses were the same used in BATMAN.
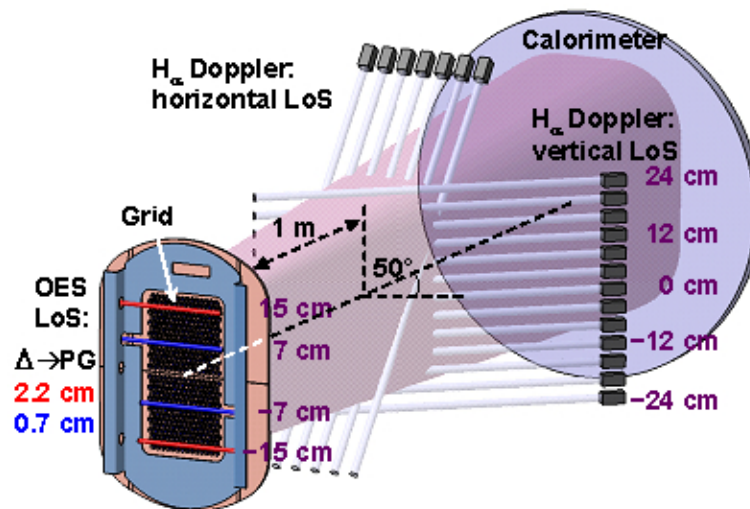
Figure 2.15: Positioning and orientation of the LOSs of the BES diagnostic in MANITU [46]. The positioning of the LOSs of the OES diagnostic next to the PG is shown, too.

Quantity	value
ϵ (e-folding) expected	$20 \div 100 \, mrad$
α (horizontal/vertical LOSs)	$56°/60°$
Distance of all LOSs from the GG along the beam axis (x)	$1.7 \, m$
Distance of horizontal LOSs from the beam axis (y)	$0.3 \, m$
Vertical separation between adjacent horizontal LOSs (z)	$4 \, cm$
Distance of vertical LOSs from the beam axis (z)	$0.3 \, m$
horizontal separation between adjacent vertical LOSs (y)	$4.6 \, cm$
Clear aperture of the lenses ($2L$)	$20 \, mm$
Diameter of fiber core	$400 \, \mu m$
Plate factor of the spect. (d)	$7 \, nm/pix$
Entrance slit width of the spect. (F)	$70 \, \mu m$
Pixel size of CCD (p_{size})	$13 \, \mu m$
Number of pixels in the CCD	1024x1024

Table 2.3: Characteristic of the BES diagnostic in MANITU [46, 39, 60].

2.4.3   The BES diagnostic in ELISE

The BES diagnostic in ELISE [12] has 20 LOSs, 4 vertical and 16 horizontal, oriented as shown in figure 2.16a; the projection of the axes of the LOSs on the vertical plane is shown in figure 2.16b, together with the positions of the apertures in the GG. The spectrometer and the CCD camera of the diagnostic are the same used in the first version of the BES diagnostic in BATMAN. With the same procedure of adopted for BATMAN and MANITU, it was calculated that $\omega = 3.9 \, mrad$ and $\Sigma_\omega = 0.9 \, mrad$ (18%). The position of the LOSs with respect to the beamlets and the divergence can influence the value of ω, but always within the range set by Σ_ω.

The algorithms used by the BES diagnostic to measure the beamlets' divergence and the fraction of stripping losses is the same used in BATMAN and MANITU.
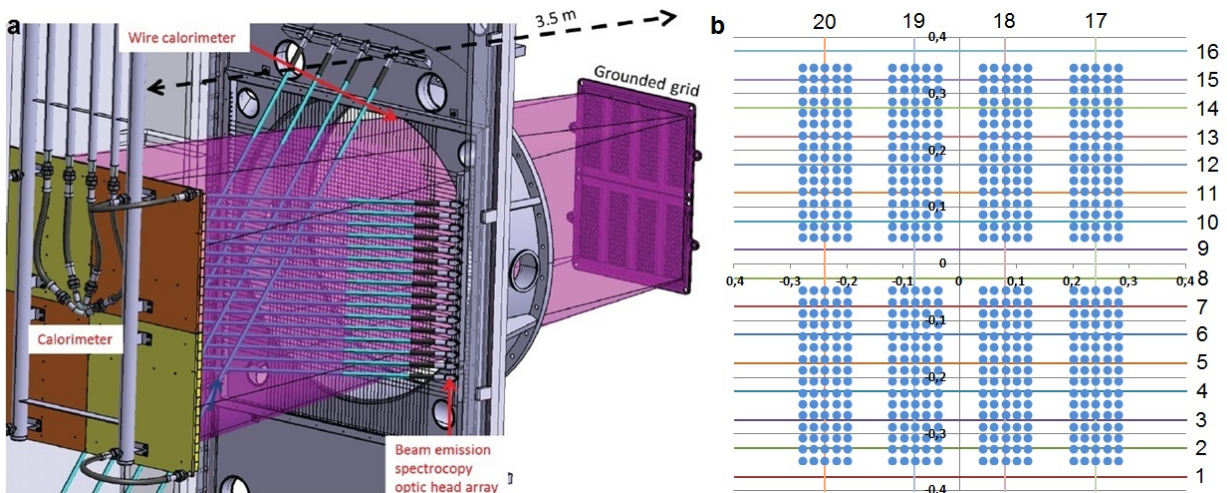

Figure 2.16: a) Positioning and orientation of the BES LOSs in ELISE with respect to the GG and the other beam diagnostics (the calorimeter and the W-wire calorimeter) [12]. b) Position and numbering of the LOSs with respect to the apertures of the GG (the units of the axes are in meters).

Quantity	value
typical range of measured values of ϵ (e-folding)	$20 \div 150\ mrad$
α	130°
Distance of LOSs from the GG along the beam axis (x)	$2\ m$
Distance of horizontal LOSs from the beam axis (y)	$0.8\ m$
Distance of vertical LOSs from the beam axis (z)	$0.9\ cm$
Clear aperture of the lenses ($2L$)	$20\ mm$
Focal length of the lenses	$30\ mm$
Diameter of fiber core	$400\ \mu m$
Plate factor of the spectrometer (d)	$7\ pm/pix$
Entrance slit width of the spect. (F)	$70\ \mu m$
$\sigma_{\lambda S}$ (sigma width of instrumental function)	$0.018\ nm$
Pixel size of CCD (p_{size})	$13\ \mu m$
Number of pixels in the CCD	1024x1024

Table 2.4: Characteristics of the BES diagnostic in ELISE [12, 44].

2.4.4   BBC-NI

The code BBC-NI [12] was developed at IPP Garching with the main purpose of identifying the physical aspects which determine the BES spectra and support the analysis of the data collected by the BES diagnostic. Whereas dBES is adopts analytical algorithms to retrieve the amount and the angular distribution of the photons collected by BES, BBC-NI is based on a Monte Carlo approach, i.e. the code simulates the trajectories and the interactions of a certain number of beam particles. BBC-NI was developed in two versions: BBC-NI advanced and BBC-NI simple.

2.4.4.1   BBC-NI advanced

In the advanced version the code considers a laminar flow of a number ($\lesssim 10^9$) of negative ions at the meniscus of the apertures of the PG. BBC-NI-advanced then calculates the evolution of the particles's trajectories through the whole acceleration stage. The calculation takes into account the electric field produced by the grids and by the charge of the ions themselves; the map of the electric field is calculated by the subprogram KOBRA3-INP [65] for a single grids' aperture and is then applied to all. BBC-NI-advanced takes also into account the collision of the particles with the gas molecules, together with the possible emission of secondary particles (eg electrons); the density profile of the gas molecules inside the acceleration system is calculated by the EXCELSTRIP [12] program. For the benchmark the magnetic field instead was not considered, because it hadn't been fully implemented in the code yet.

Downstream the GG, BBC-NI-advanced simulates the excitation of the particles by the random collision with the gas molecules of the background gas. The code then selects the points of emission of the photons which are inside the LOS volume, simulating the isotropic emission of multiple photons from each position[12]. The photons which hit the surface of the lens give rise each one to a Gaussian in the simulated spectrum, whose central wavelength is given by speed and direction of the de-excited particle, and whose width is the same of the spectrometer instrumental function. This algorithm allows to take into account 3 phenomena which distort the shape of the main Doppler peak with respect to a Gaussian curve:

1. The **volume effect**, due to the fact that the solid angle of collection of the optics falls with the distance from the optic head. The light emitted by the sides of the beamlets closer to the optic heads is more efficiently collected respect to the light coming from the opposite sides. If $\alpha < 90°$, the low energy side of the main Doppler peaks is higher with respect to the high energy one; the

---

[12]Multiple photons are emitted from each single point to reduce the calculation time and improve the statistic of the simulation.

situation is reversed if $\alpha < 90°$. This effect is more pronounced if the beamlets are closer to the optic head, or if the volume shared by beamlets and LOS is more elongated; this last case happens at high divergences or at values of α far from $90°$.

2. The **area effect**, which consists in the fact that the section of the LOS can vary with the distance from the optic head. This effect, as the volume one, is sensible to the elongation of the beamlets inside the LOS and therefore is influenced also by α and ϵ. As result the full energy component becomes asymmetric, in the opposite way with respect to the volume effect.

3. The **origin effect**, based on the fact that a LOS intercepts a beamlet with a given distance between the axes of LOS and beamlet. For certain angular distributions of the beamlet particles, the angular distribution of the collected photons varies whether the core or the tail of a beamlet is observed. In other words, the photons received by a optic head are produced by a group of particles whose angular distribution is distorted with respect to the one of the whole beamlet.

With respect to BBC-NI-advanced, dBES keeps these effects into account only in the calculation of the amount of collected photons, but not in the angular distribution of the photons themselves.

2.4.4.2   BBC-NI simple and the parametrization method

In the simplified version of BBC-NI the extraction and the acceleration of the beamlets' particles are not simulated. A bunch of negative ions is considered directly at the exit of the GG for each aperture, the direction of the ions is set according to the azimuthal and polar angles (γ_a, γ_p):

$$\gamma_a = \epsilon \cdot \mathrm{erf}^{-1}\left(z_1\right); \qquad \gamma_p = 2\pi z_2 \tag{2.53}$$

where z_1 and z_2 are two random numbers uniformly distributed in the interval $[0, 1]$. The random excitation of the beamlets' particles, the emission of the photons and the generation of the BES spectrum is the same as in BBC-NI-advanced. Also BBC-NI simple is therefore able to fully take into account the volume, area and origin effects.

An important difference between dBES and BBC-NI simple is that in dBES the power density distribution of the beamlets follows a Gaussian function, while in BBC-NI simple it's the angular distribution of the particles which follows a Gaussian. In the second case, the power density of the particles with an angle between θ and $\theta + d\theta$ is proportional to the number of particles divided by $2\theta d\theta$. In comparison to dBES, the power density profile corresponding to the model used in BBC-NI-simple is much narrower and with more pronounced tails at the side. This difference clearly influences the angular distribution of the particle observed by a LOS. In particular, these two angular distributions are differently affected by the 3 distorsion effects mentioned in par. 2.4.4.1. In the case of dBES, the origin effect does not affect the BES spectra: to demonstrate it, let's consider an horizontal LOS, infinitely thin, which observes a beamlet perpendicularly and off-axis; a representation of this is shown in figure 2.17.
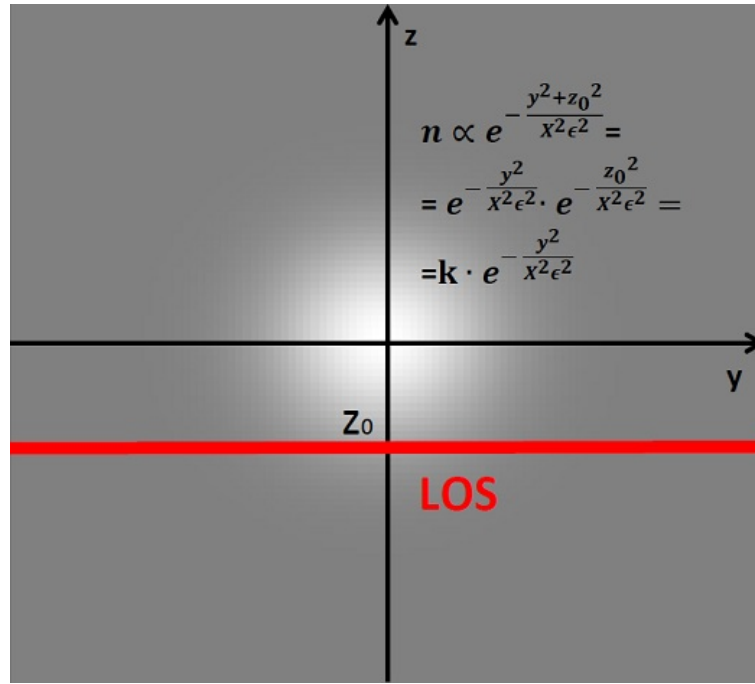
$$n \propto e^{-\frac{y^2+z_0{}^2}{X^2\epsilon^2}} =$$

$$= e^{-\frac{y^2}{X^2\epsilon^2}} \cdot e^{-\frac{z_0{}^2}{X^2\epsilon^2}} =$$

$$= k \cdot e^{-\frac{y^2}{X^2\epsilon^2}}$$

Figure 2.17: Scheme of an horizontal LOS passing perpendicularly near a beamlet with a Gaussian power density profile.

Adopting a Gaussian power density profile (white area in figure 2.17), the beamlet density has a Gaussian dependence from the distance from the beamlet axis. This dependence can be easily decoupled along the coordinates y,z of the plane perpendicular to the beamlet axis. Since the points belonging to the LOS have the same vertical coordinate z_0, the variation of the density along the LOS is controlled only by y. The density profile of the beamlet's particles along the LOS is then a Gaussian curve, whose width is ϵ and whose integral is reduced of a factor $k = \exp\left(-z_0^2/X^2\epsilon^2\right)$ with respect to the case with $z_0 = 0$. Because the amount of collected H_α/D_α photons is proportional to the density of the beamlet's particles along the LOS, the angular distribution of the photons with respect to the LOS direction is a Gaussian of width ϵ. The real LOSs have an intrinsic width, therefore on the plane yz they can be represented by a sum of nearby lines. Each one will give a Gaussian of different intensity but of the same width, therefore the total sum will be a Gaussian of width ϵ. This result however is only valid if the angle of obervation α is equal or close to 90°, and the volume and area effects are still present.

With the particle distribution of BBC-NI-simple, instead, what happens is different: the angular distribution of the collected photons depends also on the relative distance between the axes of LOS and beamlets. Using the same scheme of figure 2.17, it can be seen that at high values of $|z_0|$ the only particles which can be observed by the LOS have large angles with respect to the axis, which are however small if projected on a horizontal plane. This phenomenon happens also with the distribution adopted by dBES, but in this case the width of the angular distribution is not conserved. It happens that the spectral contributions of beamlets with their axes far from the LOS are narrower than those of the closer beamlets; the final result of BBC-NI simple is a full energy component with a narrow core and broader tails, similarly to what often happens in the experimental spectra.

To take the volume, area and origin effects into account in the measurement of the divergence from the BES spectra, the so called parametrization method was developed at IPP[12, 44]. It consists in using BBC-NI simple to simulate BES spectra for different input values of divergence, extraction voltage U_{ext} and acceleration voltage U_{acc}. The sets of values for these parameters are chosen in order to cover the typical operative scenarios of the considered test facility. For each produced spectrum the main Doppler

peak is fitted with a user defined function F to measure its spectral width w (which clearly depends on the definition of F); the Lorentzian function was found to best fit the shape of the main Doppler peak in the spectra collected at BATMAN. At this point an empirical function g is determined so that $\varepsilon = g(w, U_{ext}, U_{acc})$. After some preliminary studies g was defined as three nested linear functions: $\varepsilon = mw + t$, with coefficients m and t which linearly depend on U_{ext} according to coefficients linearly dependent on U_{acc}. The final form of g has constants which are fitted to the inputs (ε, U_{ext}, U_{acc}) and the outputs (w) of the simulations of BBC-NI simple. The values of these constants are different from LOS to LOS, because the distribution of the photons collected by the optic head depends on the position and the orientation of the optic head itself. At last, when an spectrum is acquired by a BES diagnostic the full energy peak is fitted with the function F: the measured value of w, together with U_{ext} and U_{acc} (known from the operational settings), is given in input to the function g to get the divergence. Further details and results of this analysis method can be found in ref. [12].

2.4.5   EAMCC

The EAMCC code [60, 61] simulates the trajectories of the beam particles inside the acceleration system, with the aim of optimizing the optics of the apertures of the grids and estimate the power deposition of the beam particles on the grids themselves. Analogously to BBC-NI advanced the program simulates the interaction of the negative ions with the gas molecules and the grids' surfaces, keeping track of the trajectories of the possible secondary particles produced; for this task, the gas density profile inside the acceleration system is calculated separately by the AVOCADO program[66]. The electric field is obtained by the SLACCAD program, whereas the magnetic field is calculated by PerMag[67]; the magnetic field however was not considered in the simulations performed for this benchmark. To reduce the computation time EAMCC simulates just one beamlet[13], applying periodic boundary conditions.

2.4.6   dBES-2

dBES-2 is a modified version of dBES, created to fully reproduce the volume, area and origin effects on the shape of the main Doppler peak. The program considers a single beamlet with Gaussian power density profile, placed at the center of the GG. In the same horizontal plane in which the beamlet lays an optic head is considered, with the positioning and orientation of the real optic heads. The frame of reference has cylindrical coordinates (l,ρ,φ), where l is the coordinate along the LOS axis and ρ and φ are the polar coordinates of a LOS section perpendicular to the axis. The LOS is considered as a truncated cone, where the minor base is the lens of the optic head. The beamlet instead is considered as a cone whose surface corresponds to $3\epsilon/\sqrt{2}$ (3 sigma); the minimum and maximum values of l for which the beamlet falls inside the LOS are calculated. In this way the volume of intersection between beamlet and LOS is defined as a truncated cone, which is further discretized along the 3 coordinates in 40^3 cell elements[14]. The intensity of H_α radiation produced inside each cell element is calculated and weighted with its solid angle. The corresponding contributions to the simulated spectrum are Gaussians centered on the wavelength given by the values of α of each cell element. The width of these gaussians was determined with formula 2.25, setting $\epsilon = 0$ and using the specific values of α and ω [15] of each cell element.

To better study the 3 distorsion effects the position of the beamlet with respect to the optic head can be varied, moreover all the beamlets composing the beam can be simulated at once.

---

[13]In the cases in which the magnetic field is kept int account EAMCC simulates two adjacent beamlets, with opposite fields at the EG.

[14]It was verified a posteriori that a finer discretization does not change the shape of the simulated spectrum (but increases the calculation time according to a N^3 law).

[15]ω is calculated using formula 2.23.

2.4.7 dBES-3

dBES-3 is another modified version of dBES, which mimics the Monte Carlo algorithms of BBC-NI-simple to study the angular distribution of the particles observed by the LOS and of the collected photons. Similarly to dBES-2 the code considers a beamlet emitted from the center of the GG, together an horizontal LOS at the same height of the beamlet. The position of the beamlet with respect to the optic head can be varied, optionally all the beamlets can be simulated. For each beamlet a number (10^5) of particles starts from a defined point of the GG and propagates according to eq. 2.53. The particles whose trajectories fall in the LOS volume are selected analytically; for these ones the points of intersection between the trajectory and the "surface" of the LOS volume are determined. In this way for each observed trajectory a segment is selected, within which 6 equidistant points are determined. Each one of these points contributes to the spectrum with a Gaussian function, whose central wavelength is calculated from the angle α between the lines which connect the point to the center of the beamlet at the GG and to the center of the lens. The width of the Gaussians is calculated with formula 2.25, neglecting the broadening caused by the divergence and using the values of α and ω of the considered points. The integrals of the Gaussians are proportional to the length of the segment to which the points belong.

2.5   Benchmark of dBES on BATMAN and MANITU

The first benchmark of the dBES code was performed comparing the results of its simulations with the spectra acquired by the BES diagnostic of BATMAN before the upgrade and by the the BES diagnostic of MANITU. To produce the BES spectra dBES has been fed with the measurements of the extracted and accelerated voltages, the accelerated current density, the tank pressure and the stripping fraction of a specific pulse. The input values of ϵ and σ_{GG} (radius equivalent to ϵ at the GG) were obtained for BATMAN and MANITU by means respectively of the codes BBC-NI-advanced[12] and EAMCC [60, 61]. The two codes calculated the trajectories of the beamlets' particles from the PG up to a distance of $3.5\,cm$ downstream the GG. At this position dBES divided the full energy particles from the stripping losses and calculated their relative fraction. Separate values of σ_{GG} and ϵ were calculated for the two types of particles. σ_{GG} was estimated as $\sqrt{2}$ times the distance from the beamlets axis within which the 68% of the beamlet' particles is present; ϵ is obtained by a Gaussian fit applied to the angular distribution of the beamlet particles with respect to the axis of the LOS.

  The spectra simulated by dBES were finally compared to those acquired by the BES diagnostic, not only qualitatively, but in terms of the divergence measured on the spectra themselves. To perform this comparison the measurement algorithm of dBES (par. 2.3.7) was used. In the case of BATMAN, the spectra generated by dBES were compared also to the ones calculated by BBC-NI-advanced.

2.5.1   Benchmark on BATMAN

The work of simulation and analysis was concentrated on 7 particular pulses in hydrogen, realized before the upgrade of the BES diagnostic: 84966, 84967, 84968, 84969, 84971, 84972 and 84973. For simplicity only the spectra of the LOS 1 were used; this LOS should be close to the center of the beam, because in the selected pulses the magnetic filter filed caused a shift of the beam downwards. The specific characteristics of these pulses required in input by dBES are listed in table 2.5, the normalized perveance is indicated, too. The selected pulses represent a scan in perveance of the source.

Pulse	U_{ext} **(kV)**	j_{acc} **(A/m²)**	P/P_0	U_{acc} **(kV)**
84966	8.66	260	0.073	~13.14
84967	7.75	254	0.084	**Tank pres. (Pa)**
84968	6.73	240	0.098	~9.1·10⁻²
84969	5.74	227	0.118	
84971	4.73	213	0.148	
84972	3.73	195	0.194	
84973	2.72	145	0.233	

Table 2.5: Main parameters of the considered BATMAN pulses [63]. j_{acc} is the accelerated current density.

Figure 2.18 shows the spectra generated by dBES coupled to BBC-NI advanced for the pulses 84966 and 84973, compared to the spectra acquired by the BES diagnostic; the background of the real spectra was previously detected and removed. The figure shows also the spectra directly generated by BBC-NI-advanced. Since there wasn't an estimation of the optical losses in the diagnostic for dBES, the intensities of all the spectra were normalized respect to the height of the Doppler shifted peaks.
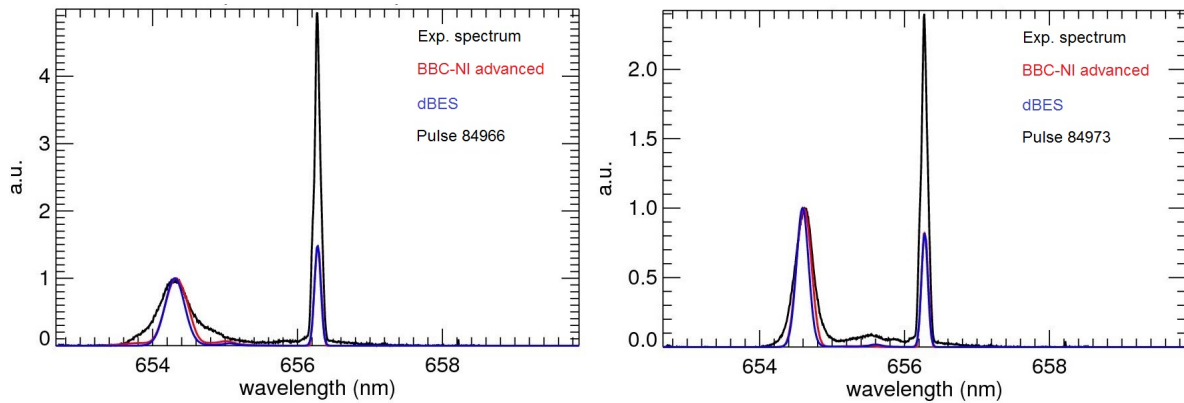
Figure 2.18: Comparison of the spectrum acquired by the BES diagnostic (black) with those simulated by BBC-NI-advanced (red) and dBES. The two cases are referred to pulses 84966 and 84973, LOS 1.

The main differences between the spectra obtained by the two simulation codes and the experimental data are substantially 4: firstly, the intensity of the H_α unshifted peak is underestimated by both codes by a factor 2; the extra H_α radiation is due to a reflection of light coming from the ion source. Secondly, the intensity of the part of the experimental spectrum related to stripping losses is higher with respect to the simulations; this can be due to an incorrect estimation of the H_2 density profile in the acceleration stage. The discrepancy can be better observed in figure 2.19, which gives an enlarged view on the base of the spectra of figure 2.19. It can be noticed also that the curves of the three spectra corresponding to the stripping losses have completely different shapes. Last but not least, the H_α shifted peak of the real spectrum exhibits two large tails at the base, perhaps due to the origin effect and/or to the halo (not reproduced by the codes).
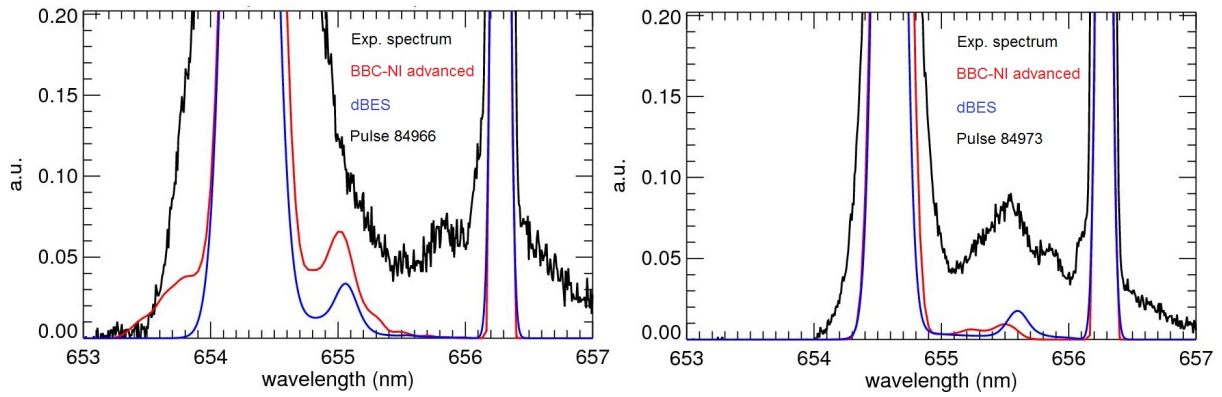
Figure 2.19: Zoom at the base of the spectra acquired by the BES diagnostic (black) and of those simulated by BBC-NI-advanced (red) and dBES. The two cases are referred to pulses 84966 and 84973, LOS 1.

The last highlighted problem is of particular importance for its effects on the measurement of the beamlets' divergence: this quantity is indeed determined by the shape of the peak, through a Gaussian line fitting procedure. However, as shown in figure 2.20a, a simple Gaussian curve cannot reproduce the shape of the curve[16]. The solution adopted by the IPP standard evaluation was to ignore the part of the peak below 30% of the height of the peak itself. An alternative solution was tried, consisting in fitting the Doppler peak with the sum of two Gaussians having different widths and integrals but the same centroid (figure 2.20b)[17]. In this case the divergence is calculated from the width of the narrower Gaussian, which is "above" the wider one. Both the methods with 1 or 2 Gaussians were tested, applying the fit to the whole peak except a part on the low energy side[18]in order to avoid the overlapping with the contribution of the stripping losses. The fit with two Gaussians better reproduces the experimental data, but it is not clear what the source of the wider contribution is. It could hardly be the halo of the beamlets, because it must be considered that the integral of the wider Gaussian is more than the half of the integral of the whole peak!
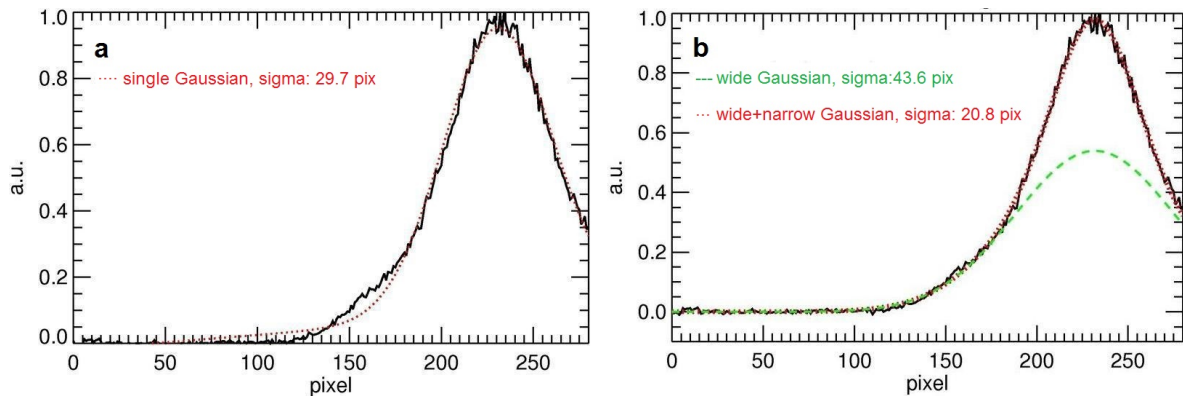
Figure 2.20: Two different methods to fit the Doppler shifted peak. In a) the BES spectrum (black curve) is fitted with a Gaussian (red dotted curve), in b) instead the fitting function is the sum of two Gaussians with the same centroid (plus a constant). In case b) the green dashed line represents the wider Gaussian, whereas the red dotted line is the sum of the Gaussians. In both the plots the analyzed spectrum was acquired by LOS 1 during the pulse 84966.

The values of divergence obtained with these two methods (single and double Gaussian fit) are compared in figure 2.21; the single Gaussian fit was applied to the experimental spectra (blue solid

---

[16]The fit routines are applied always after the removal of the background of the spectrum.
[17]This solution was adopted also in [68]
[18]The fitted part of the peak is exactly the one shown in figure2.20.

line) and the spectra obtained by dBES (red curve) and BBC-NI-advanced (green curve), whereas the double Gaussian fit was applied to the spectra acquired by the BES diagnostic (blue dashed line). In all the cases the divergence is calculated from the considered spectral width using the analysis algorithm of dBES, described in par. 2.3.7. It was verified that the trends of the data series shown in the figure don't vary by slightly changing the fitted range of the Doppler shifted peak. The first interesting fact is that the divergences obtained by the simulated spectra are quite different, though dBES takes the input values of divergence from the data of BBC-NI-advanced. Secondly, the values of divergence retrieved by the spectra of BBC-NI-advanced are in good agreement (except one point) with the values of the experimental spectra analyzed with the method of the two Gaussians. In third place, the values obtained by the experimental spectra with a single Gaussian fit are higher than all the others (except one point) but seem to have the same trend of the values of dBES, as if there were an additive constant between the two data series.
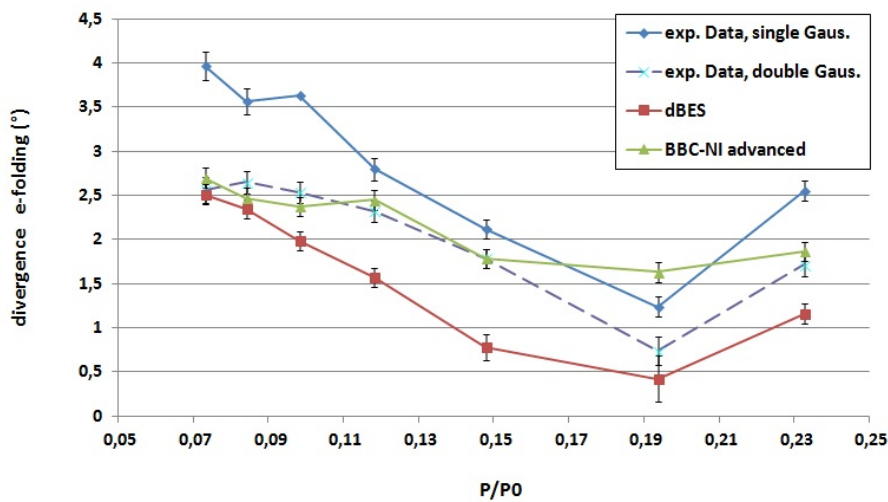
Figure 2.21:   Values of divergence measured on the spectra acquired in BATMAN (blue) and on the spectra simulated by dBES (red) and BBC-NI-advanced (green). The values are showed as function of the normalized perveance of their respective spectra. The solid line represent data obtained with a single gaussian fit on the spectrum, instead the dashed line represents values of divergence calculated from a double Gaussian fit, using the width of the narrower Gaussian.

2.5.2   Benchmark on MANITU

The benchmark of dBES against the data of the MANITU test facility followed the same procedure applied for BATMAN. For simplicity a single horizontal LOS (the sixth from the bottom, i.e. the LOS observing the center of the beam) was chosen for all the simulations.

The pulses which were object of the study are those from 87850 to 87860, all operated in deuterium; the characteristics of the pulses which are needed in input by dBES are listed in table 2.6. The normalized perveance of of the pulses is indicated, too; the sequence of pulses represents a scan in perveance, below the best value of P/P_0 to get the mimum beamlets' divergence.

Pulse	U_{ext} (kV)	j_{acc} (A/m^2)	P/P_0	U_{acc} (kV)
87850	2.54	44	0.119	~15.43
87851	3.45	68	0.113	**Tank pres. (Pa)**
87852	4.47	94	0.105	~6.5·10⁻⁴
87853	5.48	109	0.089	
87854	5.99	115	0.082	
87855	6.49	119	0.075	
87856	6.99	122	0.069	
87857	7.49	125	0.064	
87858	7.91	128	0.060	
87859	8.51	131	0.056	
87860	9.03	134	0.052	

Table 2.6: Main parameters of the considered MANITU pulses [63].

The spectra simulated by dBES were compared to those actually collected by the diagnostic. One example is shown in figure 2.22.; similarly to BATMAN, the background of the experimental spectra was previously removed.
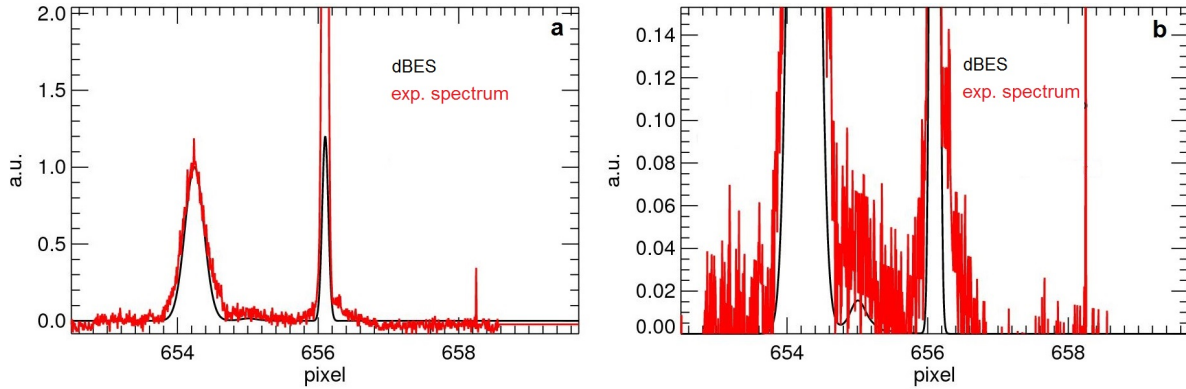
Figure 2.22: Comparison between the spectrum acquired by the BES diagnosticin MANITU (red) and the one produced by dBES (black) (a). The considered case refers to the pulse 87860 and the LOS 6. The view of the same curves was enlarged on the plot b) to better observe the parts related to the stripping losses.

As in BATMAN, the experimental unshifted H_α peak is underestimated by the code. This is quite surprising, because in MANITU the inner surface opposite to the optic head was blackened exactly to suppress possible light reflections into the LOS; it is clear that the difference must come from another source with respect to the reactions exploited by BES. Other interesting facts are that the contribution of the stripping losses is stronger in the experimental spectrum than in the simulation, and that the background shows a sort of pedestal in an interval including the two main peaks.

The values of divergence measurable on the dBES spectra were compared to those obtained from the experimental data. The Doppler peak on the dBES spectra was fitted with a single Gaussian; the resulting values of divergence are shown in figure 2.23 (red line) as function of the normalized perveance. For the spectra acquired by the BES diagnostic the Doppler peak was fitted with a single Gaussian and with the sum of two Gaussians; the fit has been applied only to the low energy side of the peak, roughly at 30% of its height. The values of ϵ calculated with the two methods are shown in figure 2.23 respectively with the green and blue lines. It is evident that for MANITU the complication of fitting the peak with the sum of two Gaussians is not necessary. It emerges also that EAMCC and dBES, apart from a malfunction of dBES at pulse 87859, reproduce correctly the trend of the divergence of the experimental values, apart from an additive constant.
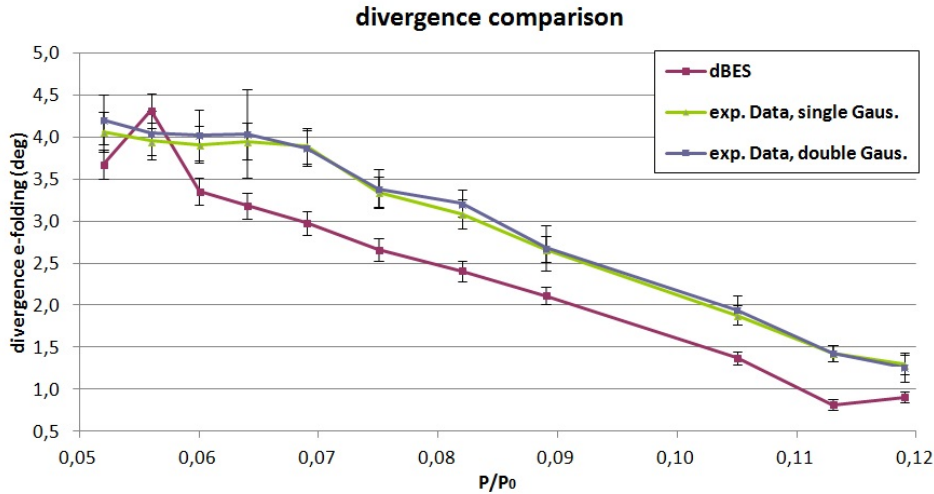
Figure 2.23: Comparison of the values of divergence obtained by the analysis of the real spectra (green and blue lines) and of the spectra created by dBES (red line). The values have been obtained fitting the Doppler peak with a single Gaussian, except for the data of the blue line: in that case the two Gaussian fit was used, ϵ was then calculated from the width of the narrower Gaussian.

2.5.3   Discussion of the results

The dBES code was succesfully coupled to the codes BBC-NI advanced and EAMCC, the spectra produced by the simulations were compared to those acquired by the BES diagnostics in BATMAN and MANITU. In the case of BATMAN, the spectra of dBES were compared also to those calculated by the BBC-NI advanced code. The consideration which can be drawn by the comparison of the spectra are the following:

- For BATMAN the spectrum produced by BBC-NI-advanced is sometimes completely different from the one created by dBES, even if the data of the test particles exiting the GG are the same. This difference is noticeable also in the values of divergence measured on the spectra simulated by the 2 codes (figure 2.21). The most plausible explanation is that dBES calculates σ_{GG} and ϵ as global parameters from the spatial and angular distribution of the particles simulated by BBC-NI advanced, neglecting position and direction of each single particle. This loss of information could be at the base of the discrepancies between the outputs of dBES and BBC-NI advanced.

- In the spectra acquired in the BES diagnostic in BATMAN the full energy peak has large tails at the base. A fitting model based on two Gaussians was tested and gave results in agreement with those of BBC-NI-advanced (figure 2.21), but not with those of the single Gaussian fit method nor with those of dBES. Moreover it is unrealistic to think that the cause of the wider Gaussian is the halo. The better agreement with the data could be simply given by the increased number of parameters in the fit. Comparing the spectra of BATMAN and MANITU, it can be noticed that for similar values of divergence the effect of the tails at the base of the Doppler peak is much more pronounced in BATMAN than in MANITU: a proof of this is that in the analysis of the spectra of MANITU there is no need to fit the main Doppler peak with a double Gaussian. Another example is given by the spectra of pulses 84966 in BATMAN (figure 2.18 on the left) and 87860 in MANITU (figure 2.22), for which the measured divergence is about 4°. The LOSs chosen for the benchmark in BATMAN and MANITU are observing respectively the center of the lower half of the beam and the center of the beam. It is therefore unlikely that the only origin effect is sufficient to explain the broadening of the base of the peak.

- The values of divergence obtained with a single Gaussian fit by the experimental spectra of BAT-MAN and MANITU follow the same trend of those given by dBES. The systematic difference between the two values series can have two sources: a wrong estimation of the broadening factors for the spectrum in dBES or a bad modelization of the space charge compensation in BBC-NI-advanced/EAMCC. Numerical studies with KOBRA3-INP [69] and dedicated experimental tests [44] verified that the space charge compensation and its modelization in the codes have a central role in the prediction of the beamlets' divergence. To check the validity of the analysis algorithm of dBES the values of divergence measured by BES could be compared with those obtained by the calorimeter; necessary conditions for this comparison are that the calorimeter must be able to measure ϵ with enough spatial resolution, and that the gas pressure in the vacuum vessel of the test facilities must be high enough to ensure a full space charge compensation of the beamlets between the BES LOSs and the calorimeter.

2.6 Study of the volume, area and origin effects

The second benchmark carried out at IPP for dBES had the aim of determining the predictive limits of the algorithms adopted in code. Since dBES doesn't take into account the volume, area and origin effects in the calculation of the angular distribution of the photons collected by the optic heads, it is necessary to quantify the impact of these effects on the measurements of divergence. In addition, it must be established whether the broadening of a beamlet can be better described with a Gaussian power density distribution (dBES) or with a Gaussian angular distribution of the beamlet particles (BBC-NI simple).

To clarify these issues the spectra acquired by the upgraded BES diagnostic in BATMAN and by the BES diagnostic in ELISE were compared with those generated by dBES and BBC-NI-simple. dBES-2 was used to numerically investigate the influence of position, direction and divergence of the single beamlets on the shape of the BES spectrum; dBES-3 was used instead to better study the physical models implemented in BBC-NI simple.

These numerical studies were accompanied by the analysis of the spectra acquired by the BES diagnostics in the BATMAN and ELISE test facilities, to better characterize the consequences of the volume, area and origin effect on the measurements of divergence.

2.6.1 Input data

The characteristics of the pulses of BATMAN and ELISE considered in the benchmark are shown in tables 2.7 and 2.8; all the selected pulses are in hydrogen. The spectra of the LOS 2 in BATMAN and of the LOSs 3 and 11 in ELISE were selected for the benchmark; their positioning is shown in figure 2.14 and 2.16: the LOS 2 of BATMAN and the LOS 3 of ELISE observe the lower section of the beams, while the LOS 11 monitors the upper section of the beam. Other LOSs have been considered during the benchmark, too. The divergence measured on the spectra by means of the IPP standard evaluation method was used as input for dBES, dBES-2, dBES-3 and BBC-NI simple. In the case of ELISE, it can be noticed from table 2.8 that the divergence measured on the upper section of the beam is slightly higher that what measured in the lower section. The dBES code also reproduced the contribution of the stripping losses to the spectrum, using the values of stripping fraction measured with the IPP algorithm (par. 2.4.1) and assuming that all the stripping losses are accelerated at the extraction energy.

Pulse	U_{ext} (*kV*)	U_{acc} (*kV*)	j_{acc} (A/m^2)	ϵ (*mrad*) **LOS 2** **IPP standard ev.**	Tank pres. (10^{-2} *Pa*)
97721	4.7	15.1	158	52	3.74
97386	4.6	13.2	155	61	2.51
97368	4.6	11.2	162	65	2.71
97843	8.4	13.3	190	93	2.02
97835	8.5	13.2	183	103	2.03
98075	8.6	13.1	170	124	2.20

Table 2.7: Main parameters of the considered BATMAN pulses [63]. The values of divergence have been calculated with the upgraded BES diagnostic, applying the IPP standard evaluation method to the spectra of the LOS 2.

Pulse	U_{ext} (*kV*)	U_{acc} (*kV*)	j_{acc} (A/m^2)	ϵ (*mrad*) **LOS 3** **IPP standard ev.**	ϵ (*mrad*) **LOS 11** **IPP standard ev.**	Tank pres. (10^{-2} *Pa*)
6314	4.54	25.1	127	32	34	2.60
6673	6.42	30.1	211	35	39	3.01
6674	7.38	30.1	221	43	47	2.92
6675	8.33	30.1	229	50	54	2.84
6677	9.36	30.1	240	59	63	2.67
6678	9.80	30.1	243	62	66	2.72
6682	9.81	30.1	249	71	73	1.21

Table 2.8: Main parameters of the considered BATMAN pulses [63]. The values of divergence have been calculated with the upgraded BES diagnostic, applying the IPP standard evaluation method to the spectra of LOS 2 and LOS 11.

2.6.2   dBES and BBC-NI-simple

The spectra simulated by dBES were compared to those simulated by BBC-NI simple and those acquired experimentally by the diagnostic. As example, figure 2.24 shows the experimental spectrum and the 2 simulations, in BATMAN (a) and in ELISE (b). As already found in sec. 2.5 the codes are not able to reproduce the shape and the intensity of the unshifted H_α component, and the fraction of stripping losses is lower than expected. Moreover, the profile of the full energy component is slightly asymmetrical and has broader tails than in a Gaussian curve. BBC-NI-simple seems however to better reproduce the shape of the main Doppler peak, especially for BATMAN. The difference between the 2 codes lies in the fact that BBC-NI simple takes into account the volume, area and origin effect, and uses a different model for the angular distribution of the beamlet particles. For this reason the two issues (deformation effects of the Doppler peak and model of the beamlets) were then decoupled and further investigated by means of the dBES-2 and dBES-3 codes.
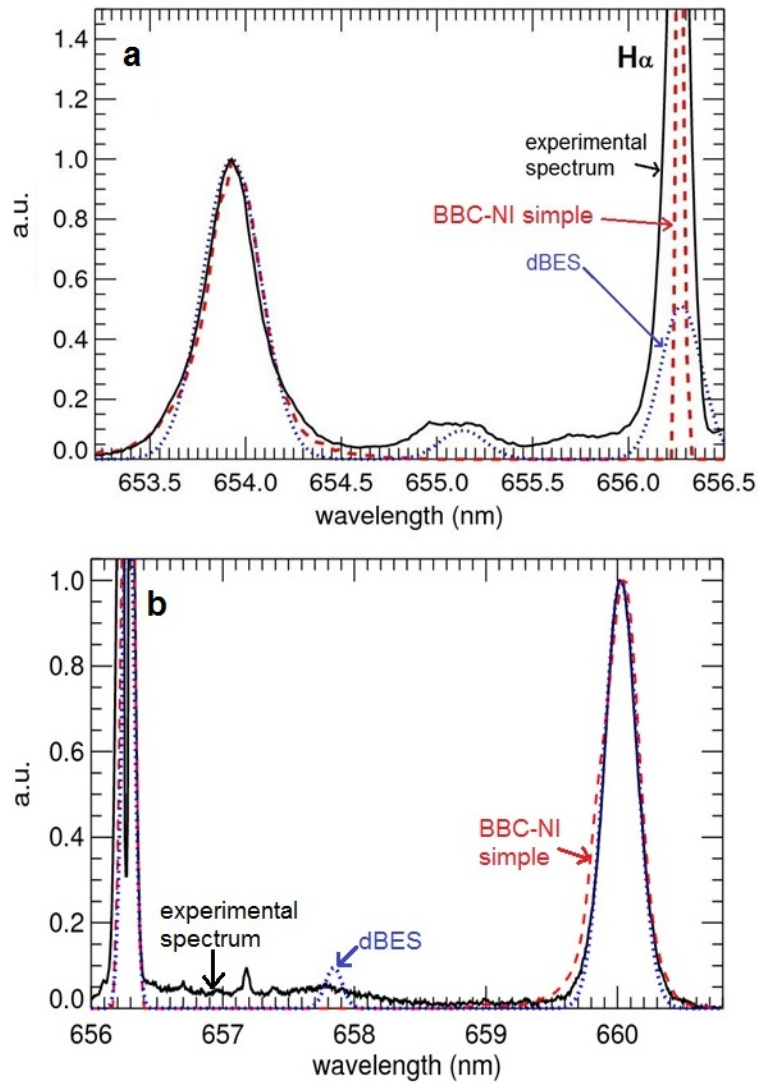
Figure 2.24: Comparison between the spectra simulated by the dBES code and the BBC-NI-simple code, plus the spectrum acquired by the real BES diagnostic. The example a) is referred to the LOS n°3 and the pulse 97721 of BATMAN, while the case b) is referred to the LOS 6 and the pulse 6673 of ELISE. The irregularity of the unshifted H_α peak in case b) is due to the high intensity of the peak itself.

2.6.3 Simulations of the volume, area and origin effects

dBES-2 is a version of dBES capable of simulating the volume, area and origin effects on the shape of the full energy peak, still using a Gaussian power density profile for the beamlets. With this code it was possible to study how the 3 effects are affected by the position and the divergence of the beamlets. dBES-2 was initially set to simulate just one beamlet at the center of the GG and a horizontal LOS looking exactly at the same height. The ELISE facility and more precisely the pulse 6675 was chosen as reference case. The divergence of the beamlet was varied from 4 *mrad* to 100 *mrad* to check the distortion of the Doppler peak at different values of ϵ. The result of the simulation at $\epsilon = 100\,mrad$ is shown in Figure 2.25a. As expected the distortion of the shape of the full energy component increases with the divergence, its peak position is shifted at higher wavelengths (affecting the measurement of α) and its right side has a higher slope with respect to the left one. To quantify the distortion of the peak the divergence was measured on the simulated spectrum by fitting only one side of the peak; the high energy side was chosen, cutting the part of the signal below the 20% of the height of the Doppler peak. Applying this method, it results that the measures of ϵ are underestimated with respect to the values

given in input to the simulation (85 *mrad* instead of 100 *mrad* in the case of figure 2.25a); as better shown in figure 2.25b, this systematic error grows with ϵ. The most interesting fact however is that the measures of ϵ saturate at low values of divergence. The most plausible explanation is that the photons emitted by a particle along its trajectory inside the LOS arrive at the center of the lens with different angles; it's an effect specular to the one for which the photons emitted at a certain point can enter the lens within a finite solid angle. If real, this systematic error cannot be corrected analytically because the contributions in photons from the points of the trajectories must be weighted with the solid angle of observation. The easiest solution is to use the inverse function of the trend of points in figure 2.25b to correct the values of ϵ measured by the diagnostic.
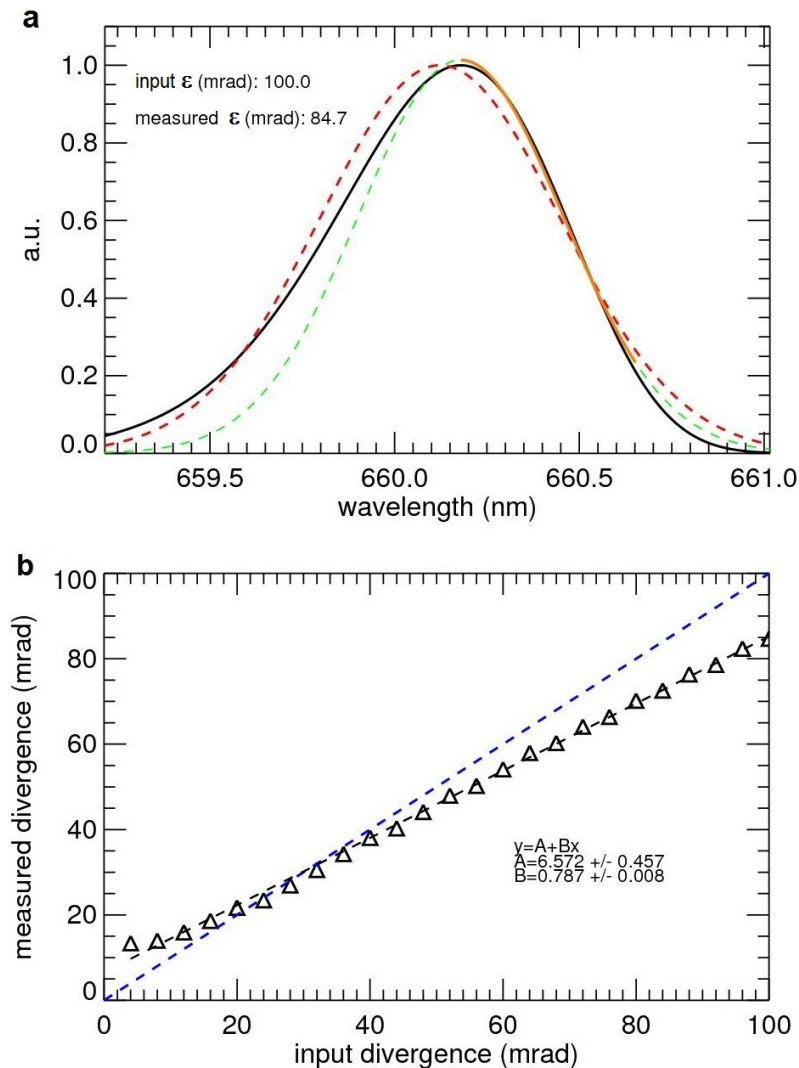
Figure 2.25: a) Simulation of the main Doppler peak (black curve) in the case of the ELISE pulse 6675, assuming $\epsilon = 100$ mrad. The red dashed curve represents the shape of the undistorted peak. The orange curve represents the Gaussian fit on the right side of the black curve above the 20% of the peak height. The whole Gaussian built on the result of the fit is represented with the green dashed line. b) Comparison between the values of divergence fitted on the simulated spectra and the values used in input for the simulation. The black dashed line is the linear fit of the points, while the blue dashed line represents the ideal correspondence between the input values of and the measured values of divergence.

Since the volume and area effects distort the two sides of the peak in opposite ways, it should be possible to reduce the deviations of ϵ by applying the fit to an interval of the spectrum symmetric with respect to the center of the peak. For example, with this method the fit on the case at 100 *mrad* of figure

2.25a would yield $\epsilon = 98\,mrad$ instead of $85\,mrad$. As shown in figure 2.26, with a symmetric fit the measured divergence is generally closer to the input value.
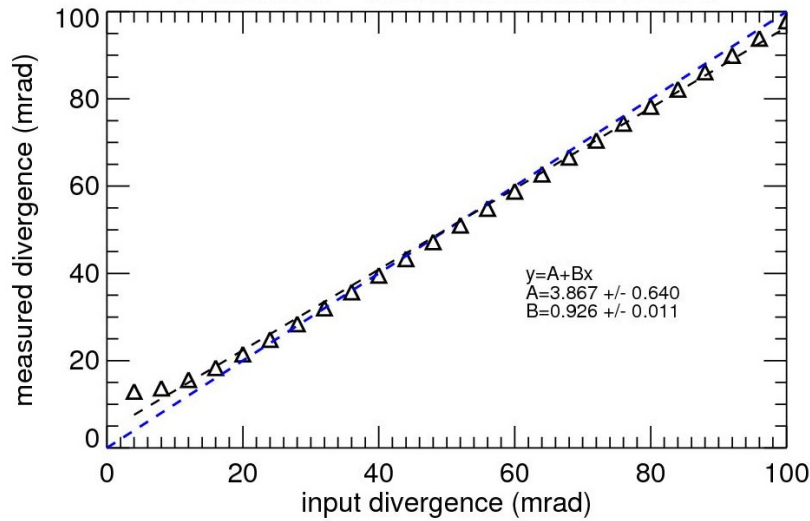
Figure 2.26: Comparison between the values of divergence fitted on the simulated spectra (fit of both the sides of the spectra, above the 20% of the peak height) and the values used in input for the simulation. The black dashed line is the linear fit of the points, while the blue dashed line represents the ideal correspondence between the input values of and the measured values of divergence.

After these calculations it was studied how the distance between the beamlet axis and the LOS axis influences the shape of the Doppler peak. The divergence of the (single) beamlet was kept at $50\,mrad$ and the beamlet was shifted away vertically from the LOS. What results is that this offset doesn't significantly affect the measures of ϵ; it was observed however that the offset between beamlet and LOS produces a shift of the position of the full energy peak (figure 2.27).
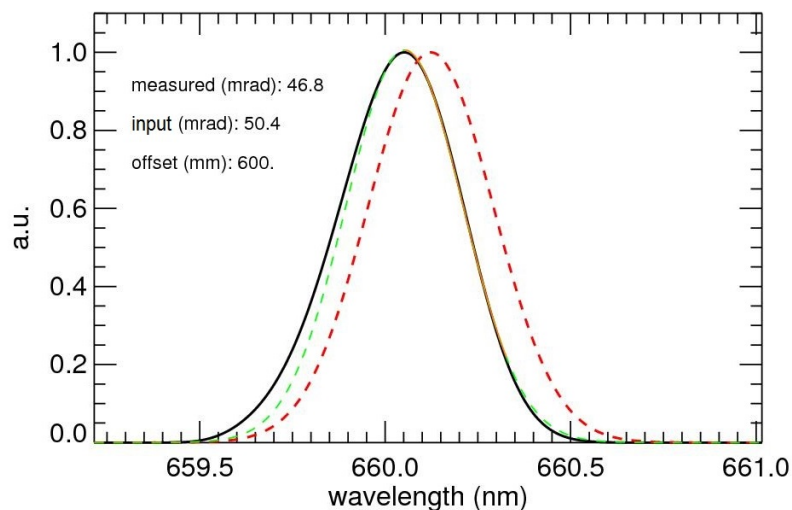
Figure 2.27: Simulation performed with a single beamlet, shifted 0.6 m above the axis of the LOS. The red dashed curve is the undistorted peak, the orange curve is the Gaussian fit of the simulation on the right side and above the 30% of the height of the peak, while the green dashed curve is a Gaussian built on the results of the fit. The systematic error on the measure of ϵ is substantially due to the distortion generated by the divergence itself, i.e. the effect described in figure 2.25.

This effect however is of little importance in the real spectra, because it becomes relevant at so high

values of offset that the amount of light received by the LOS is totally negligible. This confirms what discussed in par. 2.4.4.2, i.e. that the origin effect is negligible if the beamlets have a Gaussian power density distribution.

A similar test was performed by keeping the beamlet at the middle height of the GG, but varying the distance from the optic head according to the real positions of the apertures in the GG. The resulting values of ϵ show very small deviations, of maximum 1 *mrad* over 50 *mrad*.

Coherently with the two last tests, the spectrum calculated with one beamlet is not substantially different from the one obtained considering all the beamlets produced by the grids. This result is in contrast with the distortion of the Doppler peak noticed in the spectra generated by BBC-NI simple. The different modelization of the beamlets could then explain the differences between the results of dBES and BBC-NI.

In figure 2.28 the output of dBES-2 for the pulse 6675 is compared to the spectrum acquired by the LOS n°3 (see figure 2.16b). The value of ϵ given in input to the program was obtained from the IPP standard evaluation method applied to the experimental spectrum. More correctly, by means of the results of figure 2.26 it was determined the value of ϵ to be given in input to dBES-2 to get the same divergence measured on the experimental spectrum. The full energy component of the spectrum simulated by dBES-2 results to be too distorted on the high energy side with respect to the real one. A possible explanation of this difference could be that the power density profile of the beamlets is not Gaussian, or it's Gaussian but a non negligible component of halo is present.
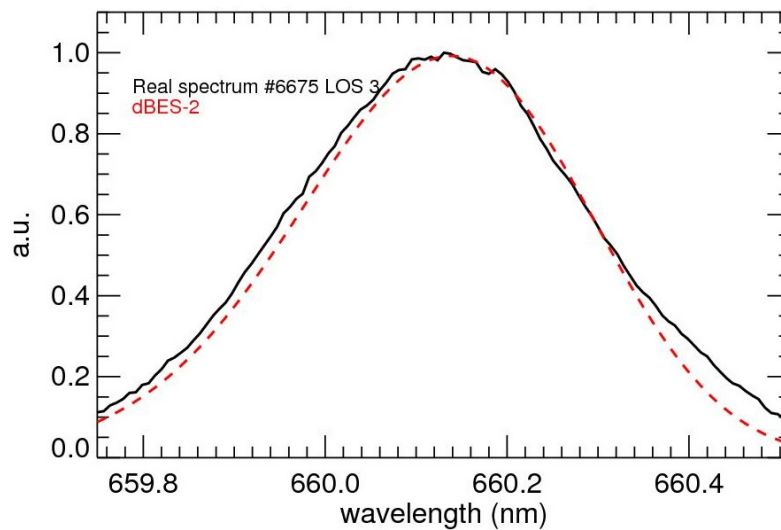
Figure 2.28: Comparison between the experimental spectrum (black curve) of the LOS 3 at the pulse 6675 of ELISE and the distorted curve simulated by the program (red dashed curve).

2.6.4 The angular distribution of the beamlets

Differently from dBES-2, dBES-3 is a Monte Carlo code in which the particles of the beamlets follow the same distribution used by BBC-NI simple. dBES-3 was then benchmarked against BBC-NI simple to verify that the 2 codes give equivalent results. dBES-3 could then be used in combination to the other codes to establish which model for the trajectories of the beamlets' particles better reproduces the experimental data; this is of particular importance for the design of the BES diagnostics in SPIDER and MITICA.

dBES-3 was applied to reproduce the case of the pulse 6673, LOS 6 ($\epsilon = 36$ *mrad*). Figure 2.29 shows the angular distribution of the particles simulated by dBES-3 and effectively observed by the LOS; the

angle of observation of the LOS ($\alpha = 130°$) corresponds to 0° in the plot. The red histogram is the angular distribution given by a single beamlet, aligned at the center of the GG and with an horizontal LOS placed at the same height; the blue curve instead represents the angular distribution of the particles observed by the LOS 6, simulating the presence of all the beamlets in ELISE. The same two cases were simulated by BBC-NI simple: the corresponding resulting angular distributions are the yellow one (single beamlet) and the black one (all the beamlets). All the curves are normalized to their peak height.
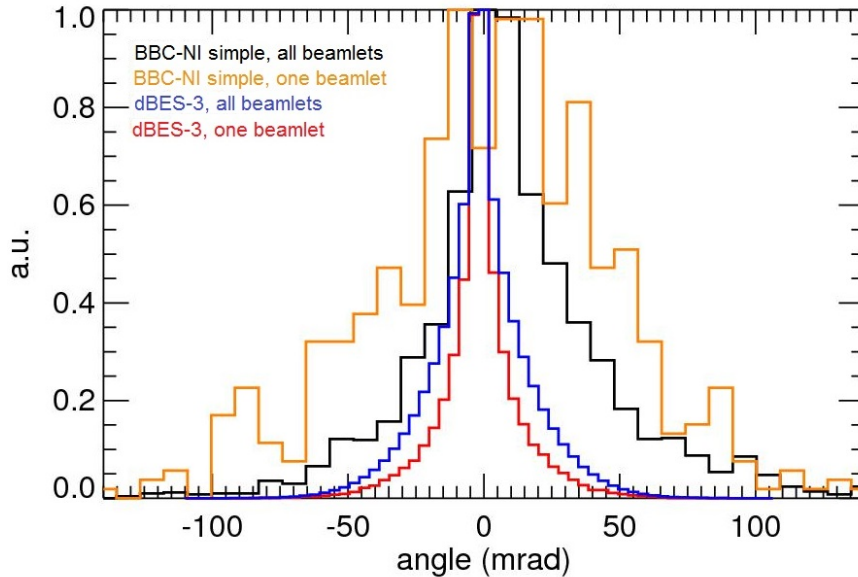
Figure 2.29: Distributions of the angles with respect to the LOS axis of the particles observed by the LOS 6 at pulse 6673 in ELISE, according to the results of BBC-NI simple and dBES-3. The angle 0° corresponds to $\alpha = 130°$. All the distributions are normalized to their peak value. The black and orange curves were obtained by BBC-NI respectively considering all the beamlets or just one at the same height of the LOS. The corresponding results obtained by the code n°2 are shown with the blue and red curves.

As expected, in the results of dBES-3 the angular distribution of the particles coming from a single beamlet has large tails respect to a Gaussian (red curve), but in absolute terms the width of this distribution is much smaller than the reference Gaussian (black dashed curve). Summing the contributions of all the beamlets broadens the distribution (blue curve), but just slightly. On the other side, the angular distribution for one beamlet in BBC-NI simple is very wide, however this seems to be caused by the low number of particles effectively observed by the LOS. Anyway, the distribution calculated by BBC-NI simple considering all the beamlets (black curve) is wider than the one (blue curve) calculated by dBES-3 for the same case. The results of dBES-3 are therefore not in agreement with those of BBC-NI-simple; further investigations are in course to determine the cause of this discrepancy.

2.6.5 Characterization of the data collected by BES

The study on the simulation codes for the BES diagnostics was closely related to the analysis of the spectra acquired experimentally in the BATMAN and ELISE test facilities. The IPP standard evaluation method fits all the Doppler peak from the 30% of the height of the peak itself. To quantify the degree of asymmetrization of the Doppler peak, the values of divergence obtained by the IPP standard method were compared to those obtained by the dBES analysis codes, fitting only the high energy side of the Doppler peak in the same spectra (i.e. avoiding the contribution of the stripping losses). The spectra acquired by the BES diagnostic were interpolated on an array of 1024 equally spaced wavelengths, since

in BATMAN the plate factor varied so much along the spectrum that it was necessary to renormalize the content of the CCD bins according to their spectral width. After having subtracted the background signal, the experimental spectra were smoothed by means of a Savitzky-Golay filter of degree 3 and a total width of 21 points in order to reduce the irregularities caused by noise; it was verified that such a filter doesn't broaden the shape of the peak. The centroid was then measured taking the maximum of the Doppler peak. The gaussian fit was applied to the high energy side of the curve, from the top of the peak down to the 20% of the height of the peak itself; in the fit the centroid was kept fixed at the previoulsy calculated value.

Figure 2.30 shows the values of divergence obtained with this method for the LOS 2 in BATMAN, comparing these results with those obtained by the IPP standard evaluation.
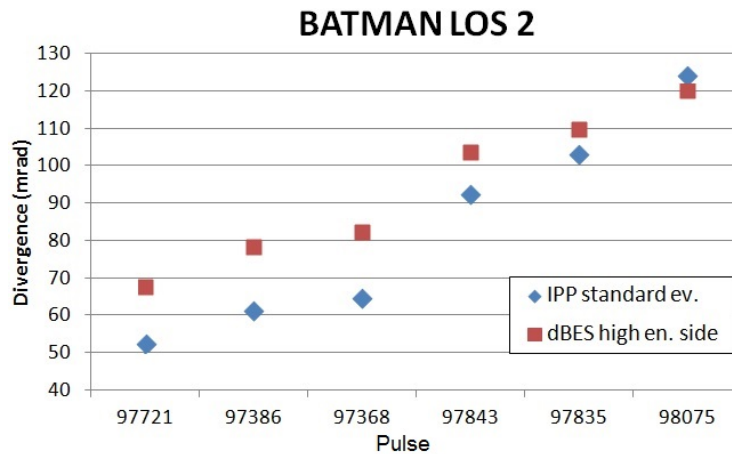
Figure 2.30: Values of divergence (e-folding) obtained with the IPP standard evaluation method and with dBES, fitting only the high energy side of the Doppler peak from the 20% of its heigth. The analyzed spectra were acquired by the LOS 2 in BATMAN, during the pulses listed in table2.7.

As it can be observed, the values of divergence obtained by the dBES analysis codes are higher that the ones given by the IPP standard evaluation method, however at high values of divergence the agreement between the values calculated by the 2 methods is much better. This phenomenon can be understood by observing the analyzed spectra, shown in figure 2.31. The experimental data are the black curves, the orange ones represent the Gaussian fit on the selected segment of the Doppler peak; the red curves show the Gaussian function calculated according to the results of the fits. At low values of divergence the Doppler peak is highly asymmetrical, with a width on the high energy side lower which is lower than the one of the other side. This behavior is in contrast to what found in the simulations of dBES-2 (par. 2.6.3). Moreover, at high values of divergence the asymmetry of the Doppler peak disappears and also the tails at the base of the peak are less pronounced. In general, the shape of the Doppler peak at high divergence is much closer to Gaussian curve. This is again in contrast with the behavior expected for the volume, area and origin effects. A possible explanation is that the directions in the horizontal plane of the observed beamlets is randomly deviated because of the repulsion of the beamlets themselves; another source of misalignment for the beamlets could be the alternated magnetic fields of the magnets embedded in the EG. The effect of the variations of the beamlets' directions on the shape of the peak would be visible at low divergence, whereas it at high values of ϵ the broadening of the peak would hide it.

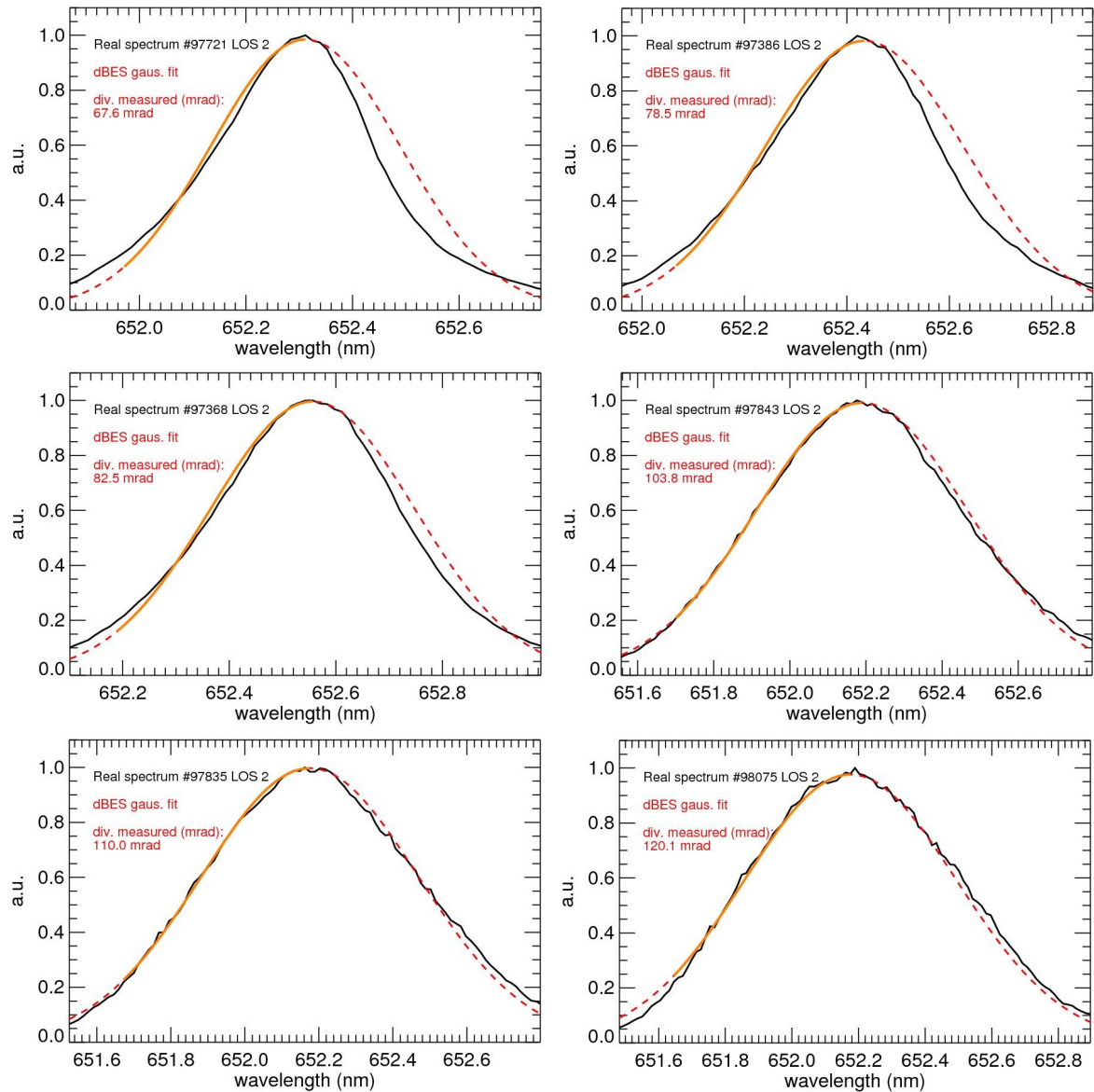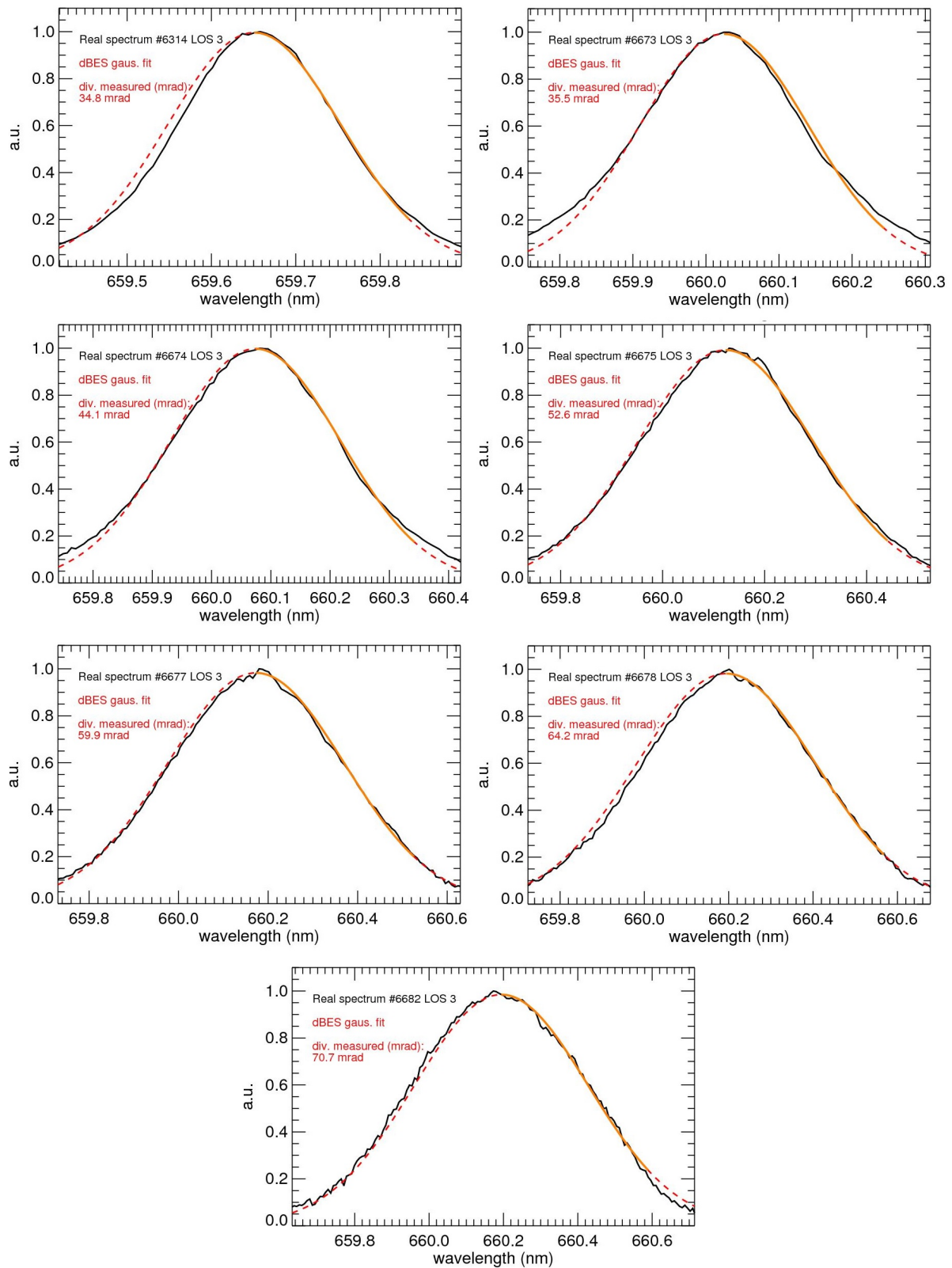*Figure 2.31: Spectra (black curve) acquired by the horizontal LOS n°2 during the pulses considered in BATMAN. The orange curves are the Gaussian fit applied on the selected interval of the experimental data. The red curves are Gaussians calculated according to the results of the fits. The measured values of divergence are indicated in the legends of the respective plots. The spectra are ordered for increasing divergence.*

The same analysis was repeated for the spectra acquired by the LOS 3 and the LOS 11 in ELISE. The obtained values of divergence are reported in table 2.9 together with those calculated with the IPP standard evaluation method. The table reports also the values of divergence measured by the IR thermography at the heights correspondent to LOS 3 and LOS 11 [48]. According to the results of the IPP standard evaluation, the divergence measured on the upper part of the beam (LOS 11) is higher with respect to that on the lower part. This relation instead is reversed on the results of the dBES analysis for the first four listed cases. This could be due to the asymmetry of the Doppler peak.

The values of divergence reported in table 2.9 are plotted in figure 2.32 according to the LOS and the pulse number. In the case of LOS 3 the measures of ϵ obtained with the 3 fitting methods are in agreement within a tolerance of 10%. The reason is shown in figure 2.33, where the Doppler peaks of all the considered spectra of LOS 3 are shown: the experimental data fit well to a Gaussian curve, in particular at high values of divergence.

Pulse	ϵ (*mrad*) LOS 3			ϵ (*mrad*) LOS 11		
	IPP stand. ev.	Calorimeter IR thermog.	dBES high energy side	IPP stand. ev.	Calorimeter IR thermog.	dBES high energy side
6314	32	34	35	34	39	30
6673	35	39	36	39	43	34
6674	43	47	44	47	52	42
6675	50	54	53	54	61	48
6677	59	61	60	63	71	61
6678	62	64	64	66	76	66
6682	71	-	70	73	-	74

Table 2.9: Values of divergence measured at LOS 3 and 11 in the pulses of ELISE listed in table 2.7. The divergence was measured with the IPP standard evaluation method and with dBES, fitting only the high energy side of the Doppler peak down to the 20% of its heigth. It is reported also the divergence measured by the IR thermography at the heights of the diagnostic calorimeter corresponding to LOS 3 and 11.
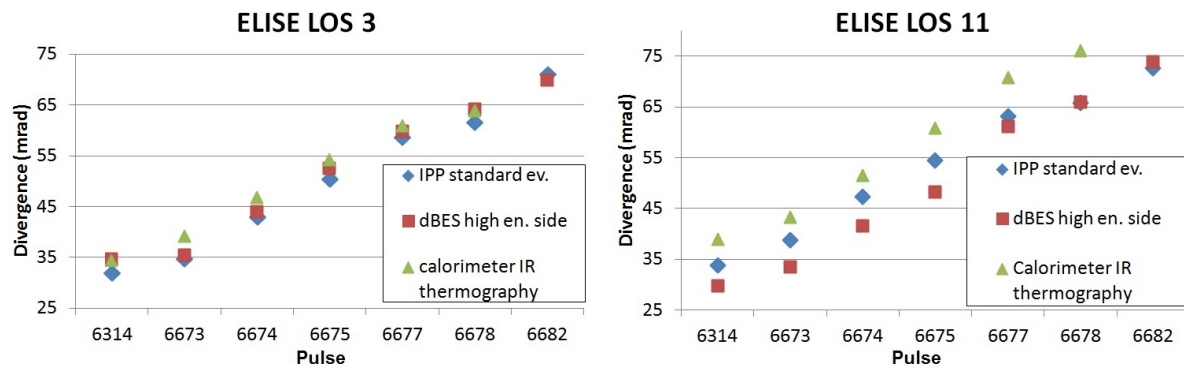
Figure 2.32: Values of divergence measured by IPP standard evaluation and dBES on the spectra of LOS 3 (left) and LOS 11 (right) in ELISE. The divergence measured by the IR thermography on the calorimeter for the lower and upper parts of the beam is shown, too.

As regards the divergence measured from LOS 11, the values obtained by the IR thermography are systematically higher than those obtained by BES. The values obtained by dBES follow the trend of data of thermography, apart from and additive constant. Figure 2.34 shows the spectra of LOS 11 and the fit operated by dBES. Contrarily from what observed in the spectra of BATMAN, the spectra corresponding to the highest values of divergence are the most asymmetric. It's interesting to notice that the asymmetry doesn't seem to grow smoothly with the divergence: the asymmetries are substantially present only in the 3 spectra corresponding to the highest values of divergence. Further investigations are needed to understand this behavior.

Figure 2.33: Spectra (black curve) acquired by the horizontal LOS n°3 during the pulses considered in ELISE. The orange curves are the Gaussian fit applied on the selected interval of the experimental data. The red curves are Gaussians calculated according to the results of the fits. The measured values of divergence are indicated in the legends of the respective plots. The spectra are ordered for increasing divergence.
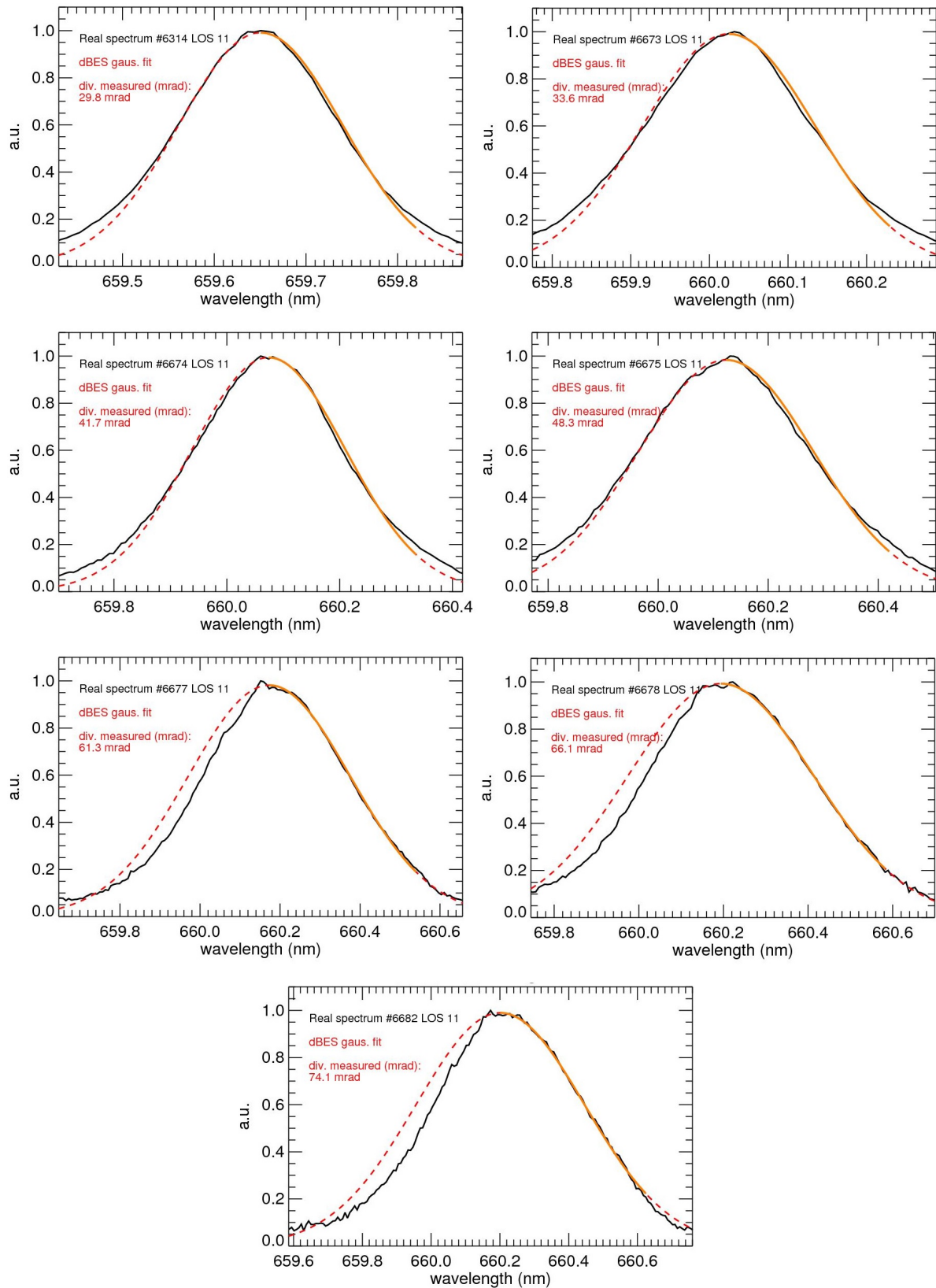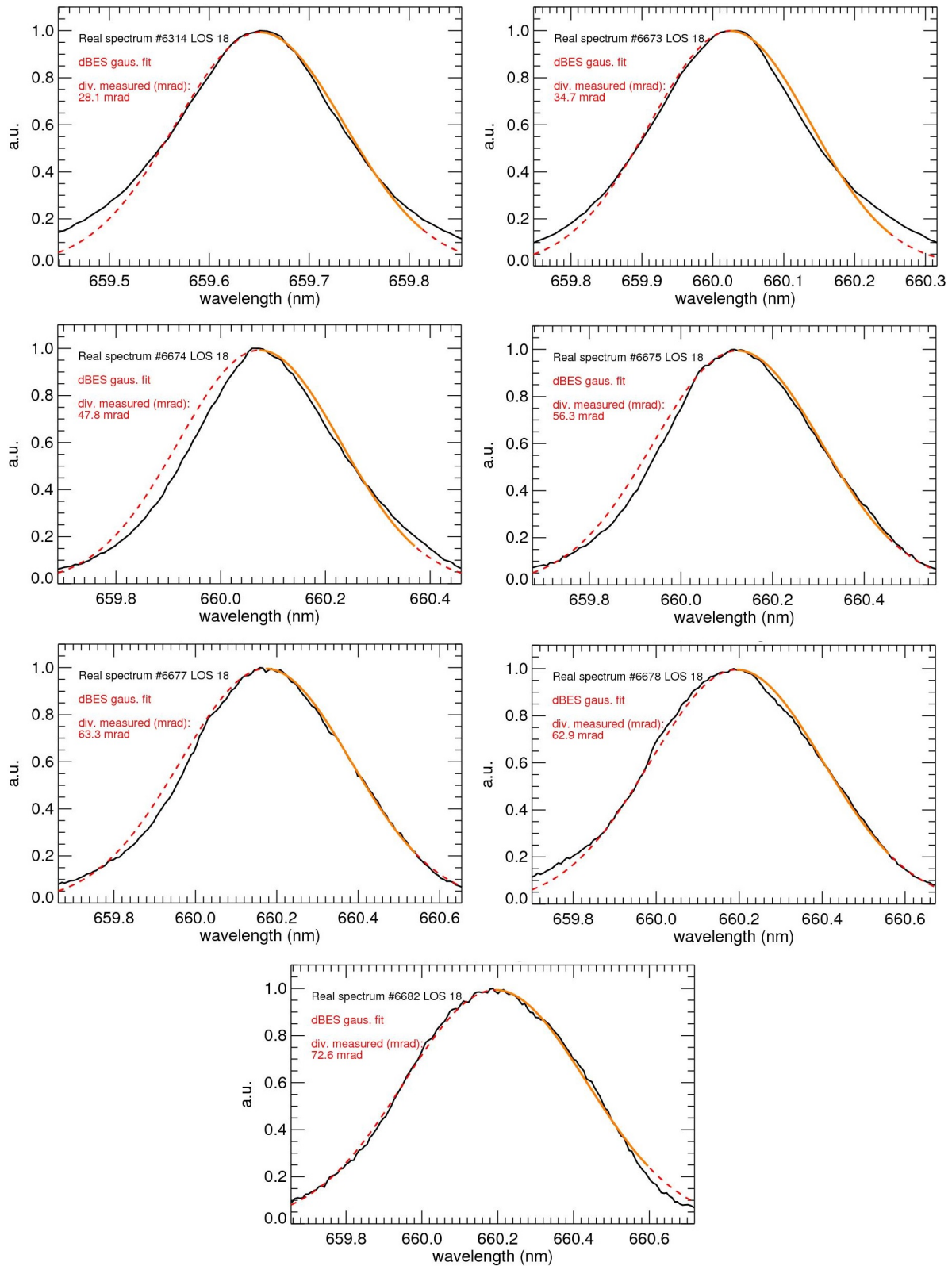
Figure 2.34: Spectra (black curve) acquired by the horizontal LOS n°11 during the pulses considered in ELISE. The orange curves are the Gaussian fit applied on the selected interval of the experimental data. The red curves are Gaussians calculated according to the results of the fits. The measured values of divergence are indicated in the legends of the respective plots. The spectra are ordered for increasing divergence.

At this point also the spectra collected by the vertical LOSs in ELISE were studied, in particular, the LOS 18 was chosen for its central position with respect to the beam. Figure 2.35a compares the values of divergence obtained with the IPP standard evaluation from the spectra of LOSs 3 and 18. The values of divergence measured by LOS 18 are slightly lower than those of LOS 3: this could be explained by the fact that possible deviations of the beamlets, which would cause a broadening of the Doppler peak and therefore an overestimation of ϵ, should be present mainly on the horizontal plane because of the orientation of the magnets in the EG. Anyway, the values of divergence of the 2 data series are compatible within a 10% margin, apart from the two pulses at lowest divergence. Figure 2.35b shows instead the divergences measured on the spectra of LOS 3 and LOS 18, fitting only the high energy side with dBES. The intermediate values of divergence of LOS 18 are higher with respect to those of LOS 3. Observing the spectra of LOS 18 in figure 2.36 it can be noticed that the Doppler peak is asymmetrical in the spectra corresponding to the anomalous points of figure 2.35b. The degree of asymmetry of the Doppler peak is therefore not always linked to the beamlets' divergence. Moreover, the asymmetries shown in figure 2.36 are difficultly referable to deviations of the beamlets, because the fluctuations of the beamlets' directions in the vertical plane are much smaller if not negligible with respect to the horizontal deviations.
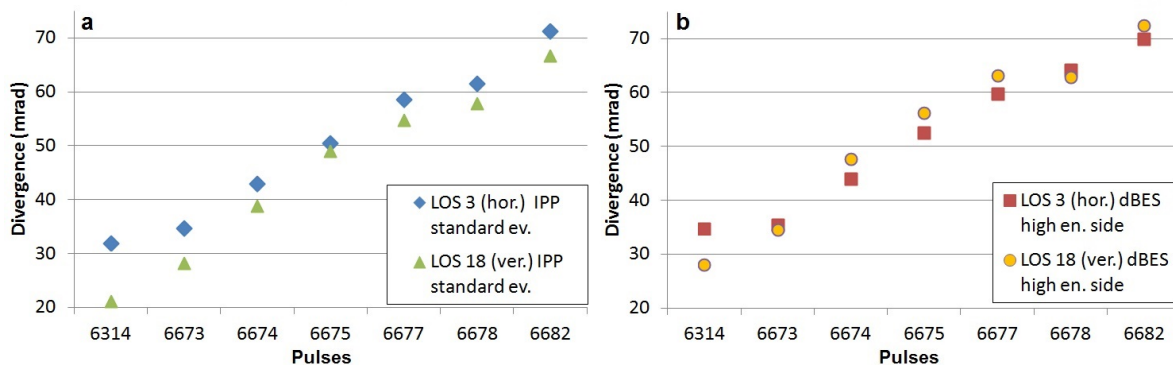
Figure 2.35: Comparison between the values of divergence obtained by the (horizontal) LOS 3 and the (vertical) LOS 18 in ELISE. The measures displayed in the plot a) are obtained by the IPP standard evaluation while the results of the plot b) are produced by dBES.

Figure 2.36: Spectra (black curve) acquired by the vertical LOS n°18 during the pulses considered in ELISE. The orange curves are the Gaussian fit applied on the selected interval of the experimental data. The red curves are Gaussians calculated according to the results of the fits. The measured values of divergence are indicated in the legends of the respective plots. The spectra are ordered for increasing divergence.

At last, it was checked whether, as expected by the origin effect, there is a correlation between the shape of the Doppler peak and the relative position of LOSs and beamlets. Figure 2.37 shows the analysis of the spectra of all the LOSs monitoring the lower row of beamlet groups in ELISE; all the curves refer to the pulse 6675 and are ordered according to the position of the optic heads from the bottom. The degree of asymmetry of the full energy component seems not follow a logical order, contrarily to what expected.
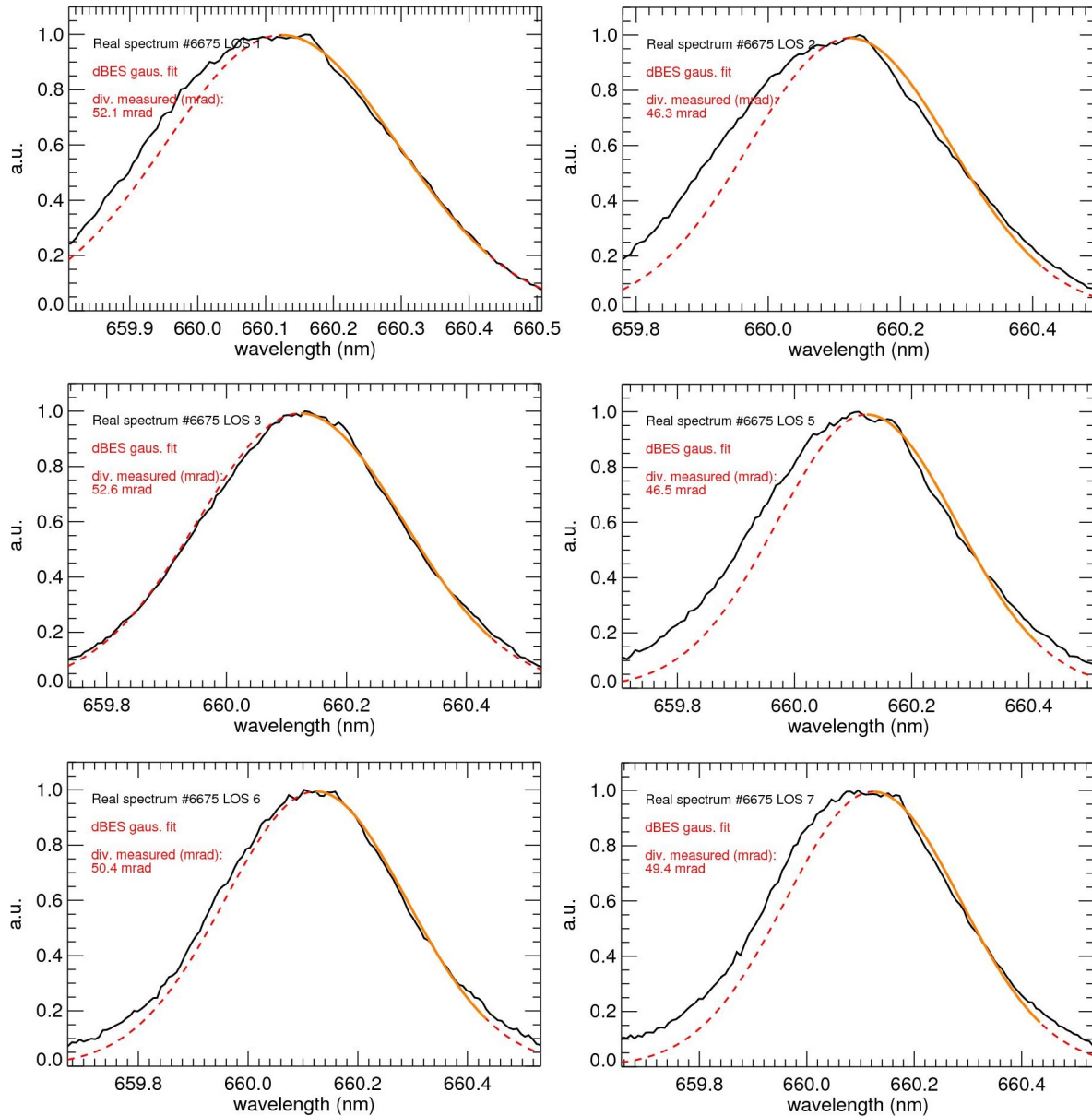
Figure 2.37: Gaussian fits (red dashed curves) of the spectra (black curves) acquired by the LOSs 1-8 of ELISE during the pulse 6675. The spectrum obtained by the LOS 4 is not reported because the signal is too low. The orange curves are the Gaussian fit applied on the selected interval of the experimental data. The red curves are Gaussians calculated according to the results of the fits. The measured values of divergence are indicated in the legends of the respective plots.

2.6.6 Discussion of the results

The benchmark of dBES showed that the volume, area and origin effects have a non negligible effect both in the simulation of the BES spectra and in the measurement of the beamlets' divergence. dBES-2

showed that, assuming that the beamlets have a Gaussian power density profile, the distortion of the Doppler peak is mainly driven by the beamlets' divergence. The values of divergence measured on the spectra simulated by dBES-2 saturated at low divergence (≤ 10 *mrad*); this result requires further investigation, being also SPIDER and MITICA's divergences expected to be lower than 10 *mrad*.

The code dBES-3 tried to simulate the spectra collected by the BES diagnostic assuming that the angular distribution of the particles of each beamlet is Gaussian, exactly as in the model used in BBC-NI simple; the results of dBES-3 and BBC-NI simple were not however in agreement between them.

The experimental spectra showed that the presence of asymmetries and tails on the full energy component does not follow clear rules; the spectra of LOS 2 in BATMAN and LOS 3 in ELISE showed that the asymmetry and the tails of the Doppler peak tend to reduce at high divergence, leading to the hypothesis that the cause of the distortion of the peak are deviations of the beamlets' direction because of their mutual repulsion and because of the magnetic fields in the acceleration system. The asymmetrization of the peak was however observed at the spectra of LOS 11 for high values of divergence, and it was observed also in a vertical LOS, i.e. in a direction along which no significant deviations of the beamlets are foreseen. In general, it is clear that the volume, area and origin effects cause a distortion of the Doppler peak, however the observed distortions don't follow the behavior of these effects (increase of the distortion with the divergence, dependence of the shape of the peak from the relative position beamlets-LOS). Moreover, because of this it was not possible to decide which one of the angular distributions used dBES and BBC-NI simple for the beamlets better reproduces the experimental data.

The analysis of both simulated and experimental spectra confirmed that the Doppler peak should be fitted in a wavelength interval symmetric to the centroid of the peak itself, in order to compensate the effects of possible asymmetries.

In future it will be necessary to identify the causes of the distortion of the Doppler peak, because the measurements of the divergence could undergo non negligible systematic errors, in particular if the measured values of divergence are very low as in SPIDER and MITICA ($3 \div 7$ *mrad*). The shape of the Doppler peak in the BES spectra should be correlated with all the operative conditions of the test facility in which the BES diagnostic is mounted. The spectra in which the Doppler peak has large tails or a high degree of asymmetry could be extensively compared to the simulations of BBC-NI simple. It is also necessary to experimentally quantify the deviations of the beamlets' directions, to understand whether they have a significant role in the asymmetrization of the Doppler peak. To do this, there should be diagnostics capable of characterize the single beamlets, and the number of beamlets observed by a LOS should be reduced as much as possible. An opportunity is represented by the NIO1 test facility, whose extracted beam has only 9 beamlets, with a divergence between 5 *mrad* and max. 40 *mrad*. The origin effect should then be less important. Moreover, NIO1 will be equipped with

- a mini-STRIKE diagnostic which could discriminate the individual beamlets, not possible on BATMAN because of the high divergence and of the distance between the GG and the BES diagnostic or the calorimeter;

- a fast emittance scanner close to the GG to study the distribution of the particles in the space of the position and of the velocity.

Chapter 3

The BES diagnostics for NIO1,SPIDER and MITICA

In this chapter the studies carried out to define the design of the BES diagnostics dedicated to the NIO1, SPIDER and MITICA test facilities will be presented. The diagnostics' main parameters have been chosen in order to reach the target performances in terms of precision in the measurement of divergence and beam uniformity. dBES was used to verify the design of the diagnostic and simulate the spectra that would be acquired by the BES system according to the design itself. The analysis of the simulated spectra confirmed the capability of measuring the beamlet divergence with the desired precision. The feasibility of the measures of beam uniformity was instead performed studying the effects of the alignment between beamlets and LOSs on the intensity of the simulated spectra. The diagnostics' design was accompanied by tests on the available instrumentation (in particular the spectrometer and the CCD camera), and by the design and test of the optic heads; these experimental activities are reported in chap. 4.

3.1   Study and design of the BES diagnostic in NIO1

3.1.1   Design of the diagnostic

As anticipated in sec. 1.7, the negative ion source NIO1 will produce a beam of $130\,mA$ composed by negative hydrogen ions accelerated at $60\,keV$. The beam is composed by a square lattice of 3x3 beamlets. To monitor the divergence and the uniformity of the beam, the BES diagnostic will be equipped with 6 telescopes, 3 oriented horizontally and 3 oriented vertically. According to the position of the viewports in the diagnostic chamber (figure 1.19), the distance of the telescopes from the GG will be $0.874\,m$ and $1.374\,m$ for the vertical optic heads and the horizontal ones, respectively. The LOSs will be aligned with the 3 rows and the 3 columns of beamlets. The divergence of the beamlets is expected to be in the range $5 \div 40\,mrad$ [50], however the design of the diagnostic was focused on the measurement of the lowest values of divergence, between $5\,mrad$ and $10\,mrad$. Similarly to what requested to the BES diagnostics in SPIDER and MITICA, the BES system in NIO1 has been designed with the target of keeping the divergence relative error below 10%.

As explained before, many factors contribute to the line broadening, so to derive the divergence from the total line width, all the other contributions must be properly evaluated and subtracted. Firstly, the measurement of the ϵ depends on the uncertainty σ_G with which the width of the Doppler peak can be measured: lacking experimental data for NIO1, a value of 0.05 pixels has been used, derived from

the analysis of real spectra acquired in RFX-mod experiment with a similar diagnostic at similar S/N ratio. The ripple in the acceleration voltages was set by the design of the accelerator stage at about 0.2% [70], while the entrance slit width of the spectrometer can be reasonably set at $100\,\mu m$. Unfortunately the plate factor of the spectrometer could not be chosen, but had to be fixed according to the available instruments: a CCD camera similar to that foreseen for SPIDER, with pixels of $13\,\mu m$ size, but a spectrometer with different focal length and grating groove density. The spectrometer available for BES on NIO1 has a focal length of $500\,mm$ (instead of $750\,nm$ in the case of SPIDER/MITICA), a grating of $1200\,gr./mm$ ($1800\,gr./mm$ in SPIDER/MITICA); this results in a plate factor of $1.8 \cdot 10^{-2}\,nm/pix$.

What could be optimized differently from SPIDER are instead the diameter and the focal length of the lenses in the optic heads. In particular, the lens diameter determines the plane angle 2ω with which the emitting particles see the lens, a parameter which contributes to the line broadening. The value of this angle is not unique, because the distance between lens and emission point changes along the LOS. ω was preliminarily calculated for all the beamlets using the approximated formula $\omega = \arctan(L/l_{los})$, where L is the radius of the clear aperture of the lens and l_{los} is the distance between the optic head and the point of emission of the photons. Considering that the viewports on which the optic heads should be mounted are $30\,cm$ far from the axis of the diagnostic chamber [71], and assuming that $\alpha = 75°$ as in SPIDER, it resulted that on average $l_{los} = 31\,cm$. Σ_ω, i.e. the standard deviation of ω in the volumes of the beamlets intersected by the LOS, was roughly estimated as the difference of the values of ω at the outermost positions of the beamlets inside the LOS. In the calculation it was assumed that the average distance of the optic heads from the post acceleration grid is $1.1\,m$, that the horizontal/vertical spacing between the axes of the beamlets is $14\,mm$ and that $\epsilon = 7\,mrad$. It resulted that $\Sigma_\omega/\omega < 7.1\%$, independently from the chosen value of L. Using the model of par. 2.3.7, the relative error of the divergence estimates was related to L and l_{los}, as shown in figure 3.1. It must be considered that the viewports are $30\,cm$ far from the axis of the diagnostic chamber .
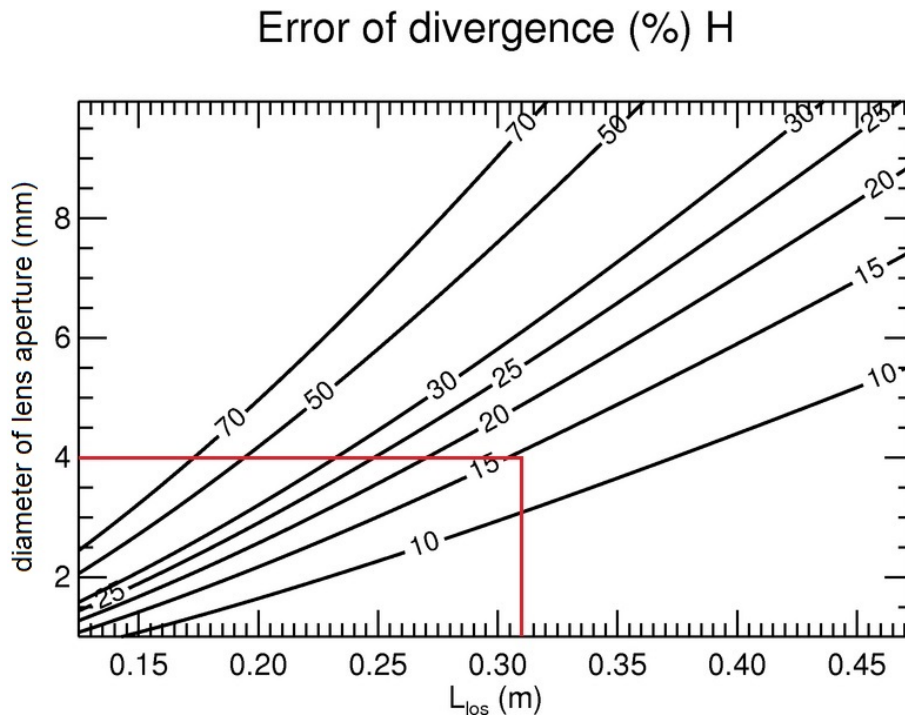

Figure 3.1: Dependence of the relative error of the divergence on the diameter of the lens and on the distance beam-optic head. The red lines indicate the chosen values for the diameter of the aperture of the optic head and for the distance between the optic heads and the center of the beam.

The correlation between ω, L and l_{los} rules the relative error of the divergence estimate, but also the amount of light collected by the diagnostic: a low ω should allow more accurate measurements of ϵ, but in practice the S/N ratio could become insufficient to make a good analysis of the spectrum. A reasonable compromise was found setting the diameter of the clear aperture of the lens at 4 mm; the chosen diameter is indicated in figure 3.1 with a red line, together with the average value of l_{los}.
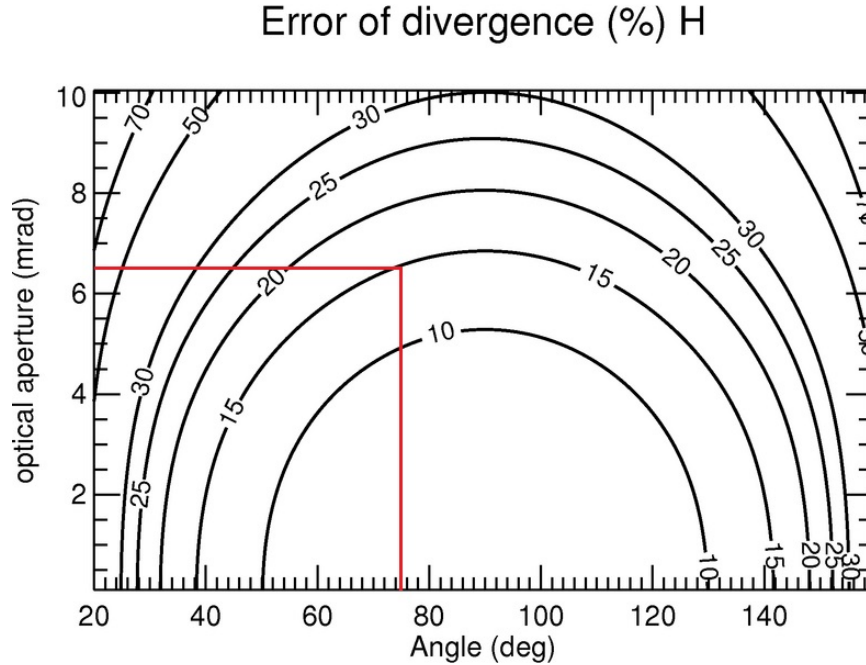
Figure 3.2: Dependence of the relative error of the divergence on ω and on the angle of observation (with $\epsilon = 7$ mrad). The red lines indicate the chosen values of α and ω.

Another diagnostic parameter that could be optimized was the observation angle α, by considering its effect on the relative error of the divergence estimate (figure 3.2). Once that ω has been fixed to 6.5 $mrad$ according to the selected lens diameter, it resulted that $\alpha = 75°$ chosen for SPIDER could be adequate also for NIO1. A smaller angle, in fact, would only worsen the error of the divergence, whereas a larger one would bring the shifted peak too much close to the H_α line[1]. With these settings, the relative error for the divergence should be about 15%: it falls outside the 10% target but it's still acceptable. Starting from these conditions, the design of the telescopes was carried out as described in sec. 4.2: the lenses adopted for the optic heads have a focal length of 50 mm, a diameter of 10 mm but a clear aperture of 4 mm as desired. The head of the fiber will be imaged at 55 cm from the lens, a distance still internal to the vacuum chamber and higher than the typical distance of the beamlets from the lens. This choice is such that the image of the fiber head has the same size of the clear aperture of the lens, in practice the LOSs have an about cylindrical shape. The effective solid angle of collection Ω was calculated as described in par. 2.3.2; figure 3.3 shows Ω as function of the axial and radial coordinates of a LOS.

The optical simulation allowed to better define ω and Σ_ω, which depend on Ω. At the distance from the GG at which the beamlets and the LOSs intersecate (about 1.3 m) the transversal dimensions of the beamlets are greater than those of the LOSs. The lines of sight are then completely filled transversally, and as figure 3.3 shows Ω and then ω vary radially. To find the most realistic values for ω and Σ_ω a first run of dBES was performed, setting an horizontal LOS observing the central row of beamlets. Following the procedure described in par. 2.3.7 and by eq. 2.23 and 2.47, it has been estimated that $\omega = 4.3$ $mrad$

---

[1]For $\alpha > 85°$ the lines join together.

and $\Sigma_\omega = 0.7$ *mrad* (17%).

With a better estimate of ω the divergence relative errore was recalculated. The results are shown in figure 3.4: the performances expected with the chosen of α and clear aperture diameter remain unchanged with respect to the first estimate shown in figure 3.2; the main change is that now the value of α could be in principle lowered down to 60° without affecting the measurement error of ϵ.
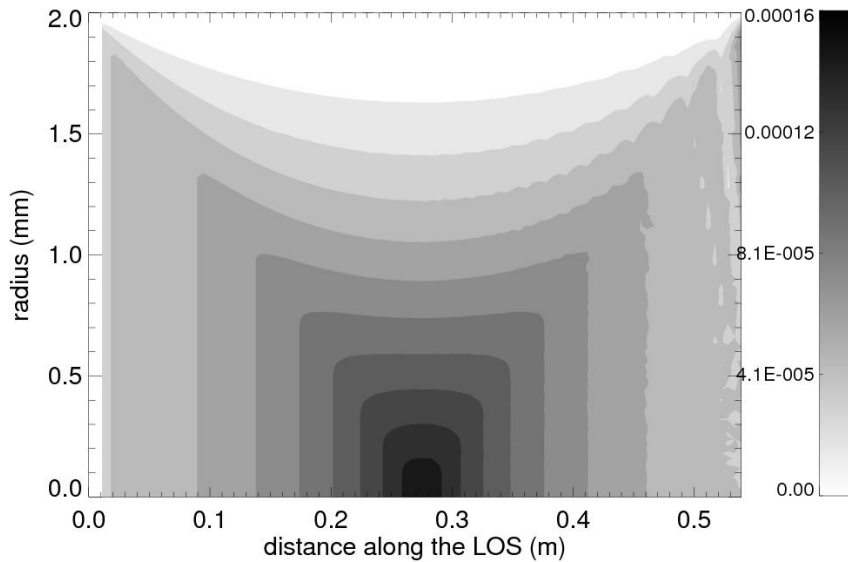

Figure 3.3: Solid angle (in srad) of collection of the telescopes in NIO1, as function of the distance from the lens and of the radial distance to the axis of the LOS
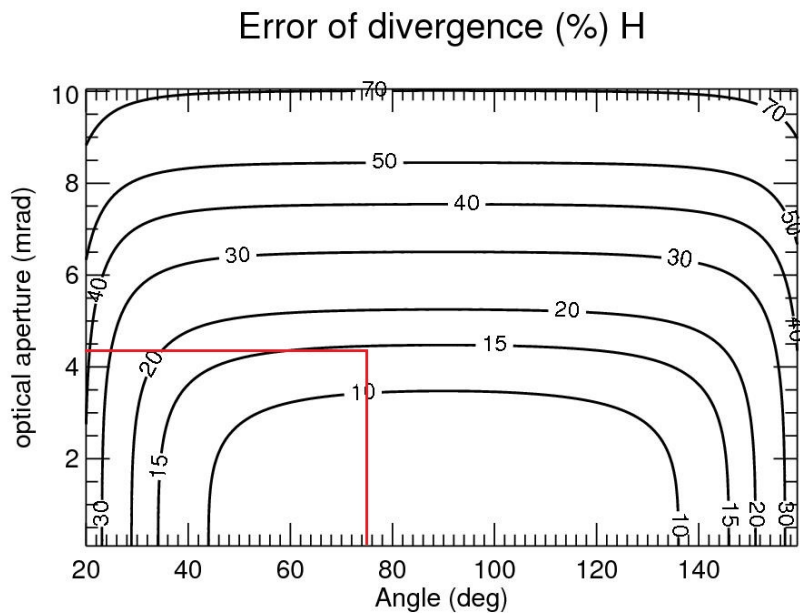
Figure 3.4: Dependence of the relative error of the divergence on ω and on the angle of observation, assuming $\epsilon = 7$ mrad and $\Sigma_\omega = 17\%$. The red lines indicate the chosen values of α and ω.

It must be remembered that these results are valid only for $\epsilon = 7$ *mrad*: as shown in figure 3.5 the relative error could reach 30% at the minimum expected divergence (5 *mrad*). A possible solution could

be to reduce the clear aperture of the lenses, but at the expense of the signal intensity.
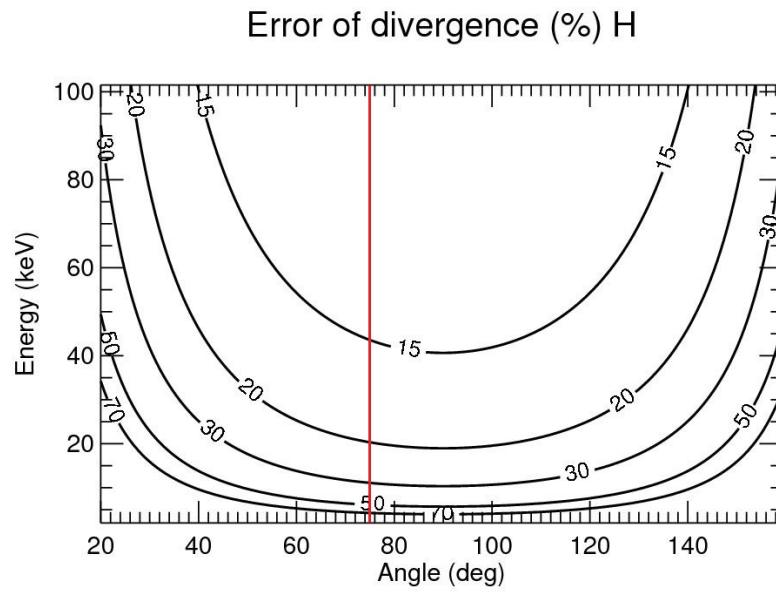
Error of divergence (%) H
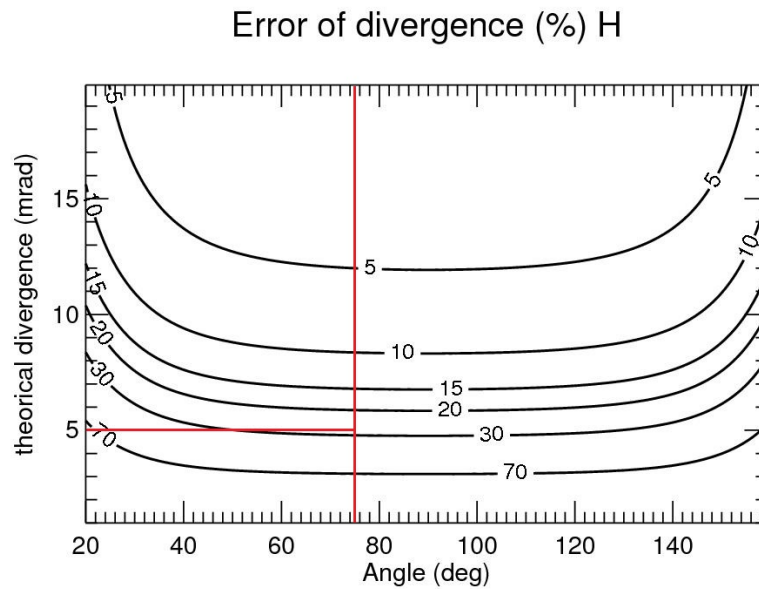
Figure 3.5: Relative error of the divergence as function of the divergence itself and of the angle of observation. The red lines indicate the chosen angle of observation and the lowest value of divergence.

Another critical issue is the plate factor: figure 3.6 shows that this quantity does not affect the error of the measurement up to a value of about $0.02 \, nm/pix$, the chosen plate factor $(0,018 \, nm/pix)$ is close to this limit. In case a lower plate factor is required, a denser grating (e.g. $1800 \, gr/mm$) could be installed instead, but it is not currently available.

Error of divergence (%) H
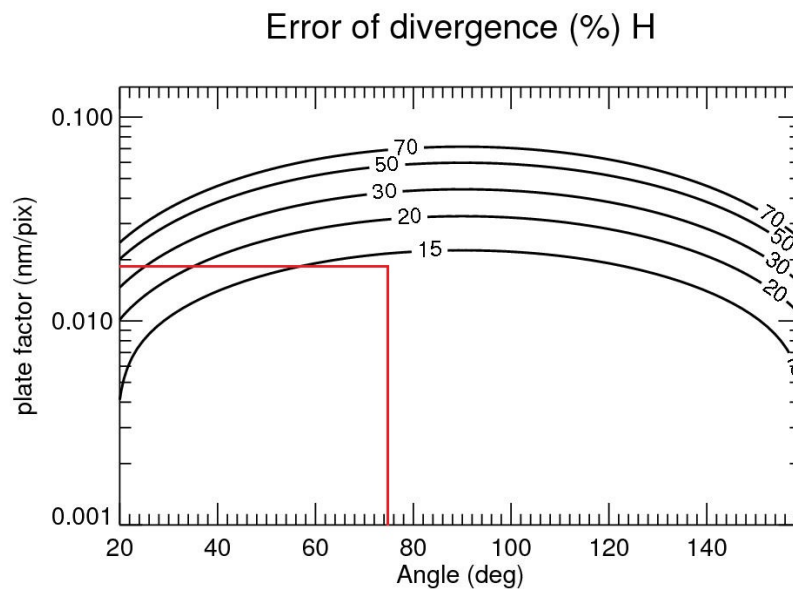
Figure 3.6: Relative error of the divergence as function of the plate factor d and of the angle of observation. The red lines indicate the chosen values of α and d.

During the commissioning of NIO1, operatins at lower acceleration voltages are foreseen; figure 3.7 shows that the BES diagnostic in NIO1 can still give acceptable measures for energies down to $25 \, keV$. Finally, figure 3.8 shows that the BES diagnostic is not substantially influenced by the ripple of the high

voltage supplies[2].

Error of divergence (%) H

Figure 3.7: Precision of the divergence as function of the energy of the ions and of the angle of observation. The red line indicates the chosen value of α.

Error of divergence (%) H
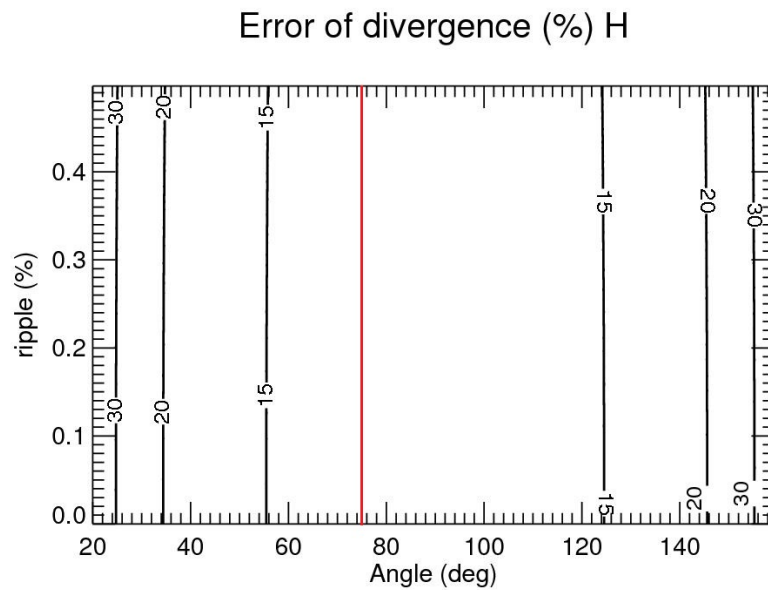
Figure 3.8: Measurement error of the divergence as function of the ripple in the energy of the ions and of the angle of observation. The red line indicates the chosen values of α.

---

[2]To be precise, the ripple at its normal level is not the dominant broadening factor for the shifted line in the spectrum.

3.1.2 Simulations

The dBES code was exploited to simulate the spectra that would be obtained by the BES diagnostic in NIO1. The values chosen in the previous paragragh for the parameters of the diagnostic were used as input. It was assumed also that the gas density in the vacuum chamber is uniform at $1.21 \cdot 10^{19} \, m^{-3}$ (corresponding to $0.05 \, Pa$ at $300°K$). The amount and the energetic distribution of the stripping losses was calculated from the data shown in figure 3.9, taking into account the width of the grids and the spacing between them; it was also roughly assumed that the electric field is uniform between the grids and 0 inside their apertures.
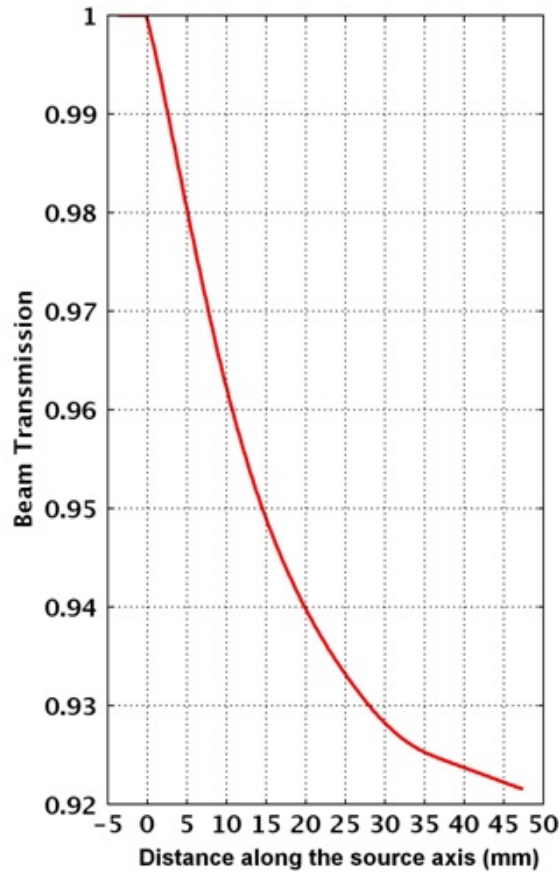
Figure 3.9: Fraction of not stripped ions within the acceleration system in NIO1, as function of the distance from the source-facing side of the PG (courtesy of P. Veltri).

Regarding the optics, it was estimated that the fibers cause negligible losses; the coupling between the fibers and the spectrometer should be responsible for a loss of 50%, whereas the reflectivity of the grating of the spectrometer was estimated to be 50% (as in the preliminary design of SPIDER [72]). The quantum efficiency of the CCD was set to 80%, the conversion factor between electrons and ADC counts at 0.4 [3], the minimum exposure time t_{exp} at $100 \, ms$.

Two LOSs have been considered, a vertical one (called `NI_V_A_1`) and an horizontal one (`NI_O_SX_1`); for simplicity their lenses have been virtually placed in the center of the viewports dedicated to BES. Figure 3.10 shows the spectra simulated by dBES for the 2 LOSs with $\epsilon = 7 \, mrad$. The spectrum of the horizontal LOS is clearly less intense because `NI_O_SX_1` is farther from the grids than `NI_V_A_1`: at longer distances the beamlets are larger and so less dense. The contribution of the stripping losses is barely visible between the Doppler peak and the unshifted H_α peak. To study the losses inside the

---

[3]This value was measured on the the CCD camera *Andor iKon-M 934*, set at amplification 2x (see sec. 4.1).

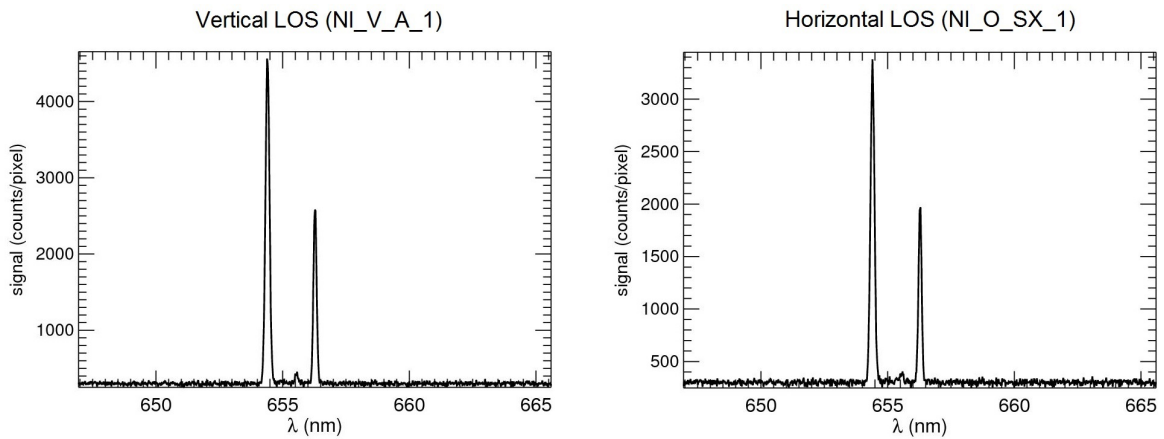accelerator the exposure time should be increased of about one order of magnitude.

Figure 3.10: Spectra simulated by dBES for the vertical (left) and horizontal (right) LOSs in NIO1. t_{exp} was set at 100 ms.

Figure 3.11 shows the spectra simulated by dBES for the horizontal LOS at $\epsilon = 20\ mrad$ and $\epsilon = 40\ mrad$, respectively; it is clear that t_{exp} should be increased also at higher values of divergence. An alternative could be to slightly increase the clear aperture of the lens, considered also that the relative error on the measurement of ϵ would still remain low in that range of divergences. However, the nominal configuration of the telescopes should be restored as soon as low values of divergence are foreseen.
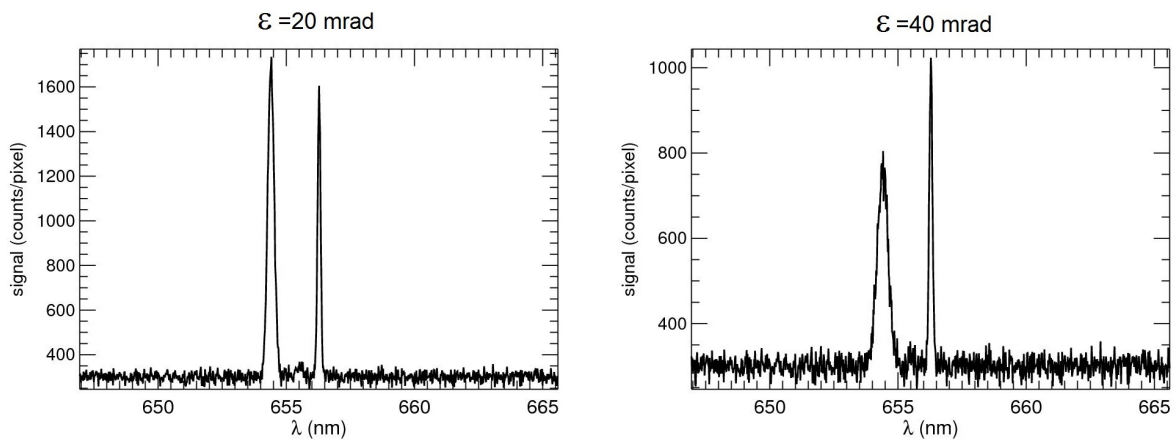
Figure 3.11: Spectra of the light collected by the LOS `NI_O_SX_1`*, assuming $\epsilon = 20\ mrad$ (left) or $\epsilon = 40\ mrad$ (right).*

The BES diagnostic can detect misalignments between beamlets, because normally the shifted peak is the sum of the contributions of only 3 beamlets. It is not possible to establish which beamlet of the three intersected is misaligned, unless the signals from horizontal and vertical LOSs are compared. Only rotations modifying α (i.e. rotations on a plane which contains also the LOS) are able to produce multiple peaks in the spectrum , otherwise a simple weakening of the line is observed. Small fluctuations of α are however not observable, because they simply produce a broadening of the full energy component; since this broadening is indistinguishable from the one induced by the divergence, it causes a systematic overestimation of the measureaments of ϵ. To get an estimate of the minimum detectable misalignment a simulation was performed by dBES for the horizontal LOS in the case of $\epsilon = 7\ mrad$; the outermost columns of beamlets where deviated by plus and minus a certain angle in the horizontal plane. For

a deviation of $\pm 20\,mrad$ (figure 3.12a) the Doppler shifted peak is deformed and less intense, but still unique; the measure of divergence on the spectrum gave $\epsilon = 29\,mrad$. Eventually, for a deviation of $\pm 40\,mrad$ (figure 3.12b) the Doppler shifted peak is split in 3 partially overlapped peaks.
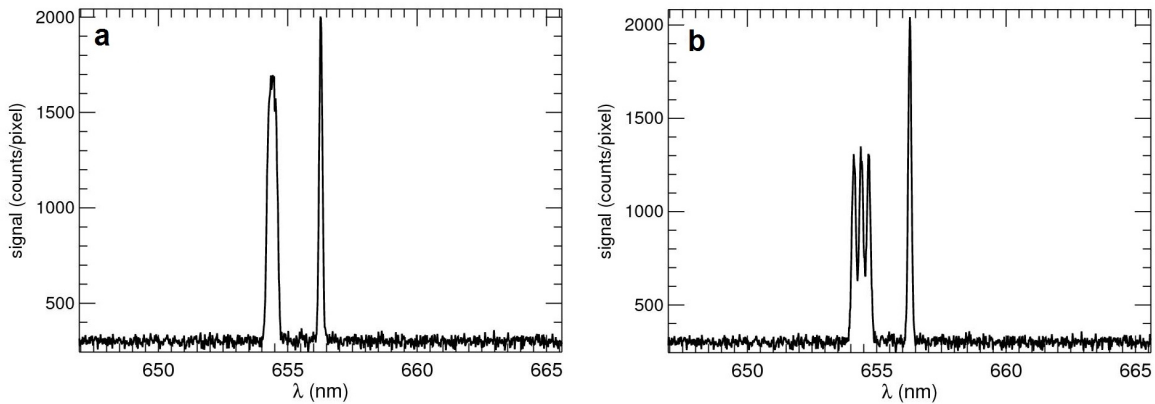

Figure 3.12: Spectra simulated for the LOS `NI_0_SX_1`, *assuming that the first and third columns of beamlets are deviated horizontally of* $\pm 20\,mrad$ *(a) or* $\pm 40\,mrad$ *(right).*

dBES allowed to study also the precision with which the optic heads should be aligned to avoid too large systematic errors in the measurements of beam uniformity. Similarly to the SPIDER BES diagnostic, the target in NIO1 is to measure values of beam uniformity above 90% with a relative error below 10%. Figure 3.13 shows, according to the simulations of dBES, how much the amplitude of the Doppler peak varies if the LOS is translated perpendicularly to the viewport and to the axis of the chamber. `NI_V_A_1` was chosen for this study because it gives more restrictive limits: it is nearer to the grids, therefore the beamlets are smaller and it's more difficult to intercept them. The maximum allowed shift depends on the divergence of the beamlets, because it influences their dimensions; figure 3.13 shows 3 cases with different values of divergence: $\epsilon = 5\,mrad$, $\epsilon = 10\,mrad$ and $\epsilon = 20\,mrad$. In the plots the intensity is normalized with respect to the maximum reached level. A minimum value > 0 in the case $\epsilon = 5\,mrad$ indicates that already at the minimum divergence adjacent beamlets mix partially together. At $\epsilon = 10\,mrad$ the contributions of the 3 beamlets is barely distinguishable, while at $\epsilon = 20\,mrad$ the LOS observes a unique beam.

The BES signal level is not critical for the measurements of divergence and to monitor the temporal relative variations of density between LOSs (if the mountings of the optics are mechanically stable). Instead, the precision and the stability of the positioning of the LOSs are crucial for the measurements of beam uniformity. To avoid signal losses[4] higher than 10% the optic head must be placed with an accuracy of $\pm 1.3\,mm$ (if $\epsilon = 5\,mrad$); this alignment could be achieved, but it must be remembered that this tolerance is linked to the relative position not between LOSs and vacuum chamber, but between beamlets and LOSs. `NI_V_A_1` intercepts the beamlets at $0.8\,m$ from the GG, therefore a horizontal deviation of the beamlets of only $1.6\,mrad$ would be enough to alter the signal intensity of 10%. On the other side, for $\epsilon > 10\,mrad$ the alignment of the beamlets is not a problem. However, it must be considered that when the beamlets overlap too much then each LOS is not able to distinguish a row/column of beamlets; the effective spatial resolution of the diagnostic is therefore reduced.

---

[4]The beam uniformity is measured comparing the integrals of the Doppler peaks in spectra of different LOSs. The Doppler peaks of the spectra simulated for figure 3.13 have all the same width, therefore the comparison is on the height of the peaks.
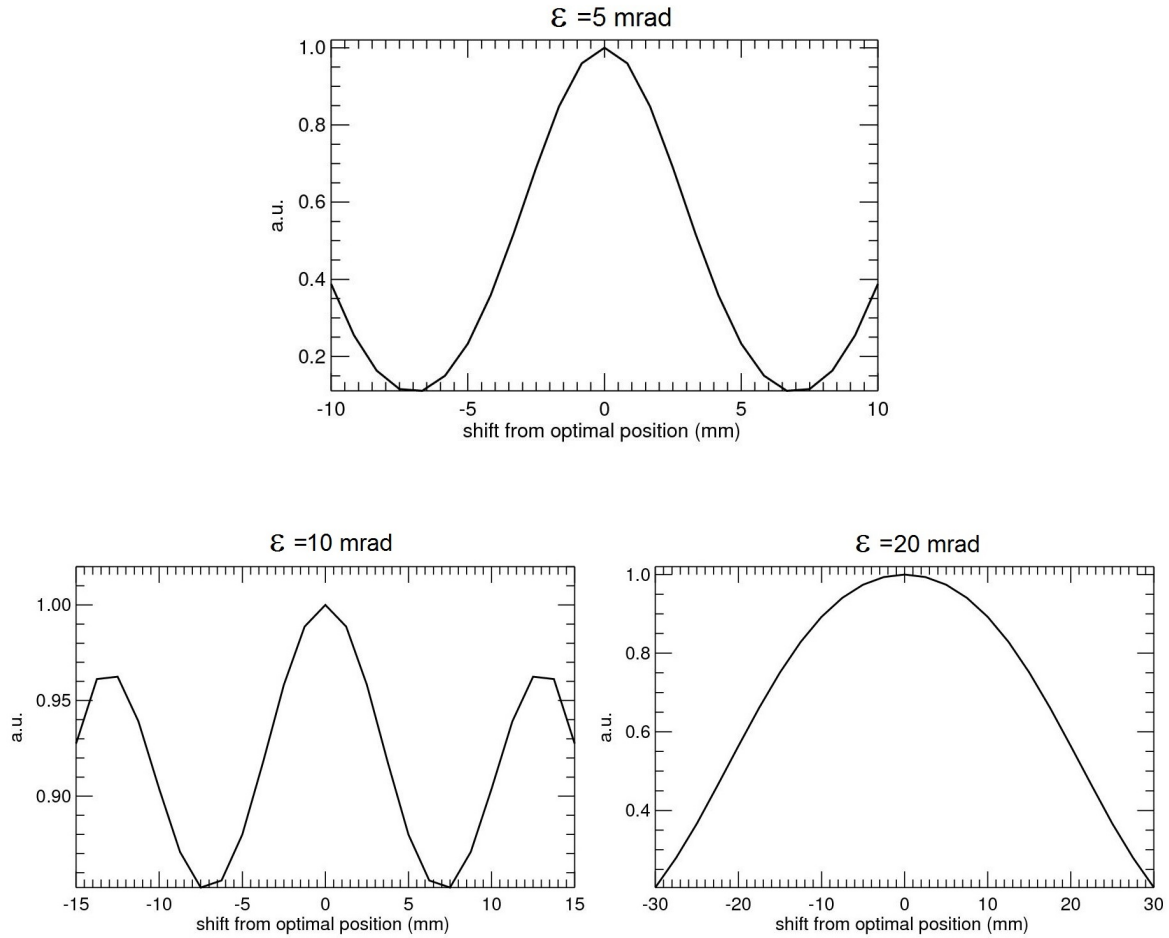
Figure 3.13: Variation of the level of the Doppler peak obtained in NIO1 by translating the vertical LOS horizontally. In the 3 cases the divergence of the beamlets was set to 5 mrad,10 mrad and 20 mrad, respectively. The intensity of the peak is normalized with respect to the maximum reached amplitude.

A similar analysis was made tilting the optic heads in perpendicular sense with respect to their plane of observation. With the same criterion used for the translation, it can be deduced from figure 3.14 that the LOSs cannot be tilted for more than ± 4 *mrad* if $\epsilon = 5$ *mrad*, while for values of divergence above 10 *mrad* the alignment is not an issue for the measures of uniformity.

At last, dBES was used to simulate spectra with input divergences between 5 *mrad* and 10 *mrad*. The spectra were then analyzed applying a Gaussian fit on the whole Doppler peak, the width (and its uncertainty) resulting from the fit was used as described in par. 2.3.5 to get a measure of ϵ. As figure 3.15 shows, the errors of ϵ (black solid line) measured on the spectra produced by dBES are in agreement with what foreseen (red dashed line) by the model described and used in par. 2.3.5 and 3.1.1. Moreover, the relative differences (blue dotted line) between the measured values of ϵ and the ones given in input to dBES are smaller than the measurement errors.
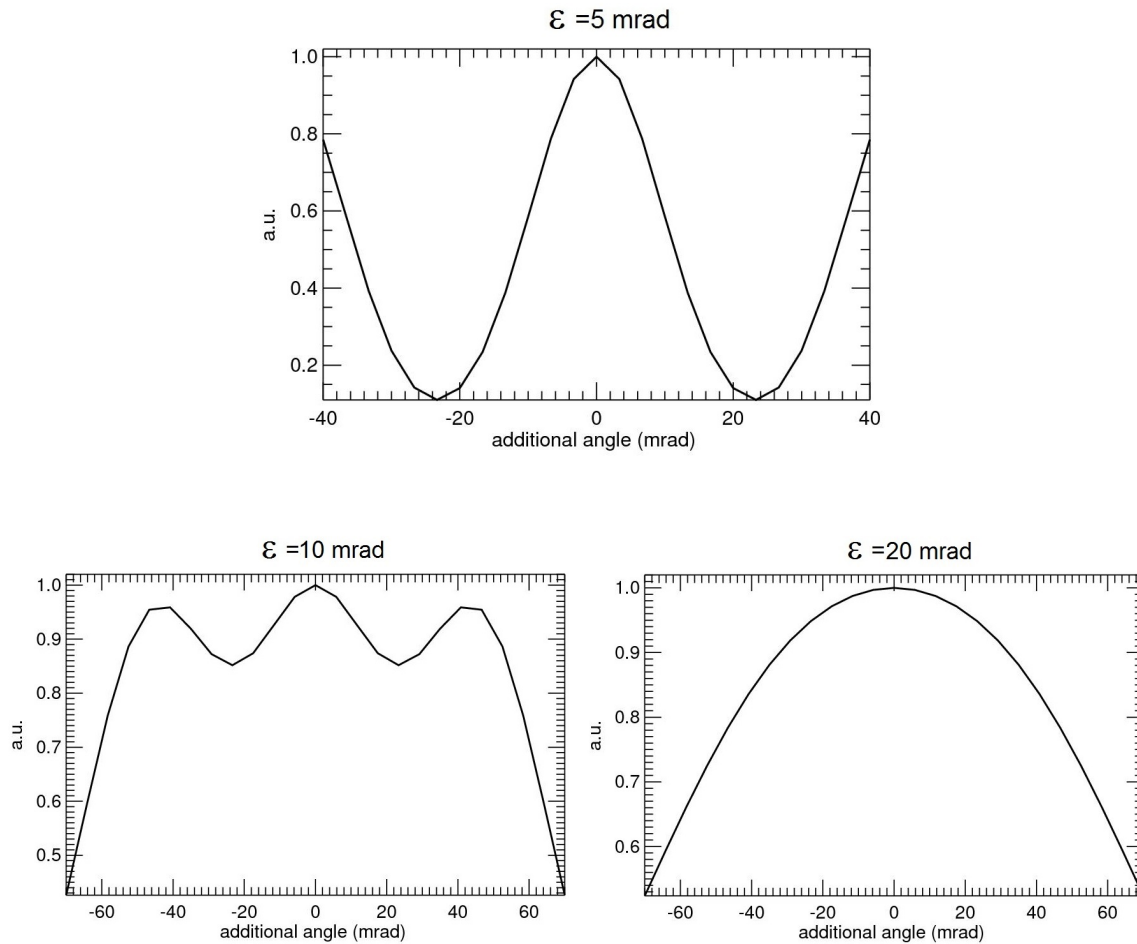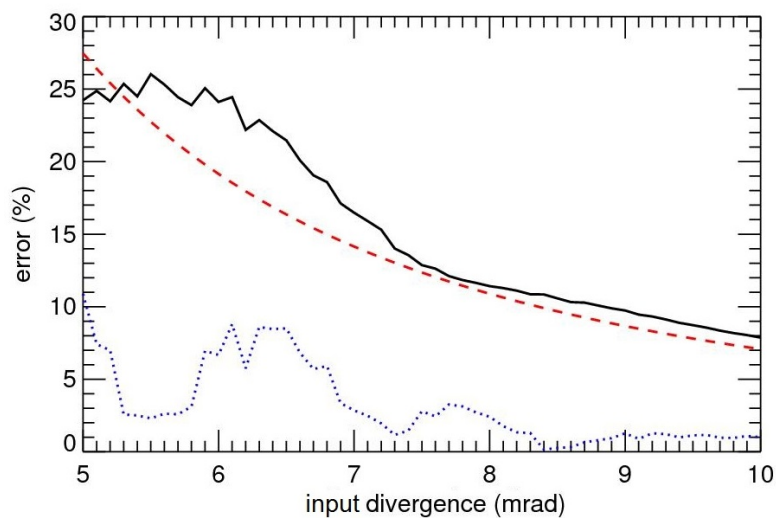
Figure 3.14: *Variation of the level of the Doppler peak obtained in NIO1 by rotating the lens of the vertical LOS in the plane perpendicular to the axis of the chamber. In the 3 cases the divergence of the beamlets was set to 5 mrad, 10 mrad and 20 mrad, respectively. The intensity of the peak is normalized with respect to the maximum reached amplitude.*

Figure 3.15: *Relative error of the measurements of divergence (black solid line) in NIO1 as function of the value of ϵ given in input to dBES. The red dashed line indicates the relative error of ϵ calculated as in par. 2.3.5, while the blue dotted line represents the relative deviation (in absolute value) of the measures of ϵ with respect to the input values used for the simulation.*

3.1.3   Summary of the results

NIO1 BES diagnostic was designed in order to measure the divergence in the range $5 \div 10\,mrad$ with a relative error below 10%. With the available instrumentations and according to the characteristics of NIO1, the design of the diagnostic would allow to measure ϵ in the indicated range with an error between 7% and 28%. The values of divergence measured on the spectra simulated by dBES differ for less than 10% respect to those given in input to the simulations. To reduce the measurement error of ϵ the diameter of the optical aperture of the lenses should be reduced with respect to the present value of $4\,mm$, but this seems to be too risky for the intensity of the collected spectra. In the measurement of ϵ it must be taken into account also that fluctuations in the direction of the beamlets up to $20 \div 30\,mrad$ could not be noticed and result in an overestimation of ϵ.

Regarding the measurements of beam uniformity, the simulations showed that at the lowest values of divergence the dependence of the intensity of the spectra on the alignment between LOSs and beamlets is too strong. In other words, the alignment between the opticheads and the beamlets is too delicate and would introduce systematic errors in the comparison between the intensities of spectra belonging to different LOSs. For divergences equal or greater than $10\,mrad$ this problem is not present, however the effective spatial resolution of the BES diagnostic is reduced: each LOS, indeed, would receive a non negligible amount of light by beamlets which are observed also by the adjacent LOSs.

3.2   Study and design of the BES diagnostics for SPIDER

The design of the BES diagnostic for the SPIDER test facility has started before the beginning of the PhD [72]. As anticipated in par. 3.1.1 the target is to measure the divergence of the beamlets and the beam uniformity according to the specifications listed in table 3.1.

Quantity	Target Performance	Target precision
Uniformity	$\geq 90\%$	$\leq 10\%$
Divergence	$\leq 7\,mrad$	$\leq 10\%$

Table 3.1: Limits and measurement precision desired for the quantities monitored by BES.

Keeping these goals as reference, the design of the diagnostic was completed and then validated by means of the dBES code with exactly the same approach adopted in the case of the NIO1 (sec. 3.1).

3.2.1   Design of the diagnostic

According to SPIDER BES diagnostic design [72], the beam will be sampled by 40 LOSs, whose optic heads will be placed on 4 viewports at the left side of the vacuum vessel (looking towards the GG), 4 on the right side and 4 at the bottom. All the telescopes are oriented so that $\alpha = 75°$; the orientation of the horizontal LOSs can be observed in figure 3.16.
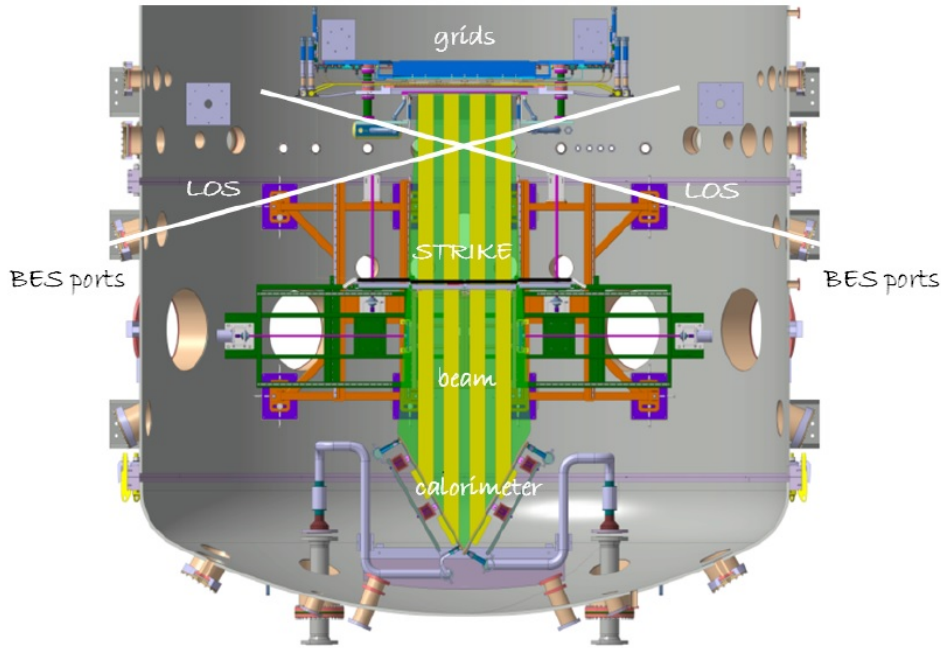
Figure 3.16: View of the horizontal LOSs inside SPIDER [72].

For the simulations with dBES one telescope is virtually placed in the center of each viewport, except for possible corrections needed to improve the intersection with the beamlets; the lines of sight were named with an abbreviation following this convention: the first two letters (`SP` for SPIDER) identify the test facility. The next two letters indicate whether the LOS is horizontal or vertical (`O` or `V`) and in what side of the vessel the lens is mounted (`A` for top, `B` for bottom, `SX` and `DX` for left and right looking towards the GG). The final number is given by counting the viewports dedicated to BES on the side of the vessel, from the bottom to the top or from the left to the right. The position of the viewports and then of the LOSs is presented in table 3.2 in terms of x, y, z coordinates (defined as in par. 2.3.1 [5]).

LOS name	x (mm)	y(mm)	z(mm)	LOS name	x (mm)	y(mm)	z(mm)
SP_O_SX_1	917	-2120	-593	SP_O_DX_3	917	2120	297
SP_O_SX_2	917	-2120	-297	SP_O_DX_4	917	2120	693
SP_O_SX_3	917	-2120	99	SP_V_B_1	1430	-260	-2089
SP_O_SX_4	917	-2120	495	SP_V_B_2	790	-80	-2089
SP_O_DX_1	917	2120	-495	SP_V_B_3	790	80	-2089
SP_O_DX_2	917	2120	-99	SP_V_B_4	790	260	-2089

Table 3.2: Coordinates (in mm) of the viewports' centers and therefore of the virtual optic heads set in the simulations of dBES for SPIDER (courtesy of M. Tollin).

The parameters [21, 72, 58] regarding the experiment and the BES diagnostic which are required by dBES are listed in table 3.3.

---

[5]The x axis is parallel to the one of the vacuum vessel and points towards the calorimeter, whereas the y and z axes lay on the GG and are respectively horizontal (rightwards) and vertical (upwards); the origin of the axes is in the center of the GG.

Quantity	value
ϵ (e-folding) foreseen	$3 \div 7\,mrad$
Observation angle α	$75°$
Total acceleration voltage ($V_0 \pm \sigma_{V_0}$)	$100\,kV \pm 1\%$
Voltage ripple ($\sigma_V \pm \Sigma_V$)	$1\,kV \pm 10\%$
Error of linewidth from gaussian fit (σ_G)	$0.05\,pix$
Diameter of fiber core	$400\,\mu m$
Plate factor of the spectrometer (d)	$6.7\,nm/pix$
Entrance slit width of the spectrometer (F)	$100\,\mu m$
Pixel size of CCD (p_{size})	$13\,\mu m$
Number of pixels in the CCD	1024x1024

Table 3.3: Information on SPIDER and the BES diagnostic required by dBES [72, 58].

The initial design of the optic heads [72] foresaw lenses with a focal length of $120\,mm$ and a clear aperture of $10\,mm$ diameter, imaging the fiber head at $3\,m$ from the lens. After some tests on the proto-type of the optic heads (described in sec. 4.2 and 4.3) the focal length was increased to $150\,mm$ and the clear aperture was reduced to $8\,mm$, keeping the distance of the image of the fiber head unvaried. The optical simulation of the optic head gave the solid angle of collection as function of the axial and radial coordinates of the LOS (figure 3.17).
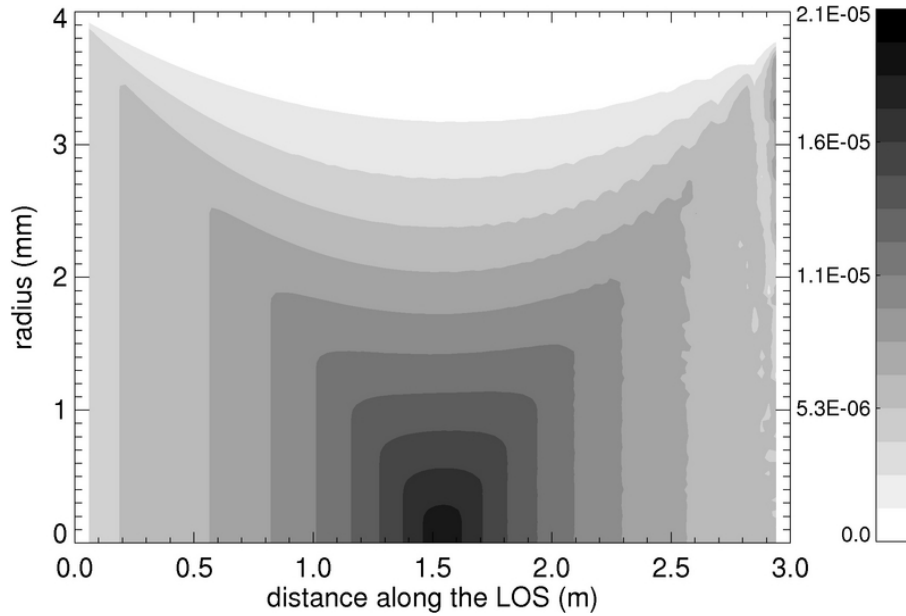
Figure 3.17: Solid angle (in srad) of collection of the telescopes in SPIDER, as function of the longitudinal and radial distances respect to the axis of the LOS (beware the different units used in the axes of the plot).

The irregularities in the plot of the figure are an effect of the limited discretization of the image and test planes (par. 2.3.2), which is not negligible when the two planes are too close. Following the method described in par. 2.3.7, using the data of figure 3.17 it was possible to establish that $\omega = 1.57\,mrad \pm 20\%$ [6]. Figure 3.18 shows that for this value of ω, assuming $\epsilon = 5\,mrad$ and using the model of par. 2.3.7, the error in the measurement of the divergence is below 10%.

---

[6] $\omega = 1.65\,mrad \pm 14\%$ for horizontal LOSs and $\omega = 1.48\,mrad \pm 26\%$ for vertical LOSs; the average value is used.
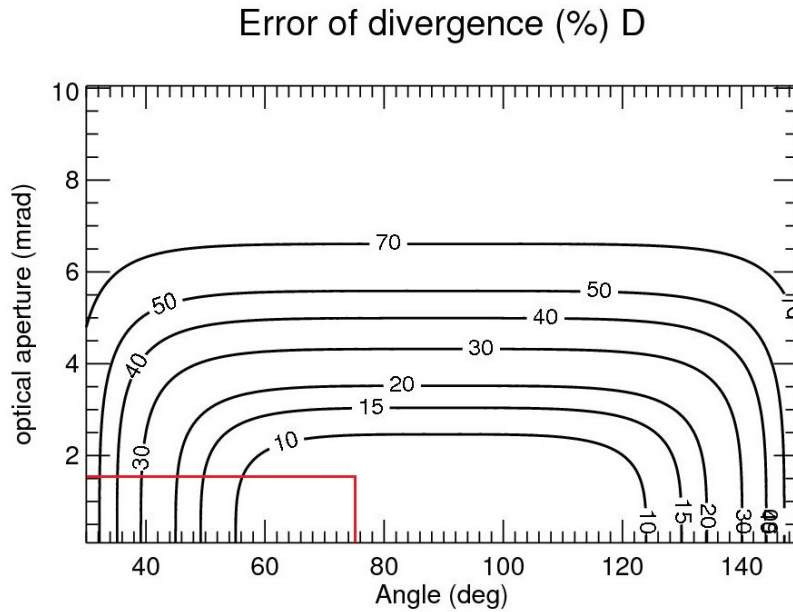
Error of divergence (%) D

Figure 3.18: Dependence of the measurement error of the divergence on ω and on the angle of observation, assuming that ε = 5 mrad and that SPIDER is working with deuterium. The red lines indicate the chosen values of α and ω.

It must be taken into account that the relative error on ϵ tends to increase for decreasing values of ϵ. Figure 3.19 shows the dependence of the relative error of ϵ on ϵ itself and on the observation angle in the case of SPIDER: the threshold of 10% could be exceeded for $\epsilon = 3\,mrad$.

Error of divergence (%) D
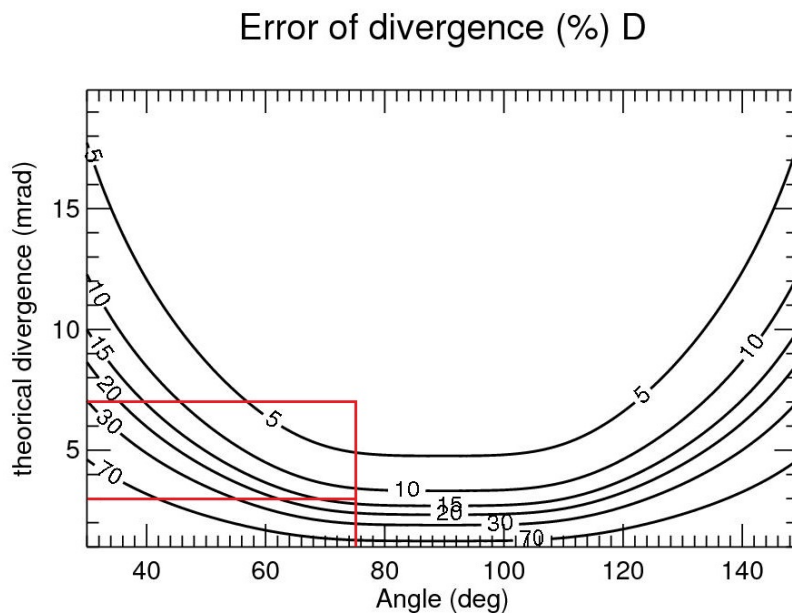
Figure 3.19: Measurement error of the divergence as function of the divergence itself and of the angle of observation, assuming that SPIDER is working with deuterium. The red lines indicate the chosen angle of observation and the extreme values of divergence.

Figure 3.20 shows instead that for $\alpha = 75°$ the plate factor can be varied without influencing significantly the relative error of ϵ, unless it exceeds $\sim 1.5 \cdot 10^{-2}\,nm/pix$.
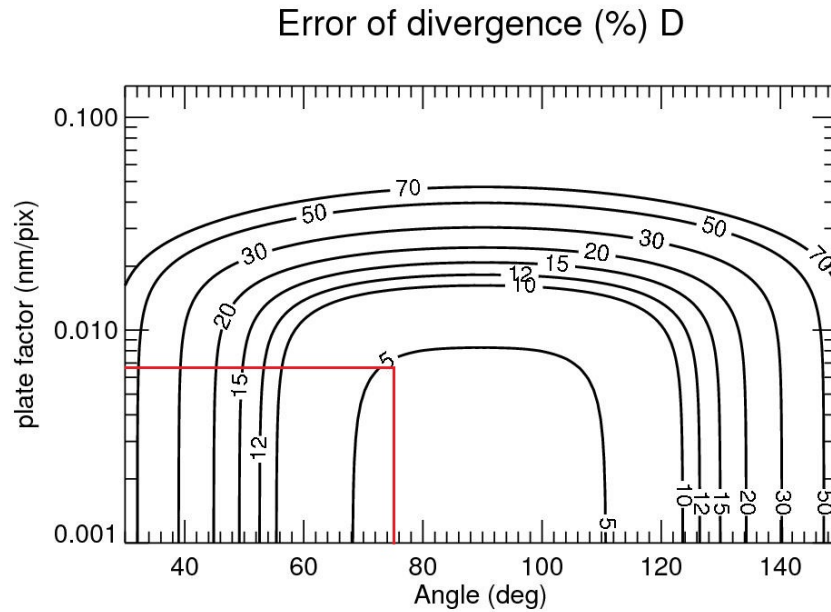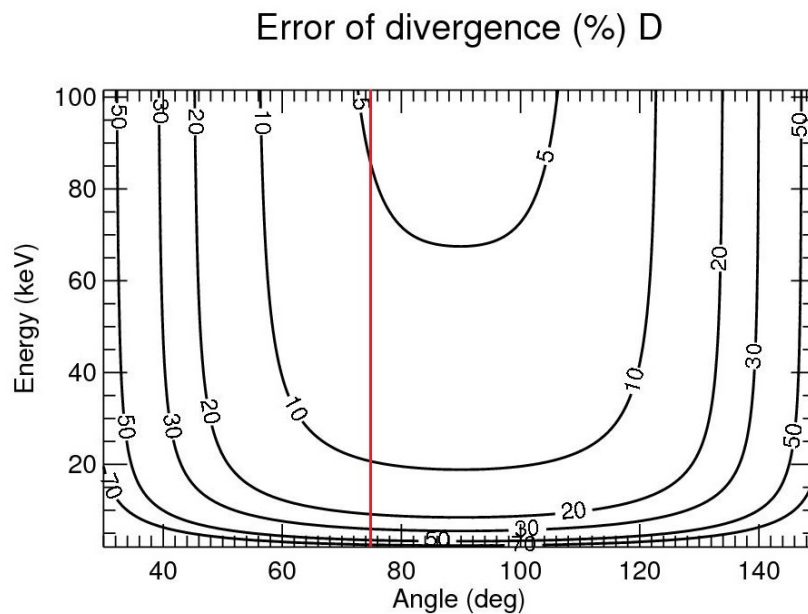
Error of divergence (%) D

Figure 3.20: *Precision of the divergence as function of the plate factor of the spectrometer and of the angle of observation, assuming that $\epsilon = 5\,mrad$ and that SPIDER is working with deuterium. The red lines indicate the chosen values of α and d.*

Figure 3.21 shows the dependence of the measurement error of ϵ on the total acceleration voltage: for $\alpha = 75°$ the voltage can be lowered to $25\,kV$ without affecting the precision of ϵ; at last, the influence of the voltage ripple on the relative error the divergence is shown in figure 3.22: for $\alpha = 75°$ the error of ϵ is below 10% if the voltage ripple doesn't exceed 2.6%.

Error of divergence (%) D

Figure 3.21: *Measurement error of the divergence as function of the total acceleration voltage and of the angle of observation, assuming that $\epsilon = 5\,mrad$ and that SPIDER is working with deuterium. The red line indicates the chosen value of α.*
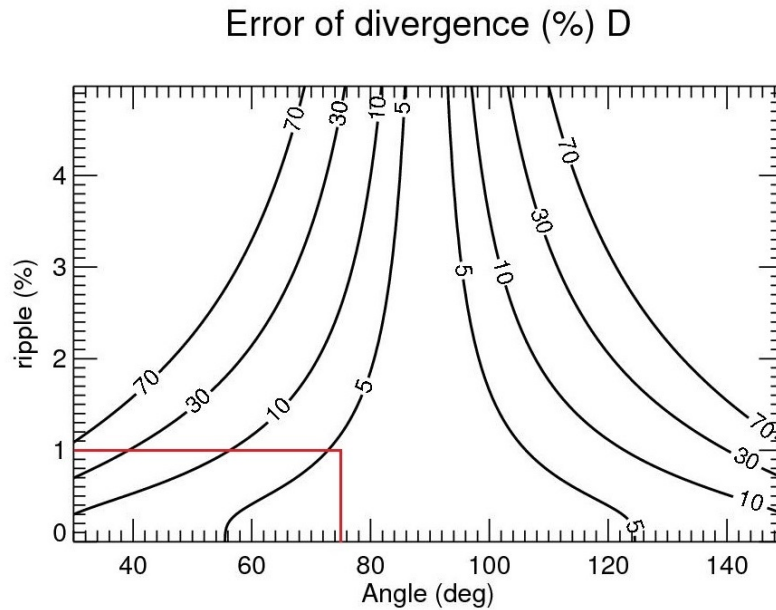
Error of divergence (%) D

Figure 3.22: Measurement error of the divergence as function of the voltage ripple and of the angle of observation, assuming that $\epsilon = 5$ mrad and that SPIDER is working with deuterium. The red lines indicate the chosen value of α and and the foreseen level of voltage ripple.

3.2.2 Simulations

The data of the design were given in input to dBES to simulate the spectra acquired by the diagnostic. It was assumed that the gas density in the vacuum chamber is uniform at $1.21 \cdot 10^{19}\ m^{-3}$ (corresponding to 0.05 Pa at 300°K). For the amount and energy distribution of the stripping losses the profile shown in figure 3.23 was adopted. The figure shows the fraction of negative ions not neutralized as function of the distance from the source-facing side of the PG; it is shown also the profile of the energy reached by the ions inside the acceleration stage, in the rough assumption that the electric field is constant between the grids and null inside their apertures.
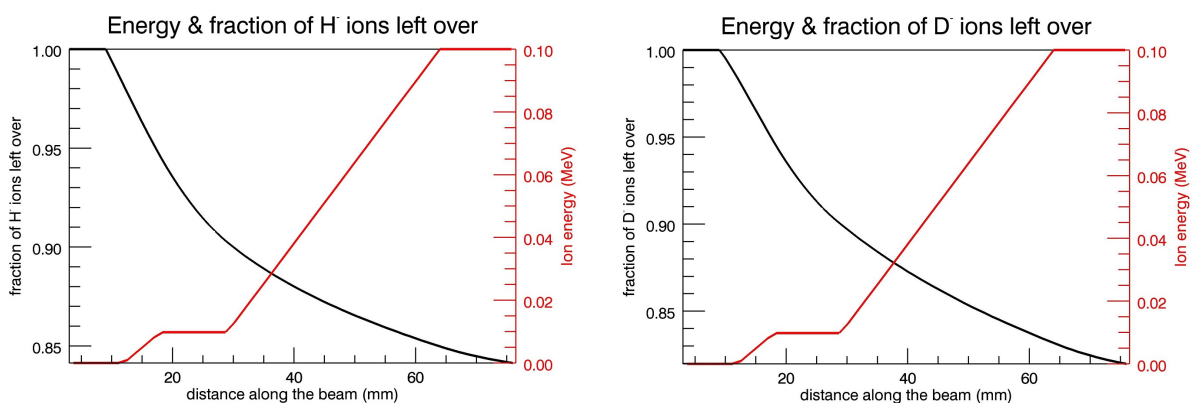

Figure 3.23: Fraction of not stripped ions within the acceleration system in SPIDER, as function of the distance from the source-facing side of the PG [73]. For the same spatial coordinate the energy reached by the negative ions is shown. The two plots refers to operations in hydrogen and deuterium, respectively.

The optical losses in the fibers which connect the optic heads to the spectrometers were estimated to be around 30%, caused mostly by the connections between the patch chords [72] which compose each fiber. The reflectivity of the grating of the spectrometer was set to 50%, and the quantum efficiency of

the CCD was set at 80%. The conversion factor given by the amplification and the sampling of the CCD was set to $0.4\,counts/e$ as in the CCD camera for NIO1. After some preliminary trials, the exposure time of the CCD was set to $50\,ms$. Two examples of spectra produced by dBES are shown in figure 3.24, belonging respectively to the horizontal LOS SP_O_SX_2 and the vertical LOS SP_V_B_1. As it can be seen, the intensity of the spectrum of the vertical LOS is roughly 3 times higher than the one of the horizontal LOS; this is due to the fact that the horizontal LOS crosses 20 beamlets, while the vertical LOS crosses 64.
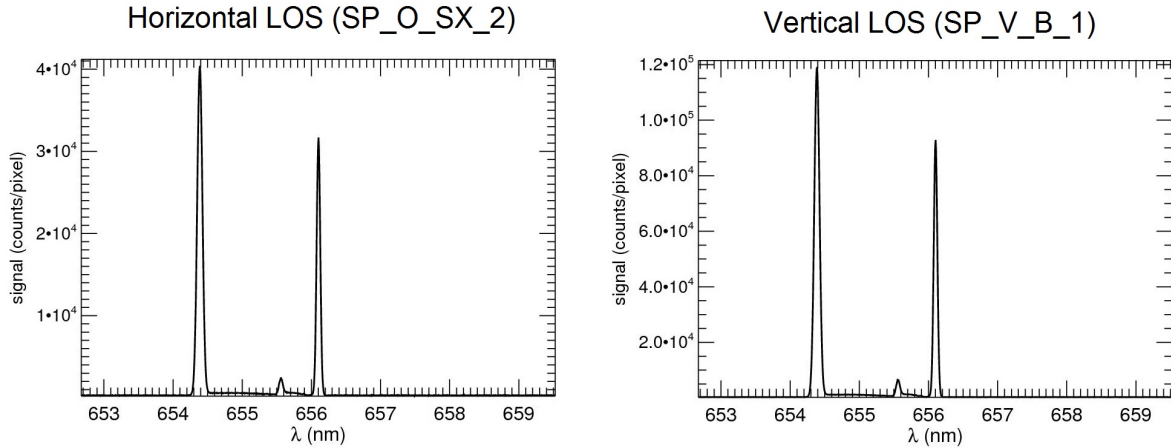
Figure 3.24: Spectra simulated by dBES for the horizontal LOS SP_O_SX_2 *and the vertical LOS* SP_V_B_1, *assuming that the source is operating with deuterium and that* $t_{exp} = 50\,ms$.

dBES was used also to understand the maximum deviations of the beamlets which cannot be detected by BES and which could cause a systematic overestimation of ϵ. For this check an horizontal LOS was selected and one column of beamlet groups was deviated horizontally of a certain angle; another column of beamlet groups was deviated with the same angle, but in opposite way. The minimum angle for which the contributions of the deviated beamlets are distinguishable in the spectrum is about $15\,mrad$: figure 3.25 shows the spectrum simulated by dBES exactly in this condition.
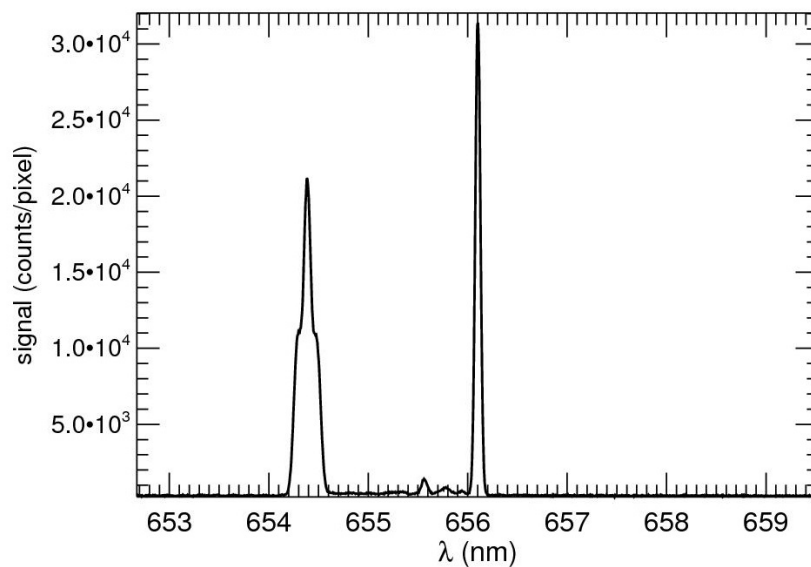

Figure 3.25: Spectrum simulated by dBES for the horizontal LOS SP_O_SX_2 *and with the source operating in deuterium. Two columns of beamlet groups were deviated horizontally of* $+15\,mrad$ *and* $-15\,mrad$ *respectively.*

To guarantee the accuracy of the measurements of beam uniformity it was studied how much the intensity of the BES spectra is influenced by the alignment of the LOSs with respect to the beamlets. Figure 3.26 shows how the intensity (and therefore the integral) of the Doppler peak varies if the optic head is shifted vertically. The data shown in the 2 plots were obtained using respectively $\epsilon = 3\,mrad$ and $\epsilon = 7\,mrad$ as input for dBES. The values of amplitude of the Doppler peak are normalized with respect to the maximum value. What results from figure 3.26 is that a vertical shift of $\pm 1\,mm$ of the optic head from the optimal position could cause a 10% systematic error in the measure of beam uniformity. Considering that the distance between the LOSs and the GG is about $35\,cm$ at the center of the beam, a vertical shift of $\pm 1\,mm$ is equivalent to a vertical deviation of the beamlets of $\pm 3\,mrad$.

Figure 3.27 shows instead the results of an analogous calculation, in which the variation of the amplitude of the Doppler peak is due to a rotation of the horizontal LOS in the the vertical plane. In order to avoid systematic errors greater than 10% in the measurement of the beam uniformity, the optic heads should not be tilted with respect to their optimal direction for more than $\pm 0.5\,mrad$.
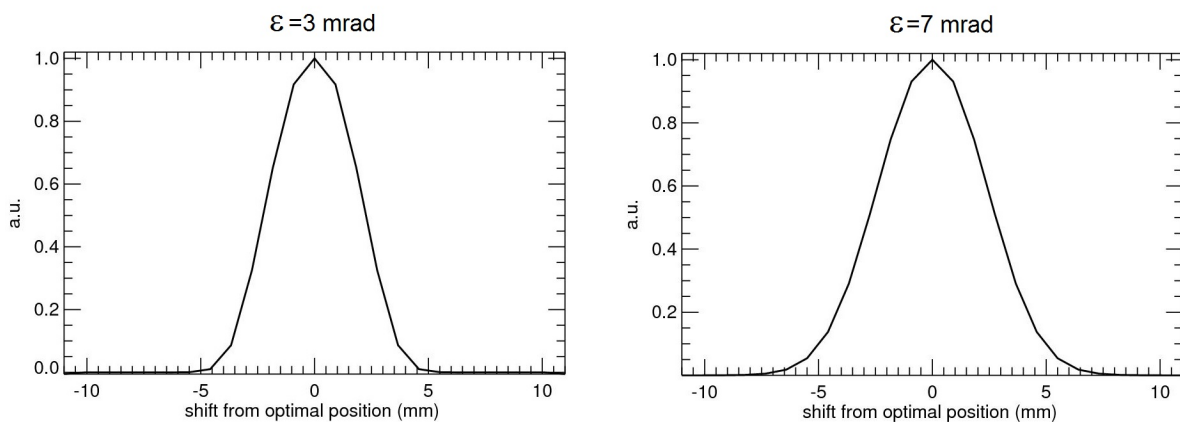

Figure 3.26: *Variation of the intensity of the Doppler peak obtained in SPIDER by translating an horizontal LOS vertically. In the plots on the left and on the right the divergence of the beamlets was set to 3 mrad and 7 mrad respectively. The intensity of the peak is normalized with respect to the maximum reached amplitude.*
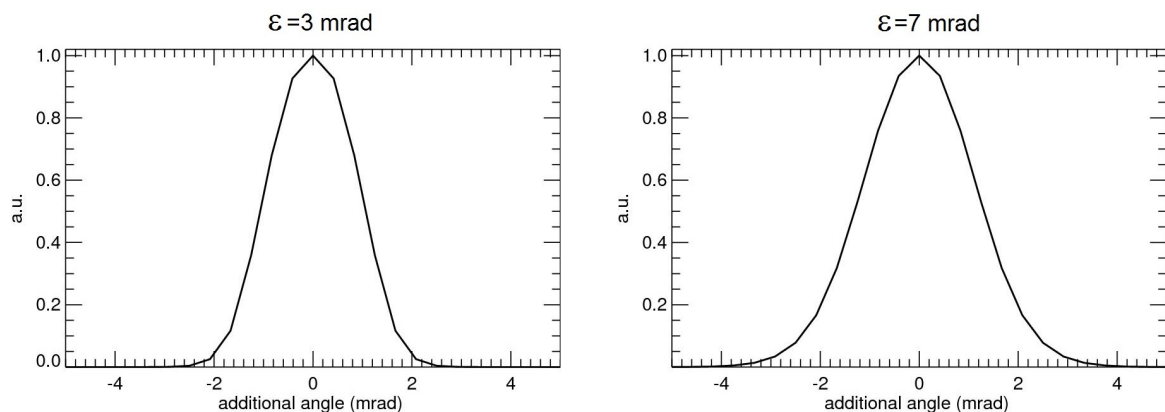

Figure 3.27: *Variation of the intensity of the Doppler peak obtained in SPIDER by rotating an horizontal LOS vertically. In the plots on the left and on the right the divergence of the beamlets was set to 3 mrad and 7 mrad respectively. The intensity of the peak is normalized with respect to the maximum reached amplitude.*

At last, dBES was used to simulate BES spectra corresponding to values of divergence within the range $3\,mrad \div 7\,mrad$. The Doppler peak of the simulated spectra was fitted with a Gaussian and the

measure of its width was used as described in par. 2.3.5 to get a measure of ϵ. The relative errors of the measures of divergence obtained by fitting the Doppler shift of the simulated spectra are shown in figure 3.28 (black line), as function of ϵ itself. The trend of the relative error is in agreement with that calculated by the model described in par. 2.3.7 (red dasched line). The measurement error of ϵ will be lower than 10% in all the interval of divergence foreseen in SPIDER, except for values close or equal to 3 *mrad*. The relative differences (blue dotted line) between the measured values of ϵ and the ones given in input to dBES are within the relative errors. The smooth trend of the blue line as function of ϵ indicates that a (small) systematic error is present in the measures of divergence and must therefore be corrected.

The same calculation of figure 3.28 was repeated assuming that 15% of the beamlets' current is given by the halo, with $\epsilon = 30$ *mrad* [21]. The analysis of the spectra simulated by dBES gave values of divergence substantially unaltered with respect to the previous case without halo.
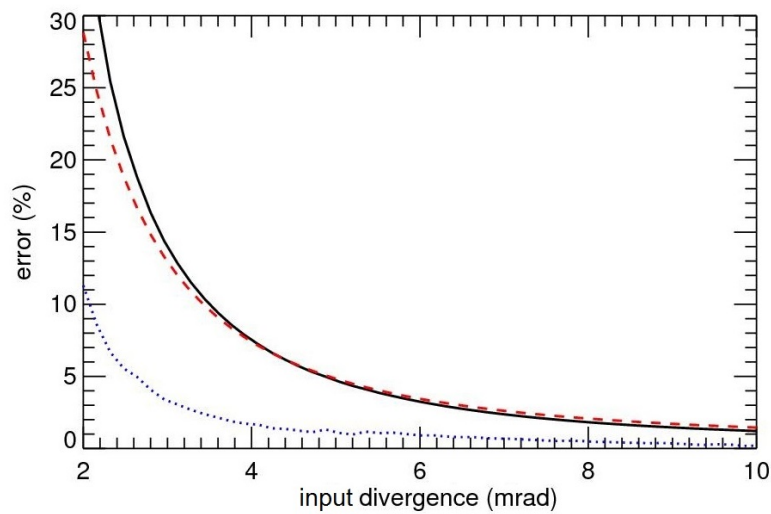

Figure 3.28: Relative error of the measurements of divergence (black solid line) in SPIDER as function of the value of ϵ given in input to dBES. The red dashed line indicates the relative error of ϵ calculated as in par. 2.3.5, while the blue dotted line represents the relative deviation of the measures of ϵ with respect to the input value used for the simulation.

3.2.3 Summary of the results

The tests carried out by means of dBES confirmed the design of the BES diagnostic for SPIDER, in particular with the new configuration of the optic heads (sec. 4.2 and 4.3). The analysis of the spectra generated by dBES confirmed that it is possible to measure the beamlets' divergence within the range 3 *mrad* $\div 7$ *mrad* with an error below 10%. At the same time, however, it must be kept into account that small deviations (up to ~ 15 *mrad*) of the beamlets' direction could broaden the Doppler peak causing an overestimation of ϵ. In SPIDER it is estimated [74] that the horizontal deflections of the beamlets could reach about ± 4 *mrad* because of the magnetic field produced by the EG.

About the measurements of beam uniformity, the precision required to align the optic heads with respect to the beamlets (offset and tilt less than respectively ± 1 *mm* and ± 0.5 *mrad*) is difficult to achieve, but other diagnostics (e.g. STRIKE) can support this task.

At last, the intensity of the BES spectra is so sensitive to possible misalignment of the optic heads (and to deviations of the beam) that, to keep the spectra at a sufficient SNR, it would be advisable to mount the optic heads on remotely adjustable supports. The optic heads will be indeed placed just outside the vacuum vessel of SPIDER, which will be inaccessible during the operation of the source

because of radiations.

3.3 Study and design of the BES diagnostic for MITICA

As for SPIDER, the target for the BES diagnostic is to measure the divergence of the beamlets and the beam uniformity according to the specifications listed in table 3.1 [75, 76]. The dBES code has been widely used to verify the conformity of the design of the diagnostic with the expected performances.

3.3.1 Design of the diagnostic

The BES diagnostic will monitor the beam in 3 sections [77, 75] of the test facility: between the GG and the neutralizer (section "GN"), between the neutralizer and the RID (section "NR") and between the RID and the calorimeter (section "RC"). The position of the 3 sections in MITICA is shown in figure 3.29. In the section GN the LOSs will be installed in 11 viewports: 4 on each vertical side, 2 on the top and one at the bottom. The viewports of the section NR (shown in figure 3.30, looking upstream) are 9: 3 on each vertical side, 2 on the top and 1 at the bottom. The section RC has 9 viewport, placed similarly to section NR.
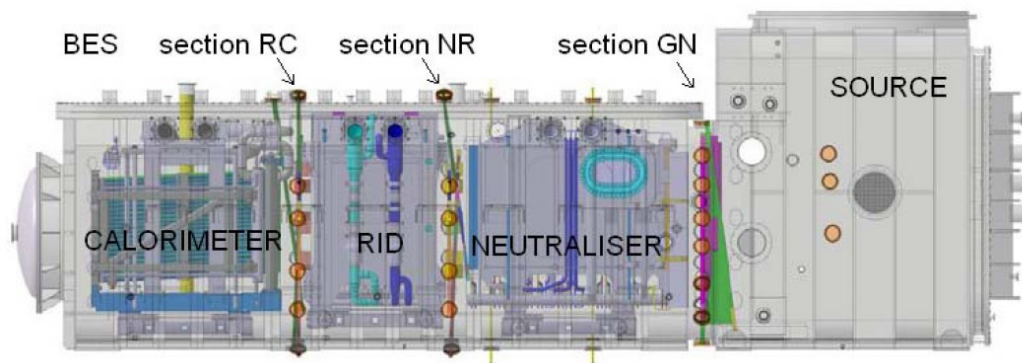

Figure 3.29: View of the sections of MITICA in which the optic heads of the BES diagnostic will be mounted [77, 75]. The direction of the LOSs is indicated, too.

For the simulations of dBES a LOS was virtually positioned at the center of each viewport. The LOSs were identified with codes similar to those used in SPIDER: the first 2 letters indicate the section (GN/NR/RC), it follows the orientation (O, horizontal, V vertical) and the side (SX left, DX right, A top, B bottom) on which the optic head is mounted; at last, a progressive number distinguishes the optic heads on the same side, from the bottom to the top and from left to right (looking upstream the beam). As example, the codes of the LOSs of the NR section are shown in figure [fig:NR]. The x ,y ,z coordinates (par. [sub:The-beamlets]) of the centers of the viewports and therefore of the LOSs are listed in table 3.4.
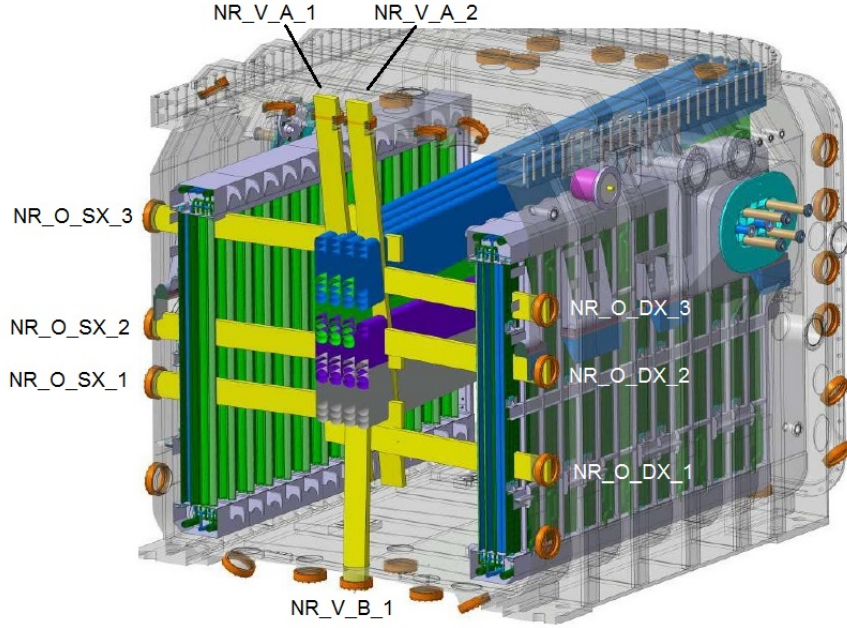
Figure 3.30: View of the section NR, looking upstream the beam. The direction of the LOSs is indicated with yellow parallelograms departing from the viewports. The codes used in dBES to indentify the LOSs are shown, too.

LOS name	x (mm)	y(mm)	z(mm)
GN_O_SX_1	1429	-1834	-995
GN_O_SX_2	1429	-1834	-540
GN_O_SX_3	1429	-1834	-95
GN_O_SX_4	1429	-1834	375
GN_V_A_1	1359	-200	1094
GN_V_A_2	1359	200	1094
GN_O_DX_1	1430	1834	-755
GN_O_DX_2	1430	1834	-345
GN_O_DX_3	1430	1834	155
GN_O_DX_4	1430	1834	585
GN_V_B_1	1430	0	-2219

LOS name	x (mm)	y(mm)	z(mm)	LOS name	x (mm)	y(mm)	z(mm)
NR_O_SX_1	5202	-1834	-930	RC_O_SX_1	7452	-1834	-930
NR_O_SX_2	5202	-1834	-465	RC_O_SX_2	7452	-1834	-465
NR_O_SX_3	5202	-1834	385	RC_O_SX_3	7452	-1834	385
NR_V_A_1	5305	-150	1438	RC_V_A_1	7446	-75	1438
NR_V_A_2	5305	150	1438	RC_V_A_2	7446	75	1438
NR_O_DX_1	5202	1834	-1125	RC_O_DX_1	7452	1834	-1125
NR_O_DX_2	5202	1834	-345	RC_O_DX_2	7452	1834	-345
NR_O_DX_3	5202	1834	-140	RC_O_DX_3	7452	1834	-140
NR_V_B_1	5163	0	-2296	RC_V_B_1	7512	0	-2296

Table 3.4: Coordinates (in mm) of the viewports' centers and therefore of the virtual optic heads set in the simulations of dBES for MITICA (courtesy of M. Tollin).

The parameters needed for the simulation of the BES diagnostic in MITICA are listed in table 3.5.

Quantity	value
ϵ (e-folding) foreseen	$3 \div 7\,mrad$
Observation angle α	85°
Total acceleration voltage ($V_0 \pm \sigma_{V_0}$)	$870\,kV \pm 1\%$ (H)
	$1\,MV \pm 1\%$ (D)
Voltage ripple ($\sigma_V \pm \Sigma_V$)	$44\,kV \pm 10\%$ (H)
	$50\,kV \pm 10\%$ (D)
Error of linewidth from gaussian fit (σ_G)	$0.2\,pix$
Diameter of fiber core	$400\,\mu m$
Plate factor of the spectrometer (d)	$6.7\,nm/pix$
Entrance slit width of the spectrometer (F)	$100\,\mu m$
Pixel size of CCD (p_{size})	$13\,\mu m$
Number of pixels in the CCD	1024x1024

Table 3.5: Information on SPIDER and the BES diagnostic required by dBES[75].

As in SPIDER, the initial design of the optic heads [75, 76] foresaw lenses with a focal length of $120\,mm$ and a clear aperture of $10\,mm$ diameter, imaging the fiber head at $3\,m$ from the lens. The tests on the prototype of the optic heads (described in sec. 4.2 and 4.3) led to increase the focal length to $150\,mm$ and reduce the clear aperture to $8\,mm$. In practice, the optic heads used in MITICA will be the same used SPIDER. The dependence of the solid angle of collection Ω on the axial and radial coordinates of the LOS is the same shown in figure 3.17). Preliminary runs of dBES for the LOSs of the section GN allowed to esteem that $\omega = 1.52\,mrad \pm 24\%$ for the vertical LOSs and $\omega = 1.64\,mrad \pm 23\%$ for the horizontal ones; these values change negligibly for the LOSs of the other sections.

Figure 3.31 shows the estimates of the measurement error of the divergence as function of the divergence itself and of the angle of observation α, using the model described in par. 2.3.7 and assuming that MITICA is operating with deuterium. The relative error of ϵ should exceed 10% for values of ϵ around $3 \div 4\,mrad$.
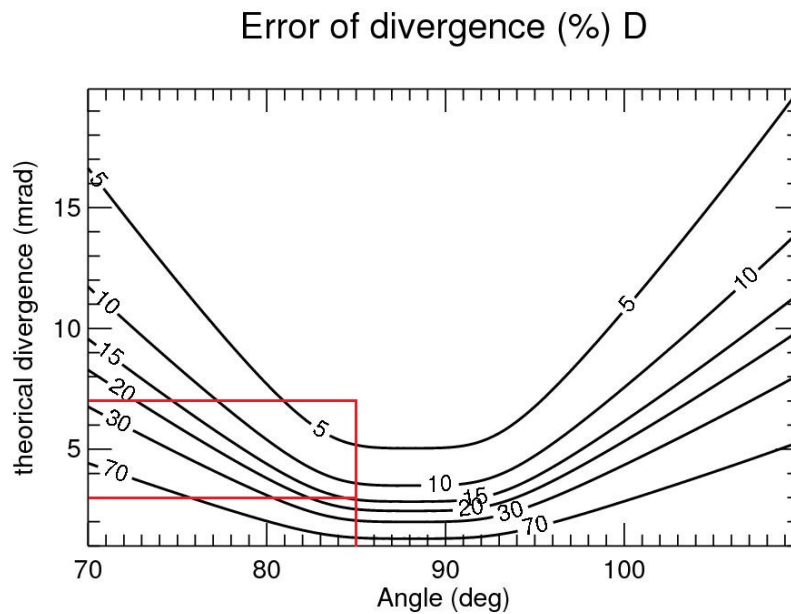

Figure 3.31: Measurement error of the divergence as function of the divergence itself and of the angle of observation, assuming that MITICA is working with deuterium. The red lines indicate the chosen angle of observation and the extreme values of divergence.

Figures 3.32, 3.33, 3.34 and 3.35 show how much the measurement error of ϵ is effectively sensitive to the angle of observation α and ω, the plate factor of the spectrometer, the total acceleration voltage and the voltage ripple. In all the cases it is assumed that $\epsilon = 5\,mrad$. It results that in agreement with the target of keeping the measurement error of ϵ below 10%:

- the diameter of the aperture of the lenses in the optic heads can be increased if necessary, but ω mustn't exceed 2 *mrad*;

- the plate factor should remain below 0.02 *nm/pix*;

- the total acceleration voltage and the voltage ripple are not critical parameters for the measurement of ϵ.

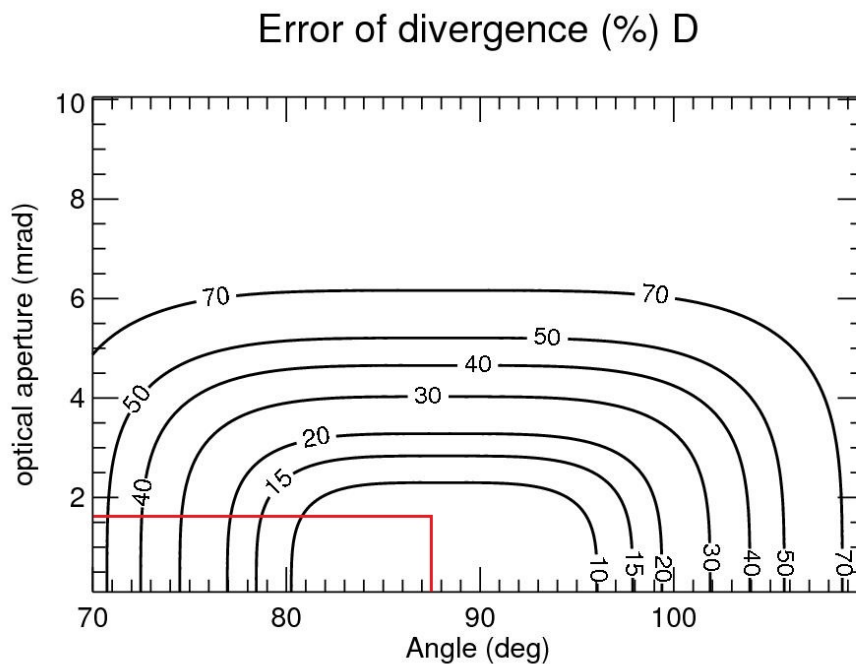The design of the diagnostic seems therefore to be robust and to reach the desired performances.

Figure 3.32: Dependence of the measurement error of the divergence on ω and on the angle of observation, assuming that $\epsilon = 5\,mrad$ and that SPIDER is working with deuterium. The red lines indicate the chosen values of α and ω.
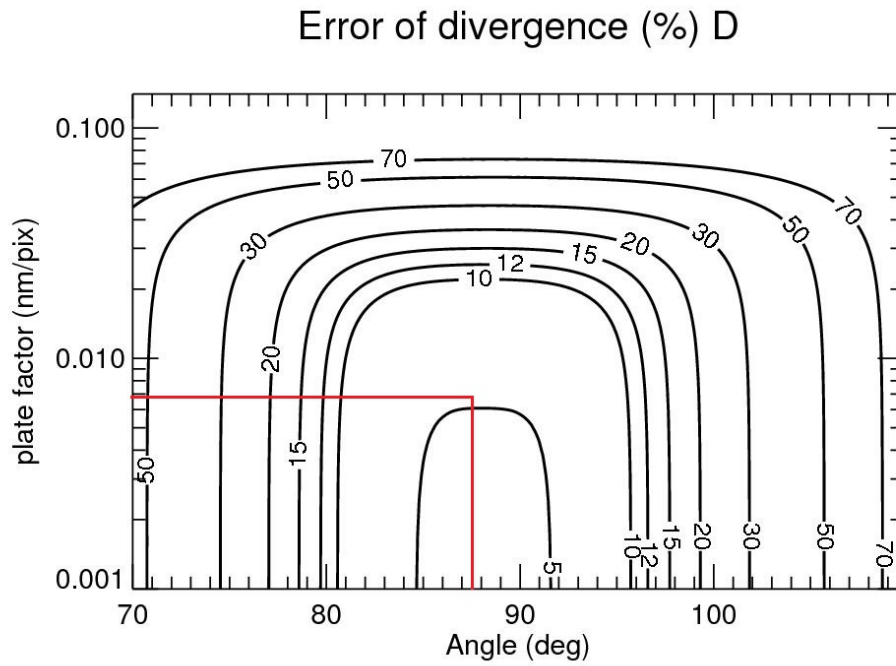
Figure 3.33: Precision of the divergence as function of the plate factor of the spectrometer and of the angle of observation, assuming that $\epsilon = 5\,mrad$ and that MITICA is working with deuterium. The red lines indicate the chosen values of α and d.
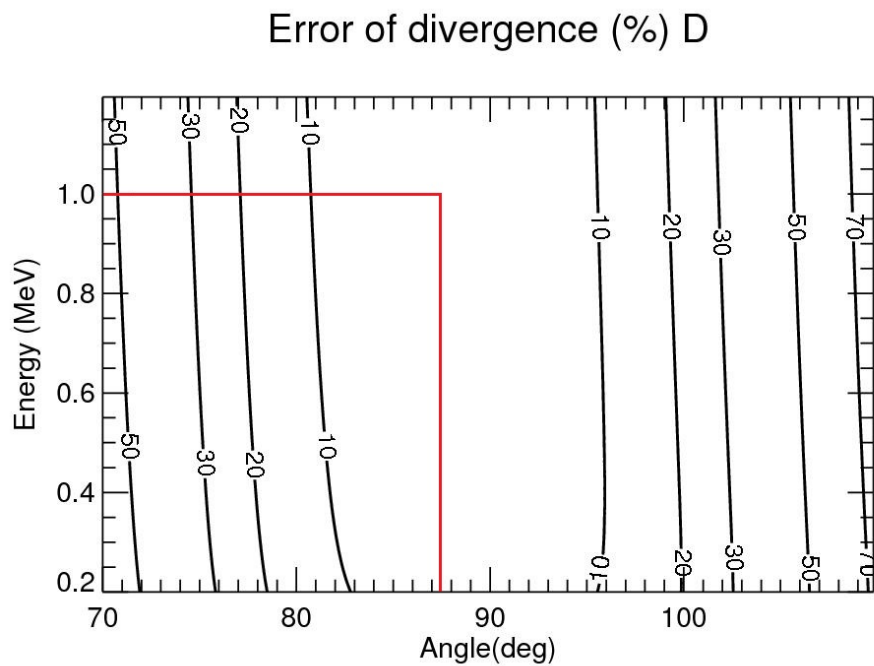

Figure 3.34: Measurement error of the divergence as function of the total acceleration voltage and of the angle of observation, assuming that $\epsilon = 5\,mrad$ and that MITICA is working with deuterium. The red lines indicate the foreseen values of α and total acceleration voltage.
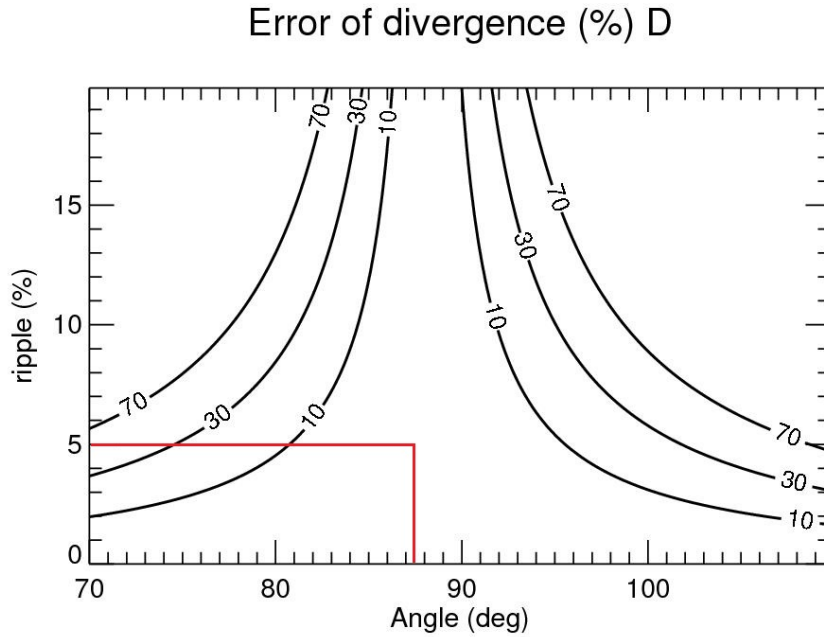
Error of divergence (%) D

Figure 3.35: Measurement error of the divergence as function of the voltage ripple and of the angle of observation, assuming that $\epsilon = 5$ mrad and that MITICA is working with deuterium. The red lines indicate the chosen value of α and and the foreseen level of voltage ripple.

3.3.2   Simulations

To better verify the design of the BES diagnostic in MITICA, the dBES code was used to simulate the spectra acquired by the diagnostic. In addition to the data presented in the previous paragraph, the gas density profile shown in figure 2.3 was adopted. Moreover, the energetic distribution of the stripping losses was calculated from the data shown in figure 3.36. The figure shows the fraction of the beam still not neutralized as function of the distance from the source-facing side of the PG; it is shown also the profile of the energy reached by the ions inside the acceleration stage, assuming that the electric field is constant between the grids and null inside their apertures.
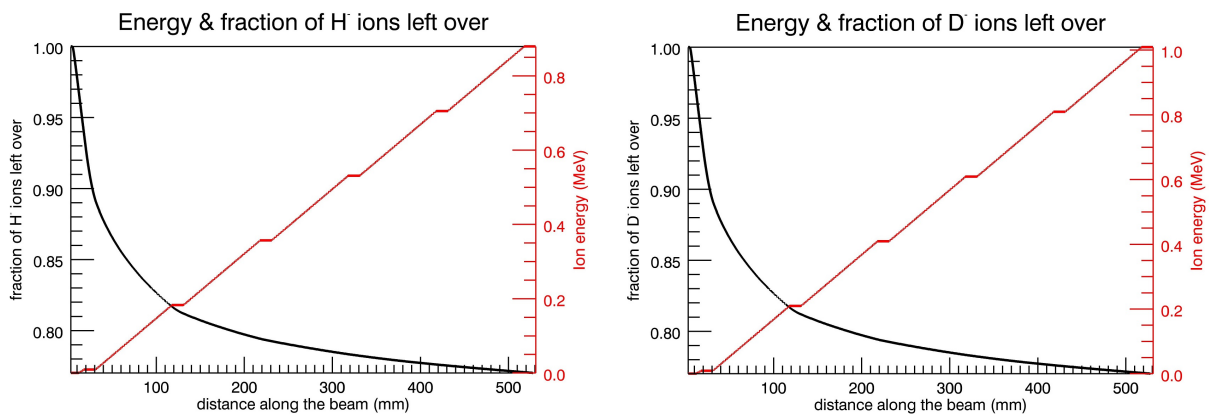

Figure 3.36: Fraction of not stripped ions within the acceleration system in MITICA, as function of the distance from the source-facing side of the PG [73]. For the same spatial coordinate the energy reached by the negative ions is shown. The two plots refers to operations in hydrogen and deuterium, respectively.

The optical losses of fibers and spectrometer were estimated to be the same as in SPIDER (65% in to-

tal); the quantum efficiency of the CCD was set at 80%, and the conversion factor given by amplification and sampling of the CCD was set to 0.4 *counts/e*. The minimum exposure time of the CCD was set to 150 *ms*.

Figure 3.37 shows the spectrum simulated by dBES for the horizontal LOS `GN_0_SX_2` and the vertical LOS `GN_V_A_1`, assuming that the beam is in deuterium. The appearance of the two spectra is quite different, because of the geometry of the beamlets adopted in MITICA (sec. 1.5). In the horizontal plane, the beamlets are not parallel but each one of the 20 columns of beamlets has a specific angle with respect to the beam axis; as consequence, in the BES spectrum there are 20 Doppler peaks, so overlapped to compose a unique wide peak. The angles in the horizontal plane between the beamlets and the beam axis range from $-15\,mrad$ to $15\,mrad$ [21]. In this condition anomalous deviations of the beamlets in the horizontal plane, estimated to be about $\pm3\,mrad$ [78], cannot be detected and would affect the width of the "comprehensive" Doppler peak negligibly. In the spectrum acquired from vertical LOSs instead 4 partially overlapped Doppler peaks are present: in the vertical plane, indeed, each row of beamlet groups forms a specific angle with respect to the beam axis [21]. The 4 Doppler peaks therefore correspond to 4 different beamlet groups, which can be monitored separately. The vertical fluctuations of the directions of the beamlets are negligible [78].
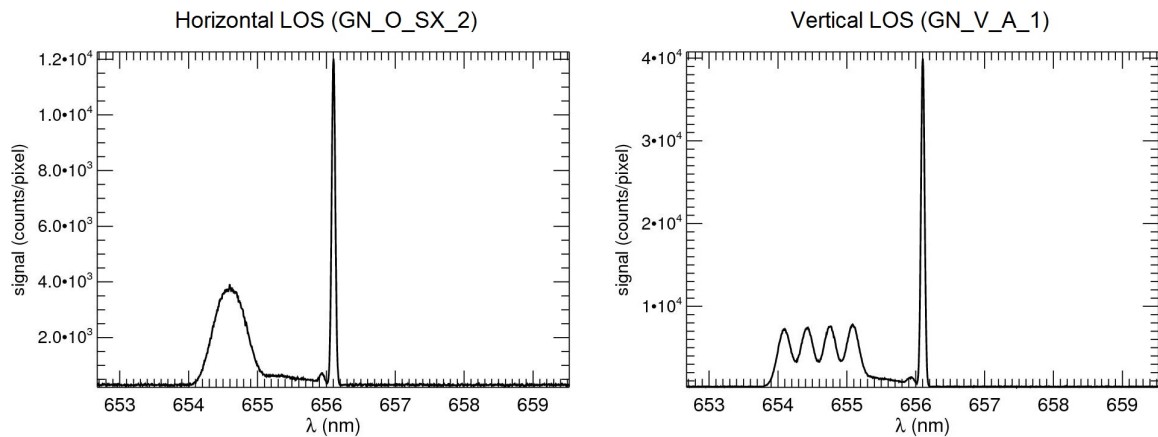

Figure 3.37: Spectra simulated by dBES for the horizontal LOS `GN_0_SX_2` *and the vertical LOS* `GN_V_A_1`, *assuming that the source is operating with deuterium and that* $t_{exp} = 150\,ms$.

The LOSs considered in figure 3.37 belong to the section `GN`, which is the closest to the GG. At the farther section the beamlets will be broader and then less dense, with a consequent reduction of the intensity of the spectra. Moreover, the LOSs at the RC section receive even less light because part of the beam particles was removed upstream by the RID. Figure 3.38 shows the spectra simulated by dBES for the horizontal LOSs `NR_0_SX_2` and `RC_0_SX_2`.

As mentioned in sec. 2.2 the speed of the beam particles in MITICA is so high that the distance covered by an excited particle during the de-excitation time is not negligible. The longest decay length is reached when the beam is composed by hydrogen particles at $870\,keV$. Taking into account the decay time of the excited particles (i.e. using formula 2.38 instead of 2.37), it resulted that the intensity of a horizontal LOS of the section `GN` is 10% higher than what obtained by dBES with the standard calculations. Analogously, the spectra of horizontal LOSs in the sections `NR` and `RC` result to be 66% and 50%

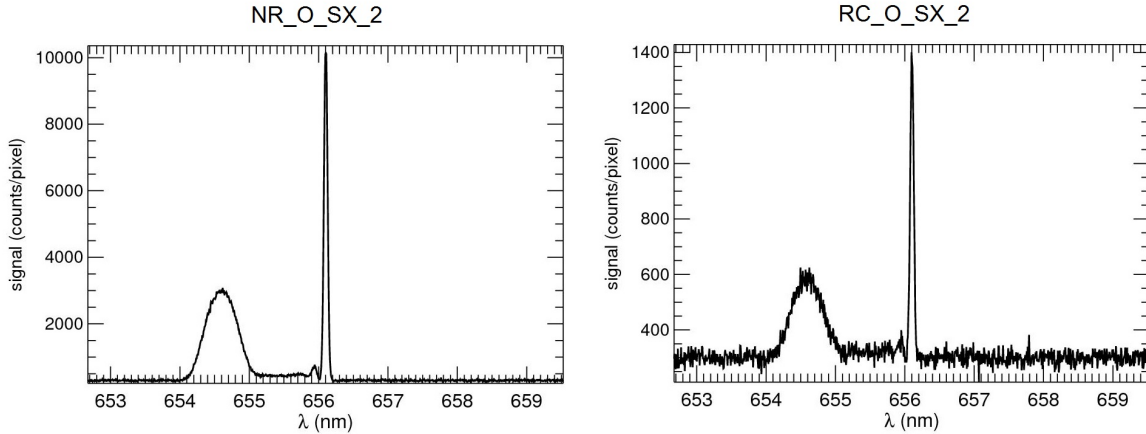higher. The effect of the finite de-excitation time on the intensity of the spectra is then not negligible.

Figure 3.38: Spectra simulated by dBES for the LOSs `NR_O_SX_2` and `RC_O_SX_2`, assuming $t_{exp} = 150\,ms$ and that the beam is in deuterium.

The target of measuring the beam uniformity with an error below 10% imposes to align the LOSs with respect to the beamlets with a certain precision. By means of dBES the spectrum of an horizontal LOS was simulated for slightly different vertical positions of the optic head. A LOS of the `GN` section was chosen because it gives the most restrictive limits: the `GN` section is the closest to the GG, therefore the beamlets are smaller and it's more difficult to intercept them. Figure 3.39 shows how the intensity of the Doppler peak (normalized with respect to the maximum achievable amplitude) and therefore its integral vary with the vertical offset, assuming $\epsilon = 3\,mrad$ and $\epsilon = 7\,mrad$ respectively for the 2 plots. A fall of 10% in the intensity of the peak can be obtained by an offset of about $\pm1.5\,mm$ and $\pm3\,mm$ respectively for the cases at $\epsilon = 3\,mrad$ and $\epsilon = 7\,mrad$. The considered LOS intercepts the beamlets at an average distance from the GG of 1.3 m, therefore the effects of a shift of the LOS of $\pm1.5\,mm$ can be due also to a deviation of the beamlets of $\pm1.2\,mrad$.

Figure 3.40 shows how much the amplitude of the Doppler peak can vary if the optic head is tilted vertically: in the cases with $\epsilon = 3\,mrad$ and $\epsilon = 7\,mrad$ the maximum allowed tilt is about $\pm0.8\,mrad$ and $\pm1.7\,mrad$ respectively.

Figure 3.39: Variation of the intensity of the Doppler peak in the spectrum of LOS `GN_O_SX_2` when the optic head is translated vertically. In the plots on the left and on the right the divergence of the beamlets was set to 3 mrad and 7 mrad respectively. The intensity of the peak is normalized with respect to the maximum reached amplitude.
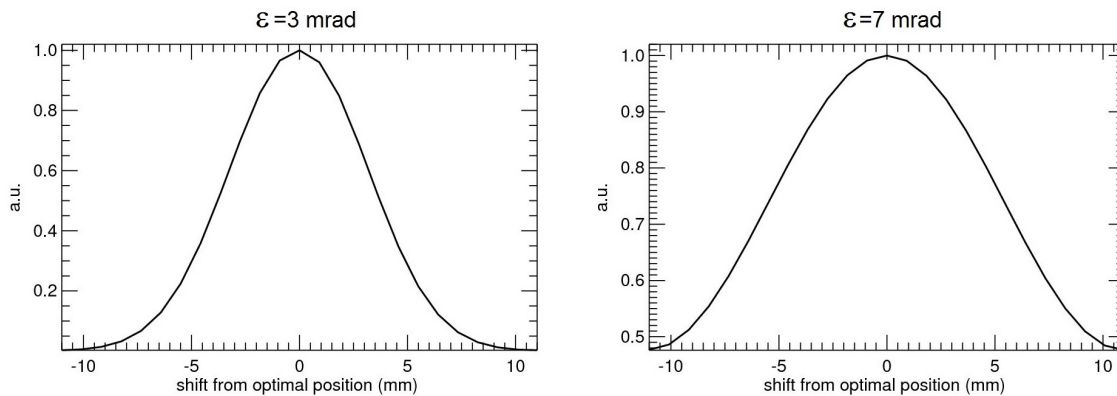
Figure 3.40: Variation of the intensity of the Doppler peak in the spectrum of LOS `GN_0_SX_2` when the optic head is translated vertically. In the plots on the left and on the right the divergence of the beamlets was set to 3 mrad and7 mrad respectively. The intensity of the peak is normalized with respect to the maximum reached amplitude.
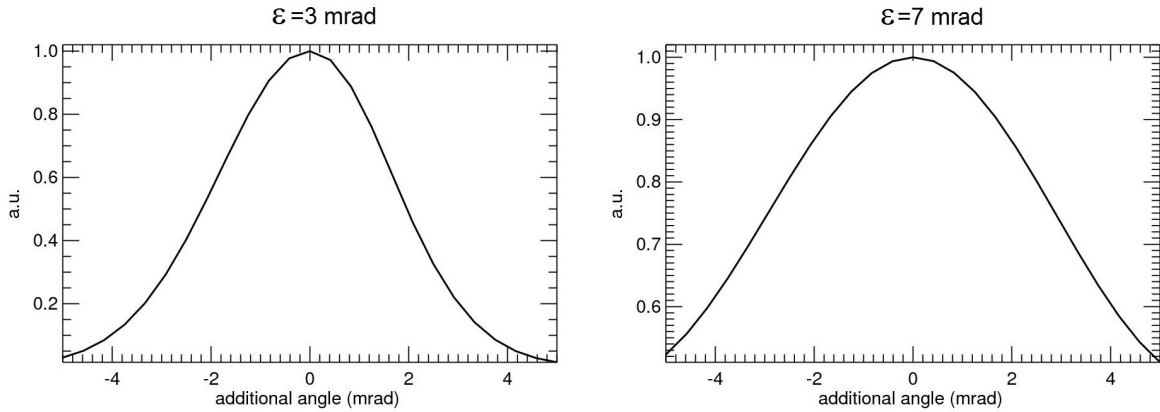
To test the effective precision with which the beamlets' divergence can be measured dBES was used to simulate BES spectra for ϵ between 3 *mrad* and 7 *mrad*. The analysis method is different for the spectra of horizontal and vertical LOSs. In the case of the horizontal LOSs a Gaussian fit is applied to the Doppler peak to establish the angle α between the LOS and the beam. α is added to the 20 angles[7] the beamlets form with the beam main direction The Doppler peak is then fitted with the sum of 20 Gaussians, all with the same amplitude and the same width, and whose centroids are given by the previously calculated angles. From the width of the 20 Gaussians the average divergence of the observed beamlets can be calculated. Figure 3.41 shows the measurement error (black line) of divergence as function of the value of ϵ given in input to dBES to simulate the analyzed spectrum. For $\epsilon \geq 3$ *mrad* the relative errors from the measurements follow the trend (red dashed line) foreseen by the model of par. 2.3.7. The relative differences between the measured values of divergence and the ones given in input to dBES are in some cases higher than the relative error; this is probably due to the complexity of the fit applied to the Doppler peak.

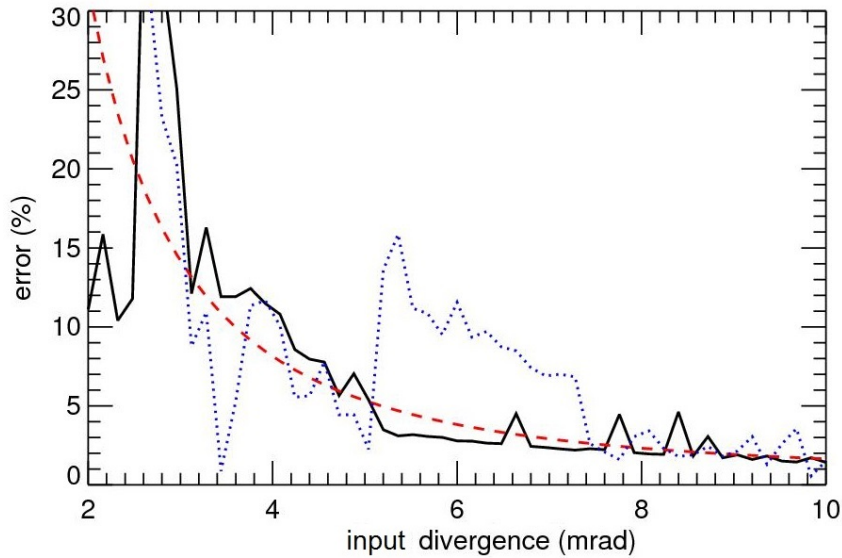[7]It is not possible to measure these angles, therefore the values foreseen in the design [21] of MITICA are adopted.

Figure 3.41: Relative error of the measurements of divergence (black solid line) in MITICA for horizontal LOS, as function of the value of ϵ given in input to dBES. The red dashed line indicates the relative error of ϵ calculated as in par. 2.3.5, while the blue dotted line represents the relative deviation of the measures of ϵ with respect to the input value used for the simulation.
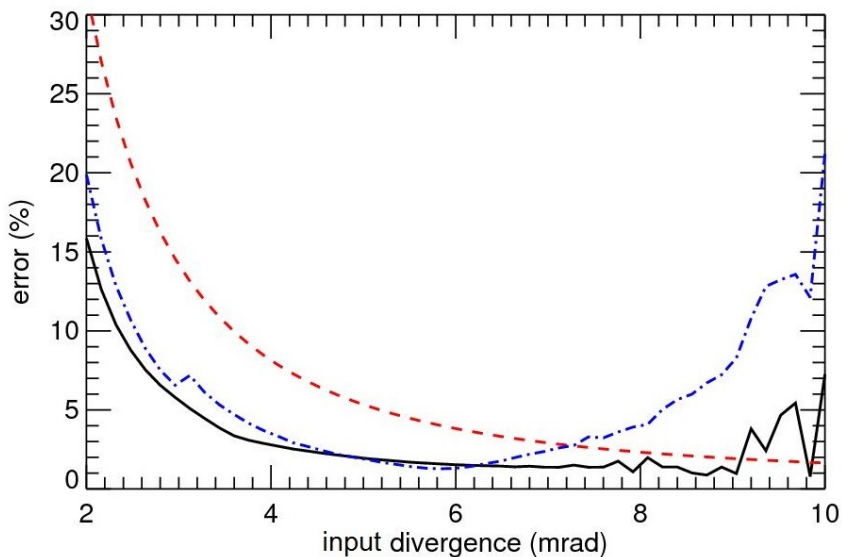

Figure 3.42: Average of the relative errors of the measurements of divergence (black solid line) obtained by the 4 Doppler peaks in the spectra of a vertical LOS in MITICA. The relative errors are shown as function of the value of ϵ given in input to dBES. The red dashed line indicates the relative error of ϵ calculated as in par. 2.3.5, while the blue dash-dot line represents the maximum relative deviation among the measures of ϵ, with respect to the input value used for the simulation.

In the case of the vertical LOSs 4 Doppler peaks are present in the BES spectra, even if partially overlapped. The curve of the spectrum is fitted with the sum of 4 Gaussians, so that it is possible to measure the integral and the width of each one separately. Figure 3.42 shows the relative error of these measurements of divergence (the black line indicates the average of the 4 relative errors of each spectrum) in comparison to the values foreseen by the model of par. 2.3.7. (red dashed line). The measurement errors of ϵ are lower than expected because the error of the fit in the estimation of the

widths of the 4 peaks is lower than the value of σ_G used in the calculation of the red curve. Figure 3.42 shows also the relative difference (blue curve) between the measured values of ϵ and those given in input to dBES. For precision, the blue curve indicates the maximum relative deviation (in modulus) of the 4 obtained by the fit. For $\epsilon > 7\ mrad$ the measured values of divergence are not compatible with the input values of ϵ. With the increase of the divergence, indeed, the 4 Doppler peaks broaden more and more, increasing the overlapping of the peaks themselves and therefore compromising the stability of the fit.

To check the influence of the beamlets' halo on the measurements of ϵ, the spectra of both horizontal and vertical LOSs were simulated assuming as worst scenario [21] that the halo is the 15% of the beam and has a divergence of 30 $mrad$. The measurements of divergence were not significantly affected.

3.3.3   Summary of the results

The simulations of dBES confirmed that with the current design of the diagnostic and the updated configuration of the optic heads it will be possible to measure the beamlets' divergence in the foreseen interval 3 $mrad \div 7\ mrad$ with an error below 10%. Particular attention must be paid to the stability of the fit algorithm. Possible deviations of the beamlets in the horizontal plane, foreseen in the order of $\pm 3\ mrad$ [78], shouldn't affect the shape of the Doppler peak neither the consequent measures of divergence. This is due to the particular shape of the Doppler peak in the spectra of the horizontal LOS, which is already broadened because of the 20 different directions of the observed beamlets with respect to the beam axis.

As in SPIDER, it is not feasible to align the LOSs with the beamlets with such a precision to avoid systematic errors larger than 10% in the measures of uniformity. This is at least what was determined from the LOSs of the section GN. The farther LOSs give less stringent conditions on the alignment of the optic heads, but the effective spatial resolution of the diagnostic is reduced because of the overlapping of the beamlets.

At last, to counteract excessive misalignments of the beamlets with respect to the LOSs it would be preferable to mount the optic heads on remotely adjustable supports. As in SPIDER, indeed, the optic heads won't be accessible during the operation of the test facility.

Chapter 4

Experimental activities

A number of experimental activities were carried out to test or design the instrumentation for the OES and BES diagnostics in NIO1, SPIDER and MITICA. Most of them was focused on the CCD camera for the BES diagnostic and on the optic heads (sec. 4.2) for both OES and BES.

4.1   The camera for the BES diagnostics

A possible candidate as detector of the BES spectra in NIO1, SPIDER and MITICA is the CCD camera *Andor iKon-M 934*. The main features of this instrument are summarized in table 4.1.

Number of pixels	1024x1024
Pixel size	13 μm
Pixel readout rates	0.05, 1, 3, 5 MHz
Digitization	16 bit
Vertical clock speed	5.7, 11.3, 22.5, 44.9, 67.3 μs
QE @ H$_\alpha$	95%
Gain	1x, 2x, 4x
Full well capacity	100 ke
Readout noise	2.9e, 6.6e, 11.6e, 18e at respectively 0.05, 1, 3, 5 MHz
Min. temperature	-70°C (air cooling), -100°C (water cooling),
Binning options	no binning, full vertical binning (FVB), multitrack (definable by the user)
Acquisition modes	single scan, accumulation (sum), kinetic, fast kinetic kinetic (sequence of single scans), fast kinetic (frame transfer)
Connections	USB, I^{2}C, Fire and shutter signals (CMOS output on SMB/B), ext. trigger signal (CMOS/TTL input on SMB/B)
Other characteristics	The CCD is backilluminated. Shutter's times to open/close are separately selectable.

Table 4.1: Main features of the camera Andor iKon-M 934.

Since the camera has to reach a given time resolution, the first tests done aimed to verify its readout time. The parameters that influence it are:

- the ADC readout rate, the time needed to convert the charge collected by a single pixel into digital counts;

109

- the vertical shift time, i.e. the time it takes for the charge to be transferred to the nearest row while moving towards the exit register;

- the readout pattern, i.e. the scheme with which the charge collected by adjacent pixels must be summed together before being read. In spectroscopy the vertical dimension of the collected spectra carries no useful information, so their pixels can be added together. In particular, 9 spectra will have to be simultaneously acquired from the spectrometer dedicated to BES in NIO1 (sec. 3.1); in the BES diagnostics of SPIDER and MITICA up to 20 spectra will have to be acquired by each CCD camera [72, 79] .

The readout time was measured varying the ADC readout rate and the vertical shift time; the CCD sensible area was vertically binned into multiple (10/20) tracks, adjacent or separated by some rows of pixels. It resulted that vertical binning greatly improves the time resolution of the camera, reaching less than 20 ms for reading 20 tracks of 1024 pixels (at ADC readout rates $\geq 3\,MHz$ and vertical shift time 5.7 μs). The readout time is lower if no pixels are left between each track; at last, doubling the number of tracks from 10 to 20 does not increase the readout time for more than 10 ms.

The camera mustn't be only fast enough for the diagnostic, but has also to be reliable in measuring the image received by the spectrometer. In fact, a too strong reduction of the row shift time may affect the efficiency in the charge transfer resulting in data smearing and loss of linearity. To test the presence of smearing effects, the camera was coupled to a CINEL 780/0.5 spectrometer (dedicated to the BES diagnostic in NIO1), illuminated by a mercury lamp. No evident increase in the smearing has been noticed lowering the rowshift time down to 5.68 μs. The shutter operations may also produce smearing effects: it was noticed that the acquired mercury spectra were smeared, unless the time $t_{shutter}$ left to the shutter to open or close, weren't above a certain value $t_{threshold}$. It was verified that this $t_{threshold}$ depends on the readout rate and slightly on the exposure time t_{exp}. To explain this, it must be considered that each shutter has two intrinsic characteristic times, the time to open t_o and the time to close t_c, only roughly known. In programming the functioning of the CCD shutter two parameters have to be selected, that play the role of t_o and t_c: the time t_{open} between the start of the opening of the shutter and the beginning of t_{exp}, and the time t_{close} between the start of the shutter closing and the beginning of the readout operation. Since these two parameters can be chosen different from t_o and t_c , unwanted effects may result. If, for example, t_{close} were lower than t_c, then the CCD would be still partially illuminated during the readout. The smearing of the image is then greater for quicker readings[1], as with higher readout rates.

The fact that the camera is collecting light during the shutter opening and closing, may affect the linearity test, since the amount of light received does not only depend on t_{exp}. In addition, if t_{open} is lower than t_o, then part of t_{exp} would be used to complete the opening process. But also if t_{open} exceeds t_o then part of t_{open} would contribute to t_{exp} (once the shutter is open, all the time that follows contributes to the charge collection). For this reason a linearity test represents a method for measuring t_o and t_c. A set of measurements was performed, monitoring the a spectral line of Cd at $t_{exp} = 2\,ms$, frame rate 3 MHz, vertical shift time 11,3 μs, $t_{close} = 50\,ms$ and increasing values of t_{open}. The total counts of the line grow linearly with t_{open} only if $t_{open} \geq 60\,ms$. This limit represents a measure of the shutter opening time t_o.

A lower limit should exist for t_{close} as well as for t_{open}. In this case the integral of the same spectral line was measured for increasing values of t_{close} , leaving t_{open} at 50 ms and the other acquisition options unchanged. The integral saturated at $t_{close} = 50\,ms$, this is therefore the time t_c required by the shutter to close.

---

[1]The smaller the readout time, the higher the fraction of the readout time itself in which the unwanted illumination is present.

Another important parameter that was tested is the readout noise; this quantity is usually expressed in electrons, so a conversion coefficient k between counts and electrons must be used. k is useful also for dBES to determine the intensity of the BES spectra acquired by the camera. The technique to measure k consists in taking acquisitions at different intensities of a uniform light source, from total darkness to saturation, without varying the exposure time. This was achieved exposing the camera to the light of the room and covering the entrance hole with a paper diffuser and a variable number of objects which absorb light (opaque plastic, paper or plastic sheets,etc). The standard acquisition parameters were: readout rate 3 MHz, vertical shift time 11 μs, temperature $-60°C$, $t_{exp} = 0\,ms$, $t_{open} = t_{close} = 50\,ms$. Figure 4.1 shows one of this acquisitions; the corners of the image are darker because they remained covered by the shutter for a longer time.

Figure 4.1: Example of acquisition of a uniform illumination field, $t_{exp} = 0\,ms$, $t_{open} = t_{close} = 50\,ms$.

Fixed pattern noise is also present, it's recognizable as a series of oblique bands. Since the calculation of k is based on the measurement of the shot noise, this other type of noise must be eliminated. For this purpose two images were acquired for each level of illumination, and the difference between them was computed. The variance of the signal was calculated over a 100x100 pix area[2] in the most illuminated point of the CCD; the variance was divided by 2 since it was computed on the subtraction of two images. Let's define η the number of collected electrons; it's easy to understand that the variance is proportional to $\left(k\sqrt{\eta}\right)^2 = k^2\eta$, whereas the signal level is proportional to $k\eta$. To get k it is sufficient to plot the variance against the average of the signal (always in the selected area) and calculate the slope of the linear trend. This was done for each of the 3 available amplification levels (1x,2x,4x) The measured values of k are reported in table 4.2; their ratios give the effective values of gain, shown in the same table.

Amplification (declared)	k (counts/e)	real gain (respect to 1x)
1x	0.207±0.001	(1)
2x	0.411±0.003	1.99±0.02
4x	0.851±0.007	4.11±0.04

Table 4.2: The value of the conversion factor k between counts and electrons, for different levels of amplification. The real amplifications calculated on the values of k are reported, too.

---

[2]The chosen dimensions of this area were the largest possible to have a flat signal profile.

The readout noise of the CCD camera was then measured as the standard deviation of a not illuminated image. Table 4.3 shows the measured values of noise (converted in electrons thanks to the values of table 4.2) as function of the readout rate and the gain factor. The levels of noise are higher than those declared by the producer (table 4.1) and are just compatible with the specifications requested by the BES diagnostic (noise $\leq 10e$ at $1\ MHz$ readout frequency [72]). As expected, the noise increases with the readout frequency, but unexpectedly it falls with the gain; this latter dependency might be caused by the additional noise induced by the amplification stage.

Readout	noise (st. dev., electrons)		
rate (*MHz*)	amp. 1x	amp. 2x	amp. 4x
0.05	4.7	3.6	3.2
1	10.5	7.6	6.8
3	17.3	12.1	11
5	26.6	17.0	14.4

Table 4.3: Dependence of the background noise on the amplification level. The CCD was at $-60°C$, with vertical shift time $11,3\ \mu s$; the standard deviation was calculated on an area of 1024x1024 pixels.

At last, a rough estimate of the dark current was obtained: for this purpose the mean value of a bias frame[3] was subtracted to the average of a long ($t_{exp} = 2000\ s$) acquisition with the shutter closed; the result was then divided by t_{exp}. The obtained values of dark current are so low that they don't represent a concern for acquisitions with the typical exposure times required by BES.

4.2   The optic heads for the OES and BES diagnostics

As already mentioned in par. 2.3.2, a BES optic head (figure 4.2) consists of a lens installed in a cylindrical support and a fiber holder which keeps the optical fiber on axis with the support and at the right distance from the lens. Two different types of fiber holders were designed and built: one with 2 cylindrical stoppers, one of rubber and one of plastic, through which the fiber passes (fiber holder in figure 4.2, case A), and one with a side lid which compresses a piece of rubber on the central fiber (same figure, case B). The axial position of the fiber holder can be adjusted by means of a sliding screw to vary the distance lens-fiber input. The optic head indeed must be focused at a proper distance so that the lens creates an image of the fiber head beyond the furthest emitting position, along the LOS[4]. The variables which characterize this optical system are: the clear aperture C_a and the focal length f of the lens, the distance lens-fiber P and the diameter d_{fib} ($400\ \mu m$) of the fiber core.

The choice of the values of these variables is limited by some constraints:

- the $F/\# = f/C_a$ filling the fiber should be compatible with the fiber NA and with the spectrometer $F/\#$;

- a too high $F/\#$ limits the collected light resulting in a low SNR;

- a too high C_a could spoil the spatial resolution of the measurements; in the case of BES, excessive values of the clear aperture would have a detrimental effect on the precision of the divergence measurements;

- the positioning of the fiber from the lens should not be critical, so that it's possible to easily adjust the position of the sliding screw;

---

[3]A bias frame is an acquisition with the shutter permanently closed and $t_{exp} = 0\ s$.

[4]It was chosen that the image of the fiber must be formed at $3\ m$ (SPIDER/MITICA) / $55\ cm$ (NIO1) from the lens (sec. 3.1 and 3.2)

- the external diameter of the cylindrical support should not exceed the minimum distance between LOSs [71, 25, 79]on the same window.

- In the case of the OES diagnostics for SPIDER/MITICA, the LOSs look at the plasma through holes of 6 or 10 *mm* diameter [24, 25], drilled on the source case; the LOSs of OES in NIO1 instead must pass through pipes of 8 or 12 *mm* diameter. In both cases the diameter of the LOSs must be limited to avoid vignetting.

The initial design of the OES and BES diagnostics [25, 72] led to the adoption of lenses with diameter 15 *mm*, $f = 120$ *mm* and $C_a = 10$ *mm*. For the OES and BES diagnostics in NIO1 a lens of diameter 10 *mm*, $f = 50$ *mm* and $C_a = 4mm$ was chosen.
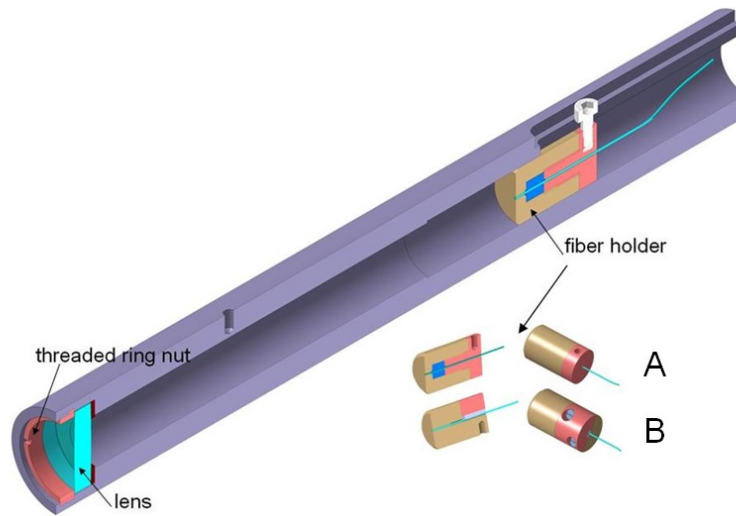

Figure 4.2: *Schematic view of a telescope. Two alternative designs of the fiber holder are shown.*

4.2.1 Tests

To validate the optical configurations with the two types of lenses, two prototype telescopes were realized, with 194 *mm* length, 25 *mm* diameter and 95 *mm* length, 20 *mm* diameter, respectively. To test different values of C_a thin rings with internal diameters of 4,6,8,10 *mm* were built; these rings could be inserted next to the lens to reduce its aperture. Lenses of different type and slightly different focal length (table 4.4) were tested, too.

	Type	f (*mm*)
	Plano-convex	120
SPIDER/MITICA	Achromatic doublet	120
	Plano-convex	150
NIO1	Achromatic doublet	40
	Plano-convex	50

Table 4.4: Characteristics of the lenses tested with the prototype supports.

The telescopes were mounted trying both types of fiber holder; the one with the side lid was chosen as default design because it was easier to mount the fiber and because this was kept fixed more stably. The following tests were aimed to studying the width of the LOS along its axis, when a certain lens is used and the image plane is set to the established distance. To do this a short fiber of 400 μm diameter was connected to the fiber holder on one side and illuminated by a lamp on the other. Through trial and

error, the fiber holder was fixed in the right position to have the image of the head of the fiber at $3\,m$ (SPIDER/MITICA) or $55\,cm$ (NIO1) from the lens. At this point a screen made of graph paper was placed at various intermediate distances from the lens to measure the width of the light spot (corresponding to the width of the LOS).

As expected it resulted that in the case of NIO1 the LOSs determined by the lens with $f = 50\,mm$ are narrower than those with $f = 40\,mm$. The former lens therefore seems more suitable to pass through the $10\,mm$ apertures of OES. Analogously the $f = 150\,mm$ lenses for SPIDER/MITICA should be preferred over the ones with $f = 120\,mm$. From the data it resulted also clear that there is no significant benefit in using a doublet instead of a simpler and cheaper plano-convex lens.

4.2.2 Simulation of the LOSs

The width measurements of the LOSs were used not only to properly select the lenses to mount for OES and BES, but also to benchmark the algorithm of dBES calculating the shape of the LOS (par. 2.3.2). The case shown in figure 4.3 is the result of a simulation for $f = 40\,mm$, $C_a = 6\,mm$ and the image plane at $550\,mm$ from the lens: the solid angle Ω has not a flat radial profile over the section of the LOS. The irregularities of the profile at the distance $567\,mm$ are due to the fact that when the analyzed plane[5] and the image plane are too close the effects of the discretization are not negligible.
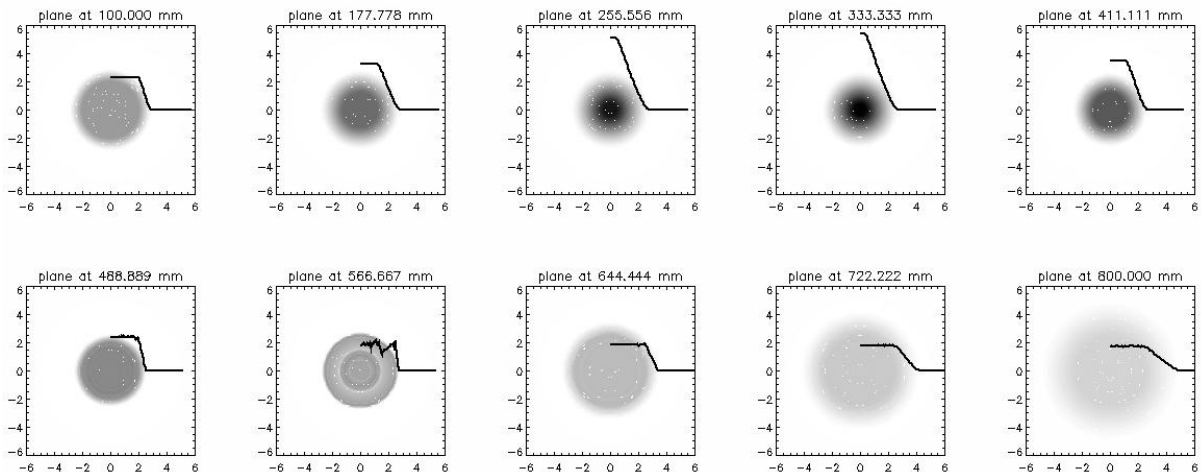

Figure 4.3: 2D and radial profile of the solid angle of collection for planes at various distances from the lens ($f = 40\,mm$, $C_a = 6\,mm$, image plane is at $550\,mm$).

The setup simulated by the code was reproduced in laboratory, and the width of the LOS was measured detecting the edge of the light spot by eyes at different distances from the lens. These measurements could be compared to the simulations, being the intensity of the LOS sections proportional to Ω. Since the eye sensibility was not known a priori, the code calculated the spot dimension for different threshold levels. This method was preliminarily applied to a case of a lens with $f = 40\,mm$, $C_a = 6\,mm$; the results are shown in figure 4.4.

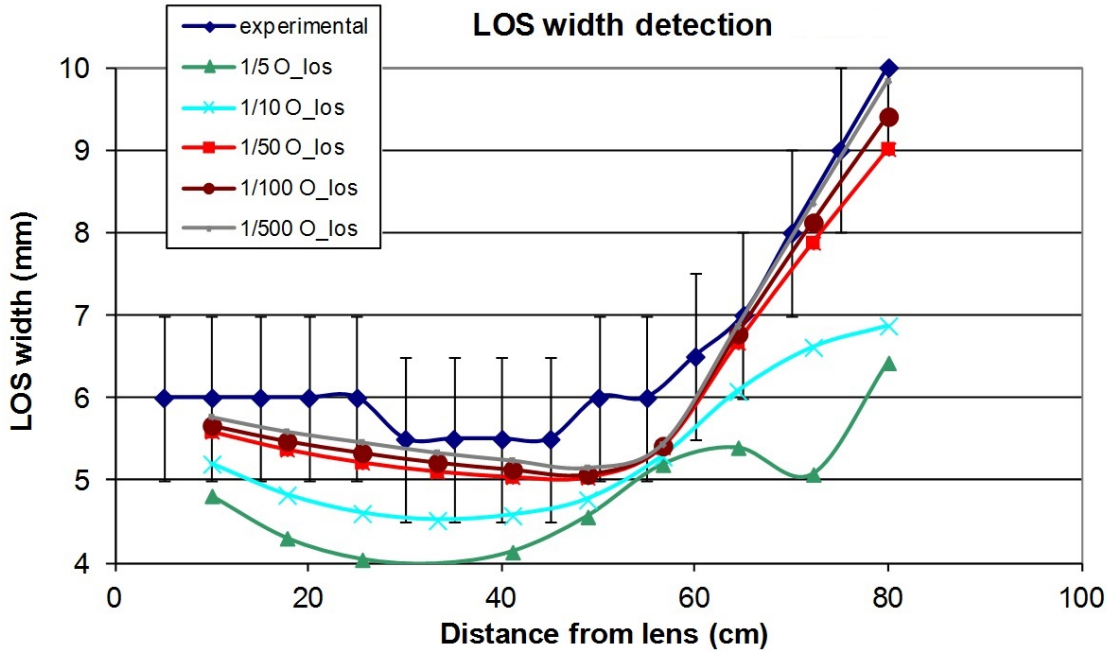[5]the plane at distance p in figure 2.2.

Figure 4.4: Estimations of the LOS width along the optical axis for different values of threshold of the solid angle. The experimental width of the LOS is drawn (blue) for comparison. The case is referred to a lens with $f = 40\,mm$, $C_a = 6\,mm$, image plane at $55\,cm$.

The best agreement with the experimental data was reached with $1/500$ of the maximum value of Ω reached in the LOS. The largest differences between the curves are found substantially in the intermediate position between the lens and the image plane, where the radial profile of solid angle has the lowest slope.

Once having chosen the threshold of $\Omega_{los}/500$ as edge of the LOS, the simulations were performed also for the other optical configurations. The comparison between experimental data and simulations is shown in figure 4.5.
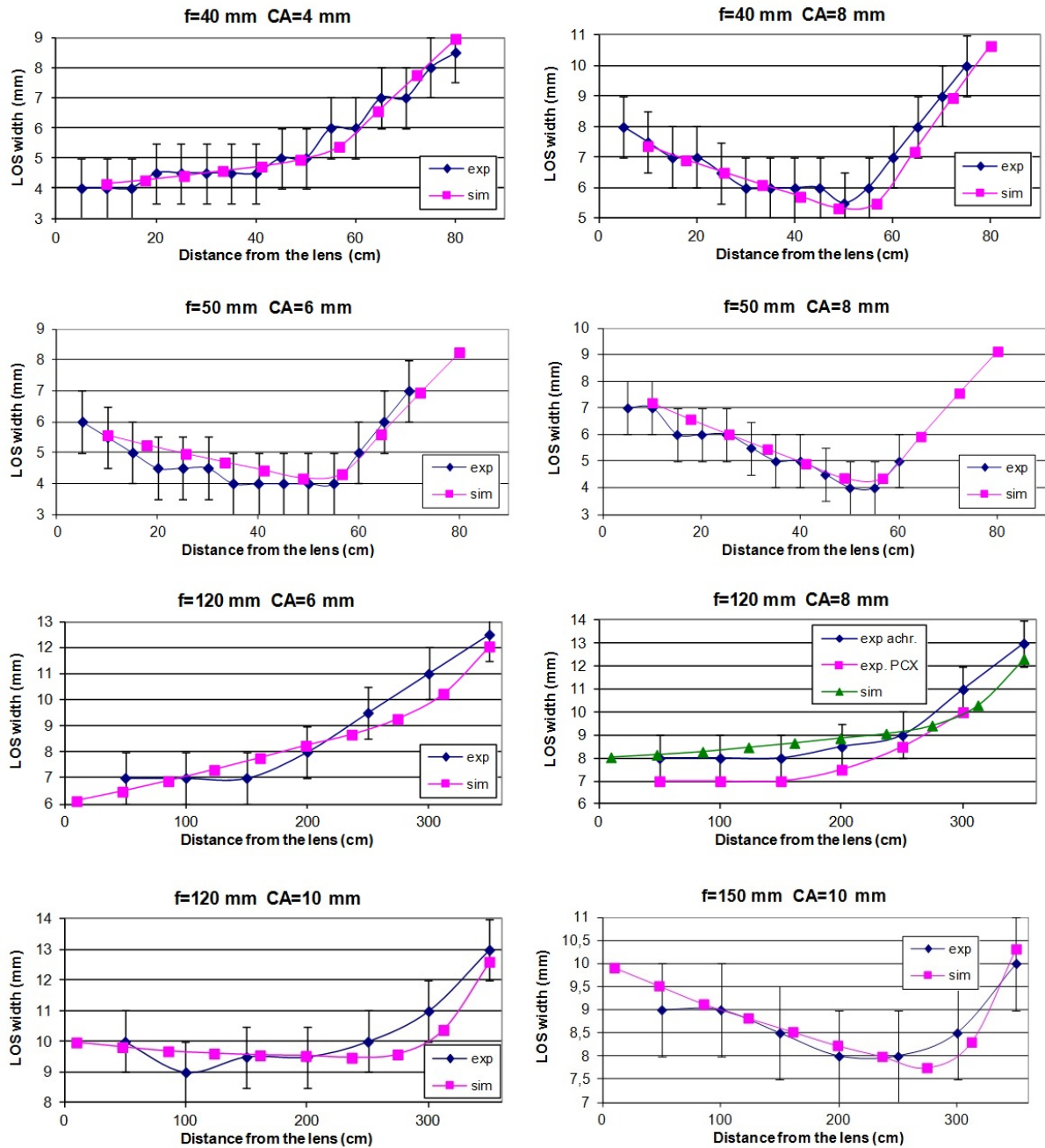
Figure 4.5: Comparison of the width of the LOS measured experimentally (blue points) along the optical axis and the results of the simulations (pink points), for various values of f and C_a. It was empirically estimated that the width measurements have an error of about $\pm 1\,mm$.

The agreement between the experiment and simulations is good. The algorithm can then be used to make predictions for optical configuration which were not tested and make further comparisons. For example, figure 4.6 compares the test on the lens with $f = 40\,mm$ and $C_a = 4\,mm$ with the simulation for a lens of $f = 50\,mm$ and same C_a. Figure 4.7 instead compares the test on the lens with $f = 120\,mm$ and $C_a = 6\,mm$ with the simulation for a lens of $f = 150\,mm$ and same C_a. Once more the lenses with the narrower LOSs are those with $f = 50\,mm$ and $f = 150\,mm$ in the respective cases.

NIO1, CA=4 mm

Figure 4.6: Comparison of the LOS width simulated for the cases of the doublet with $f = 40\,mm$ (experimental data) and of the lens with $f = 50\,mm$, both with $C_a = 4\,mm$.

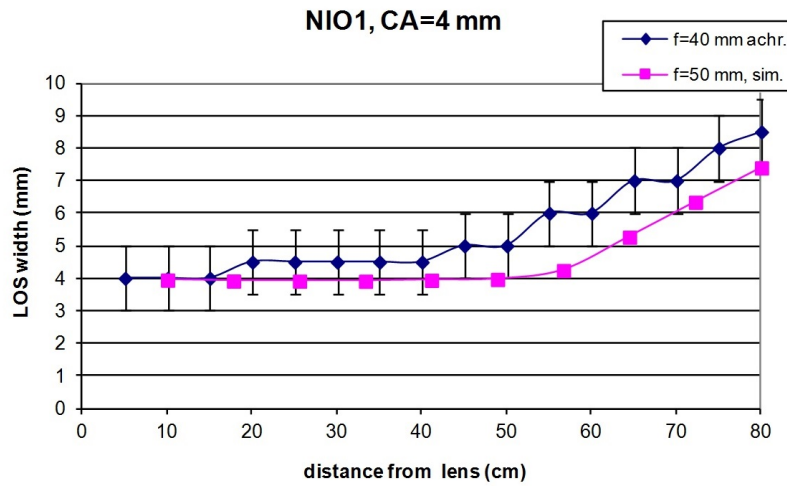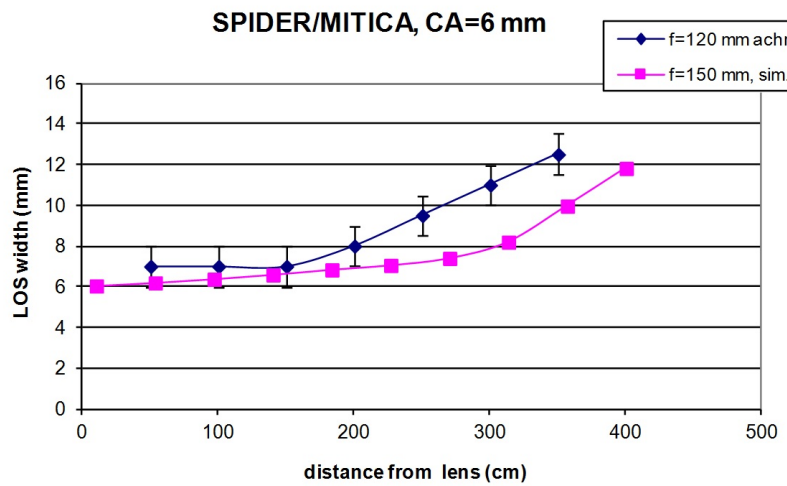**SPIDER/MITICA, CA=6 mm**

Figure 4.7: Comparison of the LOS width simulated the cases of the doublet with $f = 120\,mm$ (experimental data) and of the lens with $f = 150\,mm$, both with $C_a = 6\,mm$.

4.2.3 Mechanical tests

As previously mentioned, in the case of the OES diagnostic for SPIDER the LOSs have to pass through holes of 10 *mm* diameter, drilled on the source walls. The LOSs must not only enter the source but also exit at the opposite side . This allows to illuminate the LOSs from the viewports opposite to the telescopes, for example for the absolute calibration. Another advantage is that the alignment of the LOSs can be checked by backilluminating the fibers connected to the telescopes. To reach such strict alignment requisites it is not sufficient to properly choose the characteristics of the lenses (and therefore the dimension of the LOSs), but also a great care must be given to the design and the realization of the supports for the telescopes. Since a SPIDER viewport could host up to 7 optic heads, it had been explored the possibility to prealign them before the installation on the viewport. A first prototype of the support (figure 4.8) was tested in 2014. It should keep all the telescopes in position without further adjustments.

Figure 4.8: Prototype of the support for the optic heads dedicated to the OES diagnostic in SPIDER.

The telescopes designed for SPIDER have the dimensions indicated in figure 4.9. When inserted in the support, they stop at the disk-like protrusion on their external surface ; they then can be fastened with particular metal washers, visible in the photo of figure **??**, which are screwed on the main block. The support was tested by mounting the telescopes on all the apertures; the fibers of the telescopes were backilluminated so that the LOSs are made visible as light spots. The position of the light beams was checked at the distance corresponding to the exit of the LOSs from the source case. It resulted that the LOSs were too much misaligned respect the limits imposed by the apertures in the source. To eliminate the misalignments the telescopes were rotated and exchanged between the available apertures of the support, but in vain.
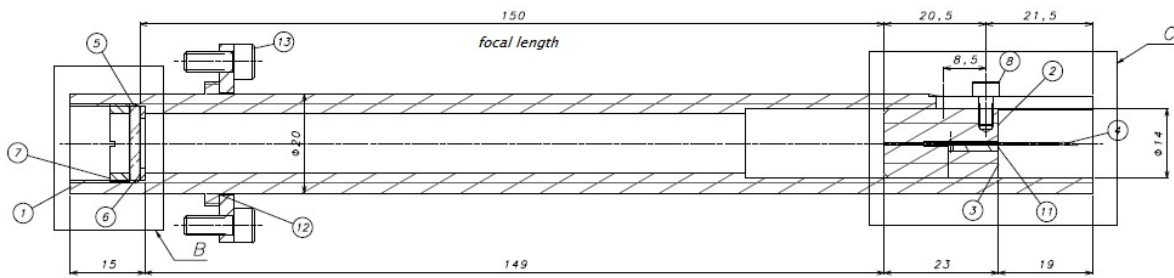
Figure 4.9: Scheme and realization of the prototype of the telescopes for the OES diagnostic in SPIDER.

It was noticed also that even small forces applied perpendicularly to a telescope can produce not negligible (even if reversible) deviations of the LOS. This is mainly due to derlin, the plastic material with which both the support and the telescopes are built. It is therefore clear that in to reach the necessary alignment the telescopes shouldn't be fastened in static positions defined by the construction of the support.

During the tests the optical fibers frequently broke at the point in which they exit from the fiber holder. As countermeasure the fibers were enclosed in thin plastic tubes, fastened by the fiber holder. This solution however didn't give the desired results; as alternative the fibers will be connected to the fiber holder (and protected) by means of FC or SMA connectors. This solution will be adopted for all the telescopes of the OES diagnostic. For example, the upgraded design of the telescopes for NIO1 is shown in figure 4.10.
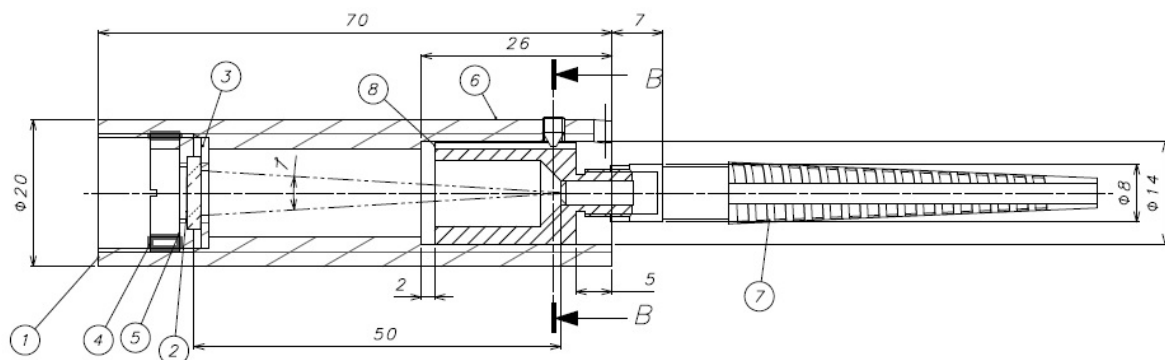

Figure 4.10: Upgraded scheme of the prototype of the telescopes for the OES diagnostic in SPIDER. The fiber is fastened by means of a SMA connector.

4.3   Discussion of the results

The reported tests provide useful information about the performances and the best use of the considered components for the OES and BES diagnostics. The camera *Andor iKon-M 934* can be used in NIO1, SPIDER and MITICA for BES. A readout rate of $3\,MHz$ and a vertical shift time of $11.3\,\mu s$ can be used as reference parameters for the normal operation of the camera; however, to maintain the noise level under $10\,e$ the readout rate should be lowered to $1\,MHz$. The only issue to care about is the time required by the shutter in order to have reliable measurements. Assuming that $t_{open} = 62\,ms$, $t_{close} = 50\,ms$, that t_{exp} should be at least $50\,ms$ in the case of SPIDER (sec. 3.1 and 3.2) and that the readout process may require about $35\,ms$, then the maximum frame rate for BES would be of about $5.1\,fps$. This value reduces to $4.0\,fps$ in the case of NIO1, for which $t_{exp} \geq 100\,ms$ (sec. 3.1), and to $3.4\,fps$ in the case of MITICA, for which $t_{exp} \geq 150\,ms$ (sec. 3.2).

The tests on the prototypes of the optic heads confirmed their functionality, in particular the possibility of adjusting the position of the fiber by hand to reach the correct focusing. The design of the fiber holder was chosen in order to ensure the best stability of the position of the fiber. The comparison between the shapes of the LOSs produced by lenses with different focal length and clear aperture led to the choice of adopting the following lenses:

	Diagnostic	f **(mm)**	C_a **(mm)**
SPIDER	OES	150	8
& MITICA	BES	150	8
	OES	40	6
NIO1	OES (2nd choice)	50	4
	BES	50	4

Table 4.5: The values of f and C_a chosen for the lenses of the optic heads.

The simulations of the optic heads in the various configurations are in good agreement with the measurements; this provided a first validation of the algorithm used in dBES to calculate the solid angle of collection of the optic heads. At last, the tests on the prototype of the support for the telescopes of the OES diagnostic in SPIDER suggested that the telescopes must not be mounted all together in a fixed position, but it should be possible to finely adjust the alignment of each one of them.

Chapter 5

Summary

Aim of the PhD research activity has been to design a BES diagnostic for the NIO1 test facility and to improve the design of the BES diagnostics for the SPIDER and MITICA test facilities. Beam emission spectroscopy will allow to measure the divergence and the direction of the beamlets produced in the test facilities; monitoring the divergence and the orientation of the beamlets is crucial to prevent an excessive thermal load in the beam line components. BES will also measure the beam uniformity, which is requested to be higher than 90%. The design of the BES diagnostics was performed with the ultimate goal of allowing the diagnostics to measure divergence and beam uniformity with an error below 10%.

To support the design of the BES diagnostics the dBES code was developed: the program simulates the spectra acquired by the diagnostics, keeping into account the geometry and the divergence of the beamlets, besides the optic properties of the devices which compose the diagnostic. dBES has also routines to analyze the BES spectra acquired by a diagnostic or simulated by dBES or other codes.

The validity of dBES as tool for the design of BES diagnostics was checked by benchmarking the results of the simulations against the BES spectra experimentally acquired at the BATMAN, MANITU and ELISE test facilities of IPP Garching. dBES was benchmarked also against the Monte Carlo codes BBC-NI simple and BBC-NI advanced, developed at IPP Garching to study the spectra acquired by of the BES diagnostic and to support advanced methods of analysis of the spectra themselves. It was possible to check in which conditions the volume, area and origin effects on the the shape of the Doppler peak are not negligible and can significantly alter the measurements of divergence. The dBES code, in its standard version, doesn't consider the 3 just mentioned effects in the calculation of the shape of the Doppler peak, therefore it was necessary to check when this approximation is valid. Assuming that the beamlets have a Gaussian power density profile, it was calculated that the distortion of the Doppler peak is mainly driven by the beamlets' divergence, while the origin effect is negligible. To partially compensate the effects of the distortions of the Doppler peak on the measurement of ϵ it is necessary to fit the Doppler peak in an interval of wavelengths symmetrical with respect to the centroid of the peak itself.

The analysis of the experimental data and of the spectra simulated by dBES and BBC-NI simple didn't allow to establish whether the beamlets have a Gaussian power density distribution or if the angular distribution of the beamlets' particles with respect to their axes is Gaussian.

The analysis of the spectra acquired by the BES diagnostics in BATMAN and ELISE showed that the Doppler peak in the spectrum deviates from a Gaussian shape especially at low values of divergence, contrarily to what expected from the volume, area and origin effects. This behavior was not however found in all the experimental data considered in the analysis. A plausible hypothesis is that the asymmetries of the Doppler peak are due to deviations of the beamlets, in turn caused by the mutual repulsion of the beamlets and by the alternated magnetic filter fields of the magnets embedded in the EG. This

hypothesis would be supported by the evidence that the divergence measured from the spectra of the vertical LOSs is slightly lower than the values given by the horizontal LOSs; the deviations of the beamlets due to the EG magnets are indeed expected to be in the horizontal plane, not in the vertical one. Non negligible asymmetries were however observed also in the Doppler peaks of spectra acquired by vertical LOSs. Anyway, the possible deviations of the beamlets' direction from the nominal one represent a serious issue for the measurements of divergence, because the broadenings of the Doppler peak caused by the divergence and by (slight) random deviations of the beamlets cannot be distinguished.

The dBES code has been used to design the BES diagnostic in NIO1 employing the available instrumentation. It is foreseen that the BES system will be able to measure the beamlets' divergence in the range $5\,mrad \div 10\,mrad$ with an error between 7% and 28%. Values of divergence from $10\,mrad$ to $40\,mrad$ will be measured with an even lower relative error. It must be considered that unwanted deviations of the beamlets can cause non negligible systematic errors, especially when low values of divergence are measured.

The simulations of the dBES code confirmed that the BES diagnostics in SPIDER and MITICA will be able to measure the beamlets' divergence with an error below 10%. In the case of the BES spectra simulated for MITICA the particular shape of the Doppler peaks required to develop specific fitting procedures to measure ϵ; the stability of these algorithms must be monitored, especially if the contribution of the stripping losses were important and overlapped with the Doppler peak. It was verified instead that the beamlets' halo shouldn't represent a concern for the measurements of divergence. The simulations of dBES for MITICA showed that in this case the finite de-excitation time of the beam particles must be taken into account to correctly reproduce the intensity of the BES spectra.

With dBES it was possible to estimate the precision with which the LOSs should be aligned to the beamlets in order to keep the systematic errors of the measures of beam uniformity below 10%. It resulted that measuring the beam uniformity by comparing the integrals of the Doppler peak of spectra acquired by different LOSs is a too inaccurate method. The alignment of the optic heads could be improved with an iterative process, trying to maximize the intensity of the acquired spectra. Alternatively, the measures of uniformity could then be performed as it is currently done at IPP Garching, i.e. by considering the divergence profiles of the beam in horizontal and vertical direction, which are related to the analogous profiles of extracted current.

It was demonstrated that in the case of SPIDER and MITICA the intensity of the spectra collected by BES are particularly sensitive to the alignment of the optic heads with the beamlets. Since the position and the orientation of the optic heads cannot be adjusted manually during the operation of the test facilities, the supports on which the optic heads are mounted should preferably be remotely controllable.

The work of simulation and design was accompanied by experimental tests on the instrumentation dedicated to the BES diagnostics. The tests on the camera which will be used in the BES diagnostics allowed to establish the best temporal resolution achievable by the diagnostics: from $3.4\,fps$ in the case of MITICA to $4.0\,fps$ in the case of NIO1 and $5.1\,fps$ in the case of SPIDER. The tests on the optic heads for the BES and OES diagnostics allowed to optimize their optical configuration, in particular to minimize the vignetting caused by the holes which should allow the LOSs to enter the ion source. The data collected during the tests gave a first validation of the optical simulations used in dBES to calculate the solid angle of collection of the photons.

To improve the analysis of the BES spectra it will be necessary to establish how and how much the volume, area and origin effects really influence the measurements of divergence. The distortion of the peak caused by these effects must be decoupled from the angular distribution of the particles in each beamlet and by the effective direction of these beamlets. To do this, the number of beamlets intersected by each LOS should be as low as possible, and the analysis of the BES spectra must be supported by other

diagnostics capable of resolving the properties of the single beamlets (like the mini-STRIKE diagnostic). The NIO1 test facility seems to have all the characteristics to perform these further studies.

Published articles

Articles published as first author

- M. Barbisan, B. Zaniol, M. Cavenago and R. Pasqualotto, *Modeling and design of a BES diagnostic for the negative ion source NIO1*, Rev. Sci. Instrum. 85, 02A708 (2014)

- M. Barbisan, B. Zaniol and R. Pasqualotto, *Modeling and simulation of a beam emission spectroscopy diagnostic for the ITER prototype neutral beam injector*, Rev. Sci. Instrum. 85, 11E430 (2014)

Articles published as co-author

- B. Zaniol, R. Pasqualotto and M. Barbisan, *Design of a beam emission spectroscopy diagnostic for negative ions radio frequency source SPIDER*, Rev. Sci. Instrum. 83, 043117 (2012).

- P. Sonato, D. Boilson, T. Bonicelli, AK. Chakraborty, C. Day, P. Franzen, G. Gorini, T. Inoue, J. Milnes, T. Minea, HPL De Esch, P. Agostinetti, M. Agostini, V. Antoni, M. Barbisan et al., *Design of the MITICA neutral beam injector: from physics analysis to engineering design*. Proc. 24th IAEA Fusion Energy Conf.(San Diego, CA, October 2012). 2012.

- P. Martin, M.E. Puiatti, P. Agostinetti, M. Agostini, J.A. Alonso, V. Antoni, L. Apolloni, F. Auriemma, F. Avino, A. Barbalace, M. Barbisan et al., *Overview of the RFX-mod fusion science programme*. Nuclear Fusion 53(10), 104018 (2013).

- M. Cavenago, G. Serianni, T. Kulevoy, S. Petrenko, P. Agostinetti, V. Antoni, M. Bigi, D. Conventi, F. Fellin, A. Minarello, M. De Muri, R. Pasqualotto, M. Recchia, M. Rigato, M. Sattin, M. Barbisan et al., *Construction of a versatile negative ion source and related developments*. Third international symposium on Negative Ions, Beams and Sources (NIBS 2012). Vol. 1515. No. 1. AIP Publishing, 2013.

- R.S. Delogu, M. Brombin, B. Zaniol, M. Agostini, M. Barbisan, N. Fonnesu, M. Tollin, R. Pasqualotto, *Optical layout and alignment methods for visible tomography and emission spectroscopy diagnostics in SPIDER*. IEEE 25th Symposium on Fusion Engineering (SOFE 2013), IEEE, 2013.

- M. Cavenago, G. Serianni, V. Antoni, M. Barbisan, M. Bigi, M. De Muri, E. Fagotti, F. Fellin, T. Kulevoy, A. Minarello et al., *Installation of a versatile multiaperture negative ion source*, Rev. Sci. Instrum. 85(2), 02A704 (2014).

- F. Bonomo, B. Ruf, M. Barbisan, S. Cristofaro, L. Schiesko, U. Fantz, P. Franzen, R. Pasqualotto, R. Riedl, G. Serianni, D. Wünderlich and the NNBI-Team, *BATMAN Beam Properties Characterization by the Beam Emission Spectroscopy Diagnostic*, Fourth international symposium on Negative Ions, Beams and Sources (NIBS 2014), in course of publication.

- B. Zaniol, M. Cavenago, G.Serianni, M. De Muri, M. Barbisan, A. Mimo, R. Pasqualotto, *NIO1 diagnostics*, Fourth international symposium on Negative Ions, Beams and Sources (NIBS 2014), in course of publication.

- M. Cavenago, G. Serianni, V. Antoni, M. Bigi, M. De Muri, R. Pasqualotto, M. Recchia, P. Veltri, P. Agostinetti, M. Barbisan et al., *Development of versatile multiaperture negative ion sources*, Fourth international symposium on Negative Ions, Beams and Sources (NIBS 2014), in course of publication.

Technical notes

- M. Barbisan, B. Zaniol, R. Pasqualotto, *Modelling of a BES diagnostic prototype for SPIDER/MITICA to be tested on NIO1 RF source*, RFX-SPIDER-TN-213, F4E grant F4E-RFX-PMS-A-WP-2012, task deliverable T3.3/P1, 2012.

- M. Barbisan, B. Zaniol, *Test bench of the candidate cameras and spectrometers for the OES in NIO1, SPIDER and MITICA*, RFX-SPIDER-TN-219, F4E grant F4E-RFX-PMS-A-WP-2012, task deliverable T3.3/P1, 2012.

- B. Zaniol, M. Barbisan, *Alignment requirements in PRIMA BES diagnostics*, RFX-SPIDER-TN-226, F4E grant F4E-RFX-PMS-A-WP-2012, task deliverable T3.3/P1 and T4.9/P1, 2012.

- M. Barbisan, B. Zaniol, *Design and tests of the optic heads for optical emission spectroscopy in SPIDER, MITICA and NIO1*, RFX-SPIDER-TN-291, F4E grant F4E-RFX-PMS-A-WP-2013, task deliverable T3.3/P1, 2013.

- M. Barbisan, B. Zaniol, *Improvements to simulations and data analysis of beam emission spectroscopy in SPIDER, MITICA and NIO1*, RFX-SPIDER-TN-292, F4E grant F4E-RFX-PMS-A-WP-2013, task deliverable T3.3/P1, 2013.

Bibliography

[1] *"World Energy Resources: 2013 Survey"*. WEC - World Energy Council, 2013.

[2] UN Department of economic and social affairs population division, *""world population to 2300","* 2004.

[3] *"Human Development Report 2014"*. UNDP - United Nations Development Programme, 2014.

[4] D. MacKay, *Sustainable Energy-without the hot air*. UIT Cambridge, 2008.

[5] A. Bradshaw, T. Hamacher, and U. Fischer, "Is nuclear fusion a sustainable energy form?," *Fusion Engineering and Design*, vol. 86, no. 9-11, pp. 2770–2773, 2011. Proceedings of the 26th Symposium of Fusion Technology (SOFT-26).

[6] J. Wesson, *Tokamaks*, vol. 149. Oxford University Press, 2011.

[7] "Physicsworld.com: Fusion, the way ahead `http://physicsworld.com/cws/article/print/2006/mar/01/fusion-the-way-ahead`," 2006.

[8] T. Oikawa, J. Park, A. Polevoi, M. Schneider, *et al.*, "Benchmarking of neutral beam current drive codes as a basis for the integrated modeling for ITER," in *Proc. 22nd Int. Conf. on Fusion Energy*, 2008.

[9] R. Hemsworth, H. Decamps, J. Graceffa, B. Schunke, *et al.*, "Status of the ITER heating neutral beam system," *Nuclear Fusion*, vol. 49, no. 4, p. 045006, 2009.

[10] E. Speth, H. Falter, P. Franzen, U. Fantz, *et al.*, "Overview of the rf source development programme at IPP garching," *Nuclear Fusion*, vol. 46, no. 6, p. S220, 2006.

[11] U. Fantz, P. Franzen, W. Kraus, M. Berger, *et al.*, "Negative ion rf sources for ITER NBI: status of the development and recent achievements," *Plasma Physics and Controlled Fusion*, vol. 49, no. 12B, p. B563, 2007.

[12] B. Ruf, *Reconstruction of Negative Hydrogen Ion Beam Properties From Beamline Diagnostics*. PhD thesis, Universität Augsburg, 2014.

[13] B. Heinemann, H. Falter, U. Fantz, P. Franzen, *et al.*, "Design of the half-size ITER neutral beam source for the test facility ELISE," *Fusion Engineering and Design*, vol. 84, no. 2-6, pp. 915–922, 2009. Proceeding of the 25th Symposium on Fusion Technology (SOFT-25).

[14] I. G. Brown, *The physics and technology of ion sources*. John Wiley & Sons, 2006.

[15] R. S. Hemsworth, H. P. L. de Esch, M. Kovari, L. Svensson, *et al.*, "Status of the development of the singap accelerator for iter," *AIP Conference Proceedings*, vol. 925, no. 1, 2007.

[16] H. De Esch and L. Svensson, "Negative ion beam halo mitigation at the 1mv testbed at IRFM," *Fusion Engineering and Design*, vol. 86, no. 4, pp. 363–368, 2011.

[17] L. Grisham, P. Agostinetti, G. Barrera, P. Blatchford, *et al.*, "Recent improvements to the ITER neutral beam system design," *Fusion Engineering and Design*, vol. 87, no. 11, pp. 1805 – 1815, 2012.

[18] W. Kraus, U. Fantz, P. Franzen, *et al.*, "The development of the radio frequency driven negative ion source for neutral beam injectors (invited)," *Review of Scientific Instruments*, vol. 83, no. 2, 2012.

[19] R. Pasqualotto, "Diagnostics for high power beams in nuclear fusion experiments," 2013. presentation at the 3rd International Conference Frontiers in Diagnostic Technologies (FTD).

[20] M. De Muri, *Simulation, design and tests of a diagnostic calorimeter for the spider experiment.* PhD thesis, Università degli Studi di Padova, 2013.

[21] "Neutral beam heating and current drive system," Design Description Document (DDD) 5.3, ITER, 2001.

[22] P. Sonato, P. Agostinetti, G. Anaclerio, V. Antoni, *et al.*, "The ITER full size plasma source device design," *Fusion Engineering and Design*, vol. 84, no. 2-6, pp. 269 – 274, 2009. Proceeding of the 25th Symposium on Fusion Technology (SOFT-25).

[23] R. Pasqualotto, E. Gazza, G. Serianni, B. Zaniol, *et al.*, "Spectroscopic diagnostics for the negative ion RF source SPIDER," *Nuclear Instruments and Methods in Physics Research Section A: Accelerators, Spectrometers, Detectors and Associated Equipment*, vol. 623, no. 2, pp. 794 – 796, 2010. 1st International Conference on Frontiers in Diagnostics Technologies.

[24] E. Gazza and B. Zaniol, "SPIDER diagnostics - source emission spectroscopy," Technical note RFX-TN-SPIDER-014, Consorzio RFX, 2009. F4E Grant F4E-2008-GRT-011-01, task deliverable T3.8/D2, T3.8/D3, T4.2/D1, T5.4/D1.

[25] B. Zaniol and R. Pasqualotto, "Source emission spectroscopy diagnostic on SPIDER - system description," Technical note RFX-TN-SPIDER-124, Consorzio RFX, 2011. F4E Grant F4E-2009-GRT32-PMS-H.CD, task deliverable T3.19/D1, T3.19/D3.

[26] U. Fantz, H. Falter, P. Franzen, D. W??rlich, *et al.*, "Spectroscopy - a powerful diagnostic tool in source development," *Nuclear Fusion*, vol. 46, no. 6, p. S297, 2006.

[27] U. Fantz, "Basics of plasma spectroscopy," *Plasma sources science and technology*, vol. 15, no. 4, p. S137, 2006.

[28] D. Wünderlich, S. Dietrich, and U. Fantz, "Application of a collisional radiative model to atomic hydrogen for diagnostic purposes," *Journal of Quantitative Spectroscopy and Radiative Transfer*, vol. 110, no. 1, pp. 62–71, 2009.

[29] R. Pasqualotto, A. Alfier, and L. Lotto, "Design of a cavity ring-down spectroscopy diagnostic for negative ion RF source SPIDER," *Review of Scientific Instruments*, vol. 81, no. 10, 2010.

[30] R. Pasqualotto, M. Agostini, M. Brombin, R. Delogu, *et al.*, "Design of a visible tomography diagnostic for negative ion RF source SPIDER," *Fusion Engineering and Design*, vol. 88, no. 6, pp. 1253–1256, 2013.

[31] M. Rebai, M. Cavenago, G. Croci, M. Dalla Palma, *et al.*, "A neutron diagnostic for high current deuterium beams," *Review of scientific instruments*, vol. 83, no. 2, p. 02B721, 2012.

[32] M. Taniguchi, H. de Esch, L. Svensson, N. Umeda, *et al.*, "Development of 1 MeV H-accelerator at JAEA for ITER NB," in *American Institute of Physics Conference Series*, vol. 1097, pp. 335–343, 2009.

[33] G. Chitarin, P. Agostinetti, D. Aprile, N. Marconato, *et al.*, "Cancellation of the ion deflection due to electron-suppression magnetic field in a negative-ion accelerator," *Review of Scientific Instruments*, vol. 85, no. 2, 2014.

[34] V. Antoni, P. Agostinetti, D. Aprile, M. Cavenago, *et al.*, "Physics design of the injector source for ITER NBI," 2013. presentation held at ICIS 2013 conference.

[35] M. Brombin, M. Agostini, C. Dianin, M. Mattiolo, *et al.*, "The tomographic diagnostic of ITER neutral beam injector," *Nuclear Fusion*, vol. 53, no. 5, p. 053009, 2013.

[36] A. Krylov, D. Boilson, U. Fantz, R. Hemsworth, O. Provitina, S. Pontremoli, and B. Zaniol, "Caesium and tungsten behaviour in the filamented arc driven Kamaboko-III negative ion source," *Nuclear fusion*, vol. 46, no. 6, p. S324, 2006.

[37] E. Speth, H. Falter, P. Franzen, U. Fantz, *et al.*, "Overview of the RF source development programme at IPP garching," *Nuclear Fusion*, vol. 46, no. 6, p. S220, 2006.

[38] P. Franzen, "Negative hydrogen ion source development: Overview of the experiments," 2011. presentation held at TE Ringberg Seminar.

[39] R. Nocentini, U. Fantz, P. Franzen, M. Fr??le, *et al.*, "Beam diagnostic tools for the negative hydrogen ion source test facility ELISE," *Fusion Engineering and Design*, vol. 88, no. 6, pp. 913–917, 2013.

[40] P. Franzen, U. Fantz, W. Kraus, H. Falter, B. Heinemann, R. Nocentini, and N. Team, "Physical and experimental background of the design of the elise test facility," *AIP Conference Proceedings*, vol. 1097, no. 1, 2009.

[41] P. McNeely, S. Dudin, S. Christ-Koch, U. Fantz, and the NNBI Team, "A langmuir probe system for high power rf-driven negative ion sources on high potential," *Plasma Sources Science and Technology*, vol. 18, no. 1, p. 014011, 2009.

[42] M. Berger, U. Fantz, S. Christ-Koch, and the NNBI Team, "Cavity ring-down spectroscopy on a high power RF driven source for negative hydrogen ions," *Plasma Sources Science and Technology*, vol. 18, no. 2, p. 025004, 2009.

[43] U. Fantz and C. Wimmer, "Optimizing the laser absorption technique for quantification of caesium densities in negative hydrogen ion sources," *Journal of Physics D: Applied Physics*, vol. 44, no. 33, p. 335202, 2011.

[44] F. Bonomo, M. Barbisan, S. Cristofaro, B. Ruf, *et al.*, "BATMAN beam properties characterization by the beam emission spectrocopy diagnostic," in *4th International Symposium on Negative Ions, Beams and Sources (NIBS 2014)*, 2014.

[45] S. Cristofaro, "Characterisation of the BATMAN beam properties by H_α-doppler shift spectroscopy and mini-STRIKE calorimeter," 2014.

[46] P. Franzen, U. Fantz, and the NNBI Team, "Beam homogeneity dependence on the magnetic filter field at the ipp test facility manitu," in *SECOND INTERNATIONAL SYMPOSIUM ON NEGATIVE IONS, BEAMS AND SOURCES*, vol. 1390, pp. 310–321, AIP Publishing, 2011.

[47] D. Wünderlich, U. Fantz, P. Franzen, R. Riedl, and F. Bonomo, "Optical emission spectroscopy at the large RF driven negative ion test facility ELISE: Instrumental setup and first results," *Review of Scientific Instruments*, vol. 84, no. 9, p. 093102, 2013.

[48] A. Pimazzoni, "Investigation of ELISE beam properties by means of the diagnostic calorimeter," 2014.

[49] M. Cavenago, G. Serianni, T. Kulevoy, S. Petrenko, *et al.*, "Construction of a versatile negative ion source and related developments," in *third international symposium on negative ions, beams and sources (NIBS 2012)*, vol. 1515, pp. 157–166, AIP Publishing, 2013.

[50] M. Cavenago, G. Serianni, V. Antoni, M. Barbisan, *et al.*, "Installation of a versatile multiaperture negative ion source," *Review of Scientific Instruments*, vol. 85, no. 2, p. 02A704, 2014.

[51] M. Cavenago, G. Serianni, V. Antoni, M. Bigi, *et al.*, "Development of versatile multiaperture negative ion sources," in *4th International Symposium on Negative Ions, Beams and Sources (NIBS 2014)*, 2014.

[52] B. Zaniol, M. Cavenago, G. Serianni, M. De Muri, *et al.*, "NIO1 diagnostics," in *4th International Symposium on Negative Ions, Beams and Sources (NIBS 2014)*, 2014.

[53] A. Mimo, "Diagnostics for negative ion source NIO1," 2014.

[54] "NIST atomic spectra database: `http://physics.nist.gov/PhysRefData/ASD/lines_form.html`," 2014.

[55] E. Sartori, P. Agostinetti, S. Dal Bello, D. Marcuzzi, *et al.*, "Comparative study of beam losses and heat loads reduction methods in MITICA beam source," *Review of Scientific Instruments*, vol. 85, no. 2, 2014.

[56] E. Sartori, "Gas density distribution in MITICA beam line," Technical note RFX-TN-SPIDER-147rev1, Consorzio RFX, 2012. F4E-RFX-PMS-A-WP-2012, subtasks 4.2, 5.4.

[57] C. Barnett, "Redbook atomic data for fusion," *ORNL, New York*, vol. 1990, p. 148, 1990.

[58] B. Zaniol, "Error evaluation in the spectroscopic measurement of high power beam angular divergence," *Journal of Quantitative Spectroscopy and Radiative Transfer*, vol. 112, no. 3, pp. 513–518, 2011.

[59] V. Toigo, "Draft of ITER procurement package document for MITICA and SPIDER power supplies," Technical note RFX-TN-PRIMA-008rev1, Consorzio RFX, 2009.

[60] P. Agostinetti, G. Chitarin, P. Franzen, B. Ruf, *et al.*, "Benchmark of SLACCAD, AVOCADO and EAMCC codes against data from the MANITU testbed at IPP," Technical note RFX-TN-SPIDER-220, Consorzio RFX, 2012. F4E-RFX-PMS-A-WP-2012, task deliverable T5.4/P1.1.

[61] G. Fubiani, H. De Esch, A. Simonin, and R. Hemsworth, "Modeling of secondary emission processes in the negative ion based electrostatic accelerator of the international thermonuclear experimental reactor," *Physical Review Special Topics-Accelerators and Beams*, vol. 11, no. 1, p. 014202, 2008.

[62] P. Franzen, W. Kraus, D. Wünderlich, B. Heinemann, *et al.*, "IPP activities 2013," yearly report, IPP Garching, 2013. F4E-PRIMA-B2B.

[63] B. Ruf, private communication.

[64] F. Bonomo, M. Barbisan, S. Cristofaro, B. Ruf, *et al.*, "BATMAN beam properties characterization by the beam emission spectrocopy diagnostic," 2014. Poster presented at the 4th International Symposium on Negative Ions, Beams and Sources (NIBS 2014).

[65] P. Spädtke and C. Mühle, "Simulation of ion extraction and beam transport," *Review of Scientific Instruments*, vol. 71, no. 2, 2000.

[66] E. Sartori and P. Veltri, "AVOCADO: A numerical code to calculate gas pressure distribution," *Vacuum*, vol. 90, pp. 80–88, 2013.

[67] "Permag official website: `http://www.fieldp.com/permag.html`," 2014.

[68] W. Ott and F. Penningsfeld, "Spectroscopic determination of species and divergence of hydrogen beams in the W7AS neutral beam injectors," Technical report IPP4/258, IPP Garching, 1993.

[69] U. Fantz, P. Franzen, W. Kraus, M. Berger, *et al.*, "Physical performance analysis and progress of the development of the negative ion RF source for the ITER NBI system," *Nuclear Fusion*, vol. 49, no. 12, p. 125007, 2009.

[70] M. Recchia and M. Bigi, "Main performance specifications of NIO1 power supplies," Technical note RFX-NIO-TS-01-r1, Consorzio RFX, 2013.

[71] M. Barbisan, B. Zaniol, and R. Pasqualotto, "Modelling of a BES diagnostic prototype for SPIDER/MITICA to be tested on NIO1 RF source," Technical note RFX-SPIDER-TN-213, Consorzio RFX, 2012. F4E-RFX-PMS-A-WP-2012, task deliverable T3.3/P2.

[72] B. Zaniol and R. Pasqualotto, "Beam emission spectroscopy diagnostic on SPIDER - system description," Technical note RFX-SPIDER-TN-116, Consorzio RFX, 2009. F4E Grant F4E-2009-GRT32-PMS-H.CD, task deliverable T3.19/D1.

[73] P. Agostinetti, V. Antoni, M. Cavenago, E. Sartori, *et al.*, "Physics and engineering analyses on the MITICA accelerator," Technical note RFX-SPIDER-TN-33-rev5, Consorzio RFX, 2011. F4E Grant F4E-2009-GRT32-PMS-H.CD, tasks deliverable T4.2/D3, T6.1/D1-D2-D3, T6.2/D1.

[74] P. Agostinetti, V. Antoni, M. Cavenago, G. Chitarin, *et al.*, "Physics and engineering design of the accelerator and electron dump for SPIDER," *Nuclear Fusion*, vol. 51, no. 6, p. 063004, 2011.

[75] B. Zaniol and M. Barbisan, "Optical emission spectroscopy diagnostic on MITICA - system description," Technical note RFX-MITICA-TN-163, Consorzio RFX, 2012. F4E-RFX-PMS-A-WP-2012, task deliverable T4.9/P1.

[76] M. Barbisan, "Studio di una diagnostica spettroscopica per il fascio dell'esperimento MITICA," 2011.

[77] R. Pasqualotto, M.Tollin, W. Rigato, M. D. Palma, *et al.*, "MITICA beamline optical diagnostics lines of sight," Technical note RFX-MITICA-TN-163, Consorzio RFX, 2011. F4E Grant F4E-2011-GRT-313 (PMS-H.CD), task deliverable T4.6/P2.

[78] P. Veltri, P. Agostinetti, M. Cavenago, G. Chitarin, *et al.*, "Multi-beamlets optics studies of the MITICA accelerator," Technical note RFX-TN-MITICA-0161, Consorzio RFX, 2012. F4E-RFX-PMS-A-WP-2012, subtasks 4.2, 5.4 and 5.5.

[79] B. Zaniol, R. Pasqualotto, and M. Barbisan, "Design of a beam emission spectroscopy diagnostic for negative ions radio frequency source SPIDER," *Review of Scientific Instruments*, vol. 83, no. 4, p. 043117, 2012.

Acknowledgements